An in situ Surface Stress Study of Electrochemical Phenomena:

Electrodeposition and Molecular Adsorption

by

Thomas Heaton

A Dissertation Presented in Partial Fulfillment
of the Requirements for the Degree
Doctor of Philosophy

Approved September 2011 by the
Graduate Supervisory Committee:

Cody Friesen, Chair
Daniel Buttry
Karl Sieradzki

ARIZONA STATE UNIVERSITY

December 2011

ABSTRACT

Over the last decade copper electrodeposition has become the dominant process by which microelectronic interconnects are made. Replacing ultra-high vacuum evaporative film growth, the technology known as the Cu damascene process has been widely implemented in the microelectronics industry since the early 2000s. The transition from vacuum film growth to electrodeposition was enabled by solution chemistries that provide "bottom-up" or superfilling capability of vias and trenches. While the process has been and is used widely, the actual mechanisms responsible for superfilling remain relatively unknown. This dissertation presents and discusses the background and results of experimental investigations that have been done using in situ electrochemical surface stress monitoring techniques to study the evolution of stress on Cu{111} thin film electrodes. Because of its extreme sensitivity to the structure on both the electrode and solution sides of the interface, surface stress monitoring as analytical technique is well suited for the study of electrodeposition. These ultra-high resolution stress measurements reveal the dynamic response of copper electrodes to a number of electrochemical and chemical experimental variables. In the case of constant current pulsed deposition and stripping, the surface stress evolution depends not only on the magnitude of the current pulse, but also shows a marked response to plating bath composition. The plating bath chemistries used in this work include (1) additive free, (2) deposition suppressing solutions that include polyethylene glycol (PEG) and sodium chloride (NaCl) as well as (3) full additive solution combinations which contain PEG, NaCl, and a one of two

deposition accelerating species (bis-(sodiumsulfopropyl)disulfide (SPS) or mercaptopropane sulfonic acid (MPS)). The development of thin film stress is further investigated through a series of solution exchange experiments that correlate the magnitude of electrode exchange current density and the stress state of the film. Remarkably, stress changes as large as ~8.5 N/m are observed during solution exchanges at the open circuit potential. Overall, this research demonstrates that solution chemistry can have a large impact on thin film stress evolution, even for very small deposition thicknesses (e.g. <10 ML) or in the absence of net addition or removal of material from the electrode.

ACKNOWLEDGMENTS

At the end of this next step in my progression as a student of science, I must express my most sincere gratitude to those who have enabled me to reach this point. I would first like to thank my advisor and mentor Professor Cody Friesen for all of the time given and efforts made on my behalf. It was his guidance and optimism (not to mention patience) that spurred me to continue my education after my undergraduate experience. Previous to meeting Dr. Friesen and becoming involved in scientific research, I hadn't given so much as a single thought to pursuing a Ph.D. Through the good times and bad, I have never regretted the decision to enter graduate school and learn more about the intriguing world around me. Additionally, I must also recognize my Ph.D. committee members for their support and guidance. Both Prof. Buttry and Prof. Sieradzki have served as course instructors and research mentors to me throughout my graduate career.

I also owe a great debt of gratitude to my fellow students and lab mates that have served as both sounding boards and counselors over the years. They have picked me up in my times of difficulty and discouragement. Many times I have taken random thoughts and questions to them and have always found myself better off for it. Many students, post-docs, and research scientists have passed through our lab over the years but I especially want to acknowledge the other two "Amigos" --Jordan Kennedy and Larry Mickelson-- for everything they have done for me. The Three Amigos have been together since the beginning and it has been a pleasure and a blessing to have them as my friends and coworkers.

As any honest graduate student can tell you, a Ph.D. cannot be earned alone. I have regularly depended on a number of faculty, support staff, and research professionals throughout my career at ASU. First and foremost, I must recognize Susan Baldi for her untiring support and patience. Since the day that she became a member of our group, we have had more fun and had a better time all around because of her fun personality and unselfish nature. She is simply the best. Also, I would be remiss if I did not acknowledge all of the scientific help and advice provided to me by the members of Sieradzki group, especially by Xiaoqian Li and Dr. Lei Tang. I also want to thank Prof. Pedro Peralta for providing me with the copper single crystal that was used to construct the Cu(111) single crystals discussed in Chapter 12 and Appendix C. A big thanks to Señor Fred Peña for his help and friendship stretching back even before I entered grad school. I am also grateful for Christi Roeger and her masterful work in the glassblowing shop and for the countless times that she has saved me by fixing my clumsy mistakes. Additionally, I have relied heavily on the excellent work of the machinists here at ASU. Without them the "Maytag" could never have been anything more than a concept and a drawing. My gratitude goes out to Dave Gillespie and Marty Johnson, among others, which have had enough patience to help me throughout the years.

Of course I would not be where I am today without my God and my Family. It is through their sustaining force that I have accomplished anything good and worthwhile in my life. My parents gave me the desire to be the very best that I can and I have tried to stay true to that principle for my entire life.

Christian is the greatest source of pride that I have in my life. He is our grad school baby. Because of him, I was my privilege of striving to be a good father and scientist at the same time. He makes me laugh everyday and I wouldn't have it any other way. As for Stefanie, words cannot describe what you do for me everyday. It is because of you and everything that you do for me that I have been able to get to where I am today. My accomplishment is your success. Thank you for your love and support.

This research was funded under Professor Cody Friesen's National Science Foundation career award, "Stress and Structure Evolution in Ultra-Thin Heteroepitaxial Metallic Films." (DMR-0543666)

TABLE OF CONTENTS

Page

CHAPTER Page

APPENDIX Page

LIST OF TABLES

Table Page

LIST OF FIGURES

Figure Page

Figure Page

Figure Page

Figure Page

Figure Page

Figure Page

CHAPTER 1

INTRODUCTION

1.1 Background

The demand for continually faster devices has been a major driving force for innovation and improvement in the electronics industry. In order to meet this demand, the current state of the art technology employs microprocessor chips that contain more than a hundred million transistors per square centimeter. This ever-increasing transistor density requires a concomitant miniaturization that has necessitated technological advances in all areas of integrated circuit (IC) production. The metallic interconnects currently found in logic and memory microelectronic chips make up a complex multilevel structure of wiring that ranges from micron to nanometer-sized dimensions. The most basic function of this fine wiring structure is to facilitate transport of electronic signals between various components of the circuitry. From the inception of IC manufacturing, aluminum and silicon dioxide had been employed respectively as conductor and insulator material for on-chip device electrical interconnects. However, as the characteristic on-chip feature dimensions move below 200 nm, the signal transport speed is determined by the interconnect resistance-capacitance (RC) delay instead of the transistor switching speed[1-3]. Accordingly, the beneficial aspects of using copper as the conductor material were recognized within the industry long before it was put into commercial production and it was clear that the incorporation of copper was an essential step in maintaining a technological trajectory consistent with Moore's law[4]. The transition to copper metallurgy from

the previous aluminum metallurgy for on-chip interconnections (including lines, vias, and trenches) is one of the most important developments in the history of IC technology. The actual transition began around the late 1990s when researchers at IBM announced the accomplishment of the first working microprocessor which was soon followed by high-volume production of copper interconnect-containing chips[5-7]. Prior to this eventual development of the copper damascene electroplating process, several forms of physical vapor deposition (PVD), chemical vapor deposition (CVD), and electroless plating were explored[8]. Because "[p]lating is considered by many to be more of an art than a science; people experience a shock when they see precious wafers being immersed in the blue liquids many times during the manufacturing process[6]." Yet, it was the unique superfilling capability of electrolytic plating that finally was chosen for large scale commercial wafer processing.

In the years between the late 1980s and early 2000s, copper electrodeposition technology advanced through numerous application milestones ranging from the initial proof of concept to industrial high-volume manufacturing[9]. However, despite the widespread application of the Cu superfilling and the damascene process, the actual mechanisms responsible for the bottom-up trench filling as well as the overfill bump formation phenomena were not well understood. More specifically researchers could "not predict, even qualitatively, the occurrence of such events for their superfilling electrolyte or any others that might be derived thereof."[9]

In late 1999 and early 2000 researchers began to take a more serious interest in better understanding of the superfilling process. From that point in time, a large series of publications began to be published in what exists today as an extensive body of literature dedicated to linking damascene solution chemistries to superfilling, leveling, and other electroplating behaviors beneficial to Cu IC interconnect application[5-7, 10-25].

1.2 Layout of Chapters & Appendices

This dissertation represents the results of several projects and many types of experiments that were primarily focused on Cu thin film electrochemistry and its simultaneous surface stress evolution. The one exception to this appears in Appendix F which contains the as-published form of my first journal publication from the *Journal of Physical Chemistry C*. It contains results for electrochemical surface stress measurements that were collected using Pt and Au thin films. It was during this first project that the concept of the electrochemical surface stress cell was brought to fruition and also when the fundamental technique and protocol for its use was developed. This dissertation is divided conceptually into two major sections: Chapters 2-5 are included to briefly cover the academic background upon which this research was built and Chapters 7-12 contain the experimental procedure, results, and subsequent analysis that has been carried out in support of this doctoral research. The remaining chapters constitute the transitions to and from these two conceptual sections in order to facilitate the flow of the narrative presented in this dissertation.

Chapter 2 presents a thorough background behind the transition from vacuum based aluminum interconnect technology to the state of the art copper technology known as the (dual) damascene process. The virtues of copper as a superior interconnect material have long been recognized within the realm of scientific research as well as within the microelectronics industry. Previously, however, the obstacles preventing the implementation of copper metallurgy (e.g. possibility of silicon contamination, wet chemistry processing, etc.) proved too costly until the late 1990s.

The fundamentals of electrochemistry, specifically electrodeposition, and its relation to the damascene process are discussed in Chapter 3. In order to properly treat the several theories that have been proposed to explain the superfilling of surface features on etched silicon wafers, the reader must be somewhat familiar with electrochemical kinetics of deposition processes as well as the mechanisms of mass transfer within the electrolytic cell. Special consideration is also given to the primary, secondary, and tertiary current distribution models in order to introduce the concepts of leveling and non-uniform plating currents that are observed during the superfilling process. Finally, the strengths and relative weaknesses of the two prevailing models for superfilling, known as the diffusion-adsorption and the curvature enhanced accelerator coverage models, are discussed at length.

The background section continues with a brief introduction to surfaces and surface stress as given in Chapter 4. First the concepts of both a surfaces and an interface are given consideration followed by a more rigorous explanation of the

Gibbs surface model. The Gibbs surface model provides a good framework for a short description of the formalism behind thermodynamic surface quantities, including surface stress. It is here that the most important equation in this doctoral research, the Stoney relation, is both described qualitatively and defined mathematically. It is through proper application of the Stoney relation that quantitative thin film stress measurements are made possible.

Chapter 5 continues with additional considerations of stress related phenomena in thin film structures. Initially, the three main thin film growth modes and their relationship with growth stress evolution are described. In addition to the intrinsic film stresses associated with a growing film, a variety of other stress generation mechanisms are discussed. This includes a number of environmental factors that must be taken into account when performing stress measurements in electrochemical systems. More specifically, the role of stress in integrated circuit interconnect structures is treated in the context of residual stresses that are built into on-chip wiring during the deposition process and can have a major effect on the overall reliability of IC devices.

The narrative of the dissertation then transitions from the background section to the results section. Chapter 6 contains a concise summary of the objectives behind this experimental research and the reasoning behind the electrochemical systems and the types of experiments that were chosen for investigation. The experimental details and a description of the custom-designed electrochemical surface stress cell are contained in Chapter 7. This chapter includes the details of both the surface stress monitoring system as well as the

electrochemical techniques that were combined to produce ultra high resolution, real time electrochemical surface stress measurements.

The results section of the dissertation continues with the presentation of the solid electrocapillarity of Cu thin films in sulfuric acid solutions. Essentially, Chapter 8 shows experimental results that define the simple but important relationship between applied electrochemical potential and the resultant surface stress. Most significantly, it was found that not only is the electrocapillarity response relatively small in magnitude, but it is also opposite in sign from the potential. That is, within the potential range in which oxidative stripping of copper does not occur, the surface stress due to electrocapillarity is easily distinguished and usually of negligible magnitude with respect to film growth induced stresses.

Chapters 9 and 10 compose a significant portion of the experimental results obtained in support of this doctoral research. They include the surface stress results of electrodeposited and stripped Cu thin films in a variety copper plating solutions that are relevant to the Cu damascene process. Specifically, a well defined series of chronopotentiometric current pulses were employed at current densities of 1 & 5 mA/cm^2 in all the various solution combinations in order to observe the effects of plating additives. Overall it was found that both the compressive event stresses associated with deposition as well as the tensile event stresses due to oxidative stripping increased in magnitude as three component additive solution combinations were used as plating baths. Additionally, the bulk residual stress also increased with the use of additives,

providing powerful insight into the residual effects that these additives may have on the reliability of IC interconnects produced through this process.

Following the examination of the effects of additives on deposition and stripping induced stresses, the effect of an appreciable cuprous ion concentration is discussed in Chapter 11. In this chapter, a series of chronopotentiometric techniques, identical to that used in Chapters 9 and 10, are used to study the surface stress evolution of Cu thin films in solutions that contain both cupric (Cu^{2+}) and cuprous (Cu^{+}) ions. Because industrial damascene processing utilizes air saturated plating baths in which cuprous ions not stable, the effect of an appreciable cupreous ion concentration is not well understood. The present work was motivated by recent discussion in the literature on the role of cuprous ion complexes in trench superfilling phenomena. While it is generally accepted that Cu^{+} does indeed play role, there is some disagreement on the exact nature of that role. In Chapter 11, the effect of an appreciable cuprous ion concentration is shown to be dependent on plating solution composition. A remarkable difference in the resultant surface stresses was observed in electrodeposition suppressing solutions while no discernible effect was seen in full additive solutions.

Chapter 12 completes the experimental results section of the dissertation with a different type of experiment that was developed to study solution side phenomena in the absence of electrochemical control of the interface. These investigations are identified as *open circuit potential solution exchange* experiments due to the fact that the open circuit is monitored simultaneously with the surface stress evolution while an initial electrolytic solution is carefully

replaced by a final solution of different composition. In contrast to the other experimental results presented herein, the solution exchange experiments demonstrate that surprisingly large surface stresses can develop on thin film electrodes even in the absence of net addition/removal of material to/from the electrode surface. These changes in surface stress were found to correlate well with the concentration dependence of the electrode exchange current density as described by electrochemical theory.

Finally, a summary of the results and conclusions presented in Chapters 8-12 is given in Chapter 13. The major observations and general trends seen throughout the various systems and experimental techniques are then tied together giving a view of the overall surface stress behavior of Cu thin films in electrolytic solutions. Additionally, Appendices A-F can be found after the reference section. They contain the design (sketches & drawings) of the electrochemical surface stress cell (Appendix A), a reproduction of the first publication containing results collected using this custom designed surface stress cell (Appendix F), the Matlab script that was created to analyze data presented in Chapters 9 & 10 (Appendix B), a sketches and a brief description of the single crystal electrodes used in Chapter 12 (Appendix D), the original data plots used to create Figures 12.3, 12.4, and 12.5 (Appendix E), and the copyright permissions secured by the author in order to reproduce various figures throughout this dissertation (Appendix C).

CHAPTER 2

COPPER AS AN IC INTERCONNECT MATERIAL

2.1 Advantages of Using Copper as an Interconnect Material

The advantages of using copper as an interconnect material have been considered by many groups both academic and commercial[2, 3, 5-9, 26-30]. Ideally, this transition in conductor material was to be accompanied by a change in insulator as well. It has been estimated that a three-fold reduction in RC delay could be achieved through the use of Cu and a low dielectric constant (ε) insulator such as polyimide[27]. Nevertheless, because significant improvement is obtained by using copper as the wiring metal alone, Cu metallization was implemented without a low-ε insulator.

Since the electrical resistivity of bulk Cu (~1.7 μΩ-cm) is more than 33% lower than that of Al (~2.7 μΩ-cm), copper wiring provides for extension of IC interconnects below the size threshold limit of Al. This is mainly due to a significant reduction in joule heating at smaller wire thicknesses as power (I^2R) consumption decreases as well as the reduction of RC time delay associated with electrical signal transport. The RC delay decreases by a factor of two as the smaller Cu lines not only reduce the total line resistance but also decrease the areal contribution to inter-line capacitance. In combination with the decrease of joule heating, the reduction of capacitive charging time also reduces the total energy consumption of the IC which makes the chips more amenable to battery powered electronic devices such as laptop computers and cellular phones. The scaling down of wiring dimensions also produces a reduction in crosstalk between

IC chip components which has reduced noise characteristics during electrical signal transport[7, 8, 27, 28].

Another primary advantage of copper interconnect technology is a superior resistance to electromigration (EM), which has been a major source of interconnect and IC failure. Copper metallization has improved EM resistance of IC circuitry markedly with experiments showing several orders of magnitude improvement in interconnect time to failure (T_{50}) over aluminum and aluminum-copper alloys[1, 3]. Additionally, a reduction in EM failure rate allows for wiring architecture that can sustain higher current densities at a given wire thickness as well as scaling of interconnect linewidths to meet miniaturization goals[31].

Beside the intrinsic advantages of using copper as an interconnect material, the introduction of copper wiring also yielded improvements in the back-end-of-line (BEOL) processing. Because copper lacks a volatile compound that can be used for etching at low temperature, it requires completely different manufacturing techniques than those used for the Al architecture[32]. In fact, the process known as copper dual damascene reduced the number of required metallization steps by 20% to 30% by providing the capability of simultaneously filling multiple types of on-chip features (e.g. trenches, vias, etc) [6, 31].

2.2 Challenges of Using Copper as an Interconnect Material

In addition to the advantages afforded by the shift from aluminum to copper, many unique challenges associated with the transition to copper interconnects have arisen during the implementation of Ultra-Large-Scale Integration (ULSI). These challenges included identifying the best methodology

for copper deposition, optimizing the metal electroplating parameters within that methodology, and choosing a suitable diffusion barrier material to prevent copper contamination of the insulating and device layers[7]. Both engineering and basic scientific types of solutions are required in order to solve the problems encountered during a large technological shift such as a transition in interconnect material. This fact was readily discovered during an exploratory phase in which all of the primary methods of metal deposition were explored as a suitable replacement technology for Al metallization. Table 2.1 shows a summary of the advantages and disadvantages of each method of copper deposition as given by SEMATECH (Semiconductor Manufacturing Technology)[2]. Since IBM's transition in the late 1990s, Cu damascene has become the dominant technology for IC interconnects. However, this transition has required an entirely different approach to wafer processing.

Whereas the aluminum metallization process consists primarily of metal deposition followed by subtractive processing steps, the copper metallization process is essentially an additive process of alternating depositions of conducting and insulating layers[8, 32]. Thus, the implementation of the copper interconnects in IC production was the complete transformation from a process based on photolithography, reactive ion etching and chemical/physical vapor deposition to a wet, electrochemical based process known as copper damascene. The damascene process has roots in a long history of Cu electroplating and printed circuit board applications. Long before the idea of superfilling (i.e. filling of surface trenches and vias by electrodeposition [see Section 2.4]) had even been

conceptualized, electrochemists were using mixtures of inorganic and organic additives to produce "leveled" and "bright" electrodeposits for printed circuit boards and other surface finishing applications[26, 33, 34].

Table 2.1 - Comparison of Copper Deposition Methods[2, 7, 8]

Method	Advantages	Disadvantages
Physical Vapor Deposition (PVD)	similar to Aluminum process high metrology & film quality control	uneven coverage of surface features poor via filling characteristics
Metal Organic Vapor Deposition (MOCVD)	excellent conformal surface deposition and via filling	relatively expensive specialty organometallic chemical species required low deposition rate
Electroless Deposition	relatively inexpensive process relatively fast deposition rate no current source required relatively inexpensive processing	deposit may become unstable & decompose in solution poorly characterized & relatively unfamiliar process lack of control during plating process need for Cu seed layer to be pre-deposited on chip
Electrolytic Deposition	fast deposition rate good conformality and via filling characteristics	general concern for Cu contamination during fabrication solution disposal issues

In order to meet the demands of defect-free, bottom-up fill of high aspect ratio features, a significant amount of research and development has been done to optimize the copper damascene process. These efforts have included

investigation of the effects of varying solution compositions and concentrations, the application of dynamic potential/current profiles, and the manipulation of solution mass transfer characteristics via forced convection[8].

As an additional challenge, Cu is both a mid-band gap impurity and a fast diffusing contaminant in silicon, the combination of which can have deleterious and possibly catastrophic effects on silicon based device performance. The introduction of copper bearing species into the fabrication process consequently constitutes a major contamination concern. Furthermore, SiO_2 is both ineffectual as a Cu diffusion barrier and also poor as a Cu adhesion layer. Because of this challenge, tungsten remains as the silicon contact material at the lowest level of chip interconnects and a Cu diffusion barrier is required on all higher wiring levels between Cu metal and Si or SiO_2. The barrier metal is usually composed of TiN and/or a Ta/TaN multilayer[27, 30, 35]. The diffusion barrier further serves as a protective layer which prevents corrosion of the copper metal as well as an adhesion enhancer since a copper seed layer can be deposited on it prior to "bulk" thin film electrodeposition[32].

2.3 Aluminum vs. Copper Wafer Patterning Process

Conventional aluminum interconnect technology consists of fabrication by a subtractive method. First, a homogeneous Al thin film of about 600 nm is deposited on the substrate by physical vapor deposition. Subsequently, a layer of photoresist is deposited and cured. The photoresist is then subject to ultraviolet light exposure and developed in order to transfer the pattern from a mask to the photoresist layer. The patterned aluminum and photoresist multilayer is then

anisotropically etched through a reactive ion etching (RIE) process which removes the unprotected aluminum regions to create a network of interconnects. Next the remnant resist is stripped and the SiO_2 inter-layer dielectric (ILD) is deposited over the aluminum network by chemical vapor deposition (CVD). The ILD deposition is then followed by a chemical-mechanical-planarization (CMP) step which creates a globally smooth multilayer surface and prepares the wafer for additional interconnect levels and other subsequent fabrication processes[27, 36].

Unfortunately, the reactive ion etching process is not easily adapted for the fabrication of copper interconnects due to the low vapor pressures of copper chlorides and fluorides[37]. In fact, in order to reach reasonable etch rates, the process temperature must be raised to at least 150ºC during dry etching. At these temperatures the Cu may subject to increased oxidation and corrosion rates. Furthermore, since the other lithographic materials used in the subtractive patterning process are incompatible with such elevated temperatures, the entire process becomes more complicated and increased in cost[27]. Therefore, the implementation of Cu metallization requires a shift in the patterning scheme and approach. A simplified depiction of the two metallization processes is presented in Figure 2.1.

In contrast to the traditional subtractive patterning process, damascene metallization geometries are determined by features which are etched into a dielectric substrate. First, the substrate is blanketed by a dielectric layer (ILD) into which the desired features are patterned by a conventional etch process. After the lithographic materials are removed, a diffusion barrier layer such as TiN

or Ta/TaN is deposited on the patterned ILD substrate. Next, a thin (~100 – 1000 Å) Cu seed layer is deposited by PVD followed by bulk Cu electrochemical deposition (ECD).

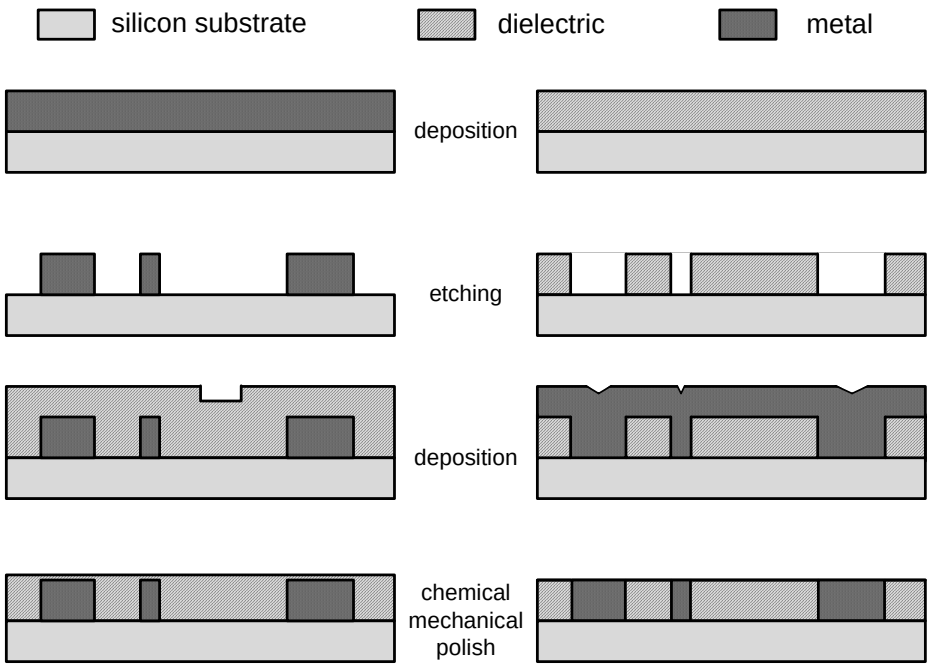

Figure 2.1 - Schematic comparison of the aluminum metallization process and copper damascene type metallization. Illustrations adapted from Reference[27].

As a result of the ECD process, excess Cu is deposited over the entire wafer surface and all interconnect structures are in a state of electrical short circuit. This excess Cu metal is known as via overfill or overburden and is finally removed during chemical-mechanical planarization. The remaining structures constitute a single level of networked Cu wiring and the process may then be

repeated depending on the number of required interconnect levels. The electrochemical nature of the Cu metallization technique, also known as dual damascene, allows for both trenches (interconnect wiring within a single level) and vias (interconnect wiring between two adjacent levels) to be filled simultaneously. Because of this the dual damascene technique drastically reduces the number processing steps and significantly reduces the cost of IC wafer fabrication[27].

2.4 Copper Damascene Deposition

The copper damascene process derives its name from the practice of creating metallic inlays as developed by artisans of Damascus in the middle ages[7]. The central concept behind the process and its unique features is the fact that submicron surface features can be filled seamlessly and produce leveled, "defect-free" thin films by employing electroplating conditions and electrolyte solutions that contain certain additives in carefully balanced concentrations. Typical plating parameters and solution compositions are given in Table 2.2.

Table 2.2 - Typical Values for Cu Damascene Process Parameters[8, 28, 38]

Nominal Cu Seed Layer Thickness	100-2000	Å
Electroplating Current Density	3-50	mA/cm^2
Deposition Fill Time	5-40	seconds
Cu^{++} Concentration	10-70	g/L
H_2SO_4 Concentration	5-325	g/L
"Accelerator" Concentration	1-25	ppm
"Suppressor" Concentration	100-2000	ppm
Cl^- Concentration	20-100	ppm

In this context, defect-free and leveled films are terms that refer to desirable film qualities such as a mesoscopically flat surface (no overfill bumps or "momentum plating") and vias that are free of voids, seams, or occluded electrolyte[5, 28]. This bottom-up filling phenomenon demonstrated by Figure **2.2** is now known as superconformal filling or just superfilling[5, 10].

While copper damascene processing avoids many of the problems associated with Cu dry etching and dielectric deposition, the need to optimize the process parameters still exists. In fact, the electrochemical characteristics of Cu deposition can be tuned for many on-chip applications ranging from low level damascene structures (>100 nm length scales) to Through-Silicon-Via (TSVs) technologies used in 3D integrated circuitry (~50–150 μm length scales). In all cases though, the main goal is to fill vias, holes, and trenches completely and without voids or seams. This becomes increasingly more difficult as the on-chip features shrink to less than 100 nm in width and reach aspect ratios as high as 10 (depth:width)[7, 27]. The difficulty arises from the need to fill high aspect ratio surface features quickly and completely. A complete fill results from a leveling action that is produced during the electrolytic deposition of metal during the damascene process.

The phenomenon of leveling is the continuous reduction of surface roughness during deposition on the surface, i.e. the seamless filling of surface recesses or asperities that often result from coarse mechanical polishing. The historical importance of this phenomenon has ties to the surface finishing industry and has been used to refer to the smoothening of a non-uniform surface by

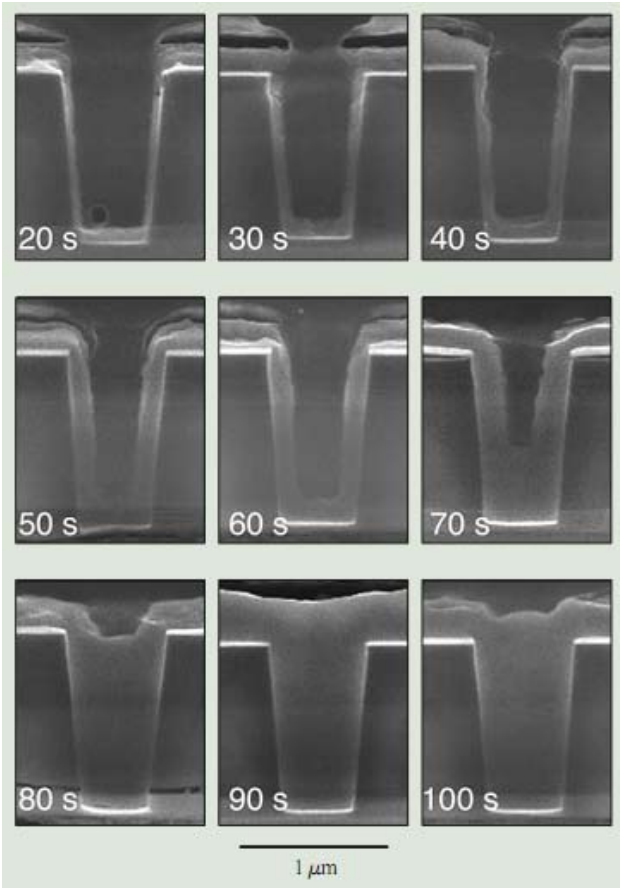

Figure 2.2 - Time sequence example of bottom up superfilling of vias using electrochemical Cu damascene technology. Reproduced with permission from Reference[10].

deposition of more metal in recesses relative to the rest of the surface. Specifically, there are two types of leveling that are relevant to the electrodeposition processes, geometric leveling and true leveling. *Geometric leveling* is produced by uniform current density and conformal deposition of

metal on a substrate surface. This type of leveling typically occurs in the absence of leveling agents and is qualitatively illustrated in Figure 2.3. It is characterized

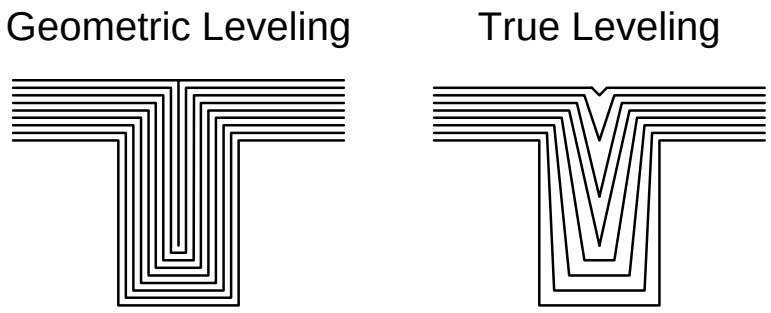

Figure 2.3 - Schematic shape evolution of a rectangular (trench) profile during feature filling process. Geometric leveling is produced by uniform current distribution and results in seam formation while true leveling produces a "defect free" bottom-up fill. Figure adapted from References[27, 39].

by deposit thicknesses that are equal on all surfaces and can result in incomplete feature filling. Leveling which occurs in the presence of leveling agents is known as true leveling and constitutes the underlying principle of superconformal deposition. *True leveling* arises from a non-uniform current distribution along a substrate profile as metal is preferentially deposited in recessed regions of the substrate surface (Figure 2.3). Increased deposition rates can only be achieved by the use of leveling agents which induce higher current densities within a surface feature relative to the top region of the substrate[39].

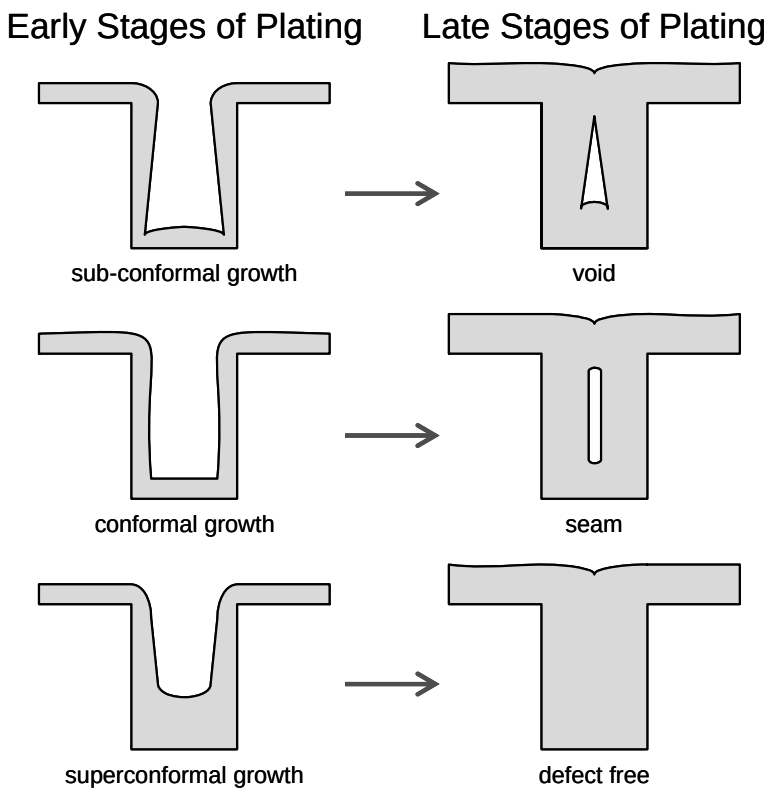

Figure 2.4 - Trench filling profiles of sub-conformal, conformal, and superconformal growth shown at early and late stages of the electroplating process. Figure adapted from Reference[5, 7].

In practice, there are several possible results for trench filling processes. Figure 2.4 shows the possible trench filling profiles of both early and late stage electroplated copper. In the conformal case, a metal layer of equal thickness is deposited over the entire feature profile (geometric leveling). For straight walled or "V"-shaped trenches, conformal filling should be capable of producing a

perfect trench fill. However, variations in deposition parameters or slightly re-entrant trench geometry can lead to the creation of a seam or void. Additionally, a subconformal filling profile may occur as a result of reduced current density at the bottom of the feature geometry relative to the top. Under these conditions surface roughness may increase, voids are likely to form inside the trench, and longer plating times can result in ramified deposits. Conversely, superconformal deposition occurs as current density and deposition rates are increased along the bottom and sides of the trench relative to the outside of the feature (true leveling). This may be accomplished through the use of leveling species that are added to the plating bath to produce a seamless, void free deposit and is known as superfilling. Copper interconnects that are free of these defects provide effective conduction pathways for signal transport in integrated circuits. However, wiring structures that do contain seams and voids within the trenches and vias are significantly more susceptible to joule heating and electromigration, phenomena which eventually lead to device failure[8].

CHAPTER 3

FUNDAMENTALS OF ELECTRODEPOSITION

Electrochemistry allows for the addition and removal of materials from metallic electrode surfaces. Both electrochemical deposition and oxidative stripping require the presence of both an ionically conductive solution and an electrically conductive electrode at an electrified interface. The difference in the conductivity mechanism between the two phases, electrons in the case of the metal and ions in the electrolyte, requires an exchange of charge across the interface. Due to the complexity of this interfacial region, the actual mechanism by which the discharge occurs can depend heavily on the details of the system such as adsorption, solution ionic conductivity, applied potential, etc. A detailed understanding of the interfacial region is an important aspect of many electrochemical processes, but is especially pertinent to the application of electrodeposition of copper in the presence of additives.

3.1 Electrochemical Kinetics

The immersion of a copper electrode into a copper salt solution creates a dynamic interface, even under open circuit conditions. At the open circuit potential (OCP), there is zero net current on the copper electrode and no charge passes between it and an auxiliary electrode in a three electrode, potentiostat setup. However, despite the absence of any measured current, a finite amount of anodic and cathodic current that is both equal and opposite exists locally at the electrode surface. This exchange of charge is a property of the chemical system known as the exchange current density, i_0. The exchange current density is directly

proportional to the standard reaction rate, k^0, the electrode surface area, A, and the Faraday constant, F, of a given chemical reaction. It represents the amount of equal and opposite cathodic and anodic charge that is exchanged across the interface in a unit time interval. When an overpotential is applied to the electrode, the cathodic and anodic currents become unequal and net electrons transfer to (reduction) or from (oxidation) the solution. The kinetic relation between electrode overpotential and current density is known as the Butler-Volmer equation[40]:

$$i = i_0\left[\exp\left(\frac{(1-\alpha)nF}{RT}(E-E^0\ )\right)-\exp\left(-\frac{\alpha nF}{RT}(E-E^0)\right)\right], \tag{3.1}$$

where i, α, n, R, T, E, & E^0 are the current density, the symmetry factor, the number electrons transferred, the gas constant, absolute temperature, applied potential, and standard reduction potential of the electrochemical system, respectively. The standard reduction potential is a thermodynamic parameter that is defined by the molar free energy of the reaction, ΔG, and the number of electrons transferred during the reduction reaction,

$$E^0 = -\frac{\Delta G}{nF}. \tag{3.2}$$

In the case of aliovalent copper, there are two ions to consider (the more highly oxidized species are quite unstable and irrelevant to this work). Both cupric (Cu^{2+}) and cuprous (Cu^{+}) ions may exist in solution and are reduced to copper

metal during an electrodeposition reaction. The corresponding reduction reactions and standard reduction potentials are[40]:

$$Cu^{+}(aq) + e^{-} \leftrightarrow Cu^{0}(s), \qquad E^{0} = 0.521\,\text{V v. SHE} \tag{3.3}$$

$$Cu^{2+}(aq) + 2e^{-} \leftrightarrow Cu^{0}(s), \qquad E^{0} = 0.337\,\text{V v. SHE.} \tag{3.4}$$

At potentials negative or cathodic to these, the respective ions are reduced to copper metal and subsequently become bonded to the electrode surface. As a result of a non-zero net current, copper ions are reduced to copper metal (cathodic case) or generated (anodic case) and material is added to or removed from the electrode surface, respectively.

3.2 Mass Transfer

The above description corresponds to an activation-controlled regime of the electroplating process. It remains valid only under conditions where the concentration of the depositing metal ions is close to that of the bulk solution and the current increases exponentially as a function of applied potential according to eq 3.1. In reality, the concentration of the electroactive species (e.g. metal ions) near the electrode surface is subject to variation as the oxidation or reduction reaction proceeds. For example, metal ions are consumed during the deposition process and the concentration near the surface decreases. In order for the plating process to be sustained, mass transfer of metal ions from the bulk of the solution to the surface must occur. Mathematically this transport of ions to the interface is described by the Nernst-Planck equation,

$$J_x = C_x v - \frac{z_x F}{RT} D_x C_x \nabla \phi - D_x \nabla C_x, \qquad (3.5)$$

where C, v, z, F, R, T, D, and ϕ are the concentration, fluid velocity, charge, Faraday and gas constants, temperature, diffusivity, and electric field, respectively, and the subscript x refers to metal ion. Here each of the terms on the right hand side of eq 3.5 corresponds to a separate ionic transport mechanism within the solution. From left to right these terms refer to convection ($C_x v$), migration ($\frac{z_x F}{RT} D_x C_x \nabla \phi$), and diffusion ($D_x \nabla C_x$), respectively, and each of these mass transport phenomena will be treated below.

Convection includes ion movement due to bulk movement of the liquid solution by means of pumping, agitation, rotation or ultrasonication of the electrode-electrolyte system. In electroplating applications, convection is often achieved by solution pumping or agitation but can also involve rotation of the electrode [8]. Generally the purpose of convection is related to maintaining a well-mixed system to ensure a nominally constant metal ion concentration across the dimensions of the electrode surface. Increased convective flow also results in a decrease in the thickness of the stagnant diffusion layer adjacent to the electrode surface. Typically, once the diffusion layer is established (e.g. ca. 100 μm in stagnant aqueous systems), metal ions must travel across the layer by means of migration and diffusion.

Migration is the movement of ions in response to an electric field that is applied between the working and counter electrodes. As a result of migration, cations tend to move towards the negatively biased electrode and anions migrate towards a positively charged electrode. Migration effects on a particular electroactive species are often rendered negligible by excess charge carriers which are often present in the solvent (e.g. H^+ and OH^- ions in water) or that are purposefully added to solution in the form of supporting electrolyte species (including acids/bases)[40, 41]. However, in the absence of convection, migration of a metal ion can become significant if the charge carrying capacity of the ion composes a significant portion of the charge carrying capacity of the entire solution. This is determined by the transport number,

$$T_x = \frac{C_x z_x D_x}{\sum C_i z_i D_i}, \tag{3.6}$$

where the subscripts x and i refer to the metal ion and the i^{th} ionic species found in the solution. As the transport number of the metal ion of concern becomes a significant fraction of unity, migration effects on the particular ion becomes a significant factor in solution phase mass transport. In typical acidified copper plating solutions, the transport number of protons in solution is so large that the migration rate of copper ions towards the electrode surface is small relative to the diffusion rate.

Diffusion is the thermally activated movement that results when a chemical species is distributed in a nonuniform fashion. On a macroscopic scale,

diffusion tends to equalize the concentration of a chemical species throughout a material and the net direction of flux is along any existing concentration gradient. It is possible to calculate the diffusional flux, *J*, of a particular chemical species using Fick's first law of diffusion,

$$J_x = - D_x \nabla C_x, \tag{3.7}$$

which can be simplified when considering a single dimension (e.g. x-direction, as in diffusion towards a planar electrode during electrolysis),

$$J_x = - D_x \frac{\partial C_x}{\partial x}, \tag{3.8}$$

which represents the only component of mass transport that cannot be neglected under any conditions during electrochemical consumption at an electrode. At room temperature, copper ions in a plating solution generally have a diffusion coefficient of order ~5×10^{-6} cm^2/s which results in a 20 μs diffusion time for a 0.1 μm distance and a 0.2 second time across a 10 μm distance[42-46]. With respect to the timescale of 5 to 20 seconds that is required for typical high aspect ratio feature filling processes, these diffusion times are small enough to allow sufficient replenishment of Cu ions within the vias and trenches during deposition. This is somewhat remarkable given the fact that at a Cu^{++} concentration of 0.25 M, the solution volume containing enough metal ions to fill a feature with Cu metal is of order 200 to 400 times larger than the feature volume[8].

At large overpotentials and/or long deposition times, the near-surface region known as the diffusion layer becomes depleted of metal ions and the rate of ion transport from the solution becomes diffusion limited. Under these circumstances, the steady state diffusion rate limits the reaction, and the process transitions from activation control to diffusion control. The distinguishing characteristic of a diffusion-controlled process is a constant current profile as a function of applied potential. In this case, eq 3.1 no longer dictates the current behavior and a form of eq 3.5 (recognizing that $i = nFJ$ and $\partial C_x/\partial x \approx C_{x,bulk}/\delta$) determines the diffusion limited current density[40],

$$i_{Diff} = \frac{nFDC_{x,bulk}}{\delta}, \tag{3.9}$$

where D and $C_{x,bulk}$ are the diffusivity and the bulk concentration of the depositing metal ion and δ is the diffusion layer thickness. Figure 3.1 illustrates the transition between the activation controlled region to the diffusion limited current density region. In addition to the activation and diffusion controlled regions, a transition period exists where the current density is under mixed control of both potential and physical transport constraints [39]. While metal deposition occurs during all three regions, often the morphology and material properties of the electrodeposited film depend on the region in which deposition occurs[46-51].

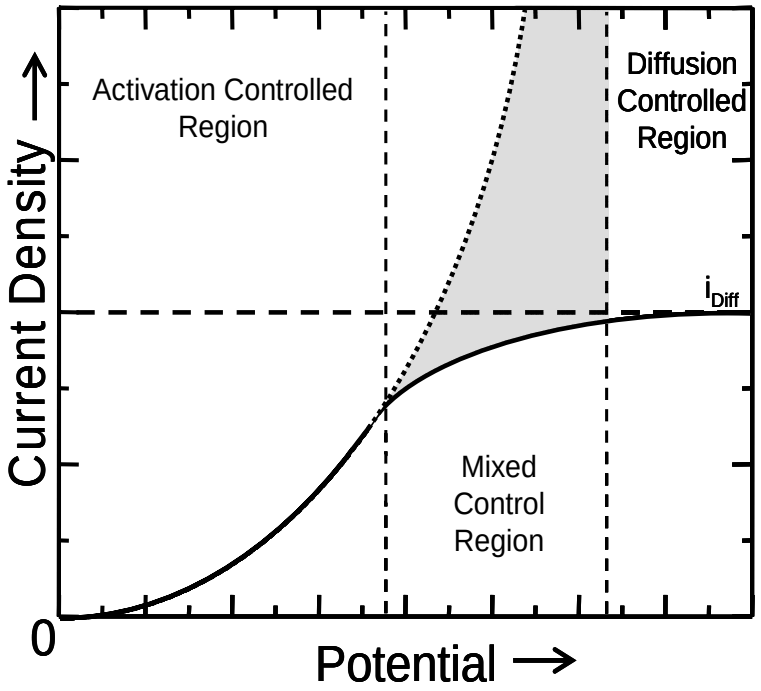

Figure 3.1 - Schematic representation of the actual (solid) current density dependence on the electrode overpotential and the behavior as predicted by Butler-Volmer kinetics (dashed). Activation, diffusion and mixed control regions are loosely defined by the comparison between the two profiles. Figure adapted from Reference[39].

3.3 The Superfilling Process

Copper damascene electrodeposition is the state of the art method by which IC interconnects are produced due to a unique phenomenon known as superfilling. This bottom-up, "defect-free" filling is the most fundamental

requirement for any damascene application. The superfilling capability of certain Cu electrolytic solutions is accomplished through the use of additives that enhance a nonuniform plating current across a non-planar substrate. While the damascene process has been successfully applied in industrial applications for many years, the superfilling mechanism is not yet well characterized. Any explanation or proposed mechanism of superfilling must predict the phenomenological observations by first taking into account the electrochemical parameters of the deposition and also by accounting for the additional modifications induced by the solution additive species.

3.3.1 Electrochemical Current Distribution

The physical and chemical laws that govern the transport of charge in an electrochemical system preclude the possibility of a completely uniform current density, even for simple electrode geometries. Electrode edges and protrusions receive higher current densities than the average unit area of surface while hollows and recesses (e.g. trenches & vias) receive lower[52]. Because the distribution of metal thickness in a deposit depends on the current efficiency as well as the cathodic current distribution, it is important to consider the multiple factors that affect electrode current distribution as it relates to electrodeposition. In the absence of polarization effects the current distribution is predicted by the *primary current model*[27, 52-55]. The primary current distribution is calculated by only considering the electric field and the geometry of the electrode; electrode kinetics (surface overpotentials) are neglected. The current is then determined only by the total ohmic resistances experienced by the current as it flows to or

from the different points along the electrode surface. Thus, the primary current model predicts that less accessible parts of the electrode will receive a lower current density due to increased resistance along a longer current path. This can be understood by considering a two electrode configuration as shown in Figure 3.2.

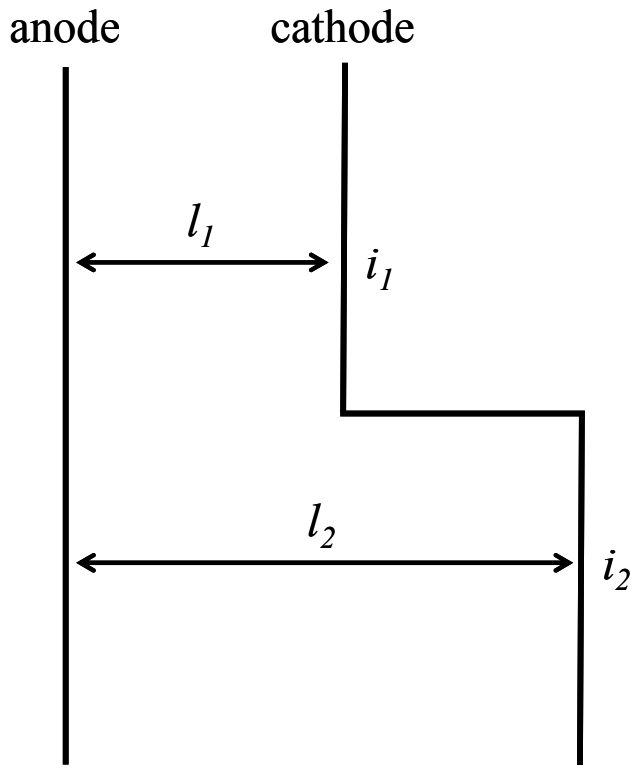

Figure 3.2 - Schematic representation of a two electrode electroplating configuration where the cathode surface is non-planar. Within the context of electrochemical current distribution theory, j_1 and j_2 are local current densities that depend on the cathode-anode distances, l_1 and l_2, respectively. Illustration adapted from Reference[27].

Since a highly conductive electrode can be assumed to be have uniform potential at all points, the ratio of current distribution along this schematic profile is given by

$$\frac{i_1}{i_2} = \frac{l_2}{l_1}, \tag{3.10}$$

where i_1 & i_2, and l_1 & l_2 are the current densities and lengths represented at either point 1 or 2, respectively, as indicated in Figure 3.2. As the average distance between anode and cathode increases the ratio, l_2/l_1, tends towards unity and the current (and metal thickness) distribution becomes more uniform. Wagner calculated the primary current distribution for the deposition of Cu on a surface profile with a rectangular slot (i.e. a surface trench) and found the current to be concentrated at the top corners of the trench. This of course would lead to the subconformal type of growth and eventual void formation as shown in Figure 2.4. Obviously this is an undesirable result for superfilling applications; however, a more accurate model of the current distribution must take into account polarization and electrode kinetics.

The *secondary current model* takes into account polarization of the electrode which is always present due to kinetic limitations. In this case, the kinetic limitations tend to moderate the extreme non-uniformity of current density that is predicted by the ohmic conditions of the primary current model. To estimate the magnitude of electrode polarization effects on current distribution, Wagner introduced a polarization parameter, $\kappa(\partial\eta/\partial i)$, that is a product of the

ionic conductivity of the electrolyte and the slope of the polarization curve, and has units of length[56]. When this polarization parameter is included in the secondary current distribution model, the ratio of current distribution along the schematic profile of Figure 3.2 becomes

$$\frac{i_1}{i_2} = \frac{l_2 + \kappa\left(\partial\eta/\partial i\right)_2}{l_1 + \kappa\left(\partial\eta/\partial i\right)_1}, \tag{3.11}$$

where κ and $(\partial\eta/\partial i)$ are the ionic conductivity of the electrolyte and the slope of the polarization curve, again represented at either point 1 or 2, respectively, as indicated in Figure 3.2. The secondary current distribution model depends on the same geometry as the primary model but the effect is attenuated by kinetic limitations that have the equivalent effect of adding distance between the anode and cathode. In fact, if the same polarization behavior applies to both points 1 & 2, the net effect is the addition of an equal distance to both current path lengths, thus moderating the non-uniformity of current density.

Whereas the primary current distribution is the same for geometrically similar micro- and macro-profiles, the absolute size of the surface feature becomes very important in the secondary model, as estimated by the dimensionless Wagner number,

$$Wa = \frac{\kappa\left(\partial\eta/\partial i\right)}{l}, \tag{3.12}$$

which is a ratio of Wagner's original polarization parameter, $\kappa(\partial\eta/\partial i)$, to the characteristic length, l, of the nonplanar surface feature in question[56]. This number serves as a measure of the extent to which electrode kinetics can make current distribution (and by extension, plating thickness) more uniform. That is, for extremely fast charge transfer kinetics, *Wa* approaches zero and the secondary current distribution model becomes equal to the primary model. However, for the more realistic case of limited electrode kinetics, *Wa* becomes much greater than unity and current density distribution becomes more uniform, if the same current-potential relationship applies to all points along the feature profile[27, 52, 56]. This assumption only holds for the situation where the kinetic parameters remain uniform along the profile. For example, at significant cathodic overpotentials (e.g. η > ~5 mV) and in the absence of diffusion limitations, eq 3.1 simplifies to the Tafel equation,

$$i = -i_0 \exp\left(-\frac{\alpha nF}{RT}(E - E_{eq})\right), \tag{3.13}$$

which gives a simple but relatively realistic relationship between applied potential and the resulting current density of an electrode reaction. The Wagner number in the case of Tafel kinetics then becomes

$$Wa_T = \left|\kappa \frac{RT}{\alpha nFil}\right|, \tag{3.14}$$

which can be used to give a sense of the degree of uniformity in current distribution and deposit thickness that can be expected (per the secondary current distribution model) for a 100 nm wide Cu damascene trench. That is, for an acid copper plating bath (no additives) at room temperature where $\alpha \approx 0.5$, $\kappa \approx 0.5$ S/cm, and a nominal current density of ~25 mA/cm^2, the Tafel-estimated Wagner number is ~51,000, which indicates an extremely uniform current density distribution. Thus it can be seen that by considering only activation overpotential, the secondary current model predicts a uniform current distribution along a nonplanar electrode profile inasmuch as the same polarization-current relationship applies at all points along the profile. The extension of this prediction to a Cu plating application is geometric leveling and conformal deposition as shown in Figure 2.4. Obviously, neither the primary nor secondary current models are able to explain true leveling or superfilling phenomena as it applies to Cu damascene applications.

The *tertiary current model* is the next step towards an accurate prediction of the actual electrochemical current density distribution along an electrode profile. The tertiary model accounts for the concentration overpotential that develops over a period of seconds following the start of deposition. This overpotential occurs because of mass transfer limitations which result from slow diffusion of reacting species from the bulk solution across the diffusion layer to the electrode surface. Within the diffusion layer, mass transport of reacting ions occurs by diffusion only. Outside this layer convection maintains a constant bulk concentration of reacting species. Initially the diffusion layer boundary tracks the

surface profile, but as the diffusion layer grows to a thickness that approaches the length scale of the surface features, the boundary begins to deviate and become more planar[27, 52]. Eventually a quasi-steady-state diffusion layer develops as the rate at which reacting species are consumed at the surface is balanced by convection in the bulk electrolyte. At this point the diffusion layer varies along the nonplanar surface and diffusion times are longer for diffusion paths into surface features. Because the diffusion rate is higher at the top of the feature relative to the bottom of the feature, the current distribution becomes nonuniform and in the case of electrodeposition this tends to produce subconformal feature filling.

3.3.2 Feature Superfilling by Nonuniform Plating Currents

Previously there has been some disagreement in the literature with respect to a distinction between leveling and superfilling processes[7, 29]. For the sake of clarity, the phenomenon of superfilling is considered here in detail and in the context of a microscopic trench. The superfilling of a surface feature is understood by considering the different deposition rates along a feature profile. First, it is reasonable to assume that the electrochemical current density at the bottom of a surface recess will vary from that of the top surface, as described by the primary, secondary and tertiary current distribution models. Of course, in the absence of some external deposition inhibition at the top of the trench, these models predict conformal deposition, at best. In order for superfilling to occur, the deposition must be enhanced at the bottom of the trench relative to the top.

More specifically, consider the illustration in Figure 3.3 in terms of the relative plating rates at several locations of a trench.

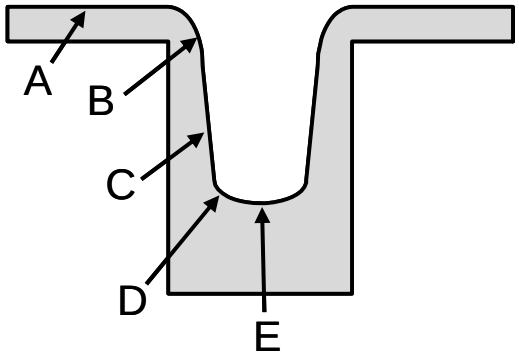

Figure 3.3 - Schematic cross section of a partially filled trench indicating the variation of deposition rate along the profile. In order to produce the superconformal filling, the local electrodeposition rate (and current density) must increase in order of A→B→C→D→E. Illustration adapted from Reference[7].

In order to fill the trench in a superconformal fashion, the current density should increase along the profile from points A to E. While the largest difference will occur between points A & E, the differential plating rate along the trench side-wall is the most critical aspect of a successful superconformal fill since the growth from the bottom of the trench must reach the top before the side-walls meet. This means that the ratio of average plating rates of the bottom growth front to side-wall growth must be at least twice the aspect ratio of the trench.

Since all points along the profile are electrically shorted, the potential difference of the Cu seed layer at all points will be zero. Thus, the difference in deposition rates must occur due to conditions on the solution side of the interface. In order to support differential plating, additive species are added to the plating bath in precise concentrations[7].

3.3.3 The Effects of Copper Plating Additives

Successful application of the Cu damascene process requires careful control of many integral process parameters. One very important control parameter is the plating solution composition which includes additives that are used in complex multicomponent combinations in order to produce the desired deposit characteristics. In traditional electroplating these characteristics include leveling and brightness of the deposits. For copper IC interconnect applications the actual nature and concentration of the additive components remains proprietary. However, a large body of literature surrounding copper feature filling has identified a prototypical set of additives that exhibits superfilling capabilities when added together in concentrations of a millimolar or less[57]. Typical superfilling bath chemistries include a deposition-suppressing species, a deposition-accelerating species, a halide ion, and in some cases a leveling agent[2, 5, 8, 10, 19, 27, 29, 31, 32, 58-62]. Suppressing species, also known as polarizing additives, are defined by an inhibition of cathodic plating current density relative to additive free conditions at a given overpotential. Similarly, the addition of accelerating species or depolarizing additives will subsequently produce an increase in current density relative to suppressing conditions. Figure 3.4 illustrates this phenomenon

with linear sweep voltammograms that show normal, inhibited, and accelerated copper deposition during cathodic potential excursions from the OCP (~400 mV v. MSE)[63]. In the literature, accelerating species have also been more accurately

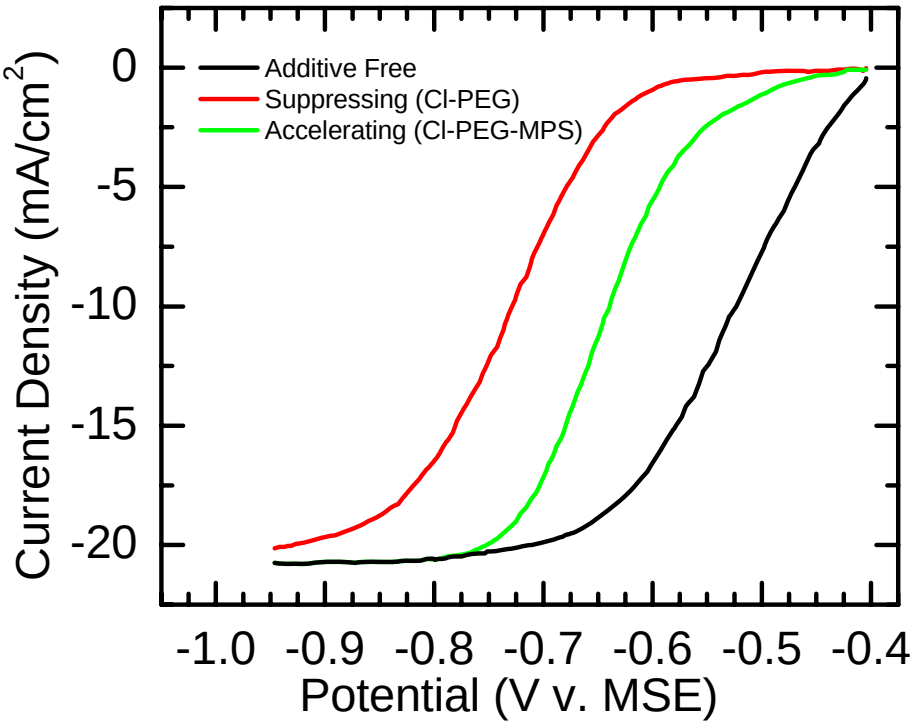

Figure 3.4 - I-E characteristics for copper deposition from various solutions. The Cl-PEG (red) mixture yields inhibition of the deposition reaction with respect to the additive free solution (black) while Cl-PEG-MPS (green) system leads to a relative acceleration of the deposition rate. Figure reproduced with permission from Reference[63].

termed antisuppressors due to the fact that the deposition rate in these types of solutions is actually less than the additive free case but greater than the fully suppressed case. The halide ion solution component (e.g. usually Cl^-) adsorbs on the copper surface in ordered surface structures presumably because the OCP is anodic to the potential of zero charge[64-68]. In the bulk solution, the halide ion acts as a copper coordination species and promotes slight acceleration of Cu deposition in solutions that are free of other organic additives[8, 19, 20]. Nevertheless, the halide ion is required for both the suppressing and accelerating actions which arise from synergies between it and the other additive species.

The suppressing agent is usually a polyether such as polyethylene glycol (PEG) or polypropylene glycol (PPG) and has surfactant properties in aqueous solutions. It suppresses deposition by adsorption on the chloride modified surface. The suppressing action is thought to occur through both an electrical screening of the copper surface as well as by the formation of a physical barrier known as the "blocking layer"[11, 59, 69, 70]. Because of the relatively large concentrations of suppressor species contained in most plating baths, the blocking layer of order one monolayer in thickness forms very quickly (~0.2 s) upon immersion. An additional advantage due to the surface active nature of PEG and PPG is a reduction of surface tension of the plating solution which aids in the wetting of the very small surface features and provides electrochemical access for deposition. The accelerating agent is generally a sulfur-bearing compound that increases the current density at a given potential relative to the suppressed case. Recently, Moffat and Yang found that the accelerating agents such as bis-

(sodiumsulfopropyl)disulfide (SPS) and mercaptopropane sulfonic acid (MPS) must contain both a thiolate ("R-S") or disulfide ("S-S") group as well as the sulfonate group ("R-SO_3") as shown in Figure 3.5[69]. The copper metal interacts strongly with the sulfur atom in the disulfide or thiolate group and the accelerator species adsorbs with the charged sulfonate group oriented away from the metal film. It is thought that the role of the sulfonate end group and the charge associated with it is then essential in the repulsion of the suppressor species and consequently the creation of a defect in the suppressing surface film or blocking

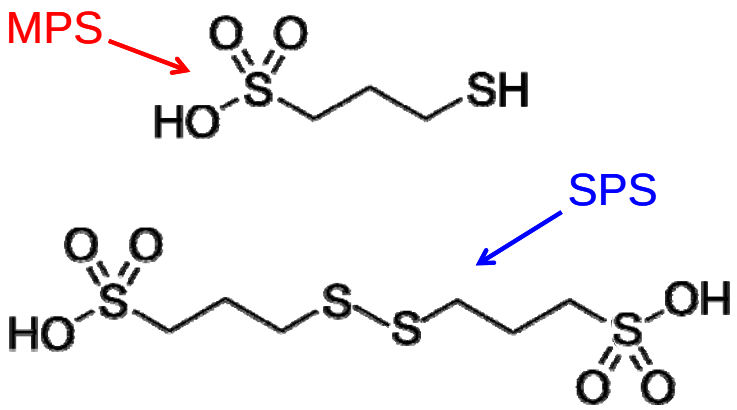

Figure 3.5 - Chemical structures of the additive species, bis-(sodiumsulfopropyl)disulfide (SPS) and mercaptopropane sulfonic acid (MPS), used in this work. Note that SPS is essentially the dimerized form of MPS. Illustrations adapted from Reference[71].

layer. The leveling agent is usually a nitrogen bearing compound (e.g. thiourea, benzotriazole, and Janus Green B) that is much more strongly suppressing than

PEG or PPG[8, 19, 72, 73]. Leveling species are added to the plating bath in very small concentrations and primarily function as current suppressors at localized regions where growth rates are relatively large. The most important example of this is the reduction of the "overfill bump" formation or "momentum plating" phenomena which occur above features which have been filled via bottom-up or superfilling action. In the present work, leveling agents are not considered. Only solution chemistries containing the halide ion, suppressing and accelerating species in various combinations are investigated.

3.3.4 Proposed Mechanisms for Superfilling Phenomenon

To date, two dominant superfilling mechanisms that involve both physical and kinetic arguments have been proposed to explain the superconformal filling phenomenon of surface features. The proposed models both involve the presence of an accelerated deposition rate at the bottom of the feature relative to the top but differences between the models are found in how each accounts for consumption, diffusion, and competitive adsorption of the several additive species. The first attempt to model the superfilling mechanism is known as the diffusion-adsorption model and was used by Andricacos *et al*[5, 29, 59, 74, 75], followed by the Curvature Enhanced Accelerator Coverage (CEAC) model which was introduced and then later refined by Moffat *et al*[10, 11, 21, 22, 60, 62, 63, 69, 70, 72, 76-80].

3.3.5 Diffusion-adsorption Mechanism Model

According to the diffusion-adsorption mechanism, the suppressing additives play an integral role in the nonuniform distribution of current that is required for bottom-up filling. This model was first proposed with respect to

plating solutions that contained a single leveling additive and produced (1) bright deposits for surface finishing as well as (2) true leveling in printed wiring board applications. The pioneering work of Foulke and Kardos as well as Watson and Edwards indicated that the most important factor for production of true leveling in these types of solutions was the diffusion control of the deposition-inhibiting species[53, 54, 81]. Basically, the explanation is analogous to the arguments presented in the tertiary current distribution model. That is, once the diffusion layer is established for the relatively dilute additive species, the inhibiting action depends on its diffusion rate from the bulk solution to the surface. While the deposition current density is kept well below the diffusion limited regime of electroactive species (deposition is activation controlled, not diffusion controlled), the consumption of the inhibitor is diffusion controlled. The inhibitor may be consumed by either incorporation into the film or by means electrochemical reaction that forms inactive product species which then desorbs and/or has no effect on the deposition. Thus, the diffusion-adsorption model for true leveling can be understood in the context of the varying thickness of the leveling agent's diffusion layer over the electrode profile, as illustrated in Figure 3.6[82]. The rate of inhibitor diffusion is greater at the peaks than at the valleys of electrode surface. This variation then produces differentiation in the degree of inhibition that occurs along the profile and promotes deposition in the valley relative to the peak. This has the effect of modifying the amount of polarization and produces different current density-overpotential relations along the profile. It is clear then that this

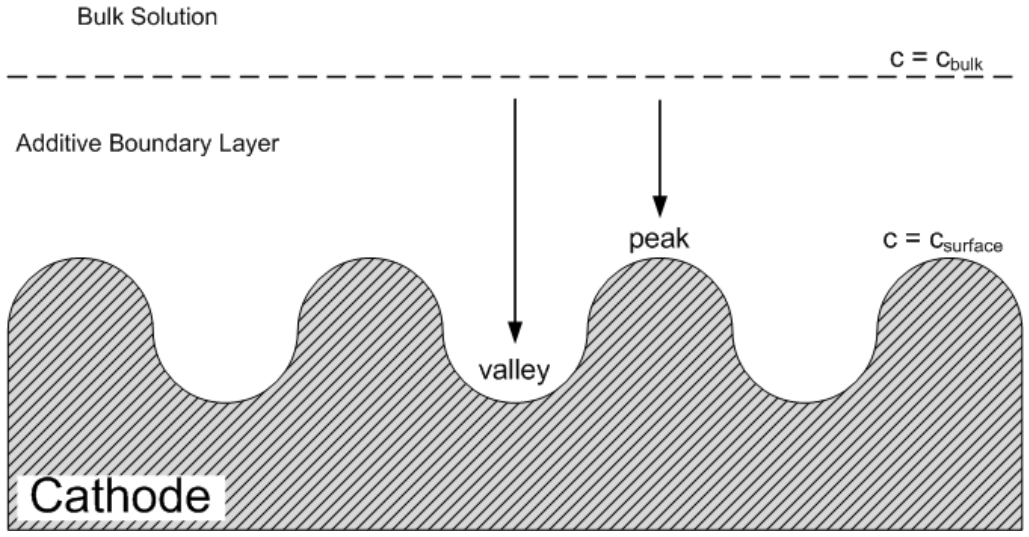

Figure 3.6 - Illustration of the diffusion-adsorption model of leveling/superfilling. Because the diffusion distance from the diffusion layer boundary to the peaks is shorter than to the valleys, the arrival rate of suppressor species is greater at the peaks. The current distribution and deposition rate are suppressed more strongly at the peaks, thus more metal is deposited in the valley and the electrode profile becomes smoother. Illustrations adapted from Reference[82].

model predicts the type of current density distribution that is necessary to produce true leveling[27].

For many years, the diffusion-adsorption model was used to adequately describe the leveling and brightening performance of single additive solutions in surface finishing and printed wiring boards applications. Most of this early

experimental works dealt with nickel or some copper plating solutions that utilized leveling agents such as coumarin, thiourea, and acetylenic brighteners[53, 54, 81-86]. This model was supported by findings which showed increased inhibition of deposition in recessed grooves and trenches as a function of decreased diffusion layer thickness as controlled by convection[73, 87]. Additionally, several groups have performed numerical investigations to predict the current distribution and deposit thicknesses on several types of profile shapes, including damascene-like trench geometries[5, 29, 74, 82, 88]. Generally, these investigations have supported the validity of this model for single additive species containing solutions, however, contemporary plating solutions (as mentioned above) contain complex mixtures of both organic and inorganic additives which act as deposition suppressors as well as accelerators. To address this, several variations of the diffusion adsorption model have been proposed which (1) consider the diffusion limited inhibition as controlled by chloride ion (not polymer suppressor species) diffusion[75], (2) take into account simultaneous surface diffusion of suppressor species into the feature[1, 57], or (3) the diffusion and adsorption of the multiple additive species[59].

A schematic set of current density-overpotential characteristics which create a framework for experimental investigation of the diffusion-adsorption mechanism is shown in Figure 3.7. The idea is that feature filling performance based on this mechanism can be approximated by electrochemical studies on planar electrodes by comparing i-η behavior on an electrode using a full additive

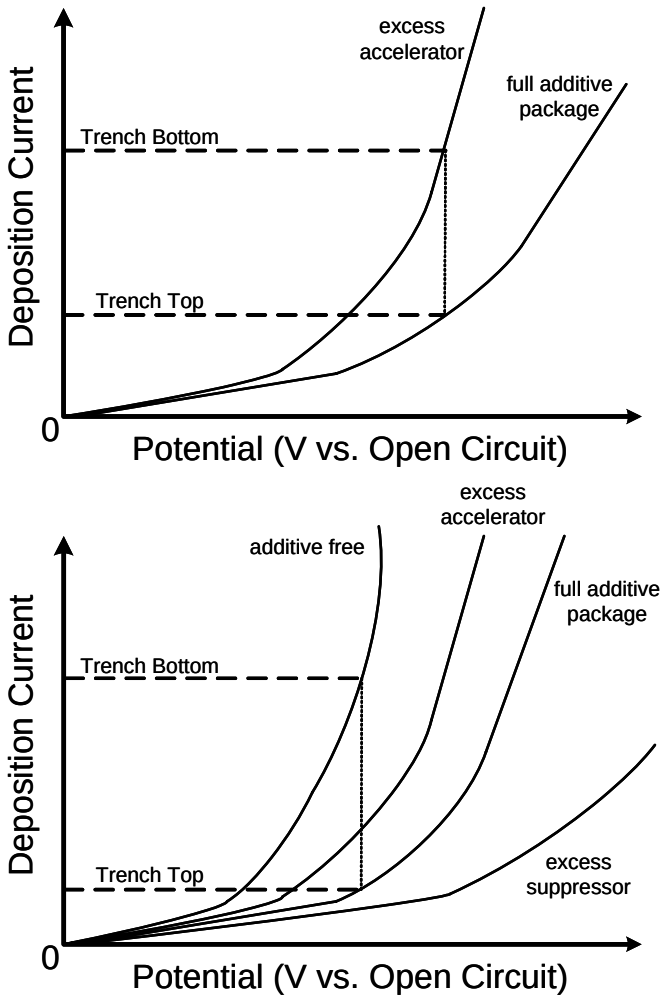

Figure 3.7 - Representation of the current-potential (i-η) characteristics of a planar electrode in several types of additive containing copper plating solutions. The dashed lines represent current values that could exist simultaneously on the non-planar electrode during electrodeposition in additive containing solutions. According to trench filling models based on the (a) diffusion-adsorption mechanism, the nonuniform deposition rate is due to the reduced additive concentration at the trench bottom relative to the top. Conversely, the (b) CEAC model attributes the superfilling action to an accumulation of accelerator species relative to the top of the trench. Illustrations adapted from Reference[8].

package (three component mixture of halide ion + suppressor + accelerator) solution to simulate deposition on top of the electrode (the field) with the additive free *i-η* behavior to simulate deposition at the trench bottom (feature base). Obviously this is not strictly representative of the circumstances as formulated by the diffusion-adsorption mechanism, but the approximation is useful. A superfilling acceleration ratio can be calculated at a given potential by comparing the resulting current density of the additive free case to that of the full additive package. Ratios as high as 30 are often calculated based on rotating disk electrode (RDE) data from both solution combinations[8].

Despite the successes and relative simplicity of the diffusion-adsorption superfilling mechanism, there are number of phenomenological observations which cannot be predicted within this model. One of these problems is the mechanism's inability to account for deposition rate differentiation within the trenches and cavities as evidenced by the rounding of internal corners. As discussed in the section 3.3.2 with respect to Figure 3.3, the current density should increase along the profile from points A to E in order to produce the superfilling effect and avoid the formation of a seam. Second, an accurate superfilling model must also predict the formation of an overfill bump (also known as momentum plating). This phenomenon is a characteristic of features that are filled using Cu damascene-type chemistries and are believed to come about as a result of sustained acceleration of metal deposition following the filling action. The presence of the overfill bump is entirely inconsistent with the diffusion-adsorption mechanism and remains one of the primary motivations

behind the use of the second model, the curvature enhanced accelerator coverage (CEAC) mechanism.

3.3.6 Curvature Enhanced Accelerator Coverage (CEAC) Mechanism Model

One of the major pitfalls of the models developed from traditional leveling theory was the lack of complexity required to account for multiple additive species. More specifically, the first versions of the diffusion-adsorption model assumed that the diffusion limited transport of a single leveling species was the determining factor responsible for the nonuniform deposition rates required for superfilling. Unfortunately, the models based on traditional transport limited leveling models fail to capture the shape evolution of the metal surface during the filling event and cannot predict the formation of the overfill bump following the fill event[8, 10, 27]. In the early 2000s, The Moffat group introduced the CEAC mechanism to explain the experimentally observed corner rounding and general shape evolution both during and after superconformal filling of copper in vias and trenches of nanometer dimensions[60, 62, 79, 80]. They concluded that superconformal deposition and corner rounding may be attributed to competitive adsorption of inhibitor and accelerator. While this model has particular value in the area of electrochemical copper superfilling for IC interconnect applications, it has also has also been applied more or less successfully to other feature filling deposition systems such as silver electrodeposition[89, 90] and copper chemical vapor deposition (CVD)[91, 92].

According to the CEAC mechanism, which can be descriptively called an *accelerator accumulation* model, additives initially adsorb on the entire copper

seed covered wafer profile with reasonable uniformity, i.e. both on the top as well as within the features of the surface. Initially, copper plating is conformal on all surfaces (geometric leveling) but as growth continues and the feature profile begins to change, the surface area within small features decreases, and composition of the adsorbed surface film changes (see Figure 3.8). The shape change is especially apparent at the bottom corners of the trench. According to the CEAC, this decrease in surface area tends to concentrate the more strongly adsorbing accelerator additives, leading to displacement of the suppressor species. Since the deposition rate is proportional to the concentration of the adsorbed accelerator species, an increased current develops within the features and naturally leads to bottom-up, superconformal film growth. This model also lends itself to similar electrochemical studies as described above for the diffusion-adsorption mechanism. Figure 3.7 illustrates that a similar estimation of filling performance based on this mechanism can be approximated by electrochemical studies on planar electrodes by comparing i-η behavior in a full additive package solution to simulate deposition on top of the electrode with the i-η behavior in a solution of excess concentration of accelerator species to simulate deposition at the trench bottom. In this case, the ratio of current at the trench bottom relative to the top has been observed to be around 10 for a typical range of potentials relevant to the Cu damascene process. This number is much more realistic (than e.g. the value of 30 cited in the diffusion-adsorption related experiments) when compared to fill acceleration rates obtained by comparing growth rates of actual feature filling experiments[8].

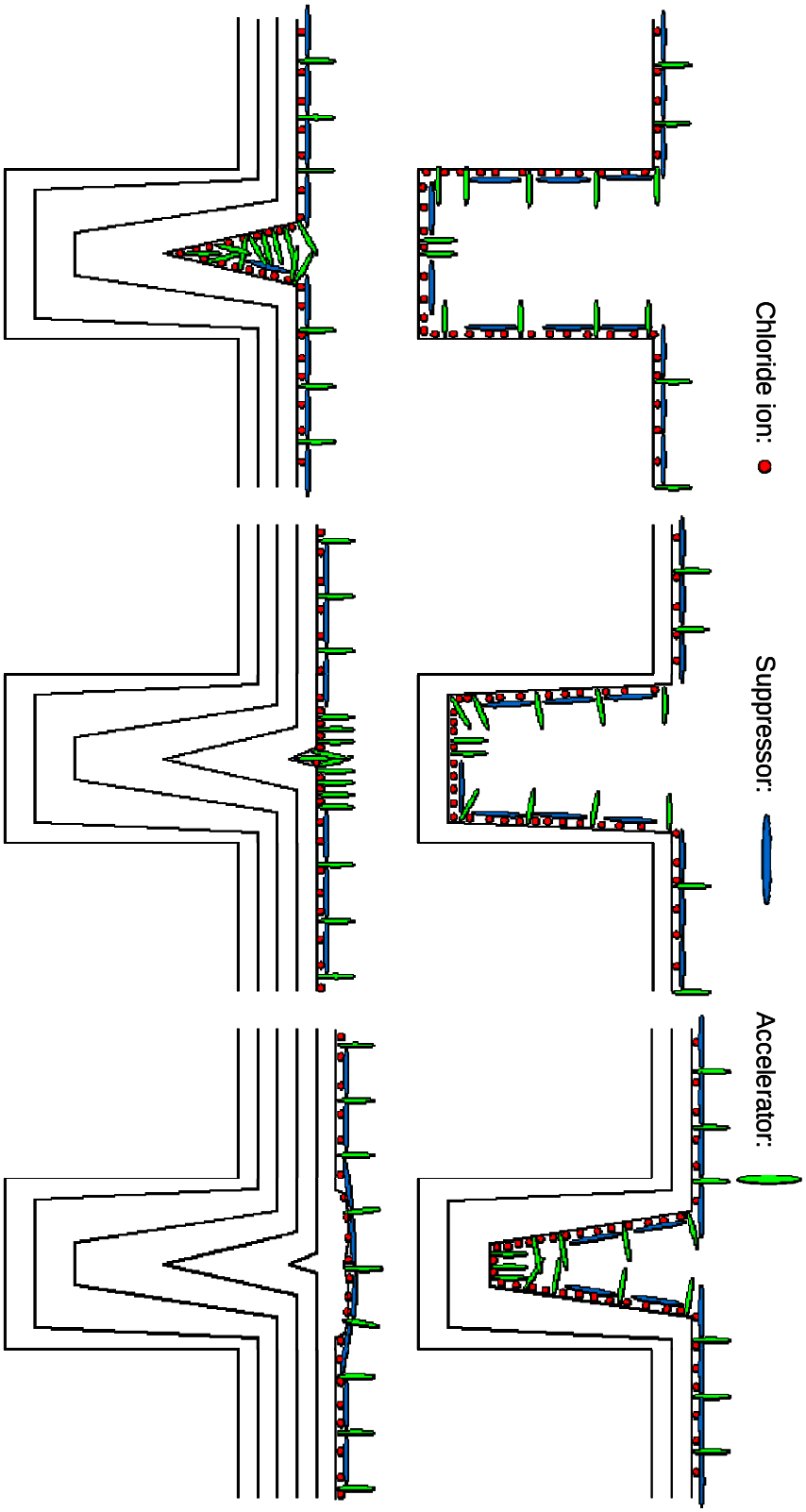
Chloride ion:
Suppressor:
Accelerator:

Figure 3.8 - Depiction of the trench fill evolution during the superfilling process as described by the curvature enhanced accelerator coverage (CEAC) model. Illustration adapted from References[8, 28, 70].

Among all of the arguments in support of the CEAC mechanism over the other proposed mechanism is an important result which seems to solidify the validity of the work done by Moffat, et al[10, 11, 21, 22, 60, 62, 63, 69, 70, 72, 76, 78-80, 93, 94]. By means of a two step process involving "derivitization", a ~30 second pretreatment of a Cu-seeded electrode by immersion in a accelerator containing acid bath, followed by electrodeposition in a suppressing solution, an acid Cu plating bath containing suppressor species only, the authors were able to successfully achieve superconformal deposition. It was found that an optimal surface coverage of accelerator (corresponding to immersion in a solution of intermediate concentration of accelerator) was required in order to achieve superfilling. For both very small and very large surface coverages, filling was ineffective and conformal deposition resulted in seam formation[10, 79]. Based on their analysis and subsequent modeling of the superfill process, Moffat et al determined that only the optimal surface concentration of accelerator species was able to produce the deposition rate differentiation necessary for superconformal filling of the trench. This result is significant because it unambiguously demonstrates that the transport of the accelerator species from the bulk solution is

unnecessary. In accordance with the CEAC mechanism, the superconformal filling of features is chiefly a product of a submonolayer quantity of surfaced confined accelerator species which becomes naturally concentrated at the feature bottom and produces a defect-free superconformal fill[10, 79].

CHAPTER 4

SURFACES AND SURFACE STRESS

Essential to the understanding of this work are the underpinning concepts and definitions of surfaces and interfaces. While the terms surface and interface are technically distinct they are often used interchangeably. For the purposes of this dissertation, the term *surface* has been adopted to describe the solid-liquid interface that forms between the electrode and solution. A surface is chemically different and has an excess energy relative to the bulk of the phase because of the non-uniform chemical environment that exists there. When accounting for the energy in macroscopic systems, the excess energy associated with a surface or interface is often negligibly small. However, in the case of systems involving material structures that have one or more dimensions in the nanometer range, surface properties can significantly affect the overall energy and behavior of the system and therefore cannot be neglected. This fundamental concept provides a framework upon which all of the work presented in this dissertation is established.

4.1 Gibbs Surface Model

One of the important contributions that Gibbs made to the development of thermodynamics is the conceptual basis of the thermodynamic representation of a surface. The central concept behind the Gibbsian surface is the accounting of surface excess quantities. A surface excess quantity is defined as a quantifiable difference at an interface between the surface of a specific material phase and the bulk of the phase. In order to define these excess quantities, a reference system is introduced in which separate homogeneous phases are separated by a sharp

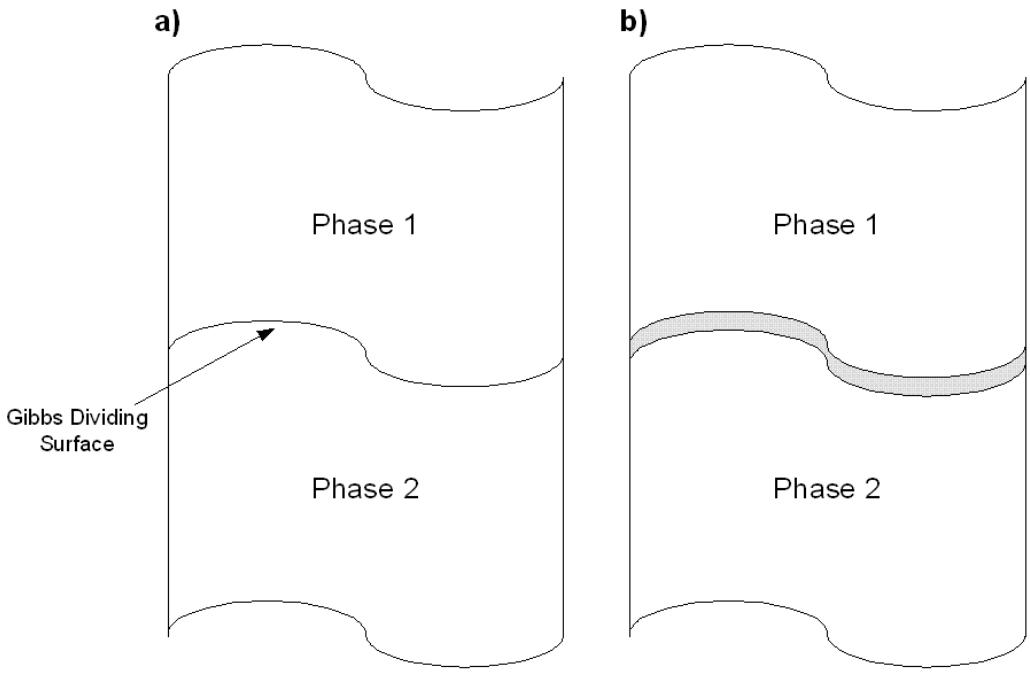

Figure 4.1 - Schematic depictions of the (a) Gibbs dividing surface and a (b) real interface between two distinct material phases. Illustrations adapted from Reference[95].

interface of infinitesimal thickness known as the Gibbs dividing surface (see Figure 4.1). For a reference system with a single interface between two phases, the variation in total Gibbs free energy is given as[96]

$$dG = -SdT + VdP + \gamma dA + \sum_i \mu_i dn_i, \tag{4.1}$$

where S, V, γ, and μ_i are the entropy, volume, interfacial energy, and chemical potential of the i^{th} species of the system and dT, dP, dA, and dn_i are the variations

in the system temperature, pressure, interfacial area between phases 1 & 2, and the number of moles of the i^{th} species. In this reference system all material properties and compositions remain at their constant bulk values directly up to the surface plane. Similarly, the incremental Gibbs free energy of each phase is given by[96]

$$\begin{aligned} dG_1 &= -S_1 dT + V_1 dP + \sum_i \mu_i dn_i^{(1)} \\ dG_2 &= -S_2 dT + V_2 dP + \sum_i \mu_i dn_i^{(2)}, \end{aligned} \tag{4.2}$$

where subscripts and $dn_i^{(1)}$ & $dn_i^{(2)}$ refer to phases 1 & 2, respectively. Because the real system maintains an interface with finite thickness over which the properties and compositions transition continuously from one phase to another, any differences between the real system and the reference system then correspond to the interface. Thus subtraction of eq 4.2 from eq 4.1 yields[96]

$$\begin{aligned} &d(G - G_1 - G_2) = \\ &-(S - S_1 - S_2)dT + (V - V_1 - V_2)dP + \gamma dA + \sum_i \mu_i d(n_i - n_i^{(1)} - n_i^{(2)}), \end{aligned} \tag{4.3}$$

which contains several terms that correspond to the surface excess quantities and are defined as

$$\begin{aligned} G^\sigma &= G - G_1 - G_2 \\ S^\sigma &= S - S_1 - S_2 \\ V^\sigma &= 0 = V - V_1 - V_2 \\ n^\sigma &= n - n_1 - n_2 \end{aligned} \tag{4.4}$$

where the σ superscript refers to the surface excess and subscripts refer the individual phases. By definition, the surface excess volume is equal to zero since the interface is infinitesimally thick. Thus the differential of excess energy due to the interface between the two phases becomes

$$dG^{\sigma} = -S^{\sigma} dT + \gamma dA + \sum_i \mu_i dn_i^{\sigma}. \tag{4.5}$$

In analogy to the case for bulk systems, a Gibbs-Duhem relation for fluid surfaces can then be derived[96]

$$0 = -SdT + Ad\gamma + \sum_i n_i^{\sigma} d\mu_i, \tag{4.6}$$

which at constant temperature is the basis for the definition of the Gibbs isotherm equation

$$d\gamma = -\sum_i \Gamma_i \, d\mu_i, \tag{4.7}$$

where $\Gamma_i = n_i^{\sigma} / A$ is known as the surface excess and is basically the excess number of species *i* at the surface, normalized to the area. The interpretation of the Gibbs isotherm is important as it pertains to the physical structure and of the surface and the associated energetics. For example, the surface excess is indeed an excess amount of a species at the surface with respect to its concentration in the bulk phase and oftentimes surface concentrations do vary from the bulk. That

is, Γ_i can take on negative or positive values which reflect lower or higher affinity for a surface, respectively.

For the case of a two component system, the position of the Gibbs dividing surface can be chosen such that one component (usually the solvent) has a surface excess of zero ($\Gamma_1 = 0$). Under these conditions, eq 4.8 simplifies to

$$d\gamma = -\Gamma_2 d\mu_2, \tag{4.8}$$

which for an ideal solution in which the concentration of species 2 is dilute, the activity coefficient is equal to one and $\mu_2 = \mu_2^\circ + RT \ln c_2$. This then allows for the rearrangement of eq 4.9

$$\Gamma_2 = -\frac{1}{RT}\left(\frac{\partial \gamma}{\partial \ln c_2}\right)_{T,P}, \tag{4.9}$$

where R and c_2 are the universal gas constant and the concentration of species 2 in the bulk solution, respectively. Thus for these specific conditions, it is understood that a solute, species 2, that decreases the surface energy with increasing bulk concentration will tend to accumulate at the surface. This result is a functional definition of surface active species or surfactants.

As described in Chapter 3 above, the adsorption of certain organic and inorganic solution additives gives rise to the superfilling effect in the Cu damascene process. It is, in fact, the synergistic effects of multiple, surface active

species in dilute concentrations induce the heterogeneous current density distribution along the profile of the vias and trenches.

4.2 Classical Electrocapillarity

Under the influence of an electric field, a charged species will behave differently than a neutral chemical species. In the case of electrochemistry, this type of interaction is of principal concern. Thus, the classical thermodynamic parameter of chemical potential must be modified to reflect this effect. The general electrochemical potential which accounts for the presence of electrical potential, ϕ, is defined as[40, 96]

$$\widetilde{\mu}_i = \mu_i + z_i F\phi, \tag{4.10}$$

where the two terms correspond to a *chemical* contribution in the form of μ_i and an *electrical* contribution in the form of $z_i F\phi$, where z_i & F are the charge of the i^{th} species and the Faraday constant, respectively. The corresponding form of the Gibbs-Duhem equation, which is also known as the electrocapillarity equation for a liquid electrode surface, can be derived by taking into account the *electrical* contribution[40]

$$d\gamma = -\left(q^M dE + \sum_i \Gamma_i \, d\mu_i \right), \tag{4.11}$$

where q^M and dE are the surface excess charge on the metallic side of the interface and the differential change in potential on the liquid metal electrode,

respectively. At constant temperature, pressure and composition, du_i goes to zero and eq 4.12 simplifies to the well known Lippman equation[40]

$$\left(\frac{\partial \gamma}{\partial E}\right)_{T,P,n_i} = -q^M, \tag{4.12}$$

and gives a direct measure of the change in surface energy (oftentimes referred to as surface tension for liquid electrodes) as a function of electrode potential. A characteristic feature of all classical liquid electrocapillarity curves is the existence of a potential at which electrocapillarity is maximized as seen in Figure 4.2. The implications of this result is that the slope of the surface energy vs. electrode potential curve is zero and by the Lippman equation, $q^M = 0$. For the net charge on the metallic side of the electrode to be equal to zero, the corresponding net charge in the solution must also be zero through the electroneutrality constraint

$$q^{tot} = 0 = q^M + q^S, \tag{4.13}$$

where q^S is the excess surface charge in the electrolytic solution that compensates for the charge on the electrode. Whereas q^{Tot} must always be equal to zero, the individual terms from both sides of the interface may take on both positive and negative values. At the maximum of the liquid electrocapillarity curve, however, the net charge on either side of the interface is equal to zero and the corresponding potential is defined as the potential of zero charge (pzc). As the

applied potential moves away from the pzc, equal and opposite excess charge accumulates on both sides of the electrode-electrolyte interface. This is manifested as a decrease in surface energy (also termed interfacial tension in by Grahame in Figure 4.2), γ, as like charges (negative ions at positive potentials and vice versa) that accumulate on the surface tend to mutually repel each other and by so doing, counteract the cohesive tension in the liquid electrode.

As a side note, Figure 4.2 illustrates that the electrocapillarity response of the mercury electrode is dependent on the supporting electrolyte species. That is, there is a shift in potential at which the maximum surface energy is recorded. This behavior occurs as the negatively charged ions in solution accumulate at the electrode surface in the absence of an electrostatic driving force. This indicates that anions (but not cations) have positive surface excess values due to some non-electrochemical interaction with the electrode. This behavior has been termed *specific adsorption* and has been observed in a wide range of electrode-electrolyte combinations [40]. With respect to the results presented in this dissertation and the theory of additive behavior, the halide ions are known to adsorb strongly on Cu electrodes. Furthermore, it has been shown that Cl^- is required in combination with the suppressing and accelerating additive species to produce the desired feature-filling phenomenon.

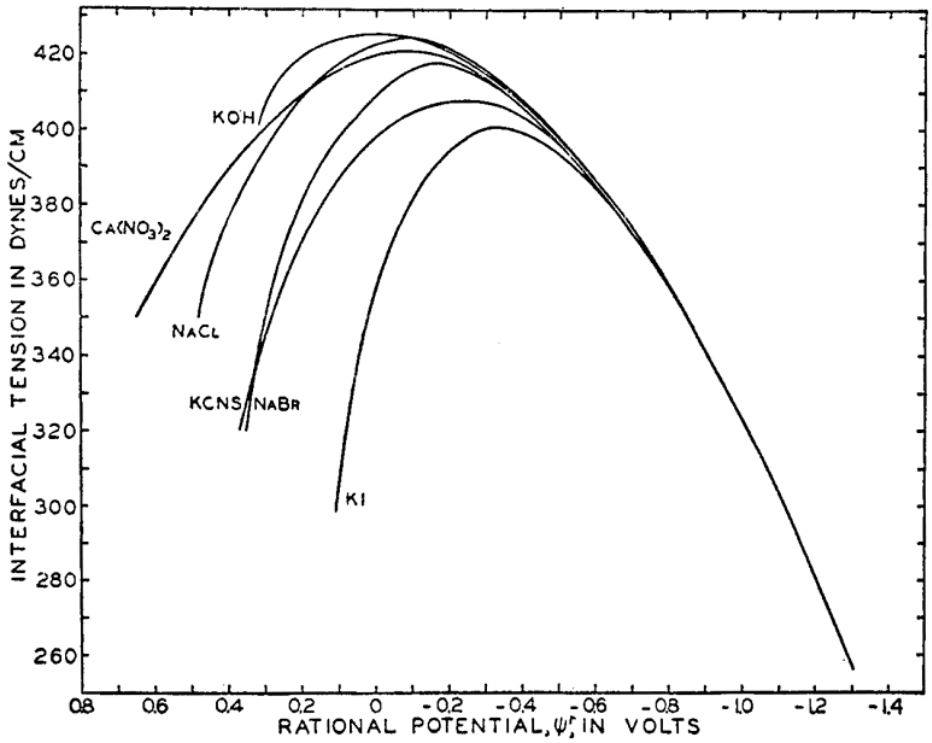

Figure 4.2 - Electrocapillarity curves showing the interfacial (surface) tension as a function of potential for a liquid mercury electrode in contact with aqueous solutions of the indicated salts. The potential is plotted with respect to the pzc of Hg in NaF (the maximum of the electrocapillarity curve). Figure reproduced with permission from Reference[97].

4.3 The Electric Double Layer

As the applied potential of an electrode immersed in electrolyte moves away from the pzc, the equal and opposite charge begin to accumulate on both the metallic and solution sides of the interface. In this sense, the system resembles a

capacitor. Because of this, electrochemical systems are often modeled as RC circuits where corresponding measurements of the capacitance of an interface are often used as analytical method to study the interface. One definition of capacitance is based on the differential change in accumulated charge due to a differential change in the applied potential (relative to the pzc)

$$\left(\frac{\partial q^M}{\partial E}\right) = C_d = -\left(\frac{\partial^2 \gamma}{\partial E^2}\right)_{T,P,n_i}, \tag{4.14}$$

and is also equal to the second derivative of surface energy with respect to applied potential[40, 98]. This differential capacitance measurement is obtained from the slope of the plot of q^M vs. E at any point but in contrast to an ideal capacitor, the capacitance of an electrode is a function of the potential. With reference to eq 4.15, Bard & Faulkner note that direct differential capacity measurements are nearly equivalent to electrocapillarity information[40]. However, for the case of solid electrodes, capacitance measurements have become relatively straightforward since the advent of electrochemical impedance spectroscopy (EIS) whereas pure surface energy measurements on solid electrodes have yet to be achieved.

Another use of the electrochemical circuit model and the associated capacitance measurements becomes important in the study of the electric double layer. Using the framework of the electrode-capacitor analogy, it is possible to construct a model that predicts the double layer structure and behavior and then compare those predictions to actual capacitance measurements. The double layer

is defined as an ordered structure that is electrically induced in a region of conductive liquid media directly adjacent to an electrically charged object. In the case of metallic electrodes, the large number and high mobility of charge carriers ensures that the potential is constant throughout the electrode. It was Helmholtz that first considered the existence of an equal countercharge on the solution side of the electrochemical interface[40, 99, 100]. In real systems the conductive liquid media usually consists of a complex mixture of solvated cations and anions in addition to a solvent (e.g. dipolar water molecules). In the original Helmholtz model of the double layer, the capacitance was proposed to be due to these two sheets of separated charges. However, this model results in a predicted capacitance that is constant and equal to that of a parallel plate capacitor [40],

$$C_d = \left(\varepsilon\varepsilon_0 / d \right), \tag{4.15}$$

where ε, ε_0, and d are the relative dielectric permittivity, the permittivity of free space, and the distance of separation between sheets of charge. Another double layer model that correctly predicted capacitance values at low electrolyte concentrations and at potentials near the pzc was independently proposed by both Gouy and Chapman [101-103]. The Gouy-Chapman model utilizes the concept of a diffuse layer of charge in solution which has a higher concentration of charge carriers near the electrode surface due to electrostatic forces. However, in this model the electrostatically induced ordering of charge near the electrode is opposed by thermal fluctuations and the distance term in eq 4.16 must be replaced

by an effective average distance between excess charge on the electrode and the charge containing diffuse layer. According to this model it is expected also that this effective average distance will be influenced by electrolyte concentration and electrode potential. As the electrolyte concentration increases or the electrode becomes more highly charged, the diffuse layer tends to collapse down over a smaller distance and as a result the capacitance increases. However, in the context of this model the effective distance of the compensating solution side charge can reach values that are not physically possible and the capacitance approaches infinity [40].

The schematic illustration of current understanding and model of the aqueous double layer is illustrated in Figure 4.3. This includes key modifications to both the original Helmholtz and Gouy-Chapman models as initially proposed by Stern [97, 105]. Stern first modified the Gouy-Chapman model by adding a distance of closest approach, effectively limiting the upper bound of electrode capacitance that is predicted. Thus, at larger applied potentials and electrolyte concentrations, the distance of closest approach is of order the radius of the adsorbing molecule or ion. Later, a second approach distance was introduced as the outer Helmholtz plane (OHP) and the Stern layer was similarly termed the inner Helmholtz plane (IHP) [40, 97, 106, 107]. The location of the IHP is defined by the locus of centers of the specifically adsorbed species that are believed to

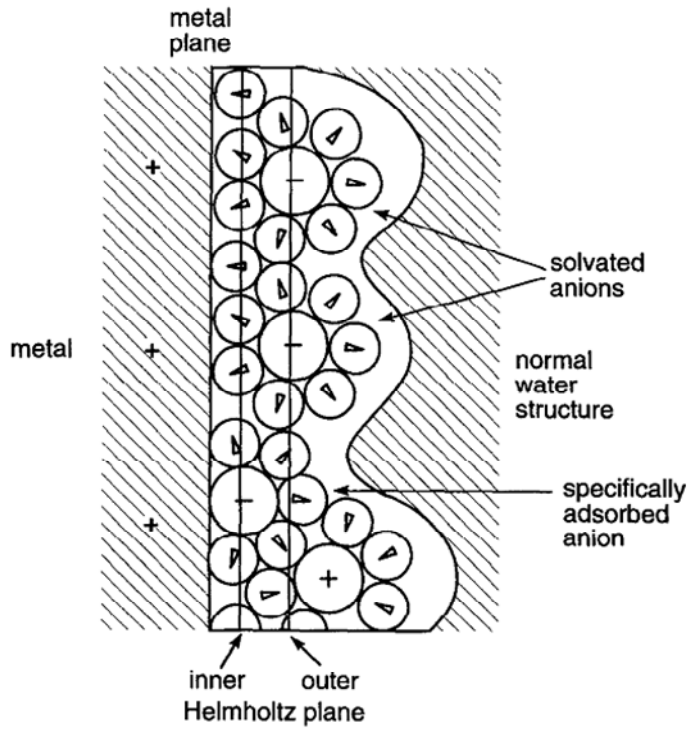

Figure 4.3 - Schematic model of the electrochemical double layer at a metal electrode surface with specifically adsorbed anions. Figure reproduced with permission from Reference[104].

penetrate the first layer of water molecules on an electrode surface. The distance of the IHP from the surface is then determined by the ionic radius of the adsorbed species and corresponds to a distinct capacitance value [106]. The OHP is composed of a second layer of solvated ions (presumed to be dominated by cations that do not specifically adsorb). All of this detail, of course, is relevant to an electrode at potentials near the pzc. At potentials far removed from the pzc, double layer theory predicts an increase in electrostatic attraction of ionic and polar species and

the multiple layers of IHP, OHP, and diffuse regions tend to collapse together into a single Helmholtz like sheet of charge.

4.4 Surface Stress

The surface free energy, γ, is defined as the reversible work per unit area required to form a new surface by exposing new atoms. This value is valid for surfaces in which the new surface is added at the bulk equilibrium interatomic spacing. This amount of energy is exactly half of the work needed to cleave a crystal and create two new surfaces in the absence of plastic deformation. However, in addition to the surface energy or surface tension term used above in the description of liquid electrocapillarity, it also possible to elastically create new surface area on solid surfaces. Thus the surface stress, f, is the amount of reversible work required to deform a surface and modify surface area by changing the atomic density of the surface[108]. The surface stress term arises during the consideration of solid surfaces which tend to change dimensions under the influence of external traction or even due to intrinsic effects associated with surface excesses (e.g. reduced electron density of metal surface relative to the bulk). Conversely, a fluid surface which cannot support a shear stress will flow in response to externally applied forces and new atoms or molecules will arrive at the surface in order to maintain a constant areal density. This results in a surface strain equal to zero and surface energy that is equal to the surface stress or fluid surface tension (e.g. as $\partial\varepsilon_{ij} \rightarrow 0$ in eq 4.17).

The origin of intrinsic surface stress can be intuitively understood by considering a clean metal surface in a vacuum. In the absence of any other external influence, a non-zero stress develops on the surface due to the absence of neighboring atoms on one side. The atoms at the surface are held in registry by the bulk atomic lattice on only one side and experience a different electronic environment than those located in the bulk. Due to this difference, the surface atoms will tend to adopt a non-bulk interatomic spacing in both the in- and out-of-plane directions but are restricted in their deformation behavior by the bulk lattice. In many cases the surface atoms will tend to a smaller atomic spacing in order to maintain a local electronic density that approaches that of the bulk metal. The sum of forces between the surface atoms and the underlying bulk atoms generally results in a tensile surface stress[108].

In Gibbs' formulation of surface thermodynamics, the amount of reversible work or total excess surface free energy was defined as the product of surface free energy and surface area, γA. Furthermore, both Gibbs[109] & Shuttleworth[110] noted that the amount of work required to generate a new surface area of a solid must account for newly created surface as well as the change in surface area due to strain. By accounting for these, Shuttleworth introduced the mathematical formalism that defines the surface stress tensor as[110]

$$f_{ij}(\vec{x}) = \gamma(\vec{x})\delta_{ij} + \frac{\partial \gamma(\vec{x})}{\partial \varepsilon_{ij}}, \tag{4.16}$$

where $f_{ij}(\vec{x})$, $\gamma(\vec{x})$, δ_{ij}, and ε_{ij} are the surface stress, surface energy, Kronecker delta, and surface strain, respectively. For a surface of ≥3-fold symmetry the Shuttleworth equation simplifies to a scalar (e.g. $f = \gamma + \partial\gamma/\partial\varepsilon$). In general, clean metal surfaces in vacuum have intrinsic surface stress values in the range of ±1-6 N/m and generally f and γ are not equal[108]. Similar to the intrinsic case, extrinsic factors can modify the stresses supported by the material surface. For example, surface processes such as adsorption, deposition, oxidative stripping and other surface mediated reactions can influence the stress supported on a surface. However, these processes can be very complicated and in many cases the actual interaction mechanisms responsible for modifying the stress state are not well understood.

With respect to the solid/electrolyte interface, Couchman and Davidson derived the Gibbs adsorption equation as[111]

$$d\gamma = -sdT - qdV + 2(f-\gamma)d\varepsilon - \Gamma_i d\mu_i, \tag{4.17}$$

where ε is the linear elastic strain, μ_i is the chemical potential of species i, and s, Γ_i, and q are respectively, surface excesses of entropy, species i, and charge, per unit area. Furthermore, when T and μ_i are held constant, the electrocapillarity equation for solid electrodes is generated[108, 112],

$$\left(\frac{d\gamma}{dV}\right)_{T,\mu_i} = -q + 2(f-\gamma)\left(\frac{d\varepsilon}{dV}\right)_{T,\mu_i}. \tag{4.18}$$

This equation describes how the solid electrode/electrolyte interfacial free energy varies in response to a change in electrode potential for an idealized electrode at constant temperature and chemical potential. This is analogous to the Lippman equation and its predictions for the liquid electrode/electrolyte interface. Moreover, the standard Lippman equation for a liquid electrode is recovered by setting $f = \gamma$. Electrocapillarity measurements have been performed on both liquid and solid electrodes in which the measured response (e.g. electrode displacement, curvature, etc.) is proportional to surface energy and surface stress, respectively. In the case of liquid metal electrodes, surface energy is maximized at the potential of zero charge (pzc) whereas surface stress can have a significant slope around the pzc[97, 98].

4.5 The Stoney Relation

In 1909, Stoney made observations that a when a metal film was electrodeposited on a relatively thick steel substrate, the substrate would bend due to the stress in the film. In an attempt to analyze the process and quantify the magnitude of the stress, he proposed a form of the now widely used Stoney relation[113, 114]

$$f = \sigma_f h_f = \frac{E_s^{el} h_s^2}{6(1-\nu_s)}\kappa, \tag{4.19}$$

where $\sigma_f h_f$ is the stress-thickness of the metallic film and E_s^{el}, h_s, ν_s, κ are the elastic modulus, thickness, Poisson's ratio, and curvature of the substrate, respectively. The following thought experiment provides insight into the

derivation of this important relation between substrate curvature and film stress. Consider the film-substrate system illustrated schematically in Figure 4.4. The film here is initially under a biaxial state of stress (σ_f) which is supported by traction of the film to the substrate. As the film is removed from the substrate and allowed to relax the stress, it assumes new dimensions. Next, the film is returned to the original dimensions of the interface by application of a biaxial membrane force per unit width of $F = \sigma_f * h_f$ (Figure 4.4). The film is then brought back into contact with the substrate and subsequently bonded to it. The membrane force, F, is removed from the film and a balance of forces brings a force per unit width of equal but opposite magnitude on the substrate surface.

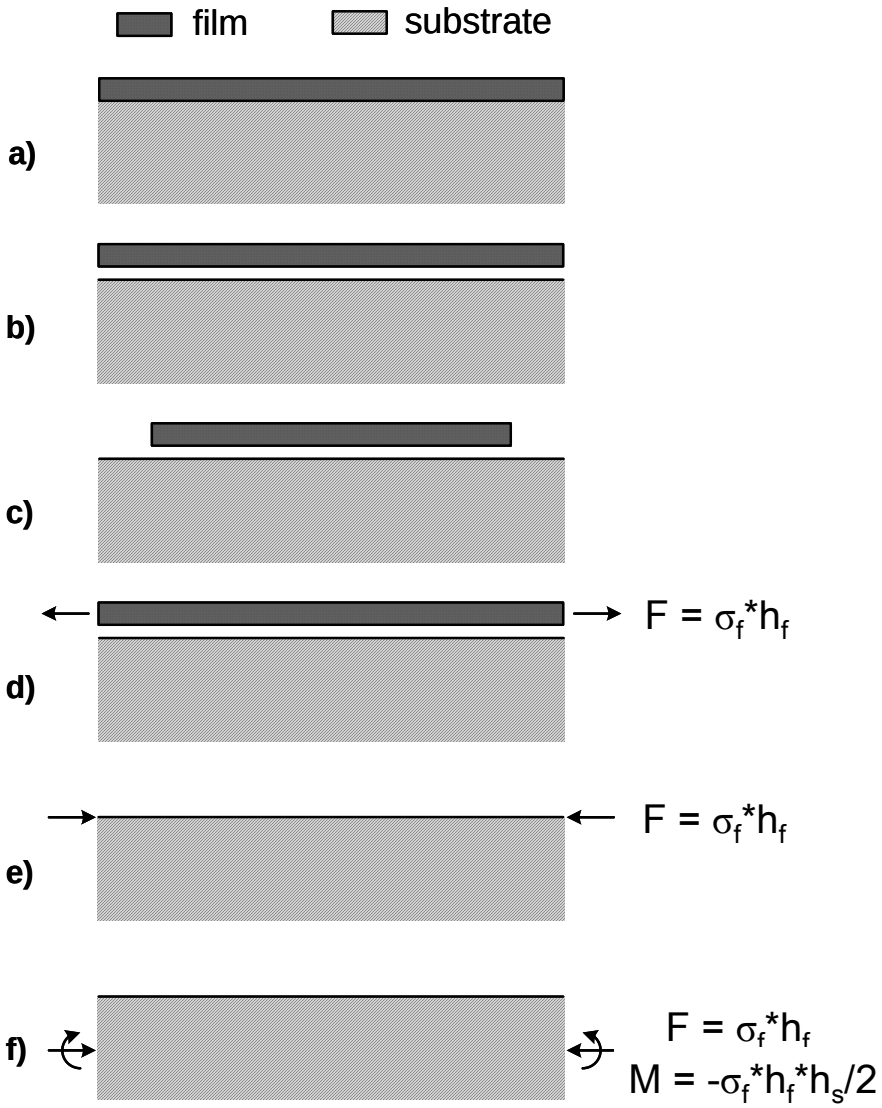

Figure 4.4 - Illustration of the thought experiment used to demonstrate the mechanical interactions in a stressed thin film/thick substrate composite system. The analytical treatment of this process is used to derive the Stoney equation (eq 4.28). Illustrations adapted from Reference[115].

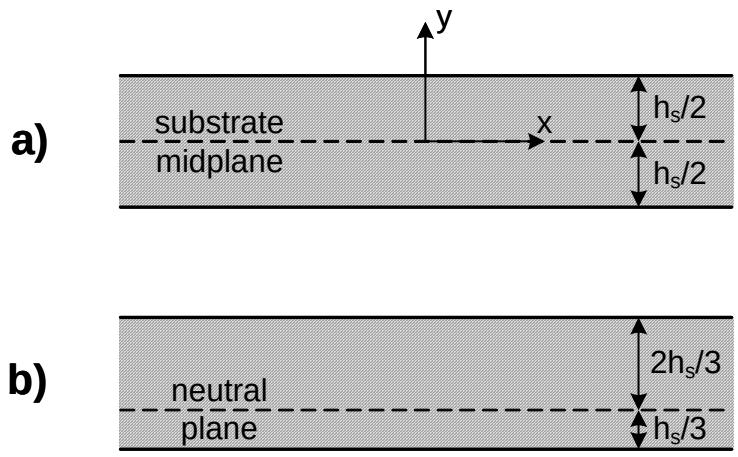

Figure 4.5 - Definition of the coordinate system used in the derivation the Stoney equation. The illustrations show the locations of both the (a) midplane and the (b) neutral plane as described in the text. Illustration adapted from Reference[115].

From this thought experiment, an analysis of the internal stresses can be made. First, the surface force is represented by an equivalent combination of a force per unit, *F*, width and a moment per unit width, *M*, at the substrate midplane. By defining a coordinate system as in Figure 4.5, the stress distribution in the substrate can be represented by

$$\Delta\sigma_{xx}^{axial} = \Delta\sigma_{yy}^{axial} = -\frac{h_f}{h_s}\sigma_f, \tag{4.20}$$

$$\Delta\sigma_{xx}^{bend} = \Delta\sigma_{yy}^{bend} = -\frac{12M}{h_s^3}z = \frac{12\sigma_f h_f}{h_s^2}z, \tag{4.21}$$

where the $\Delta\sigma_{xx}^{axial} = \Delta\sigma_{yy}^{axial}$ represent the axial stresses at the substrate midplane, $\Delta\sigma_{xx}^{bend} = \Delta\sigma_{yy}^{bend}$ represent the stress due to the moment applied at the midplane and where h_f, h_s, and z are the film thickness, substrate thickness, and the distance from coordinate form the substrate midplane, respectively[115]. By summing these two stress components and setting the biaxial strain components equal to zero, the location of the neutral plane within the substrate can be calculated

$$\varepsilon_{xx}\left(z = z_{np}\right) = \varepsilon_{yy}\left(z = z_{np}\right) = 0; z_{np} = -\frac{h_f}{6}, \tag{4.22}$$

where z_{np} is the distance between the substrate midplane and the plane which retains its original dimensions (see Figure 4.5). From this neutral plane, the biaxial strain at the surface of the substrate is calculated by

$$\varepsilon_{xx} = \varepsilon_{yy} = -\frac{2h_s}{3R}, \tag{4.23}$$

where R is the radius of curvature of the curved substrate surface. Furthermore, the equation for biaxial strain as a function of stress is defined by Hooke's law

$$\varepsilon_{xx} = \frac{\left(1-\nu_s\right)}{E_s^{el}}\sigma_{xx}, \tag{4.24}$$

where the biaxial strain was determined above and $[(1-\nu_s)/E_s^{el}]$ is the reciprocal of the biaxial modulus of the substrate. The stress at the substrate surface is found

by summing the two axial and bending stress terms acting at the midplane, $z = h_s/2$,

$$\sigma_{xx} = -\frac{\sigma_f h_f}{h_s} - \frac{6\sigma_f h_f}{h_s^2} z = -\frac{4\sigma_f h_f}{h_s}. \tag{4.25}$$

The combination of eqs 4.24, 4.25, & 4.26 yields a relation between stress and strain of the thin film system

$$\varepsilon_{xx} = -\frac{(1-\nu_s)}{E_s^{el}}\left(\frac{4\sigma_f h_f}{h_s}\right) = -\frac{2h_s}{3R}, \tag{4.26}$$

and rearrangement of eq 4.27 produces the well known Stoney equation,

$$\sigma_f h_f = -\frac{E_s^{el}}{6(1-\nu_s)}\frac{h_s^2}{R} = \frac{M_s^{el} h_s^2}{6R}, \tag{4.27}$$

in terms of the radius of curvature, R, and the biaxial modulus of the substrate, $M_s^{el} = [E_s^{el}/(1-\nu_s)]$. This relation is made equivalent to eq 4.20 above by replacing the radius of curvature with the reciprocal of the curvature, κ^{-1}. A consequence of the form of the Stoney equation is that the stress-thickness product (in units of Newton per meter) is directly proportional to the induced curvature of the substrate[113-115]. The stress-thickness product is also numerically equivalent to surface stress. In the literature, these types of measurements are often presented as average stress in the film which is obtained by dividing the stress-thickness by the thickness of the film. However, the units and the stress distribution must be

carefully considered when analyzing experimental stress results derived from the Stoney relation and substrate curvature data. For example, in the case of intercalation processes where, species such as hydrogen or lithium are inserted into electrode/matrix, the average stress is an appropriate parameter[116, 117]. Conversely, processes that are confined to an electrode or substrate surface such as underpotential deposition or island nucleation during heteroepitaxial film growth are more suited to treatment in terms of stress-thickness or surface stress[108, 118-120]. When doing thin film stress investigations, great care must be taken to consider these types of system details as well as the assumptions that are implicit in the preceding derivation of the Stoney relation. Some of these assumptions are considered in the following section.

4.6 Application of the Stoney Relation

It is very important that the details of the physical system be accounted for when applying the Stoney relation to thin film curvature results. There are several assumptions that were made in the derivation of the Stoney relation. These assumptions include the thin film approximation, an assumption that the substrate curvature is always near zero, and an assumption that the apparatus geometry is configured such that substrate curvature effects are minimized.

The thin film approximation is exactly as the name suggests, that is, a film substrate system where the thickness of the film is sufficiently thin compared to the substrate such that the mechanical properties of the film do not play a role in the support of the load. In an effort to generalize the relation between substrate curvature and thin film stress, Freund and Suresh relaxed the thin film assumption

to determine the non-negligible effects of film thickness and film modulus on substrate curvature[113]

$$\frac{\kappa}{\kappa_{St}} = \left(1+\frac{h_f}{h_s}\right)\left(1+4\frac{h_f}{h_s}\frac{M_f^{el}}{M_s^{el}}+6\frac{h_f^2}{h_s^2}\frac{M_f^{el}}{M_s^{el}}+4\frac{h_f^3}{h_s^3}\frac{M_f^{el}}{M_s^{el}}+\frac{h_f^4}{h_s^4}\frac{M_f^{el}}{M_s^{el}}\right)^{-1}, \quad (4.28)$$

where κ/κ_{St} is the ratio of the actual curvature to that predicted by the Stoney relation, and M_s^{el}, M_f^{el}, h_s, and h_f are the biaxial moduli of the substrate and film and the thicknesses of the substrate and film, respectively. The interpretation of this relation is that a curvature ratio near unity validates the use of the Stoney relation and a departure from unity indicates the need to take into account non-negligible thickness and stiffness of the film. With respect to the work presented in this dissertation, the ratio of curvatures is found to be ~0.98, producing an error of <2% for the thin film stress measurements presented here.

In addition to film thickness considerations, the accuracy of the measurements also depends on other constraints associated with the geometry of experimental apparatus. Friesen noted that the cantilever sample must be thin enough to provide adequate sensitivity to stress induced curvature but also must be thick enough to ensure that the resonant frequency be much greater than the timescale associated with the stress inducing phenomena[115]. He also pointed out that while the stress in the film is generally biaxial, edge effects at the boundaries of the film will likely induce non-zero shear components. According to Doerner and Nix, the shear stresses become negligible at distances from the edge that are much larger than the film thickness and thus the in-plane dimensions of the films

should be orders of magnitude larger than the thickness to minimize errors[115, 121]. In this work the films were prepared in all cases such that ratio of width to thickness was of order 35,000.

Another important consideration relating to the curvature of the thin film samples is the effect of clamping stresses. Clamping stresses are those which arise from the boundary conditions set by the cantilevered sample. The sample is clamped on the fixed end of the cantilever in order to enable deflection/curvature measurements. This clamp restricts the curvature of the sample to be identically zero along the width of the clamp-sample interface. It is, of course, important that the clamping surface be as flat as possible and that the aspect ratio (length/width) of the sample be as large as possible. Dahmen et al developed a finite element analysis based on the "dimensionality" of the bending due to the clamping and the resulting effect on the measured deflection/curvature as a function of aspect ratio and Poisson's ratio[122]. This elegant model predicts that for cantilevered beams of aspect ratio <0.2, the curvature along the width is restricted to zero (dimensionality = 1), whereas for high aspect ratio beams, spherical bending (dimensionality = 2) is restored at distances from the clamp that are greater than twice the width. Furthermore, the authors demonstrate a smooth, well defined transition between these two cases that depends on the Poisson's ratio of the substrate. Previously, Mickelson has applied this analysis to the sample geometry used for the work presented in this dissertation. Due to the fact that the width of the metallic films is less than the width of the glass substrate, Mickelson defined two aspect ratios, 2.0 and 0.91, which correspond to the length of the film divided

by the widths of the film and substrate, respectively. Per Dahmen et al's analysis, the curvature ratios, κ/κ_{St}, that follow from these respective aspect ratios are 1.04 and 1.076. Moreover, Mickelson concluded that since the clamp extends the width of the substrate, the bending is likely defined by glass substrate width and that the resulting curvature is overestimated by 7.6%[117, 122].

Another possible curvature effect that merits consideration is the phenomenon known as bifurcation. A thorough explanation of this phenomenon and the driving force behind it has been reviewed by Freund and Suresh[113]. It is defined as a sudden transition from spherical curvature to cylindrical curvature in response to film strains that are larger than some critical value. The driving force behind the transition is reduction in elastic strain energy which is relieved when the curvature in some principle direction increases significantly, in concert with the reduction of curvature in the orthogonal in-plane direction. The critical strain value associated with this transition is dependent on the aspect ratio of the sample as well as the induced sample curvature[123]. Based on the analysis of Finot and Suresh, a reasonable estimate of the critical stress-thickness for the sample geometry used in this work is of order 1000 N/m, which is several orders of magnitude larger than any stresses presented here.

CHAPTER 5

STRESS RELATED PHENOMENA IN THIN FILMS

Thin solid films have wide application across many types engineering systems. They are used in many cases where the reduced dimensionality (two dimensions) of the material becomes advantageous due to size constraints within the system environment, e.g. integrated circuits, micro-electro-mechanical systems (MEMS), or due to relative cost or scarcity of the film material, e.g. precious metal films for catalysis.

A thin film is defined as a material with constrained geometry in one dimension. Moreover, thin films generally refer to material layers which range from one atomic/molecular layer up to several hundreds of nanometers in thickness. The properties of a thin film are dependent on the methods by which it is deposited or formed. The range of possible deposition methods includes ultra high vacuum (UHV) techniques, aqueous & non-aqueous electrochemical methods, as well as chemical processes which may occur via adsorption phenomena. For the purpose of this work, the thin film samples of concern are metallic films formed by UHV physical vapor deposition (PVD) on glass substrates. Following UHV sample preparation, the films are immersed in electrochemical plating solutions and used for the surface stress monitoring experiments. For all cases herein, the initial thin film surface area was of order 2 cm^2 with film thicknesses of order several hundred nanometers.

5.1 Thin film Growth Modes

The fundamental growth modes of thin films can be classified into three different growth modes owing to the relative properties of the substrate and the depositing species. For a depositing material "A" that is deposited on a substrate material "B", the properties which most significantly affect the growth behavior include the A-A & A-B interaction energies and the respective crystallographic structures and lattice parameters of both A & B. Initially, the influence of the substrate on the growth behavior of the depositing materials is large but this influence is subsequently attenuated as the deposit grows increasingly thick. The study of these growth modes dates back to the seminal paper published by Bauer in 1958[124]. The three modes are defined as (1) island, or Volmer-Weber growth, (2) layer-by-layer, or Frank-van der Merwe growth, and (3) layer-plus-island, or Stranski-Krastanov growth. A schematic representation of these three growth modes at different stages growth is illustrated in Figure 5.1[115, 125].

The Volmer-Weber (VW) growth mode is characterized by individual islands which nucleate on the substrate surface and grow until they impinge on each other. Following impingement, the network of islands grows to a continuous layer which then thickens with continued deposition. According to the classic work by Bauer and subsequent authors, the thermodynamic criteria for VW growth can be summarized by $\gamma_f > \gamma_s + \gamma_i$, where γ_f, γ_s, and γ_i are the film surface energy, the substrate surface energy and the interface energy, respectively[115, 124, 125]. This criterion can be qualitatively understood as a film which tends to bond to itself due to relatively high film surface energy and is seen often for metallic thin

film deposits. The island network grows to impingement and dictates the film grain structure. For deposition processes which are performed at high film homologous temperatures, the grains grow to equiaxed grains which are oriented randomly in the film plane and have low energy orientations out of the plane. For films grown at low homologous temperatures, the preferentially oriented island/grains will grow to occlude the other grains[113, 115, 126].

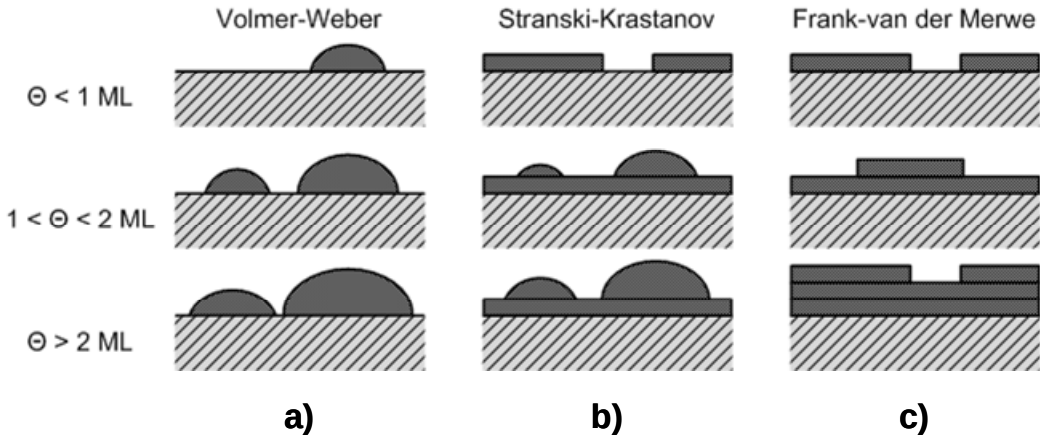

Figure 5.1 - Schematic representation of the three thin film main growth modes at several stages of film thickness (θ). The (a) Volmer-Weber (VW) growth mode occurs through island nucleation and growth, the (b) Stranski-Krastanov (SK) mode through a layer plus island progression and the (c) Frank-van der Merwe (FvM) mode grows by a layer plus layer process. Illustration adapted from References[115, 125].

The Frank-van der Merwe (FvM) growth mode consists of layer-by-layer growth which arises from a favorable energetic interaction of the deposit and substrate materials at the interface. The criterion for this type of thin film is $\gamma_s \geq \gamma_f + \gamma_i$ and results in a wetting overlayer of the substrate which forms upon deposition of a single film layer. An additional kinetic requirement for this type of growth is that the deposition flux must be sufficiently low and the surface diffusion must be large enough for the film surface to avoid critical adatom concentration thresholds and remain in the two-dimensional regime.

The third growth mode is an intermediate case known as Stranski-Krastanov (SK) growth. This growth mode is characterized by a thin wetting layer which initially form on the substrate followed by a transition to island growth. Thermodynamically, the requirement for SK growth is the same as FvM case, however, for SK films a significant lattice mismatch between the substrate and the film must exist. The strain in the film due to the lattice mismatch causes the eventual transition form layer growth to islanding in order to reduce the strain energy of the composite substrate-film system[115, 125].

5.2 Sources of Stress in Thin Films

During film growth in both electrochemical and vacuum conditions and the ensuing film service conditions, thin films are subject to a variety of influences that generate stresses within the films. Under vacuum conditions, the growth stresses and environmental factors have been studied widely and for many systems[113, 115, 119, 120, 126-152]. In electrochemical environments, the conditions are more complex and consequently less well understood. In this section, many of

the possible sources of stress generation are described briefly. In the chapters that follow, the specific case of stress evolution of metallic thin film electrodes in additive-free as well as damascene-like solution chemistries is explored experimentally.

5.2.1 Epitaxial Stress

For some thin film systems, an epitaxial stress will be generated as material is deposited on a substrate surface. During heteroepitaxial growth, the substrate provides a template for the arriving atoms of the film. The film will only grow pseudomorphically in systems where free energy can be minimized through a coherent interface between film and substrate. In other words, there must be a small lattice mismatch in order for the strain energy in the film to remain small. The lattice mismatch is defined as[113, 115]

$$m_l = \frac{a_s - a_f}{a_s} \tag{5.1}$$

where a_s and a_f are the substrate and film lattice constants, respectively. For some FCC metals, the lattice mismatch may range from very small (e.g. 0.002 in the case of Ag/Au) to very large mismatches (e.g. 0.114 in the case of Cu/Au). As the thickness of the epitaxial layer increases, strain energy per unit area remains uniform and the strain energy per unit volume remains constant. This essentially leads to an increasing amount of total strain energy in the film until it becomes more favorable to form misfit dislocations at the interface. Cammarata developed a thermodynamic model to determine a critical thickness at which the epitaxial

layer will lose complete registry with the substrate due to built-up strain energy. By accounting for the (1) volume elastic energy, (2) the work associated with changing the film substrate interfacial structure, and the (3) work required to stretch the film surface, Cammarata et al determined that an equilibrium strain value as well as the critical film thickness can be calculated by energy minimization techniques[138, 139]

5.2.2 Film Growth: Initial Compressive Stress in Volmer-Weber Films

The deposition conditions that lead to epitaxial growth are very specific and depend on the film material, the substrate, growth temperature, the deposition rate, and the conditions of the deposition system environment. For a large number of materials systems, however, films tend to grow in the VW growth mode and retain a polycrystalline microstructure. This is the case for films deposited both in UHV as well electrochemical environments[58, 153-155]. As described above, VW growth begins with island nucleation on the substrate followed by growth and coalescence of the islands. The growth then proceeds from island coalescence to full film contiguity followed by deposit thickening and grain coarsening. Due to the development of high resolution thin film stress monitoring, measurement of real time stress-structure evolution has become a common technique in the field of thin film science[113, 144, 156, 157]. These real time measurements have provided insights into the many physical processes that occur during film formation and the dynamic relationship between these processes and thin film stress evolution.

The initial change in stress that is observed during VW film growth is a compressive transient that corresponds to the island nucleation events that occur as the depositing species first impinge on the substrate. Because the nuclei are small with respect to bulk material, an excess surface stress due to large particle curvature creates a Laplace pressure which causes the nuclei to take smaller atomic lattice spacing. As the nuclei reach a critical size and become firmly adhered to the substrate they become constrained from any further increase in lattice spacing due to traction from the substrate. Any further size dependent change in the equilibrium lattice spacing is prevented by the substrate and results in a compressive film stress[141]. The stress that is communicated through the film-substrate interface acts to deform the substrate and is estimated by[113]

$$\sigma = \frac{2f}{R_{ld}}\left(\frac{R_{ld}}{R} - 1\right) \tag{5.2}$$

where f is the surface stress, R is the radius of the nucleus and R_{ld} is the "lock-down" radius of the crystallite (e.g. the radius at which the nucleus becomes locked into traction with the substrate).

5.2.3 Film Growth: Tensile Stress Due to Grain Boundary Formation in Volmer-Weber Films

Following compressive stress during nucleation and the initial growth stages, a tensile stress is often observed during thin film deposition. The most widely accepted interpretation of this behavior is related the coalescence of surface islands to form grain boundaries[113, 128, 158, 159]. In this model, the small

gaps between encroaching island boundaries are closed by the formation of grain boundaries between the island-grains. In order to form the boundary in the absence of extra material, the islands deform elastically in order to reduce free surface area and the excess energy associated with that area. This process results in the elimination of these two free surfaces and a reduction of the total energy of the system. The resulting stress can be estimated based on a simplified version of this model given by Freund and Suresh[113]

$$\sigma = \left(\frac{E^{el}}{1-\nu}\right)_f \left(\frac{\delta_{gap}}{d_{gr}}\right) \tag{5.3}$$

where the term $[E^{el}/(1\text{-}\nu)]_f$ is the biaxial modulus of the film, d_{gr} is the size of the island-grain, and δ_{gap} is the distance between the impinging island edges. Additionally, the authors suggest that the largest nominal gap that could be closed by this phenomenon is of the order $\delta_{gap} = 0.17$ nm, yielding an tensile coalescence stress estimate of order 1 GPa[113]. Further approaches to this problem have included hertzian contact modeling, reverse crack growth, as well as finite element modeling and have yielded a wide range of values in the magnitude of film stress generation[115, 159].

5.2.4 Film Growth: Late Stage Compressive Stress Generation in Volmer-Weber Films

During the early stages of polycrystalline VW thin film growth of high mobility materials, there is another transition from the net-tensile film stress described above to a net-compressive film stress. This transition indicates that

there must be an additional compressive stress generation mechanism in addition to the possible existence of relaxation mechanisms which would tend to relax the tensile island coalescence stresses. Often, the average stress in the film will approach a constant value of compressive stress that is dependent on the magnitude of the deposition flux as well as the temperature. While the experimental observation of this behavior has been widely documented, the exact mechanism behind the compressive stress remains a topic of research and debate in the literature[115, 119, 127, 133, 143, 156, 157, 160]. The proposed mechanisms for this compressive stress generation have been based on reconciling the observations of constant average compressive stress and the presence of reversible stress during growth interruptions[58, 115, 119, 127, 129, 134, 141, 143, 150, 155, 160-168]. These so called reversible stresses are relaxations of the film stress to decreased magnitudes once film growth ceases. They are reversible in that the magnitude of the compressive growth stress is re-established as film growth is resumed. Additionally, it has been suggested that grain boundaries (GBs) play an important role in the generation of the long term growth stress evolution. Long term tensile stresses have been observed for Pd films grown on a Pt single crystal surface and whereas Pd films grown on polycrystalline Pt substrates exhibit compressive stresses[113]. Thus, it seems possible that the compressive stresses are generated by incorporation of extra material into the grain boundaries during the growth process. According to Spaepen, a small number of excess atoms incorporated into the grain boundaries could generate the magnitude of compressive stress that has been observed experimentally[163]. His model accounts for the incorporation of the

extra atoms into the grain boundary through a trapping mechanism that is proposed to occur as adjacent ledges merge on a growing film. Another model proposed by Chason et al, argues that a supersaturation of high energy, high mobility adatoms on a growing film surface will establish a chemical potential gradient between the film surface and grain boundaries. The supersaturation is provided by the impinging deposition flux and adatoms are subsequently driven to migrate down into grain boundaries. A compressive stress develops in the film which opposes further adatom migration into the GBs and a steady-state stress evolution is established[134, 143, 145, 162, 165]. This model is convenient to the explanation of reversible stresses with high adatom mobility and it is argued that upon interruption of the deposition flux the compressive stress may be relaxed by the reverse migration of adatoms from the GB in the absence of a supersaturation of adatoms on the film surface.

5.2.5 Stress Generation by Surface Defects

In many cases of thin film growth, the deposition flux to the surface creates a large, non-equilibrium concentration of adatoms. An excess population of "positive" surface defects (adatoms) may arise due to slow diffusive kinetics relative to depositional flux. Analogously, in electrochemical systems a non-equilibrium number of surface vacancies or "negative" defects may also exist under requisite values of electrode potential and solution pH. Under the conditions of low mobility such as low homologous temperature or diffusive energy barriers (e.g. Ehrlich-Schwoebel), defect mobility is limited and an excess amount of steady state stress is generated in a metal film. In addition to

interactions between adatoms or between vacancies, step ledges and kinks may also interact and modify the stress state of the film surface. One of the earliest treatments of these types of systems was done by Lau and Kohn[169]. These authors found that the isotropic strain field due to the force-dipole associated with homo-adatom on an isotropically elastic surface to be

$$u(r) = \left(\frac{1-\nu^2}{\pi E^{el}}\right)\left(\frac{A}{r^2}\right) \tag{5.4}$$

where E^{el} is the elastic modulus and ν is Poisson's ratio of the material, where r and A are the radial distance from and force dipole associated with the homo-adatom on the film surface. Using this type of model, surface stresses arising from overlapping strain fields of excess surface defects may be estimated. For identical atoms the interaction is repulsive, generating a compressive stress whereas for dissimilar surface adatoms the interaction may be either repulsive or attractive[170]. Friesen et al have used force-dipole arguments to explain the presence of compressive stress during the growth of VW films. They found that in the pre-coalescence regime of VW film growth, the presence of a non-equilibrium adatom concentration could likely account for the observed stresses in absence of grain boundaries. Furthermore, embedded atom method calculations yielded a value for the force-dipole magnitude (A) that was in agreement with that calculated from experimental stress data taken during deposition of Cu on Cu{111}[119, 120]. The transient nature of the surface defect populations allow this model to be applied to the reversible stresses observed through VW thin film

growth. Based on arguments and observations of several groups, it seems likely that both this force-dipole model and the adatom-grain boundary model (explained above) are applicable to stress generation in thin film systems depending on the specific conditions of and during certain phases of the deposition process.

5.2.6 Thermally Induced Stresses

During the process of UHV film deposition, the substrate/film composite structure may be subject to several different temperature variations arising from many sources. These sources include controlled heating sources that are used to produce desired microstructures, radiative heating sources from deposition sources, as well as any other thermal components of the deposition system. As the temperature departs from the service temperature of the sample, a stress may develop in the film due to a difference in thermal expansion behaviors of the film and substrate materials. For a change in temperature, the thermal stress of the film can be calculated by

$$\sigma^{thermal} = \left(\alpha_s - \alpha_f\right)\left(\frac{E^{el}}{1-\nu}\right)_f \Delta T \tag{5.5}$$

where α_s and α_f are the coefficients of thermal expansion of the substrate and the film, $[E^{el}/(1\text{-}\nu)]_f$ is the biaxial modulus of the film and ΔT is the temperature difference imposed on the sample[121, 152]. For the case of a film in service, joule heating can lead to large temperature changes and concomitant thermal stresses. Joule heating induced thermal stresses thus represent an especially important

problem for IC interconnects in relation to the reliability of conducting interconnect lines which are subject to large current densities (~10^6 A/cm^2) at gigahertz frequencies while in service[36].

5.2.7 Grain Growth Stresses

Film growth under non-equilibrium conditions can result in excess grain boundary length within the microstructure of the film. Following the deposition process, a tensile stress may develop via grain growth or grain boundary elimination. Chaudhari was one of the first to consider a model for this mechanism as a source of stress in thin films[171]. Basically, this model considers the tensile stress to be a result of the competition between two physical processes. The first process is the reduction of excess energy associated with grain boundaries. This basically derives from the excess nature of the grain boundary energy relative to that of the lattice within a grain. Under non-equilibrium conditions, excess grain boundary area within the film will tend to decrease in order reduce the total energy of the film. However, the densification process leads to an increase in elastic energy stored in the film due to the mechanical constraints of film adhesion to the substrate. Thus the grain growth induced film stress can be calculated using the initial and final average grain sizes, L_0 and L, the excess volume per unit grain boundary area, Δa, and the biaxial modulus, $[E^{el}/(1\text{-}\nu)]_f$[121],

$$\sigma_{gg} = -2\Delta a\left(\frac{E^{el}}{1-\nu}\right)_f\left(\frac{1}{L}-\frac{1}{L_0}\right). \tag{5.6}$$

5.2.8 Stress Due to Excess Vacancy Reduction

The deposition of a film onto a substrate held at low temperatures can induce an excess concentration of vacancies in the growing film. This occurs when the deposition flux creates a film growth rate that overcomes the diffusive flux of vacancies to the free surface and a non-equilibrium film structure is formed. The increased number of vacancies in the film experiences a relatively large driving force to diffuse to and be annihilated at the surface, grain boundaries, dislocations and the film/substrate interface. Because the individual grains are constrained at the interface by the substrate or at grain boundaries by the adjacent grains, a tensile stress in generated upon annihilation of the vacancies. At grain boundaries, the vacancy is annihilated by the combination with a grain boundary atom and the magnitude of stress is estimated by

$$\sigma^{vac} = \frac{-\Delta c}{3}\left(\frac{E^{el}}{1-\nu}\right)_f \left(\Omega - \Omega_v\right), \tag{5.7}$$

where Δc is the total number of annihilating vacancies regardless of where they annihilate, Ω, and Ω_v are the atomic volume and the vacancy volume of the film material, respectively. Whereas this estimate may yield stresses of order several GPa, the effective contribution to the stress is likely to be mitigated by other atomic scale mechanisms such as dislocation motion and unconstrained grain boundary void growth.

5.2.9 Nanotwin Formation

A recent study has been published on the role of twin formation in electrolytically deposited Cu films[172]. The motivation behind this study and other studies of highly twinned Cu stems from the fact that a high density of nanotwins in Cu has been shown to improve mechanical strength while maintaining both advantageous levels of electrical conductivity and ductility[173]. According to first principles calculations, nanotwin formation is driven by the energy difference between strain relaxed nanotwinned Cu and highly strained FCC Cu, which is much less stable[174]. Because pulsed electrodeposition of Cu leads to a higher density of twin boundaries, Xu et al were able to use in situ surface stress monitoring to study the real time stress response of pulsed deposition of Cu on a gold substrate. The film was deposited by unusually large current density pulses (100-200 mA/cm^2) over very short periods of 0.5 seconds or less. Due to the deposition rate, large tensile stresses (of order a few N/m) were generated initially during the current pulses followed by compressive relaxations which were both smaller (~60% of the growth stress) and slower and occurred during ~10 second intervals between deposition pulses. By means of ex situ, post deposition microscopy techniques, the authors correlated the compressive stress relaxations with nanotwin formation which they argue occurs by recrystallization of small nonequilibrium grains which resulted from the high deposition rate. It is apparent from this study, in addition to other numerous studies of the stress relaxation transient behavior, that the overall stress evolution may be the result of a combination of factors. In the case of the relaxation processes following high rate,

pulsed electrodeposition of Cu, the relaxation process involves an atomic rearrangement which is a true relaxation process in the sense that the relaxation process is (1) smaller in magnitude, (2) opposite in sign from that of the growth stress and (3) occurs in the absence of deposition flux.

5.2.10 Contaminant Inclusion & Trapping of Electrolyte

It has been found that contaminant inclusion in growing thin films can have a significant effect on the residual stress as well as other post deposition stress related phenomena. While it is apparent that the incorporation of excess, foreign material in the film would likely influence the stress evolution, a definitive understanding or model of contaminant effects is not available. Hoffman assumed that a decrease in surface energy and increase in compressive film stress would result from impurity atoms and molecules that become trapped or tend to migrate into grain boundaries[158]. More recently, Kennedy *et al* demonstrated that even small concentrations of oxygen contamination in Cu films grown under vacuum conditions contribute significantly to compressive stress generation[131]. Under electrochemical conditions, the problem becomes significantly more complex. In fact, the complexity increases drastically for common electroplating conditions due to additive and electrolyte chemistry. Several studies have found an increase in contamination for deposition processes performed in the presence of additives[61, 175, 176]. Additive species were found to have a profound impact on the recrystallization behavior and simultaneous internal stress evolution of damascene copper films following the electroplating process, a phenomenon known as "self annealing." The self-annealing

phenomenon (explained in detail below) is only observed on copper films that are plated in additive containing solutions and is characterized by a favorable decrease in film resistivity as well as a compressive film stress relaxation. Direct evidence is not available as to the sign or magnitude of the stress associated with additive incorporation; however, it will be shown in this work that the electrochemically induced film stresses are larger in magnitude for films deposited in the presence of additive species.

5.2.11 In-situ Surface Stress Contributions: Electrochemical Considerations

The transition from thin film stress analysis in UHV environments to electrochemical environments requires the consideration a significantly larger number of stress causing factors. For example, the main purpose behind UHV work is to virtually eliminate the presence of unwanted influences (e.g. contaminants, temperature gradients, etc.) and create an ultra clean environment. In fact, ultra high vacuum work has the advantage of pressure monitoring and real time residual gas analysis (RGA) which both yield information that is directly related to the composition of the environment surrounding the sample [131]. Conversely, electrochemical environments require the immersion of the sample into a condensed phase which is often subject to non-uniform temperature gradients, convective transport, and is usually multicomponent in nature. Furthermore, potential control of an electrode sample affords the electrochemist much more control over the prevailing thermodynamic state of the sample. It is therefore extremely important to eliminate, minimize or account for all of the possible stress generation factors during electrochemical stress investigations.

Electrodeposition is the process by which material is added to the electrode surface by reduction of ionic species. Depending on the solution composition and the experimental details (e.g. potential, etc.), the material may be added in the form of molecular adsorbates, adatoms, ledge and kink site attachments, two dimensional islands, or ramified (three dimensional) deposits. While the stress that is generated by electrolytic deposition is highly dependent on many factors such as temperature, geometry/crystallography of the substrate, deposition rate, and plating bath composition, homoepitaxial type depositions (e.g. Cu on Cu) often produce compressive stresses[114, 165, 177].

Oxidative stripping or electrochemical etching is the reverse process of electrolytic deposition. The removal of metal atoms from the surface may occur as a receding ledge or terrace or possibly as a surface vacancy. This unique ability to precisely remove material in a fashion that mirrors the deposition process (as opposed to more destructive methods such as ion milling and sputtering) is one of the main advantages of electrochemical environments over UHV techniques.

Electrocapillarity was described at length in Chapter 4 above but can be considered more simply as a change in surface stress due to a change in applied potential in the absence of significant adsorption or other chemical reaction. For liquid electrodes, a maximum in surface tension is reached at the potential of zero charge (see Figure 4.2), but for solid electrodes the surface stress generally has significant slope and may not have an experimentally accessible maximum (see Appendix F)[98, 178]. Experimental electrocapillarity information is often difficult to

collect and in many cases appears to be inaccessible by direct means due to the lack of well defined pzc values or due to the onset of surface reactions such as surface oxidation, solvent redox reactions, specific adsorption, etc. A more in depth treatment of Cu electrocapillarity in sulfuric acid as it pertains to this research is given in Chapter 8.

5.3 Reliability of Interconnect Structures

As a thin film is deposited, internal stresses build up and can affect the properties of the film. This introduction of residual stress due to fabrication processing is very difficult to avoid. Residual stresses can induce a number of undesirable consequences including, excessive deformation, fracture, delamination, and microstructural changes in the films. Despite these prevailing conditions, many thin film structures have been successfully employed in engineering systems to produce a wide range of technological improvements that affect both fundamental scientific studies as well as everyday life. Because the mechanical integrity of nanoscale structures remains a major limitation in many technologies, the need for characterization of and engineering solutions for stress related failures is an ever greater challenge[113]. As it relates to the reliability of IC interconnect structures, knowledge of stress generation during film growth, during the production steps that follow deposition, as well as during the service lifetime of the IC become crucial.

5.3.1 Recrystallization/Self Anneal

During deposition of Cu films from additive containing solutions, nucleation characteristics are drastically different from those of the UHV or additive free deposition cases. Grains are continually formed throughout the deposition process under damascene like conditions and the average grain size is relatively small (i.e. <100 nm)[8, 179]. Because the grain structure is not at equilibrium following the deposition process (large excess defect energy associated with dislocations and stacking faults), the films undergo a grain growth process at room temperature that begins immediately following the film deposition[180-182]. During the grain growth process, these Cu grains have been observed to grow to dimensions that are several times larger than the nominal film thickness. In addition to grain growth processes, other characteristics of the films evolve simultaneously to yield electrodeposits that are more ductile, softer, have greater {111} texture and are ~20% more conductive. The time duration of the evolution of these properties has been known last from a few days up to a few months depending on the initial grain structure and the impurity content of the as-deposited film[8, 175, 183].

During the electrolytic plating process, bath additives become incorporated into the growing film. Despite the fact that impurity concentrations are very low (of order ~1 wt% or less), impurities are known to have significant effect on the structure and properties of the electrodeposits[184]. The incorporation process often involves redox reactions of the additive species and results in the presence of organic fragments in the grain boundaries that are relatively free to

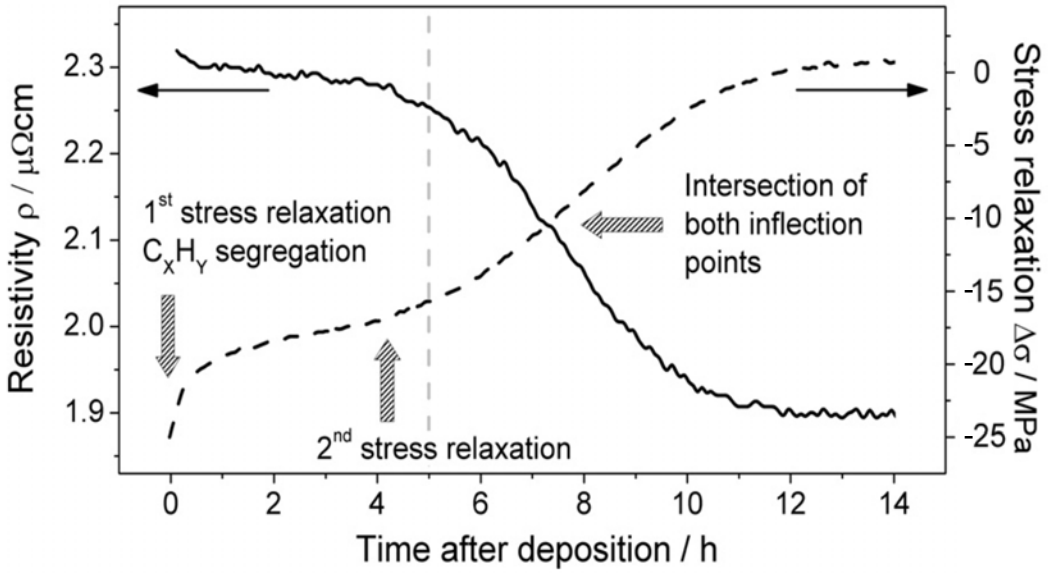

Figure 5.2 - Self-annealing of a 2000 nm electroplated Cu layer (on Ta) investigated by resistivity and stress measurements. The segregation and release of organic contaminants was measured by glow discharge optical emission spectrometry. Figure reproduced with permission from Reference[183].

diffuse to the deposit surface and eventually desorb. Stangl et al used glow discharge optical emission spectrometry to correlate the organic impurity loss phenomena with the resistivity and stress measurements during recrystallization of Cu electrodeposits shown in Figure 5.2[175, 183]. The first 5 hours that follow deposition are interpreted as an incubation time that is needed for new secondary grains to nucleate within the high energy, fine-grained deposit. Over this period, the resistivity decreases only slightly while a segregation of incorporated

impurities occurs. After ~5 hours, significant recrystallization begins and is associated with a steep decrease in both resistivity and compressive film stress. Following the recrystallization process (~14 hours total), residual stress asymptotically approaches zero while the resistivity approaches a constant value that is close to the theoretical value for bulk Cu, 1.9 and 1.7 μΩ-cm respectively.

5.3.2 Delamination

Metallic interconnect structures are subject to a wide range of stresses during wafer processing, including intrinsic growth stresses and extrinsic thermal cycling stresses[185]. Because Cu lines are surrounded by diffusion barriers, interlayer dielectric layers and the silicon substrate, serious consideration of the effect of thermal fluctuations must be considered. Each interface in this multilayer structure has unique mechanical properties and may be subject to failure. According to work done by Dunders et al, crack growth at the interface of two materials is dependent on both the elastic moduli and Poisson ratio of both sides of the interface as well as the stress intensity factors for both mode I & II crack loading[113, 186]. The susceptibility of these structures to stress induced fracture is enhanced relative to planar thin films because of the complex geometry of the metallized structures. The multiple edges and interfaces can function as stress concentration sites. Unfortunately, the combination of a non-zero nominal stress and a large number of stress concentration sites makes Cu interconnect structures vulnerable to failure by delamination.

5.3.3 Electromigration

A typical interconnect structure contains metal lines that are smaller 500 nm wide and sustain currents of around 1 mA. In the most extreme cases, this results in line current densities of order 10^6 A/cm^2. In combination with the large amount of heat that is generated due to resistive losses in the metal lines, a

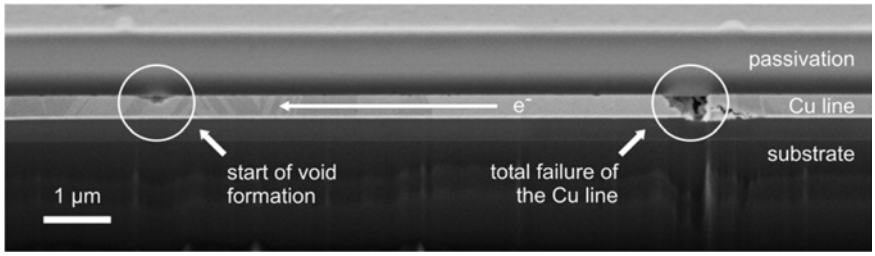

Figure 5.3 - Focused ion beam cross section image of a Cu interconnect line after an EM lifetime experiment. The left side shows nascent void formation in the line and the right side reveals complete disconnection by the formation of a void. Figure reproduced with permission from Reference[176].

process known as electromigration (EM) can occur. Electromigration phenomena was first observed in circuit interconnects during the 1960s in Al circuit wiring of computer chips[3]. It constitutes one of the most common failure mechanisms of IC interconnects whereby the lines fail by means of metal extrusion (hillock formation) or void formation (see Figure 5.3). Due to a transfer of momentum from the "electron wind" to the atoms along the conducting pathway, enhanced

atomic displacement occurs as diffusing atoms preferentially move in the direction of electron transport[187, 188]. The building up of atoms near the electron sink generates a compressively stressed region and the depletion of metal atoms near the electron source results in a tensile-stress region and eventually film rupture and/or voiding can occur[181, 187]. The transition to copper interconnects brought about a greater resistance to EM and longer chip lifetimes, yet the issue remains as a primary concern for the reliability of IC interconnects[3].

One of the main advantages of copper versus aluminum is a higher melting temperature. This makes the typical IC working temperature (e.g. 100º C) a relatively low homologous temperature for Cu as compared to Al and ensures that atomic diffusion rates are significantly smaller (see Table 5.1)[188].

Table 5.1 - Melting Point and Diffusivities for Cu and Al[188]

	Melting Point (K)	Homologous Temperature at 100°C	Diffusivity at 100°C (cm^2/s)
Copper	1356	0.275	$D_l = 7*10^{-28}$
			$D_{GB} = 3*10^{-15}$
			$D_s = 10^{-12}$
Aluminum	933	0.4	$D_l = 1.5*10^{-19}$
			$D_{GB} = 6*10^{-11}$

The subscripts of the different diffusivities refer to diffusion paths through the lattice, *l*, and along the grain boundary, *GB*, or a free surface, *s*.

However, as it turns out the improvement is not as large one might expect. Whereas grain boundary is the dominant path for EM induced mass flux in Al

interconnects, Cu electromigration damage occurs by surface diffusion at interfaces. Surface diffusion is important in these cases due to the poor adhesion characteristics of Cu structures at barrier layer and interlayer dielectric (ILD) interfaces, creating major short circuit pathways for diffusion that leads to eventual voids or ruptures. In combination with thermally induced stresses and stress migration (see below) type of behavior, EM is an insidious phenomenon which remains a major problem and current subject of study[3, 125, 176, 187-195].

5.3.4 Stress migration

In addition to the residual stresses due to film growth and the EM induced mass flux, another contributing factor to stress in IC interconnects is thermal expansion mismatch between interconnect and layer/cladding materials[2, 179, 196]. In fact, like EM, stress migration behavior of Cu interconnects depends strongly on the characteristics of the diffusion barrier-Cu seed and Cu line-capping layer interfaces. While the stress gradient is generally very anisotropic in Cu lines, the hydrostatic stress (i.e. the driving force for void nucleation) has been found to be weakly dependent on line thickness[179]. The term *stress migration* is used to refer to a phenomenon that is different from but related to EM. That is, stress migration and stress voiding is thought to occur through the diffusion of a supersaturated vacancy population and perhaps micron-scale voids that result from the Cu deposition and annealing processes[8]. For stress migration related failures, the root cause is usually a void or opening that forms near the base of a via that ultimately leads to an open circuit. Of course if a Cu strip is not confined by cladding or otherwise, surfaces which serve as both extremely effective

sources as well as sinks for vacancies and are less susceptible to rupture since stresses can be relaxed at the free surface[188]. However, for Cu interconnects encased in relatively rigid dielectric and cladding material, stresses can build inside the lines and are only slowly relieved by vacancy diffusion and void formation[196]. Vacancy diffusion occurs in response to internal stress gradient and constitutes a mass flux which is similar to the atomic diffusion observed in EM. However, stress is the driving force for vacancy movement whereas electron transport is the mechanism by which atoms migrate.

It has been found that the severity of the stress migration behavior is dependent upon a variety of factors including Cu purity, film thickness, geometry, fill quality, etc. Stress measurements of Cu during thermal cycling has indicated that high purity films that have greater strength and lower ductility tend to accumulate more stress than the low purity films[8]. Similarly, Alers et al determined that thicker films with lower yield stresses allow for plastic dissipation of strain energy and are therefore less susceptible to failure by stress migration[196]. Also, the presence of voids due to incomplete filling of high aspect ratio trenches can lead to early failure by stress migration. Under these circumstances, stress migration testing is very sensitive to fill quality because the fill related voids tend to migrate to the feature sidewalls or the line-via intersection during testing causing premature failure[8].

CHAPTER 6

OBJECTIVES OF THIS WORK

The work presented in this dissertation is a product of the unique ability to combine real time, in situ, ultra high resolution surface stress monitoring with other experimental techniques that have been developed within the Friesen Research Group. The measurements presented herein and in other publications produced by the group not only constitute some of the highest resolution surface stress measurements published to date, they also represent a strategic combination of the group's expertise and experience in surface stress monitoring with both electrochemistry and UHV techniques[98, 116, 131, 178, 197].

Under electrochemical conditions, surface stress monitoring as an analytical tool features high sensitivity to both the electrode surface and the near-surface solution region, including the structure of the electrochemical double-layer and any adsorbed species. Because of this sensitivity, surface stress measurements are well suited for the study of a variety of systems involving surfaces (interfaces). This technique has been previously used to measure both the small stress changes due to atomic/molecular scale processes such as adsorption and adsorbate re-orientation[98, 112, 198-200] and underpotential deposition (upd) of metals[108, 118, 155, 201-203] as well as larger bulk stress changes[58, 116, 128, 129, 146, 153-155, 172] in structures approaching the micron scale in size.

The strategy that was used in this work consisted of either characterization or minimization of certain stress generating processes in order to distinguish the stress contribution from a particular process of interest. For example, a large

portion of this dissertation is centered on the surface stress evolution of short deposition/stripping pulses performed on Cu films in damascene like solutions. The stress results from these experiments include contributions from electrocapillarity (ecap) effects and other solution side processes (such as adsorption, etc.) in addition to film-growth and -etching induced surface stresses. Because electrocapillarity effects are always present, it was necessary to characterize the ecap behavior of a copper film in the acid plating solution in order to adequately account for it during other investigations. Similarly, because deposition (and stripping) effects on stress can be relatively large and because the actual surface stress magnitude depends on the amount of material that is deposited, the deposit thicknesses were limited to small values (e.g. <10 ML) in order to minimize that contribution and enable the observation of other smaller stress generation phenomena (e.g. solution side adsorption processes). Moreover, this experimental approach is reflected in all of the projects presented herein; for a given system the overall surface stress behavior was studied by considering and investigating each individual source of stress through careful control of electrochemical, chemical and physical experimental parameters. Thus, the objective of this work was to leverage the expertise of the group in both electrochemistry and surface stress monitoring and study a variety of systems in which this expertise could yield important insight. In the following chapters, the results and corresponding analysis of several projects that met this criterion are broken into various chapters or appendices and presented for consideration by the reader. These projects include (1) the stress evolution during deposition and

stripping of Cu thin metal films in damascene-like solutions (Chapters 8-10), (2) surface stress changes of Cu thin films induced by solution side effects at the open circuit potential (Chapter 12), and (3) oxygen reduction and electrocapillarity of noble metal thin films (Appendix F).

CHAPTER 7

EXPERIMENTAL DETAILS

Several types of experiments are covered within this dissertation. Generally, all of the experiments follow a single pattern which was to combine a specially prepared solution (i.e. specific composition, pH, oxygen content, etc) with a patterned, UHV-deposited metal electrode in a custom designed cell that allowed for both electrochemical control of the cantilevered electrode as well as simultaneous measurement of the stress-induced deflection. Experimental procedures ranged from typical electrochemical techniques to more unconventional electrolyte displacement procedures, all while monitoring the evolving surface stress of the electrode. In every case, the sample surface was subjected to the stimuli of an electrochemical reaction, a molecular adsorption type process, or some type of environmental change (e.g. copper ion concentration, solution additives, etc). The subsequent response at the electrode-electrolyte interface produces a change in the stress state of the electrode surface and causes the sample to bend.

7.1 Sample Preparation

The cantilever/electrode assembly consisted of a 160 μm thick cleaned glass substrate and patterned metallic film. Samples were prepared in a 5 x 10^{-9} Torr base pressure UHV system and the electrode film was patterned using a through hard-mask to produce the electrochemical working electrode and capacitance sense electrode. The electrodes were prepared by first depositing 20 Å of Cr as an adhesion layer followed by a Cu (or other electrode metal of

interest) deposition to approximately 250 nm at approximately 1 Å/s. Under the stated growth conditions the films have a strong {111}-texture as confirmed by x-ray diffraction pole figures. In all cases the working electrode surface area was 2 cm^2.

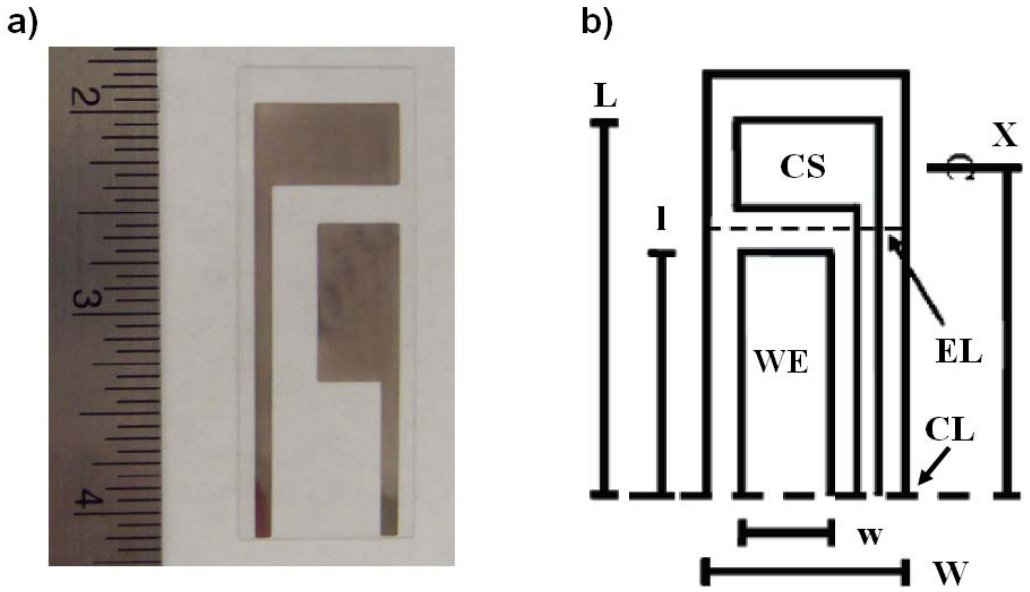

Figure 7.1 - Image (a) and illustration (b) of the patterned electrode sample used for the electrochemical surface stress measurements. The samples consisted of a working electrode (WE) film and a capacitive sense (CS) electrode film. During the experiments the sample was clamped at the level (CL) and partially submersed in the electrolyte up to a level (EL). The sample dimensions L, l, X, W, and w that are needed in order calibrate the cell per eq 7.6 and are defined in (b). Figure reproduced with permission from Reference[98].

As seen in Figure 7.1, each sample consisted of two electrically isolated films/electrodes. The first electrode located near the bottom of the glass slide is immersed in the electrolyte during the experiments and serves as the working electrode (WE) upon which the reactions occur. The other electrode serves as the capacitive sense electrode for the surface stress monitor and is used to measure stress-induced deflection of the cantilevered sample. The capacitive sense electrode must also be isolated physically and electrically from the solution in order prevent catastrophic signal interference and corrosion-type damage to the film. Both electrodes must be electrically connected to external electronics, the WE to the potentiostat and the capacitive sense electrode to the stress monitor. Obviously, it is paramount that these electrical connection requirements not interfere mechanically with the stress-induced deflections. Furthermore, the wiring connections must remain electrically isolated from the rest of the apparatus, the electrolyte, and each other. To this end, the sample geometry and corresponding UHV sample mask and holder were designed such that contact is made to both the working electrode and the capacitive sense electrode through thin metal films which are 2 mm wide and which extend to the bottom of the slide (see Figure 7.1). Contact is then made through the gold wire contacts which are integrated into the polytetrafluoroethylene (PTFE) electrochemical cell and located below the clamping level (i.e. not exposed to the electrolyte). Between the two main electrode areas (i.e. above the WE and below the capacitive sense electrode) there is a 5 mm gap which determines the fill level and the volume of solution that is loaded into the cell. Because electrical contact to the capacitive

sense electrode must be made below the clamping level, the as-deposited, 2 mm wide portion of the metal film that runs the length of the glass slide is protected by means of a thin layer of chemically inert enamel (e.g. nail polish).

As an ancillary but important detail of the sample preparation process, the careful use of an enamel is absolutely essential yet represents a possible source of contamination. Great care must be taken to minimize the probability of contamination issues arising from the use of the enamel. That is, the choice of actual brand and composition of the enamel (the product used herein for the enamel application was nail polish) as well as the method in which it is applied to the sample is important. The application of the enamel must be sufficient to cover the metal film but should minimally increase the overall thickness of the sample. The reasoning for this is two-fold. First, the enamel must be permitted to dry/cure thoroughly prior to exposure to the electrolytic solutions and a minimum amount of enamel reduces this time requirement. During this drying time the WE surface is exposed to both ambient oxygen as well as volatile organic species that are being released by the enamel as it dries, both of which may result in undesirable surface contamination. Second, because the composite thickness of the sample (glass & metal film) is small (~160 μm), the addition of superfluous amounts of enamel can have unwanted effects on the bending motion of the cantilever.

7.2 Electrochemical Surface Stress Monitoring Cell

Figure 7.2 shows a cross sectional schematic and top view photo of the assembled stress measurement cell. The major feature of the cell is that it holds both the capacitance-based surface stress sensor and vertically oriented cantilevered electrode at a fixed geometry for simplified and high throughput experimentation. Affectionately referred to as "The Maytag," the initial design of the cell was first conceptualized in 2006 by through a series of discussions

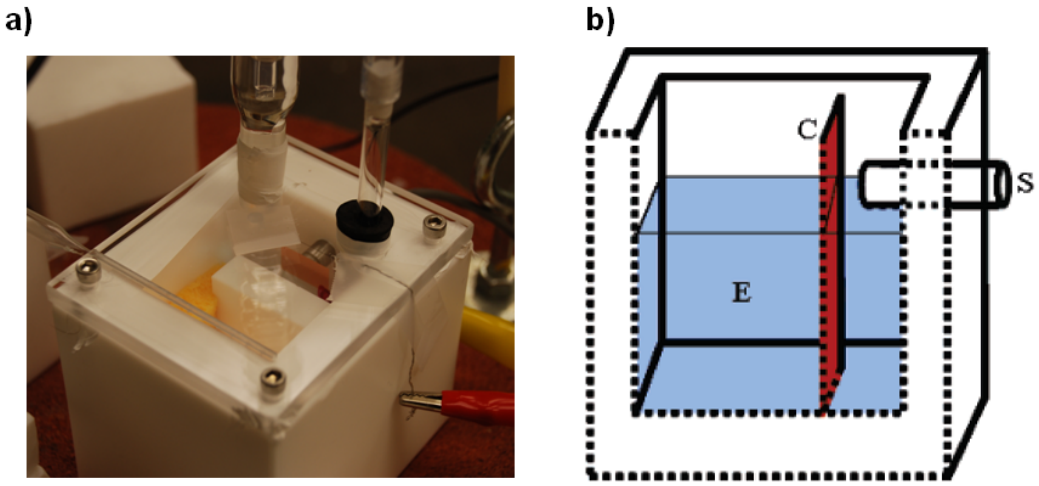

Figure 7.2 - Image (a) and illustration (b) of the custom PTFE cell used for the electrochemical surface stress measurements. The monolithic cell was machined such that a cantilever sample (C) could be clamped in place, the working electrode surface being below the electrolyte (E) level and the capacitive sense electrode directly adjacent to the surface stress monitor sensor (S). Figure reproduced with permission from Reference[98].

between Jordan Kennedy, Dr. Cody Friesen, and myself. The basic concept was adapted from a similar apparatus that has been in use in the Carl Thompson group at MIT as well as the Friesen Research Group at ASU for several years[115, 131]. The sample clamp consists of triangle "push block" (see Appendix A) in which has a milled-out groove that has the dimensions of and receives the glass slide sample during mounting, significantly reducing problems related to drift and sample placement error. The other face of the sample clamp has integrated gold contact pins for making electrical contact to both the electrochemical and capacitance sensing electrodes. The electrochemical cell consisted of a monolithic design that was machined from a single piece of PTFE. These conditions allowed for a cell that is extremely chemically inert, easy to clean, and most importantly, simple to construct and calibrate prior to the start of each experiment. Both the initial sketches and corresponding computer assisted engineering drawings that were produced in order to fabricate the cell can be found in Appendix A. The monolithic design of this cell not only provides for a simple method to take simultaneous electrochemical and surface stress measurements, it also facilities a significantly more straightforward stress measurement process over the other techniques such as the piezoelectric method, extensometric method, laser based wafer curvature monitoring, etc[204].

7.3 Surface Stress Monitor: Calibration & Data Collection

Many details associated with these experimental processes have been presented previously[98, 178]. The in situ surface stress monitoring is carried out by a cantilever curvature based technique. The surface stress sensor is a device that

monitors cantilever tip deflection by means of a capacitive measurement. The measured capacitance, C, is transduced to an output voltage, V, which scales linearly with deflection, d, (i.e. $C \propto V \propto d$). Because capacitance changes can be detected with very high sensitivity, the surface stress monitor collects data at both ultra high (sub-nanometer) deflection resolution and time base (of order 1 kHz) resolution (electronics only)[119, 127].

As explained in Chapter 4 above, the Stoney relation (eq 4.20) relates the curvature, κ, of a cantilevered sample to the in-plane stresses present in the film. However, because sample deflection is the actual experimental variable that is measured, the relation between deflection and curvature must be established based on the geometry of the sample. Recently, Mickelson has outlined the derivation of the relation between the measured deflection and the stress-thickness for an experimental apparatus identical to that used in this work[117]. The result of the derivation is a function which defines a relation between the change in stress-thickness and change in output voltage of the stress monitor, i.e.

$$\Delta\sigma_f h_f = K\Delta V, \tag{7.1}$$

where K is the calibration factor and ΔV is the change in output voltage. Basically the derivation is accomplished by first relating the curvature of the WE to the deflection, $u(x)$,

$$u(x) = \kappa l\left(x - \frac{l}{2}\right), \tag{7.2}$$

at a distance, x, from the clamped edge and where l is the length of the WE. This result is then rearranged as an expression for curvature and then substituted into eq 4.20 to produce a relation between deflection and stress-thickness for this geometry

$$\Delta f = \Delta\sigma_f h_f = \left(\frac{E_s^{el} t_s^2}{6(1-\nu_s)}\right)\left(\frac{\Delta u}{l\left(x - l/2\right)}\right), \tag{7.3}$$

where Δu is now the change in deflection. However, this relation must still be expressed in terms of the output voltage from the surface stress monitor. To accomplish this, a calibration protocol was developed utilizing gravity induced deflections of the cantilevered sample. The deflection of a cantilevered beam under uniform distributed load is given as[205],

$$u(x) = \frac{qx^2}{24E^{el}I}\left(6L^2 - 4Lx + x^2\right), \tag{7.4}$$

where q, L, E^{el}, and I are the distributed load in units of force, the total length, the elastic modulus, and the area moment of inertia of the cantilevered beam respectively. The load is applied as the assembled cell is oriented such that the sample bends in response the force of gravity (twice, both towards and away from the sensor) and a corresponding total output voltage is recorded. Thus by defining the distributed load in terms of the acceleration due to gravity (i.e. g = 9.81 m/s^2)

and the volume and density of the sample, a final relation that relates the stress monitor output voltage to stress-thickness:

$$\Delta\sigma_f h_f = \left(\frac{W}{w}\right)\left(\frac{\rho_s g}{6(1-\nu_s)}\right)\left(\frac{x^2\left(6L^2-4Lx+x^2\right)}{l\left(x-l/2\right)}\right)\left(\frac{\Delta V}{\Delta V_{tot}}\right), \tag{7.5}$$

where ρ_s is the density of the glass substrate, ΔV_{tot} is the total change in output voltage during the gravity calibration, and W/w is a term that appropriately scales the stress-voltage observation relative to the ratio of widths of the WE, w, and substrate, W. Inspection of eq 7.5 reveals a the identity of the calibration factor, K, described in eq 7.6,

$$K = \left(\frac{W}{w}\right)\left(\frac{\rho_s g}{6(1-\nu_s)}\right)\left(\frac{x^2\left(6L^2-4Lx+x^2\right)}{l\left(x-l/2\right)}\right)\left(\frac{1}{\Delta V_{tot}}\right). \tag{7.6}$$

Because the geometry of the samples is essentially identical across all of the experiments covered in this dissertation, sample to sample variation in K is small and depends only on ΔV_{tot}. The major advantage of this gravity calibration protocol can be seen by inspection of eq 7.5; calibrating the experimental setup in this fashion removes both elastic modulus, E, and thickness, h_s^2, terms by cancellation, both of which represent significant sources of error that are common to wafer curvature measurements.

7.4 Experimental Preparation and Protocol

The protocol for cleaning and preparation of the assembly of the sample and cell was virtually identical across all experiments presented in this

dissertation. All the glassware, the PTFE electrochemical cell, and the Pt counter electrode(s) utilized in the preparation of the samples and electrolytes as well as during the experiments were cleaned in heated, concentrated HNO_3 and H_2SO_4 baths followed by rinsing in 18 MΩ-cm water. For all experiments, a mercury-mercurous sulfate (MSE) electrode (+640 mV v. SHE) served as a reference electrode. For the electrodeposition experiments, a high surface area Pt wire mesh was employed as the counter (auxiliary) electrode. In this case, the Pt counter electrode (CE) was placed directly in front, at a distance of approximately 1 cm, and parallel to the working electrode surface plane. For the open circuit potential/solution exchange experiments, a Pt-Ir alloy wire braid was used as the CE.

The various solutions that were used in these experiments were prepared in a custom-made glass deaeration cell which was generally used to remove dissolved oxygen by bubbling nitrogen gas. Note that there is one exception to this step in which ultra high purity oxygen was used as the sparging gas for an experiment in which the oxygen reduction reaction (ORR) was investigated and is presented in Appendix F. Following the deaeration/gas bubbling step, the solution was then loaded into the preassembled PTFE cell in which the working, reference, and counter electrodes were already in place.

CHAPTER 8

CYCLIC VOLTAMMETRY AND SOLID ELECTROCAPILLARITY

8.1 Introduction

The electrocapillarity (ecap) of solid electrodes was described generally in the earlier chapters of this dissertation. It can be considered basically as a change in the measured surface stress due to a change in applied potential. Ideally, the surface stress signal contains components that are only related to elastic stretching of electrode surface atoms and the structure of the double layer that forms directly adjacent to the electrode surface. Unfortunately, non-ideal electrode polarization characteristics, the presence of oxygen or other contaminating species, as well as finite specific adsorption effects convolute the surface stress response and make it impossible to determine the true solid electrocapillarity behavior [108, 112, 206]. However, while this convolution of signals poses a problem from the theoretical/analytical viewpoint, it does not affect the experimental value of the results due to the fact that the "electrocapillarity" curve provides a measure of background surface stress signal. For example, when the electrode potential is scanned (as in cyclic voltammetry) or stepped (as in chronoamperometry) in order to study some electrochemical reaction such as metal deposition, the surface stress response will include electrocapillarity-type contributions in addition to the electrode response to the reaction of interest. In order to determine the portion of the signal that corresponds to the reaction being investigated, an ecap curve can be determined by performing similar electrode potential manipulations in the absence of the electrochemical reaction (e.g. metal deposition). This is may be

done by conducting experiments in “blank” solutions in which the redox species (or other species of interest) is missing from an otherwise identical solution or by performing similar potential manipulations (scanning, etc.) at potentials where the redox reaction does not occur. Obviously, it is preferable to collect the solid ecap curve at the same potentials in blank solution rather than at different potentials due to the fact that the overall ecap response may change with potential, but as in the case of e.g. electrode oxidation (which induces a significant stress response), oxidizing potentials must be avoided.

8.2 Experimental Details

The basic preparation and experimental setup for these electrocapillarity experiments was nearly identical to those of all the other experiments and was described above in Chapter 7. The purpose of this experiment was to characterize the electrocapillarity response of a Cu{111} thin film electrode over as much of potential space as possible. Because the magnitude of the surface stresses associated with electrocapillarity is relatively small (of order 0.1 N/m), it is of utmost importance that the electrode surface be clean (recently removed from the UHV deposition system) and that the experimental apparatus and electrolytic solution be contaminant free. In these cases, extra care was taken to minimize the time between removal of the sample from vacuum and the loading of the deaerated solution into the cell. The solution used for this investigation was a blank solution of 0.1 M H_2SO_4. In the absence of free copper ions in solution, undesirable redox processes are avoided by limiting the potential scans between the copper reduction potential (ca. -450 mV v. MSE) down to proton reduction at

the lower stability limit of water (ca. -640 mV v. MSE). At potentials anodic to this region, copper metal is not stable and is readily oxidized and removed from the electrode surface.

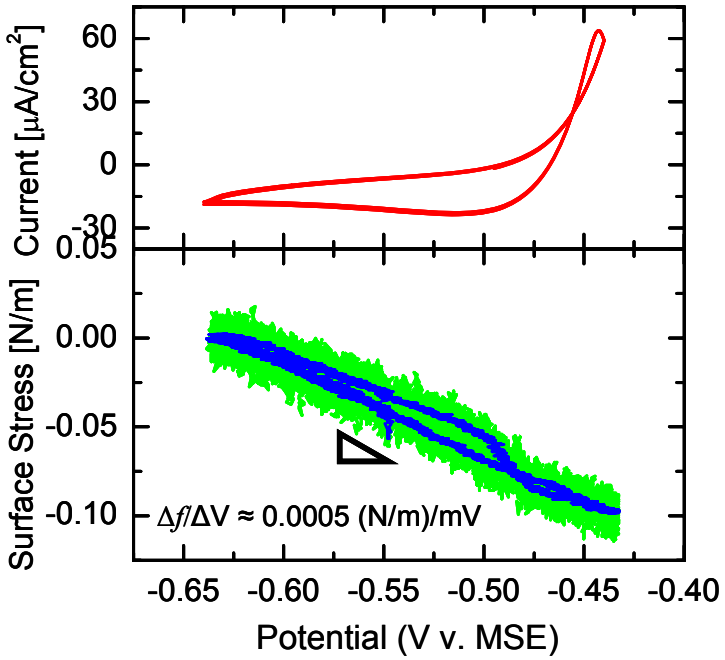

Figure 8.1 - Experimental results of the voltammetric (top) and the electrocapillary (bottom) responses of a Cu{111} thin film electrode in a blank 0.1 M H_2SO_4 solution (deaerated). The electrocapillarity response is essentially linear over this potential window and has a slope of ~0.0005 (N/m)/mV.

8.3 Results and Discussion

Figure 8.1 shows the results for both voltammetry and surface stress as a function of potential during two full cycles of a cyclic voltammetric (CV)

measurement at a scan rate of 20 mV/s. The actual choice of scan rate is relatively arbitrary since both the potentiostat and surface stress monitor have sufficiently high time resolution, but the chosen rate provided adequate experimental timescales without generating excess double layer charging effects. Prior to the scanning, the open circuit potential (OCP) was measured at ~-445 mV v. MSE and the anodic and cathodic potential limits of the CV were chosen accordingly. As shown in the current, a slight amount of oxidation current was recorded as the potential was scanned near the initial OCP. However, the effect is minimal as seen in the surface stress response which appears as a linear function of applied potential. The lower portion of Figure 8.1 displays the linear surface stress/electrocapillarity response of the Cu{111} thin film electrode over the entire potential window. Over this potential window, the only processes that are expected to occur are non-faradaic and are associated with changes in charge density within the metal and corresponding electric field-induced rearrangement of the double layer. The slope of the surface stress-potential curve is then a measure of these background electrocapillarity-type processes and is constant over the entire potential window. The $\Delta f/\Delta V$ correction or slope was calculated as ca. -0.00048 (N/m)/mV from Figure 8.1. Additionally, at a significantly faster scan rate of 50 mV/s this slope decreased slightly to ca. -0.00035 (N/m)/mV.

From the cyclic voltammetric measurements, it was shown that the electrocapillarity (ecap) response is linear and inversely proportional to the potential. This is significant because it allows us to (1) account for the expected ecap behavior in H_2SO_4 solutions and the potential region at which deposition

occurs and (2) reasonably extrapolate this linear behavior above the reduction potential of copper metal where oxidative stripping occurs. Additionally, the inverse relationship between the ecap response and the potential provides a simple explanation for the characteristic shape evolution of the surface stress directly following potential steps (e.g. after deposition/stripping pulses). This characteristic behavior is shown in Figure 8.2. The figure contains a typical surface stress curve in response to a cathodic potential pulse. In this case the pulse duration is approximately 10 seconds and the amplitude is 50 mV. As the potential is pulsed cathodically from the OCP, a tensile stress transient develops and persists over the course of ~1 second, followed by a larger compressive stress associated with copper electrodeposition. As the potential is stepped back to the OCP, a slightly steeper compressive slope is observed again for about 1 second before the stress then relaxes in the tensile direction. These short stress transients that occur as a result of the potential steps can be explained in the context of the ecap correction term ($\Delta f/\Delta V$) given above. Based on the value determined from Figure 8.1, a 50 mV pulse would be expected to produce an electrocapillary response that is the opposite sign of the potential step (ΔV) and of order 0.025 N/m in magnitude (see scale bar in the figure). As indicated in Figure 8.2, the actual ecap response is about 0.015 N/m following both the potential steps (dashed grey line) of potential pulse. Because the correction term is negative, the ecap response acts in opposition to the compressive (tensile) stress associated with incipient electrodeposition (relaxation) and the effect is somewhat mitigated leading to an actual response that is less than the predicted.

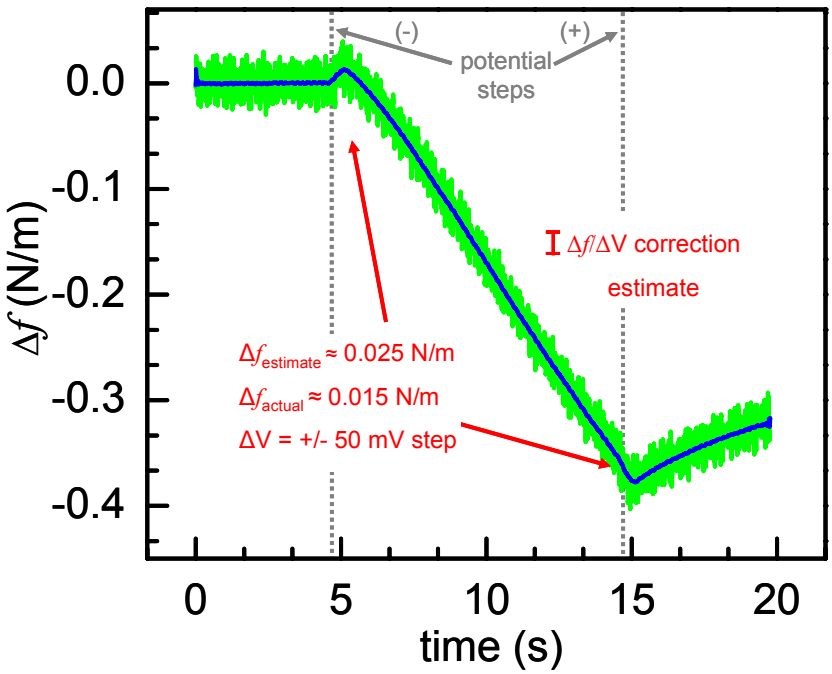

Figure 8.2 - Surface stress response of a Cu{111} thin film electrode to a -50 mV pulse from the OCP solution of 0.01 M $CuSO_4$ + 0.1 M H_2SO_4 (deaerated). The electrocapillarity (ecap) response appears as a minor perturbation, ~0.015 N/m, over a span of ~1 second following each of the potential steps. A value of ~0.025 N/m is expected from the $\Delta f/\Delta V$ estimate determined from Figure 8.1 and is shown to scale.

The most important result from this solid electrocapillarity measurement is the magnitude of the effect. That is, because the ecap correction factor is approximately 0.5 (mN/m)/mV and because the potential excursions applied/recorded in this work were generally ≤75 mV in magnitude*, the effect

was negligibly small. The overall surface stress evolution in Figure 8.2 provides a qualitative sense of this claim since the ecap contribution is approximately the same order of magnitude as the experimental noise in the raw data (black curve) and only becomes apparent in the adjacent-averaged signal (red curve). Quantitatively, the relative magnitude of the ecap response is ~4.7% of the total stress change (ca. -0.32 N/m) during the deposition pulse.

* Chapter 8 Note: The claim that the overpotentials associated with nearly all of the electrochemical techniques used in this research were ≤75 mV is confirmed by Figures 9.1 & 10.1. The single exception to this claim appears in the measurements taken in the suppressing (PEG/Cl^-) solution. For this solution, the overpotential reached values as large as ~-250 mV and ~+100 mV for deposition and stripping events, respectively. If a correction were to be made, it would be manifested as a negative and positive translation (i.e. constant correction across the entire thickness range) of the corresponding (red) curves in Figures 9.6 & 10.6, respectively. However, because (1) this correction would cause the results to become incongruent with the other curves in Figures 9.6 & 10.6 and because (2) no obvious ecap phenomena of opposite sign (as in Figure 8.2) is observed in the PEG/Cl^- stress curves (see Figures 9.3d, 9.4d, 10.3d & 10.4d), no correction has been made to the data and the assumption of negligible ecap contribution appears validated.

8.4 Summary Outline

- The ecap response is linear and inversely proportional to a change in the potential and the correction was calculated as $\Delta f/\Delta V \approx -0.00048$ (N/m)/mV from Figure 8.1.
- This correction allows for the (1) accounting of the expected ecap behavior in H_2SO_4 solutions and the potential region at which deposition occurs and for the (2) extrapolation of this linear behavior above the reduction potential of copper metal where oxidative stripping occurs.
- Most importantly, because the magnitude of the ecap effect is relatively small (~0.5 (mN/m)/mV), the effect of electrocapillarity effects are negligibly small for this work.

CHAPTER 9

CHRONOPOTENTIOMETRIC DEPOSITION

9.1 Introduction

The growth of thin films under both UHV and electrochemical conditions has been the subject of much research over the years. Thin films function in many capacities and applications that require mechanical stability in addition to other valuable material properties (e.g. electrical, thermal etc.). The original intent of the experiments described in this chapter was to mirror the deposition induced stress work that had been done previously under UHV conditions[108, 115, 119, 120, 127]. However, as the experiments progressed and our understanding of the system increased, it became apparent that this work would be best studied within the context of the copper damascene process and integrated circuit interconnect metallization. In addition to the use of plating additives, the chemistry of copper and its corresponding ionic species (Cu^{+}, Cu^{2+}, etc) provided a rich system to study.

All of the experiments presented in this chapter present surface stress profiles that consist of compressive stress growth stresses followed by tensile relaxation stresses following the deposition events. This is conspicuously different than some of the previous work done on Volmer-Weber type growth in heteroepitaxial systems and on amorphous substrates that exhibits the compressive-tensile-compressive (CTC) stress profiles associated with island nucleation, nuclei coalescence and zipping, and continuous film thickening[58, 115, 119, 120, 128, 129, 131, 132, 143, 146, 148, 150]. There are, however, some important similarities

between these studies and the results presented here. First, the increasingly compressive stresses observed during electrodeposition are analogous to the second compressive stress region observed in the CTC type stress evolution. The amount of stress generated during deposition events is dependent upon both the amount of material that is deposited as well as the deposition rate. Second, a tensile relaxation stress is observed during growth interrupts in both the present work as well as during interrupts performed in the long term compressive region of the CTC type UHV thin film growth. With respect to the UHV measurements, the relaxation has been attributed to a variety of processes including adatom migration into/out of grain boundaries (GBs), excess concentrations of surface defects, etc[115, 119, 207]. However, in the case of electrochemical growth environments, the films are subject to a variety of other physical processes such as molecular adsorption, exchange current processes, and so on that likely have an effect on the overall stress evolution. The purpose of these electrodeposition experiments was to monitor the film stress evolution during both deposition events as well as the relaxation events for depositions ranging from sub-monolayer to ~8 monolayer thicknesses.

9.2 Experimental details

Pre-experimental preparation and setup of the apparatus for the electrodeposition and oxidative stripping experiments was described in Chapter 7. The purpose of this set of experiments was to measure the real time surface stress response of a Cu{111} thin film electrode before and after the deposition event for a series of deposition thicknesses and in a variety of solution compositions.

The two types (sulfate based and perchlorate based) of solution combinations considered in these experiments correspond to three categories: additive free, suppressing, and full additive solutions. The actual compositions are shown in Tables 9.1 & 9.2. The sulfate based solutions constituted the majority of the work that was done here and represent the most common damascene-like plating formulation used in the literature[10, 19]. The perchlorate-based solutions were simply used to investigate the effect of the anion identity on the results. In order to discern the contributions to surface stress due to the multiple sources (deposition, electrocapillarity, molecular and ionic adsorption, etc), the film stress evolution due to the addition of copper metal was first characterized in the

Table 9.1 – Solution components and their corresponding concentrations for the six sulfate based solutions investigated in this work.

Solution Identifier	$[H_2SO_4]$ (mol/L)	$[CuSO_4]$ (mol/L)	[PEG]* (mol/L)	[NaCl] (mol/L)	[SPS] (mol/L)	[MPS] (mol/L)
Additive Free	1	0.25	0	0	0	0
Suppressing	1	0.25	$88*10^{-6}$	10^{-3}	0	0
5 μM SPS	1	0.25	$88*10^{-6}$	10^{-3}	$5*10^{-6}$	0
50 μM SPS	1	0.25	$88*10^{-6}$	10^{-3}	$50*10^{-6}$	0
10 μM MPS	1	0.25	$88*10^{-6}$	10^{-3}	0	$10*10^{-6}$
100 μM MPS	1	0.25	$88*10^{-6}$	10^{-3}	0	$100*10^{-6}$

additive free solutions. Then, by accounting for and minimizing this large component of the overall stress, it was possible to distinguish important differences associated with the presence of the different additive species. This was accomplished by comparing the results of the additive free experiments with the additive containing (suppressing and full additive) solution results. The range

Table 9.2 – Solution components and their corresponding concentrations for the six perchlorate solutions investigated in this work.

Solution Identifier	$[H_2ClO_4]$ (mol/L)	$[Cu(ClO_4)_2]$ (mol/L)	[PEG]* (mol/L)	[NaCl] (mol/L)	[SPS] (mol/L)
Perchlorate Additive Free	1	0.25	0	0	0
Perchlorate 50 μM SPS	1	0.25	$88*10^{-6}$	10^{-3}	$50*10^{-6}$

of deposit thicknesses was restricted to 8 monolayers or less (see Table 9.3) in order to minimize the deposition induced stress contributions and facilitate the observation of stresses generated by other processes. All of the deposition events were done using current controlled techniques. Specifically, the experiments were done as a series of double step chronopotentiometric experiments wherein the current was fixed at zero both before and after the current pulse and the square current pulse had a magnitude of either -1 or -5 mA/cm^2. Table 9.3 shows the

equivalent deposit thicknesses and the corresponding current pulse lengths that were calculated and used for the series of depositions at each current density.

Table 9.3 – Current pulse durations during deposition (& oxidative stripping) experiments at -1 & -5 mA/cm^2 current densities.

Thickness, θ (ML)	1 mA/cm^2 Deposition/Stripping Time (ms)	5 mA/cm^2 Deposition/Stripping Time (ms)
0.2	113	23
0.4	226	45
0.6	339	68
0.8	452	90
1.0	565	113
1.2	677	135
1.4	790	158
1.6	903	181
1.8	1016	203
2.0	1129	226
2.5	1411	282
3.0	1694	339
3.5	1976	395
4.0	2258	452
5.0	2823	565
6.0	3387	677
7.0	3952	790
8.0	4516	903

In order to allow for the re-equilibration of the electrode-electrolyte system after each deposition event, the ratio of current pulse time to open circuit

time was large. That is, the time spent at open circuit potential at least 100 seconds whereas the longest current pulse was ~4.5 seconds (see Table 9.3). The corresponding time profiles of both surface stress and electrode potential were recorded separately for each event and at an acquisition rate of 1 kHz.

*Chapter 9 Note: The solubility, diffusivity, and suppressing action of polyethylene glycol (PEG) are all known to be a function of the average PEG molecular weight used. For this reason, a single source of PEG (MW_{PEG}=3350 gram/mole) was utilized throughout all of the experiments. More broadly, all of the constituent chemical species and concentrations employed in this work were chosen based on the wide range of excellent studies published in the area of superfilling and copper damascene research. Specifically, the chemistry used in these investigations most closely follows the work of the Moffat group at the National Institute of Standards and Technology (NIST)[10,11,21, 22, 60, 62, 63, 69, 72, 76, 208].

9.3 Results and Discussion

During constant current chronopotentiometry, the potential is recorded as a function of time. Aside from very short-term potential transients that accompany the current step (on and off), the potentials in these experiments remained relatively constant for a given solution and at a constant current density. As shown in Figure 3.4, the solution composition can have a significant effect on the overpotential required for deposition. Similarly, Figure 9.1 shows the typical overpotentials recorded in this work for each of the solutions investigated. As described in Chapter 3, electroplating additives are often referred to a polarizing

or depolarizing in reference to the effect of increasing or decreasing, respectively, the required overpotential at a given current density.

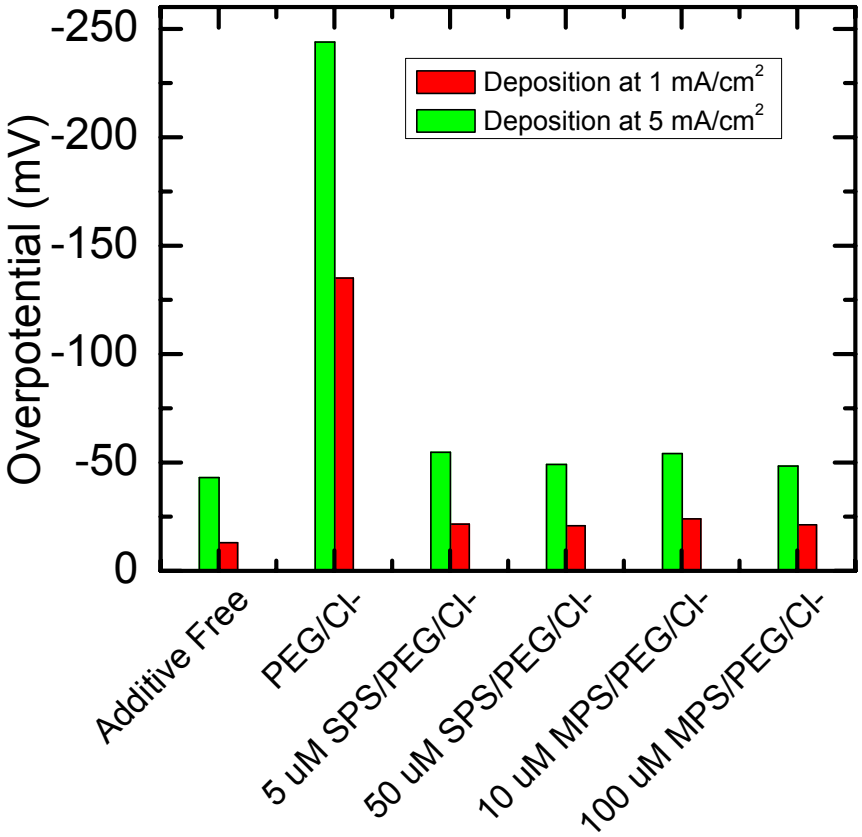

Figure 9.1 - Column plot comparison of typical overpotentials recorded on a Cu{111} thin film electrode during chronopotentiometric deposition pulses of 1 (red) or 5 (green) mA/cm^2, illustrating the polarizing (larger overpotential) and depolarizing (smaller) effect of various additive species.

The suppressing solution investigated in this work contained both PEG and chloride ions which are known to adsorb readily on the copper surface to

form a deposition blocking layer. The result of this polarizing combination of additives is a greater overpotential that is required to sustain the specified constant current density. The other solutions produce a much smaller overpotentials in order to support the specified current density. Specifically, the additive free case requires the lowest overall potential while the four full additive solutions all exhibit similar values. The full additive solutions contain an accelerating species which partially breaks up the PEG/Cl^- blocking layer and facilitates the electrocrystallization process. As was shown previously, the accelerating species do not fully deactivate the polarizing action of the PEG/Cl^-, rather they partially restore the electrode activity with respect to the additive free case (see Figure 3.4). Figure 9.1 then represents a rough confirmation of the anticipated behavior of the additive species on the electrodeposition process and indicates that these solutions do have the ability to produce the non-uniform current density distribution required for feature superfilling.

In addition to the electrochemical measurements collected during the deposition events, the real time surface stress signal was also recorded as a function of time. One of the biggest challenges of using separate data collecting equipment for in situ investigations is the need to collect data simultaneously as a function of time. Figure 9.2 shows an example of the results produced by these simultaneous data collection techniques. Here, current density, electrode potential, and surface stress are shown for a ~30 second window that captures both the evolution of these parameters during the current pulse or deposition event as well as the subsequent relaxation period that follows. In general, all of the

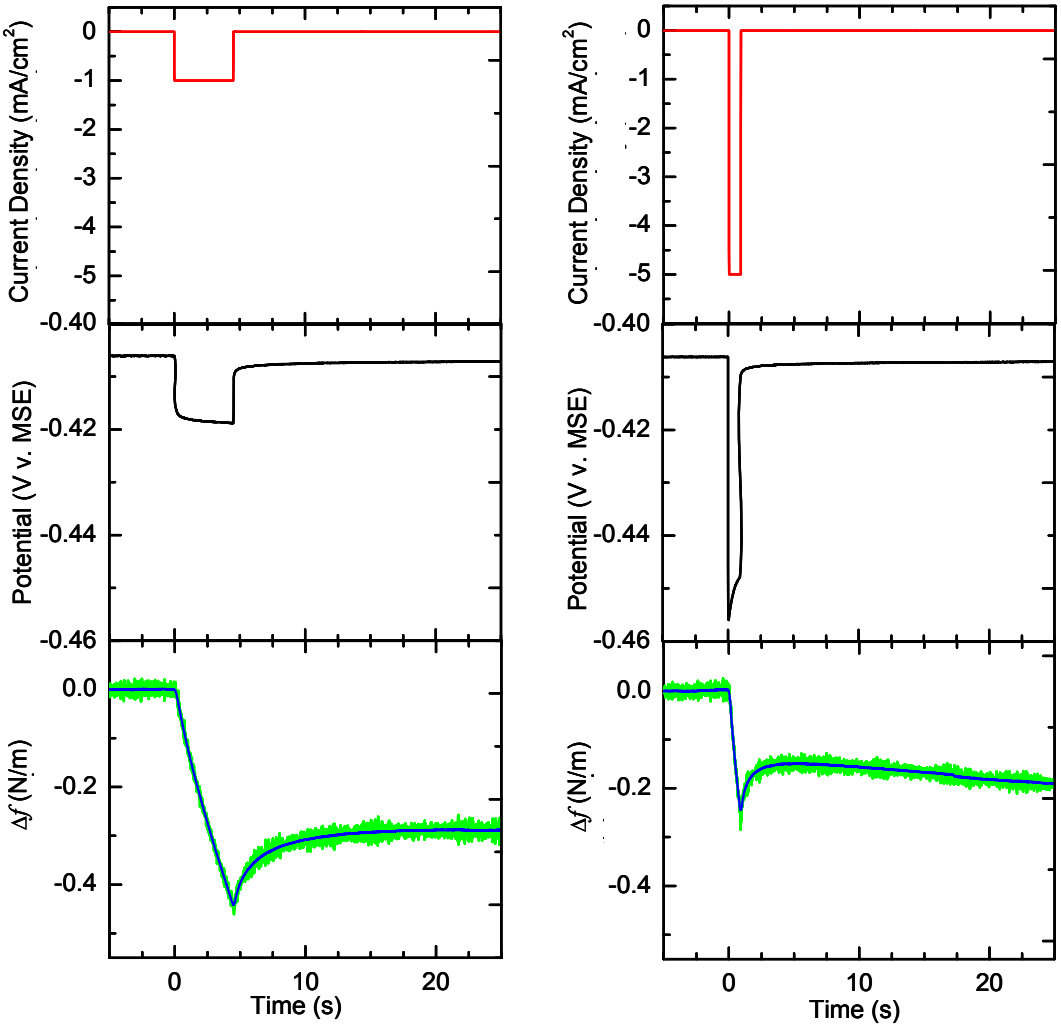

Figure 9.2 - Typical results that are collected during the constant current electrodeposition experiments. Each column shows current density (red), electrochemical potential (black), and surface stress (green) responses of a Cu{111} thin film electrode to a deposition pulse of 1 (left) or 5 (right) mA/cm^2. Pulses were done in an additive free solution and correspond to a thickness of ~ 8 ML.

measurements taken for the electrodeposition of copper in this work follow these same trends. Specifically, in the case of surface stress this translates into a compressive stress in the range of 0-2 N/m that evolves during the deposition event. Following this *event stress*, a relaxation stress transient, usually a tensile transient, evolves in the seconds that follow. The time constant associated with the relaxation processes is generally several times larger than the duration of the current pulse. That is, for the current pulse durations used in the present work (<5 seconds), the film relaxations reach steady state stress value within 30-45 seconds.

Figure 9.3 shows the results of a single galvanostatic deposition pulse in each of the six solution combinations. In each case the current density is **1 mA/cm^2** and the pulse duration is approximately 0.9 seconds and produces an equivalent thickness of ~1.6 ML. Here it is shown that each solution combination does indeed produce a compressive change in surface stress during the deposition event. The actual values measured in each case are labeled for each curve. In the case of the additive free solution, Figure 9.3a, the deposition event stress is approximately -0.2 N/m whereas the relaxation stress transient following the event is slightly greater than +0.1 N/m. Using these two values we can define a residual or intrinsic film stress of ca. -0.1 N/m that is built into the film as a total result of the addition of Cu metal to the surface in the absence of additives. Figure 9.3d shows the same process performed in a deposition suppressing solution containing both PEG and Cl^- additions to the additive free solution. The results from this suppressing solution are quantitatively similar to the additive free

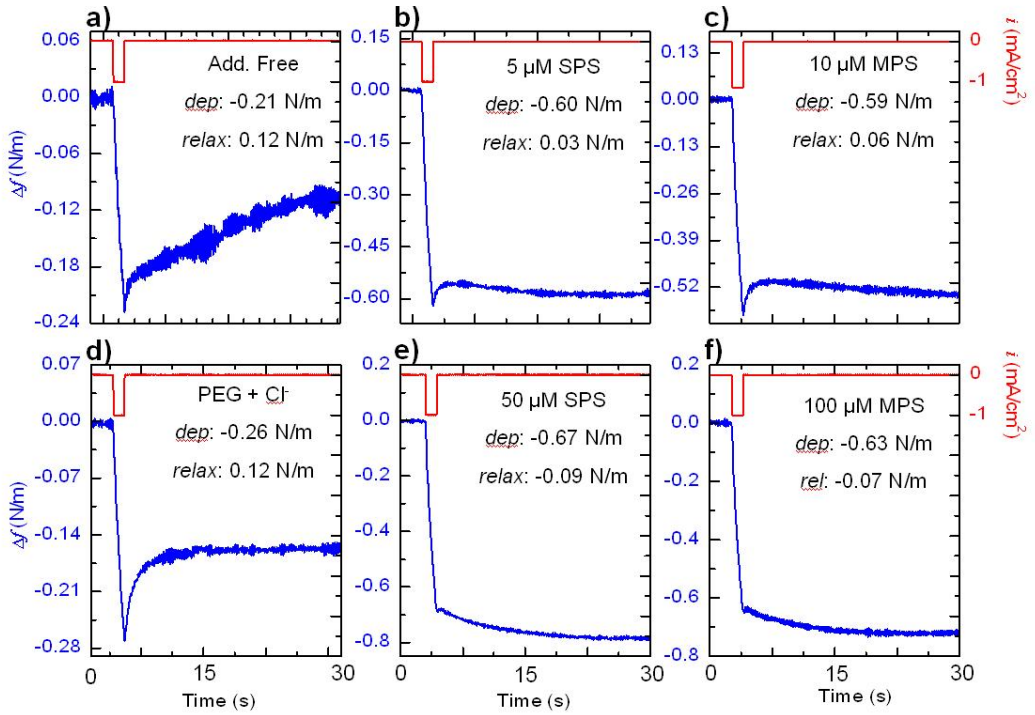

Figure 9.3 - Current density (red) and surface stress (blue) profiles collected during galvanostatic pulsed deposition of ~1.6 ML of Cu in each of the six solution combinations. Δf values corresponding to deposition (dep) and relaxation (rel) regions shown for each case. Pulsed current density = 1 mA/cm^2.

case. The event stress is ~-0.2 N/m followed by a ~+0.1 N/m relaxation. However, as seen in Figures 9.3b 9.3c, 9.3e & 9.3f the event stresses increase markedly upon addition of an accelerating species to the solution. In all four cases, the SPS or MPS containing electrolytes generate larger (≥0.6 N/m) compressive stresses during the deposition event. Alternatively, the relaxation stress transients are smaller in magnitude in the full additive package solutions

compared to the additive free and suppressing chemistries. In fact, the "relaxation transient" evolves in the compressive direction for the solutions containing higher concentrations of accelerating species, namely 100 µM MPS and 50 µM SPS combinations (Figures 9.3e & 9.3f).

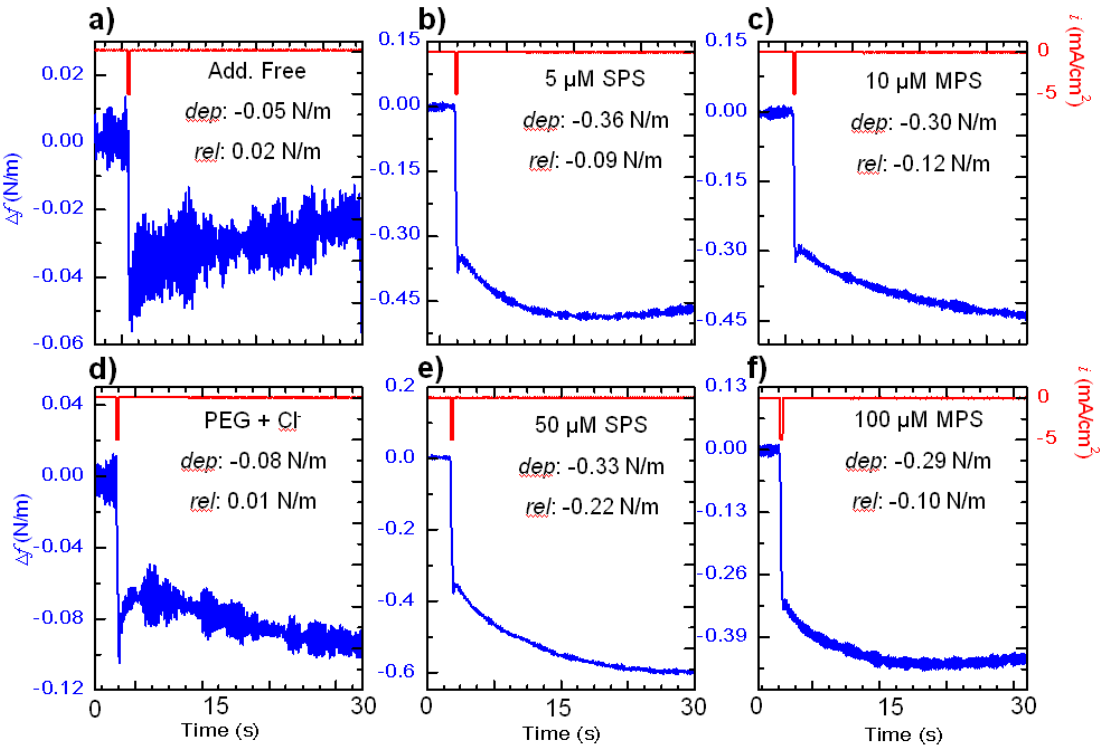

Figure 9.4 - Current density (red) and surface stress (blue) profiles collected during galvanostatic pulsed deposition of ~1.6 ML of Cu in each of the six solution combinations. Δf values corresponding to deposition (dep) and relaxation (rel) regions shown for each case. Pulsed current density = 5 mA/cm^2.

For the case of electrodeposition at 5 mA/cm^2, the same trends appear across the various solution combinations. For example, Figure 9.4 shows that a compressive stress develops during the current pulse and that the ensuing stress relaxation transient is initially tensile in direction. In contrast, however, to the lower current density case, Figure 9.4 exhibits two major differences in the stress profiles. First, all of the surface stress magnitudes associated with the compressive deposition stresses are significantly smaller than for equivalent deposit thicknesses carried out at 1 mA/cm^2. This difference is unsurprising in that previous results from both electrochemical and UHV deposition studies have shown that larger deposition rates produce less compressive steady state stresses for a variety of metal systems[165, 207, 209]. The exact mechanism responsible for the decrease in compressive stress during deposition is not well defined but has been found to agree well with predictions based on the adatom-grain boundary model proposed by Chason et al[134, 162]. The second difference observed at this larger deposition rate is the more negative evolution of stress during the relaxation region of the stress profiles following the deposition event. Whereas, at 1 mA/cm^2 the relaxations were slightly tensile for the solutions containing a low concentration of accelerating species (5 μM SPS & 10 μM MPS) and were slightly compressive for the higher concentration solutions (50 μM SPS & 100 μM MPS), all of the relaxations of the full additive solutions evolve compressively in Figure 9.4.

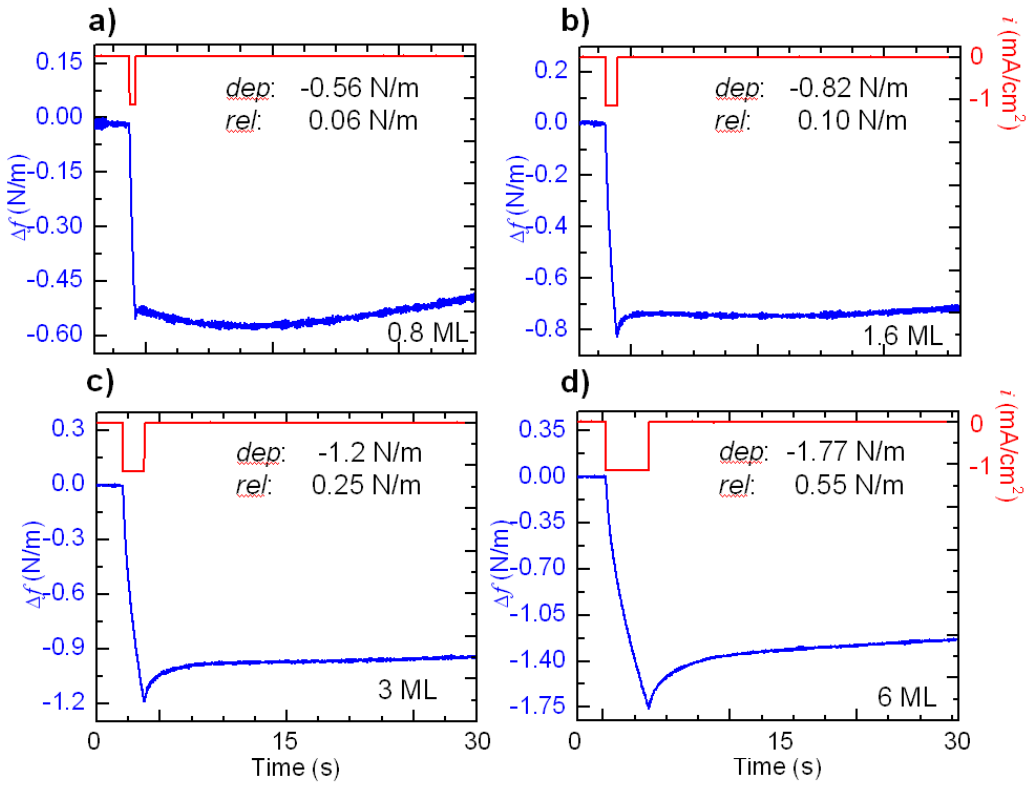

Figure 9.5 - Current density (red) and surface stress (blue) profiles collected during galvanostatic pulsed deposition events corresponding to ~0.8, 1.6, 3, & 6 ML thicknesses of Cu in the full additive, 100 μM MPS solution. Δf values corresponding to deposition (dep) and relaxation (rel) regions shown are given for each case. Current density = 1 mA/cm^2.

Next, the consideration of the event stress values as a function of deposit thickness for each solution combination yields additional insight. It follows from the previous work on Volmer-Weber growth of thin films under UHV conditions that total stress increases with the amount of material deposited. For a given plating solution (e.g. full additive 100 μM MPS), the direct relation between

stress magnitude and thickness can be confirmed qualitatively by comparing several stress profiles across a range of thicknesses, as seen in Figure 9.5. Here the direct relationship between thickness and compressive stress magnitude is confirmed for the range of 0.8 to 6 ML of copper deposited. Moreover, a comprehensive sense and the exact functional relationship is obviated by Figure 9.6, which shows the combined results of all six solutions combinations and at both galvanostatic current densities (1 & 5 mA/cm^2). For both the high and low current densities, the relationship is qualitatively similar with magnitudes being of order two times larger for the 1 mA/cm^2 case. At both current densities, the stress appears to scale linearly for all of the solutions at thicknesses greater than one or two monolayers. Additionally, Figure 9.6 illustrates the existence of two distinct groupings of curves that exist regardless of the deposition rate. The groupings consist of either (1) the full additive solutions which contain the accelerator species and generate relatively large event stresses or (2) the additive free & suppressing solutions which produce smaller event stresses. Over the range of thicknesses investigated ($0.2 \leq \theta \leq 8$ ML), significantly larger surface stresses (4-5 times) are initially imparted to the copper film during the deposition event in accelerator containing solutions. The increased surface stress values must be associated with the solution chemistry and its relationship to the deposition process. Possible explanations for the generation of these larger stresses in the presence of the accelerating species include the promotion of a different growth morphology or perhaps increased inclusion of non-metal species in the film deposits. The underlying mechanism of the behavior is discussed below but from

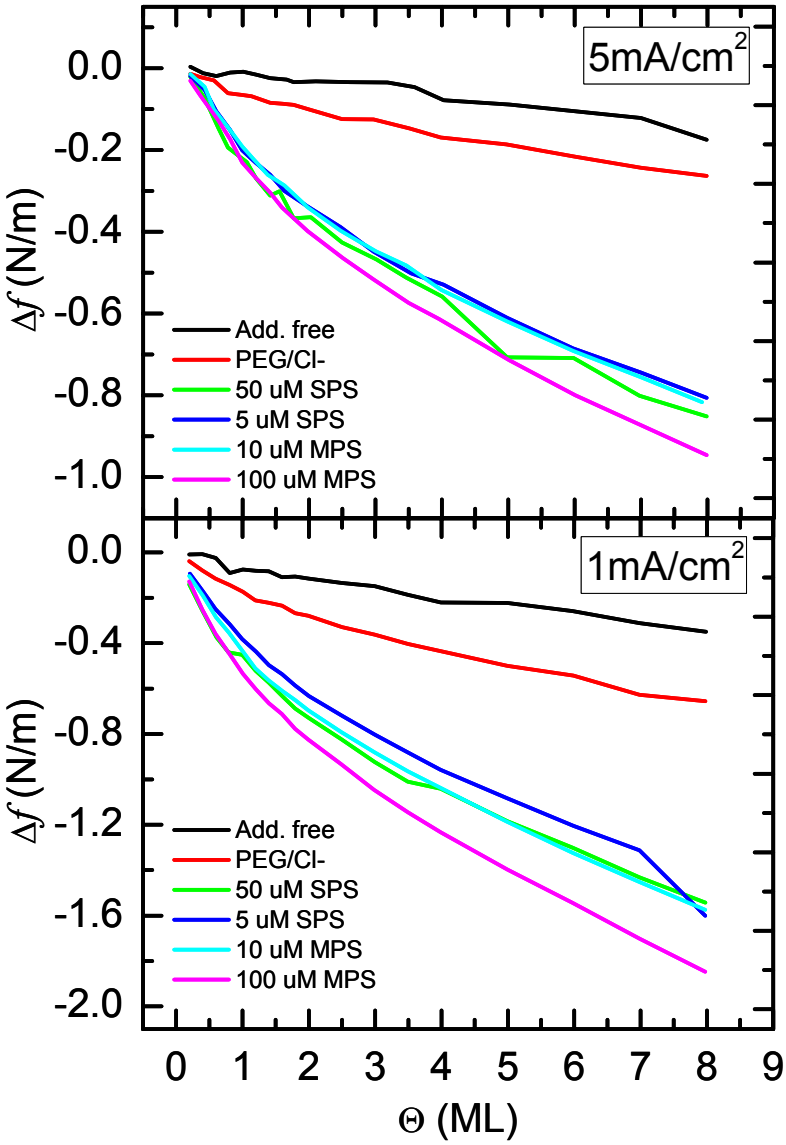

Figure 9.6 - Aggregate results of surface stress generation during galvanostatic deposition pulses of 1 (top) and 5 (bottom) mA/cm^2 for all six solution combinations as a function of deposit thickness ($0.2 \leq \theta \leq 8$ ML). Note that a larger current density yields smaller deposition pulse time for a given thickness.

these results it is clear that the solution chemistry has a significant effect on the film stress during growth processes.

Next, inspection of the relaxation region of the multiple surface stress profiles reveals important information about the response of the film to the different solution combinations. As shown in Figures 9.3 & 9.4, the relaxation transient is highly dependent upon solution chemistry. In the case of additive free (Figures 9.3a & 9.4a) and suppressing conditions (Figures 9.3d & 9.4d), a significant (up to approximately 50%) portion of the compressive stress imparted to the film by deposition is relaxed following the current pulse. A similar type of behavior is also seen during thin film growth interruptions in UHV environments[119, 120, 127, 133]. However the "quenching out" of the stress relaxation transient in full additive package solutions must again be attributed to an extra electrolyte/electrode interaction that is associated with the presence of the accelerating species of the full additive solutions. This is significant because this quenching of the tensile relaxation occurs in tandem with the increase in the compressive event stress that occurs in accelerating solutions. Thus, the driving force for film relaxation increases; yet, the extent of film relaxation decreases. Rather, the release of the compressive growth stress by means of the post-deposition relaxation processes that prevail under non-accelerating electrolytic conditions is inhibited by solutions containing all three additives. The tensile transient does eventually appear as the deposit thickness increases and the compressive stress associated with deposition approaches -1 N/m. Figure 9.5 demonstrates this phenomena for deposition events in the 100 μM MPS, full

additive solution. Initially at ~0.8 ML no tensile relaxation occurs. However, at greater thicknesses the compressive film stress becomes so large that relaxation does occur. Yet for this range of thicknesses the relaxation magnitudes remain diminished relative to the additive free case.

The results and discussion presented in this chapter with respect to the surface stress evolution associated electrodeposition are a good example of how stress monitoring as a technique can be applied as an in situ analytical technique to provide additional insight into traditional electrochemical studies. Specifically, inspection of the literature reveals several publications that suggest that the cause of various post-deposition processes (e.g. resistivity decrease, stress relaxation, etc.) is related to the inclusion of additive species or fragments within the film deposits[19, 61, 175, 176, 183, 210]. Specifically, Kang and Gewirth published a well cited study in which they utilized secondary ion mass spectrometry (SIMS) to identify the relative amounts of additive-derived contamination (i.e. carbon, chlorine, oxygen, & sulfur) in Cu films deposited from a number of solution chemistries[61]. In their study, the authors found that the SIMS results strongly suggested the inclusion of SPS, sulfate, and chloride species in films deposited from "SPS+PEG+Cl^-" solutions whereas films from additive free and "PEG+Cl^-" solutions did not contain similar contaminant levels. In Chapter 5, several studies on the segregation and release of organic impurities from copper electrodeposits were reviewed. Also, Stangl et al demonstrated a correlation between the time required for the diffusion and release of included organic impurities and the incubation time required for grain growth (also referred to as recrystallization or

the self anneal process) and the corresponding stress relaxation. From these results, the authors then infer that the diffusion and discharge of the impurities determines the incubation time required for "inhibited grain growth" and the "microstructure evolution" associated with the decrease in resistivity[175, 176, 211].

The examples described above now provide an interesting comparison to the present surface stress results. The residual stress in full additive electrolytes is observed to increase by two mechanisms: (1) the compressive stress increases during the deposition event and (2) the post deposition film relaxation is partially hindered. It seems likely then that the inclusion of additive-derived contaminants within the deposits is responsible for this bilateral increase of residual stress. Specifically, at constant deposit thickness, the compressive stress is increased relative to the additive free and suppressing cases by the introduction of non-metal species in the deposit. The inclusion of additional material within a deposit that is held under identical constraints (i.e. film clamping) would then appear in the stress evolution as an increase in compression of the surface layer. Likewise, the contaminants included in the film likely prevent the relaxation of the built in stress through grain boundary pinning or similar mechanism.

In an effort to generalize the conclusions described here with respect to the stress results collected in sulfate based solutions, a series of experiments were performed in the perchlorate based copper plating solutions shown in Table 9.2. The basic idea behind these investigations was to collect a series of results using the exact same electrochemical parameters and a pair of solutions (perchlorate solutions that were additive-free and perchlorate solutions that contained a full

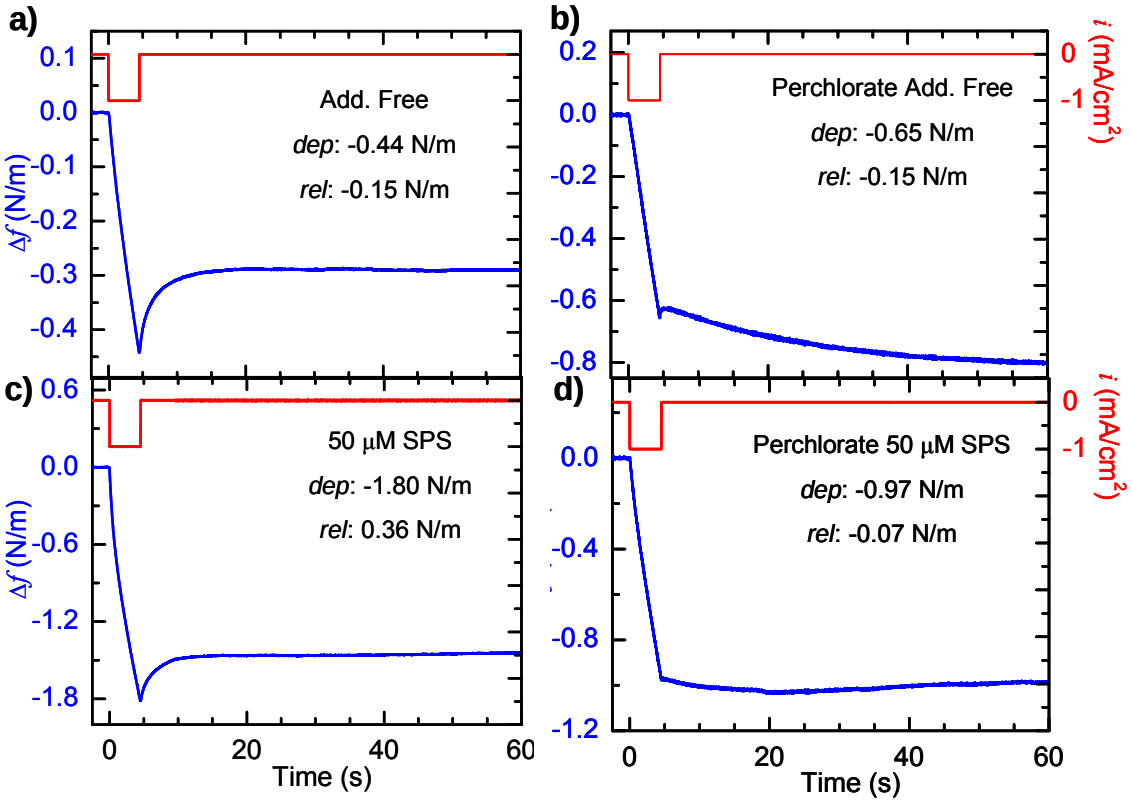

Figure 9.7 - Comparison of the surface stress profiles collected for an ~8 ML deposit thickness at 1 mA/cm^2 from additive free (a), perchlorate based additive free (b), full additive 50 µM SPS (c), and perchlorate based 50 µM SPS (d) solutions. Each deposition event generates a compressive stress followed by relaxations that are initially tensile.

additive package) in which the only difference was the identity of the supporting anion in the electrolytic solutions.

Figure 9.7 shows a single stress profile collected during the deposition of ~8 ML of copper in each of these two solutions alongside the corresponding results from the sulfate based solutions. Immediately, the similarities between the adjacent profiles are obvious. The event stresses are all compressive in direction and are of similar order of magnitude (see Figure 9.8). Additionally, the surface stress behavior in the relaxation region is initially compressive for all cases, although it is nearly indiscernible in the case of the perchlorate 50 μM SPS curve. Furthermore, Figure 9.8 is also given for comparison of the thickness dependence of the deposition induced surface stress. Here, the event stresses resulting from the deposition of 5, 6, 7, and 8 ML of copper from the perchlorate based solutions are plotted as points along with the additive free and 50 μM SPS curves from Figure 9.6. As in the case of the electrodeposition results collected in sulfate-based solutions, the perchlorate-based results show that the total amount of compressive stress built into the film during deposition increases as a function of deposit thickness and also increases at constant thickness when plating additives are used.

The importance of these perchlorate based experimental results is related to the confirmation of the generalized surface stress behavior during the electrodeposition of copper. That is, the overall qualitative shape of the stress profiles is the same in both sulfate and perchlorate solutions. The chief

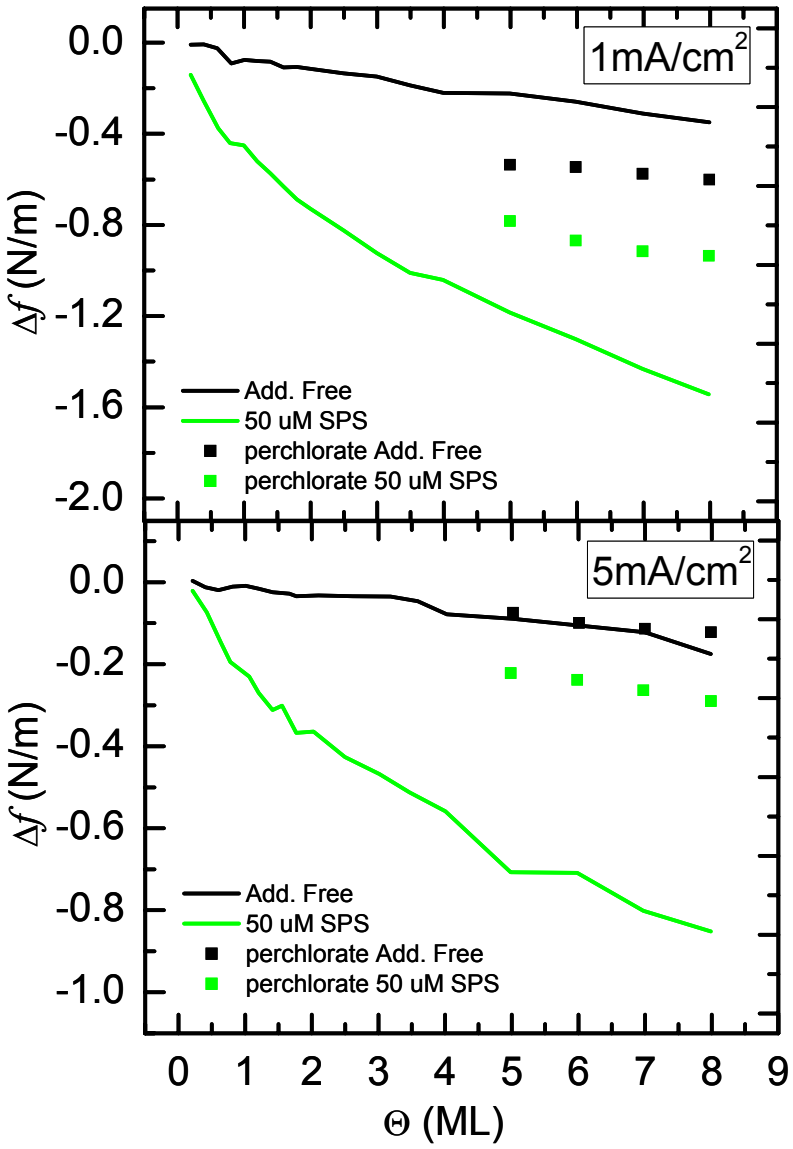

Figure 9.8 - Results from perchlorate based additive free and full additive (50 μM SPS) solutions (data points) overlaid on the previous results of the sulfate based solutions (lines) as presented in Figure 9.6. Similar to the sulfate based solutions, the perchlorate surface stress increases as a function of deposit thickness and in response to the use of plating additives, though the magnitudes of these effects vary from the sulfate based solution results.

differences between the results from the two solutions rest solely in the relative magnitudes of the individual surface stress contributions. Future work in this area would likely provide even more insight into the role of the "spectator" ions in the fundamental process of electrocrystallization, film growth, and morphology development. However, it is clear that the overall behavior is similar and therefore does not affect the conclusions drawn from the core results attained in the sulfate based solutions.

9.4 Summary Outline

- Constant current electrodeposition pulses on Cu{111} thin film electrodes produce compressive surface stresses in the range of 0-2 N/m during the deposition event in all solution combinations investigated herein. Following the event stress, a relaxation stress transient that is generally tensile in nature, evolves in the seconds that follow.
- For both the high and low current densities, the relationship between induced stress and deposit thickness is qualitatively similar with magnitudes being of order two times larger for the 1 mA/cm^2 case. At both current densities, the stress appears to scale linearly for all of the solutions at thicknesses greater than one or two monolayers.
- Electrodeposition induced event stresses decrease (are less compressive) with increasing plating rates. A result that is in agreement with previous results from both electrochemical and UHV deposition studies that have shown that larger deposition rates produce less compressive steady state stresses for a variety of metal systems.

- The magnitude of the event stresses increase markedly upon addition of an accelerating species in the plating solution. Over the range of thicknesses investigated ($0.2 \leq \theta \leq 8$ ML), significantly larger surface stresses (4-5 times) are initially imparted to the copper film during the deposition event in accelerator containing solutions (see Figure 9.6). The increased surface stress values are associated with the solution chemistry and its relationship to the deposition process.
- The residual stress ($f_{final} - f_{initial}$) in full additive electrolytes is observed to increase by two mechanisms: (1) the compressive stress increases during the deposition event and (2) the post deposition film relaxation is partially hindered. Both of which can be explained by the incorporation of solution-additive-derived contaminants within the deposits. These conclusions are supported by a number of studies that have been published on the contamination of electrodeposited films in a number of solution combinations.
- While the effect of the supporting anion is non-negligible, the overall qualitative shape of the stress profiles is the same in both sulfate and perchlorate based solutions. The chief difference that is observed between the two solutions is the difference in relative magnitudes of the individual surface stress contributions.

CHAPTER 10

CHRONOPOTENTIOMETRIC STRIPPING

10.1 Introduction

One of the greatest advantages that electrochemical investigations have over ultra high vacuum work is the ability to remove material from the electrode surface. For a metal (e.g. Cu) electrode in an acid electrolyte environment, an oxidizing current or potential induces an electrochemical etch or stripping process at the electrode-electrolyte interface. Due to the small number of applications for electrochemical etching and because the technique of surface stress monitoring was well established in the UHV community before it was really widely used in electrochemical studies, the overwhelming majority of the electrochemical surface stress studies are performed on deposition and film growth type processes. However, the unique ability to control the thermodynamic condition of an electrode in an electrochemical cell provides an opportunity to study the electrode-electrolyte interface in, for example, Cu damascene-like systems.

Oxidative stripping experiments were carried out in conjunction with the electrodeposition studies presented above in Chapter 9. As will be explained later in this chapter, these results provided a number of somewhat unexpected but important insights into the details of the copper-solution interface. In contrast to the large number of experimental studies that have been dedicated to Cu electrodeposition and the superfilling process, very little work has been done on electrochemical etching of Cu electrodes. Even though the chemistry of both copper ($Cu/Cu^{+}/Cu^{2+}$, etc.) and the additive species is the same in these

experiments, the application of oxidizing potentials and the removal of material from the electrode surface produces different results in both the event and relaxation regions of the surface stress profile (compared to deposition).

There are, however, a number of symmetries between these results and the results presented in Chapter 9. First, the magnitude of the tensile stresses that were generated during the oxidizing current pulses was dependent upon both the amount of material that was stripped as well as the stripping rate. Second, a compressive relaxation stress was observed following the stripping current pulse. Furthermore, as in the case of the stresses generated during electrodeposition of copper, both event stress profiles (i.e. during the current pulse) as well as the relaxation stress profiles were profoundly influenced by the presence of the plating additives. It appears that in this case, the effect was related to the formation of the PEG/Cl^- blocking layer. Finally, as in the case of the deposition experiments, these oxidative stripping investigations were carried out by monitoring the film stress evolution during both stripping events and the subsequent relaxations for thicknesses ranging from sub-monolayer to ~8 monolayers.

10.2 Experimental details

The oxidative stripping experiments were carried out on the same samples as the electrodeposition experiments. All of the preparation and setup of the apparatus for these experiments was covered in Section 9.2. Similarly, the current densities and pulse lengths for the oxidative stripping events were identical to those used for electrodeposition in Chapter 9 and are given in Table 9.3. The

purpose of this set of experiments was to measure the real time surface stress response of a Cu{111} thin film electrode before and after the stripping event for a series of thicknesses and in a variety of solution compositions. As in the case of deposition and the subsequent relaxation stresses, the various sources of stress contribution (oxidative removal of material from the electrode surface, electrocapillarity, molecular and ionic adsorption, etc) were studied through the use of the various solution compositions shown in Table 9.1. The stripping experiments were done in current controlled mode; specifically, double step chronopotentiometric techniques were used in which the oxidizing pulses were performed at either -1 or -5 mA/cm^2 and the current was fixed at zero both before and after the stripping pulse. The ratio of current pulse time to the time held at zero current (the open circuit potential) was the same as the deposition events and equal to at least 20. The "equilibration" time spent at zero current (equivalently the open circuit potential in potential controlled mode) was more than enough time to allow both the potential and surface stress profiles to settle into relatively stable values (i.e. a constant value in the absence of drift). The data acquisition rate was uniformly equal to 1 kHz across all of the stripping experiments as well.

10.3 Results and Discussion

As in the case of electrodeposition, the potential profiles that resulted from the oxidizing current pulses were recorded as a function of time. The steady state overpotentials corresponding to each of the solution combinations are given in Figure 10.1. In contrast to the overpotentials required for electrodeposition, the values are, as expected, much smaller for oxidative stripping. The composition of

the solution again has a significant effect on the overpotential required to sustain the 1 & 5 mA/cm^2 current densities, yet the effect is diminished with respect to the relative magnitudes of stripping overpotential. For example, the suppressing action of the PEG & Cl^- species requires a 5-fold increase in overpotential compared to that of the additive free case (~250mV/50mV) in order to deposit at 1 mA/cm^2. With respect to oxidative stripping, however, the effect is only of order 2.5 times larger (~100mV/40mV). The addition of the accelerator species to the suppressing solution restores some of the activity of the electrode and the full additive solutions exhibit values that are similar but slightly larger than the overpotential required in the additive free solution. Thus, the polarizing/depolarizing effect of additives, as described in Chapter 3 in the context of electroplating, remains relevant during oxidation of copper in the various plating solutions.

Typical examples of the simultaneous surface stress and electrochemical measurements collected during the oxidative stripping events are given in Figure 10.2 as a function of time. In this figure, the current density, electrode potential, and surface stress are shown during an equivalent ~30 second window in order to show both the oxidizing event stress associated with the positive current pulse as well as the ensuing relaxation stress transient. Generally, the curves in Figure 10.2 directly mirror the measurements shown in Figure 9.2. However, as described above, the magnitude of the measured potential transient is decreased and the surface stress profiles are also smaller in magnitude. Whereas the compressive deposition stresses ranged from <0.1 to ~1.8 N/m during copper

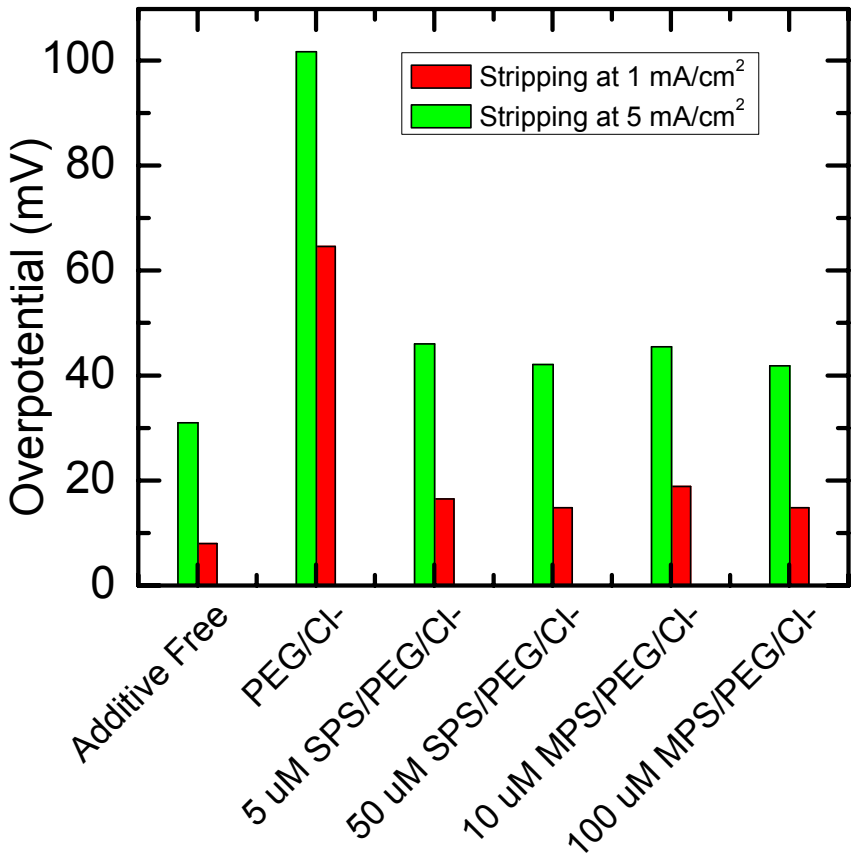

Figure 10.1 - Column plot comparison of typical overpotentials recorded on a Cu{111} thin film electrode during chronopotentiometric stripping pulses of 1 (red) or 5 (green) mA/cm^2. Here the polarizing action of the various additives has a decreased effect on the oxidative removal of material from the film compared to deposition (see Figure 9.1).

deposition, the range of stripping stresses was limited to values below 0.6 N/m. Similarly, Figure 10.2 also demonstrates that a *compressive* relaxation stress transient evolves over the course of 10-45 seconds that follow the stripping event, despite the brevity (<5 s) of the stripping current pulses.

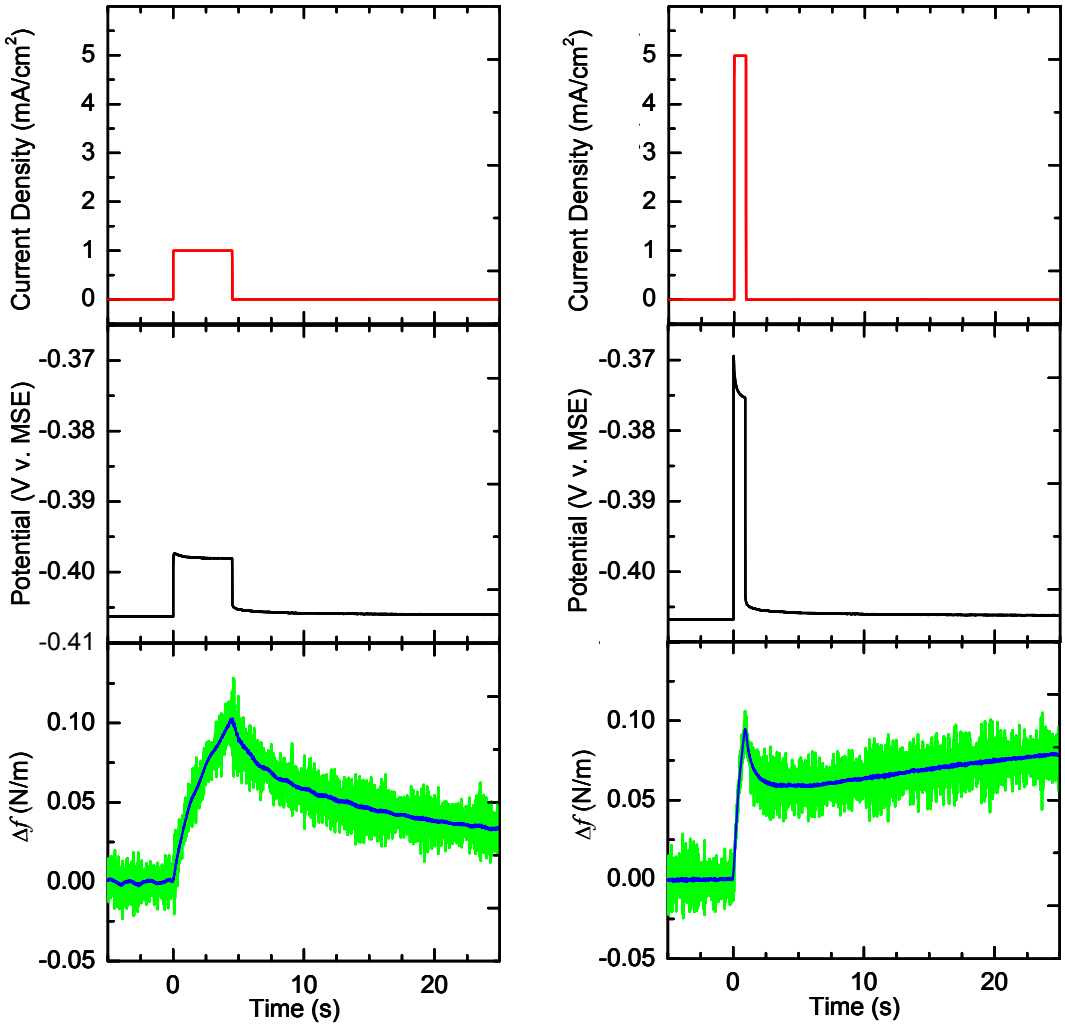

Figure 10.2 - Typical results that are collected during the constant current oxidative stripping experiments. Each column shows current density (red), electrochemical potential (black), and surface stress (green) responses of a Cu{111} thin film electrode to a stripping pulse of 1 (left) or 5 (right) mA/cm^2. Pulses were done in an additive free solution and correspond to a thickness of ~8 ML.

Figure 10.3 shows the results of a single, 0.9 second long galvanostatic stripping pulse in each of the six solution combinations. At a current density of 1 mA/cm^2, the equivalent of a ~1.6 ML thickness is removed from the electrode surface. The results in Figure 10.3 again present an interesting symmetry to the deposition case in that each stripping event produces a tensile surface stress followed by a longer time scale compressive relaxation.

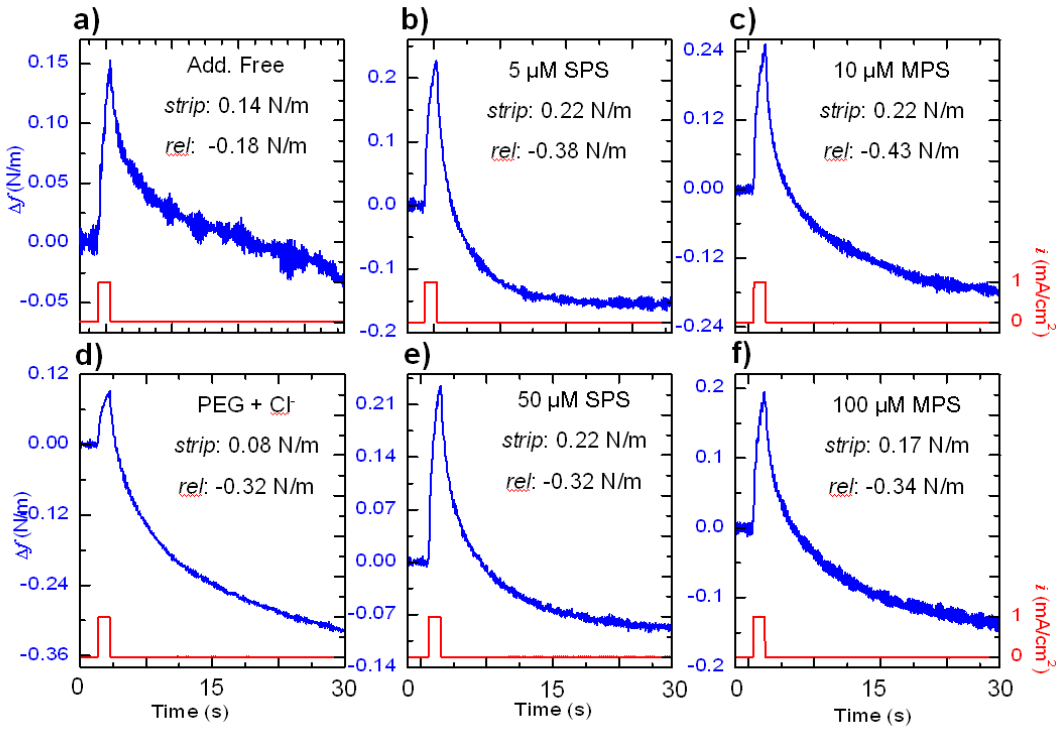

Figure 10.3 - Current density (red) and surface stress (blue) profiles of a Cu {111} electrode collected during galvanostatic oxidative stripping pulses of ~1.6 ML in the six solution combinations. Δf values corresponding to stripping (strip) and relaxation (rel) regions shown for each case. Pulsed current density = 1 mA/cm^2.

The additive free results (Figure 10.3a) show that a +0.14 N/m stress is imparted to the film during the stripping event followed by a compressive stress relaxation of nearly equal magnitude. For this case, very little residual stress remains in the film due to ~1.6 ML of Cu being removed from the copper surface. The +0.08 N/m stripping event stress in the suppressing electrolyte (Figure 10.3d) is similar to that of the additive free case, but both are again smaller than any of the event stresses generated in the full additive solutions (Figures 10.3b, 10.3c, 10.3e, & 10.3f). Each of the event stresses in the full additive solutions are approximately double the amount of surface stress that is generated by the identical process in the additive free and suppressing chemistries (~0.2 N/m). The most striking characteristic of Figure 10.3, though, occurs within the relaxation region of the stress profiles. It was noted above that the final stress state of the film that was stripped in the absence of additives was essentially equal to the initial stress value. In contrast to that, a much larger "relaxation" stress is observed for stripping events carried out in any solution containing the suppressing species, PEG and Cl^-. For the specific case of the suppressing solution, the event stress is ~+0.1 N/m while the compressive "relaxation" is nearly three times larger at ~0.3 N/m. This is significant because not only is the entire tensile event stress being relieved but an additional compressive stress of at least 0.2 N/m is being newly generated in the seconds that follow the oxidizing current pulse. Moreover, this same phenomenon of significantly larger compressive stresses being generated at the open circuit potential following an anodic current pulse is observed for <u>all</u> additive containing solutions. Because

this stress is generated in the absence of any electrochemical manipulation, any plausible explanation of it must invoke the presence of a dynamic solution side process.

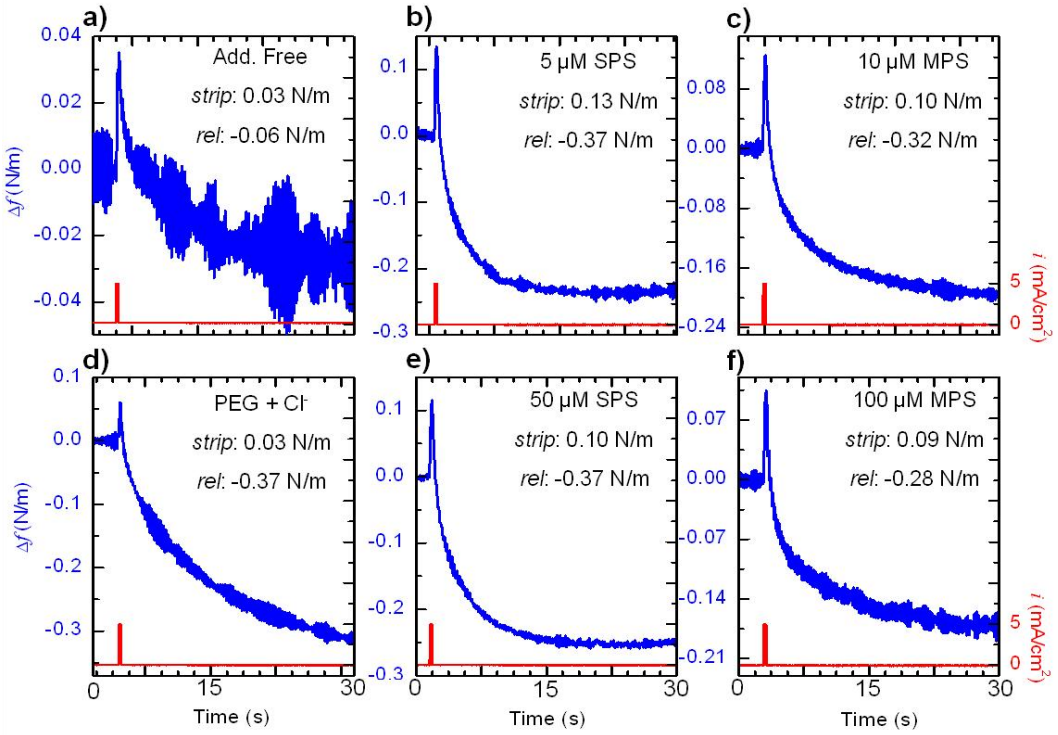

Figure 10.4 - Current density (red) and surface stress (blue) profiles of a Cu {111} electrode collected during galvanostatic oxidative stripping pulses of ~1.6 ML in the six solution combinations. Δf values corresponding to stripping (strip) and relaxation (rel) regions shown for each case. Pulsed current density = 5 mA/cm^2.

A parallel set of oxidative stripping pulses was also carried out in each of the six solutions at 5 mA/cm^2. Again, similar trends appear in Figure 10.4 across the various solution combinations. First, the stripping event stresses are tensile

and are smaller in magnitude when compared to the 1 mA/cm^2 event stresses. In the case of the additive free plating solution, the event and relaxation stresses are of similar magnitude and lead to little or no residual stress in the film. Conversely, for stripping events in the additive containing solutions, the stress profiles in Figures 10.3 & 10.4 suggest that the film is subject to a nearly identical amount of compressive "relaxation" stress independent of the applied current density. In

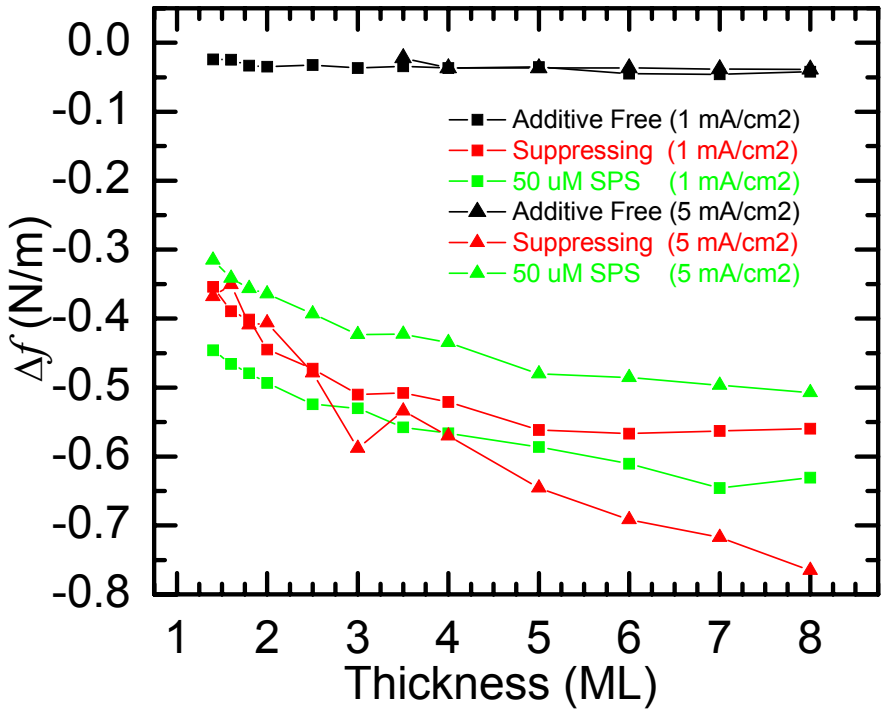

Figure 10.5 - Surface stress results for the "relaxation" transients that occur at open circuit after a range of oxidative stripping pulses ($0.2 \leq \theta \leq 8$ ML). Each curve corresponds to the additive free (black), suppressing (red) or full additive (green) solutions at either 1 (squares) and 5 (triangles) mA/cm^2.

order to confirm this behavior, the magnitude of the relaxation stress transients resulting from both the 1 & 5 mA/cm^2 series of experiments are plotted in Figure 10.5 for the additive free, suppressing, and full additive (50 μM SPS) solutions. In this figure, the relaxation results indicate that the amount of compressive stress that evolves after the anodic current pulse is not highly dependent on the current density. Rather, within the experimental noise, the relaxation transient is relatively uniform for all of the solutions that contain additives (specifically PEG and Cl^-) and is a function of the amount of material stripped.

As in the case of deposition, the stresses due to oxidative stripping are shown in Figure 10.6 for both 1 and 5 mA/cm^2 and as a function of thickness removed. Here the symmetry between the deposition and stripping results is maintained for event stresses. At both current densities, the two distinct groupings are again differentiated by magnitude; larger event stresses are generated in the full additive solutions and smaller stresses are observed for films that are stripped in additive free and suppressing solutions. The existence of this symmetry between deposition and stripping event stresses as well as the symmetry observed in overpotential (Figure 9.1 & 10.1) is a somewhat unexpected result. It may suggest a similar symmetry between the physical processes through which the accelerating species affect the addition and removal of copper from the electrode surface. However, verification of this would require future research in this area using additional analytical techniques such as scanning electrochemical microscopy, electrochemical scanning tunneling microscopy, etc. to further investigate these processes on a molecular/atomic scale.

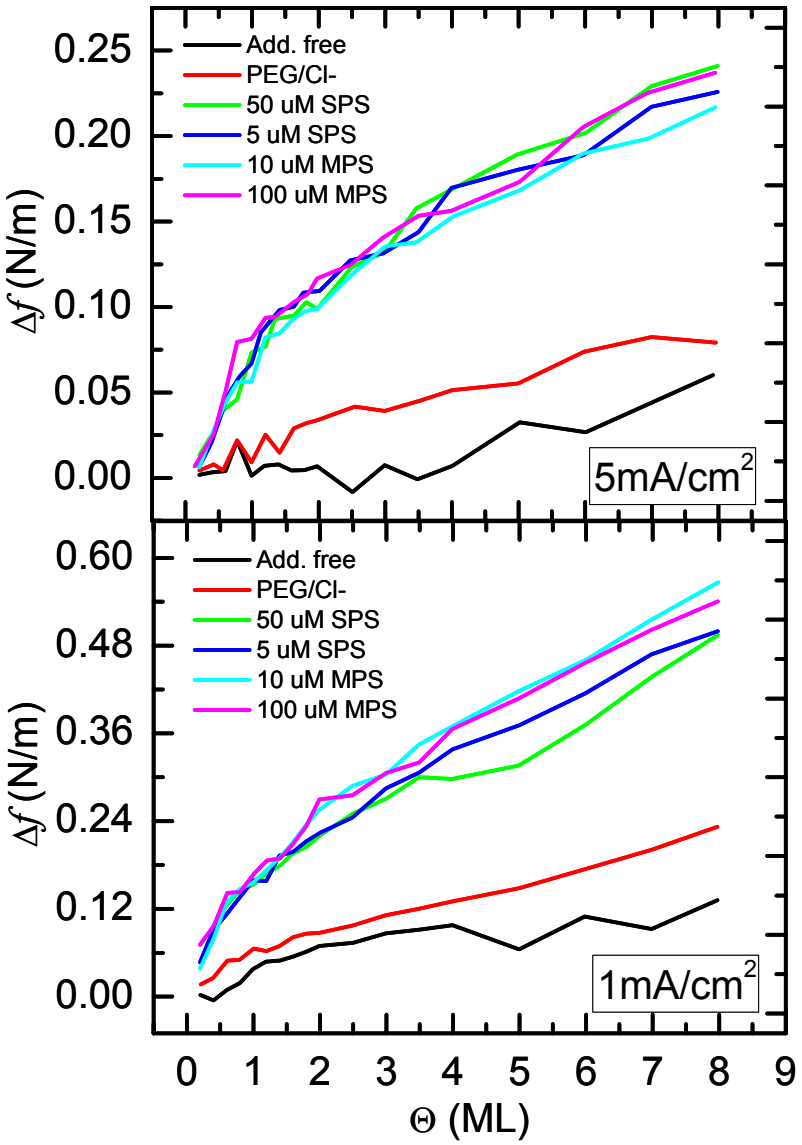

Figure 10.6 - Aggregate results of surface stress generation during galvanostatic stripping pulses of 1 (top) and 5 (bottom) mA/cm2 for all six solution combinations as a function of deposit thickness ($0.2 \leq \theta \leq 8$ ML). Similar to the behavior observed in Figure 9.6, the larger current density induces smaller surface stresses during stripping events as well.

Interestingly, the two main observations in the oxidative stripping work appear to be unrelated in origin and have different functional dependences on the amount of material stripped from the electrode. First, large relaxation stresses associated with the PEG/Cl^- additive combination are observed at both high and low current densities and are weakly dependent on thickness (Figure 10.5). Second, the stripping event stresses increase strongly as a function thickness and are also larger in accelerator containing solutions (Figure 10.6). By performing the experiments in each of the three types of solutions, these effects were observed and attributed to the different plating additive species. Specifically, the additive free solution produces small event and relaxation stresses, the suppressing solution exhibits small event but large relaxation stresses, and the full additive solutions produce large event and relaxation stresses. More explicitly, consider the two groups of curves that appear in Figures 10.5 & 10.6. First, the suppressing solution curves are grouped with the additive free solution and show small event stress generation in Figure 10.6. Second, Figure 10.5 shows that the relaxation of films in the suppressing solution was large and similar in magnitude to the full additive solutions. As stated above, the increase in event stress mirrors a similar increase in deposition event stress and is associated with the presence of the accelerating species (MPS or SPS) at the electrode surface. Additionally, the most striking characteristic of the surface stress profiles is the magnitude of the compressive "relaxation" stresses. In this case, the presence of PEG and Cl^- induces a significant compressive stress at open circuit that exceeds the amount of stress generated during the current pulsed event itself. It is well known that the

combination of these species in the plating solution produces an adsorbed blocking layer and plays an integral role in the superfilling process by suppressing the electrodeposition reaction. In the case of oxidative stripping, copper metal is oxidized to cupric and cuprous ions and material is removed from the electrode surface. One possible explanation for the excess compressive stress that evolves after the stripping event is related to the disruption of this interface by the transport of copper atoms/ions from the surface to the solution. As shown in Figure 10.5, the amount of compressive relaxation stress generated is relatively independent of the driving force, but does scale weakly with amount of material removed. If the copper atoms that are removed during the anodic pulse create new surface area by, for example, preferential etching at the grain boundaries, it is possible that the adsorption of additional PEG/Cl^- species to form the blocking layer on this new area could be responsible for the excess compressive stress. Although, other mechanisms associated with the insertion of additive species into the grain boundaries could also be possible. Future work in this area could include the investigation of film composition as a function of grain size as well as possible electrochemical scanning tunneling microscopy to look at surface evolution in response to stripping events performed in these additive containing solutions.

As described in Chapter 9, additional efforts were made in an attempt to generalize the surface stress behavior of Cu{111} thin films during deposition and stripping in acidic media. To this end, a series of experiments were performed in

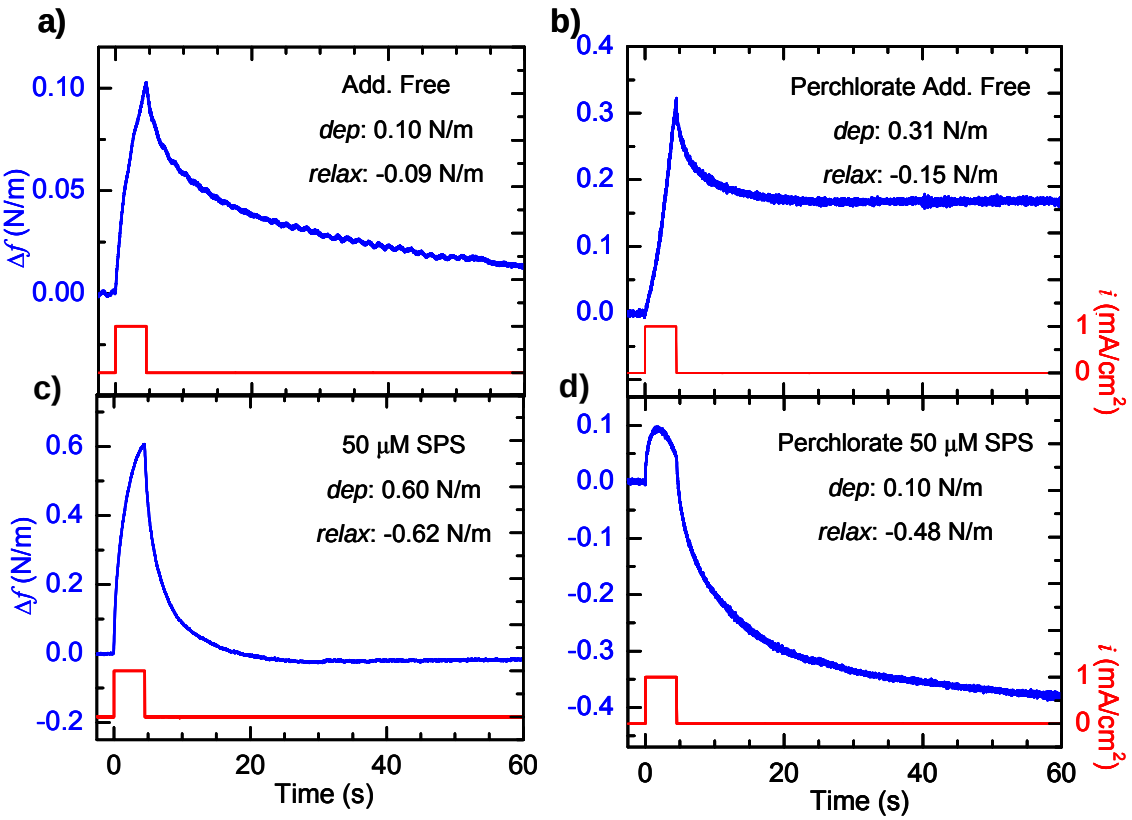

Figure 10.7 - Comparison of the Surface stress profiles collected for a stripping event of ~8 ML at 1 mA/cm^2 from additive free (a), perchlorate based additive free (b), full additive 50 µM SPS (c), and perchlorate based 50 µM SPS (d) solutions. Each stripping event generates a tensile stress followed by compressive relaxations.

the perchlorate-based copper plating solutions shown in Table 9.2. Again, the fundamental premise of this supplementary work was to perform an identical series of experiments in a pair of solutions (perchlorate additive free and perchlorate full additive) in which the only difference from the sulfate based experiments was the identity of the supporting anion. Figure 10.7 shows a single

stress profile collected during the oxidative stripping of ~8 ML of copper in each of the four solutions: additive free, 50 μM SPS, perchlorate additive free, and perchlorate 50 μM SPS. As in the case of the deposition events shown in Figure 9.7, the adjacent stripping profiles exhibit several similar characteristics. First, the stripping event stresses are tensile and the relaxations that follow are uniformly compressive. However, the relative magnitudes of each portion of the stress profiles are somewhat different. In the case of the additive free solutions, the perchlorate based solutions yield significantly larger event stresses yet the relaxation stresses are similar. For the 50 μM SPS solutions, the event stress is much smaller in the perchlorate solution while the relaxations are again comparable. The anomalous nature of these results is further evident in Figure 10.8 which provides the event stresses of these four series of oxidative stripping experiments for comparison. Again the event stresses resulting from the deposition of 5, 6, 7, and 8 ML of copper from the perchlorate based solutions are plotted as points along with the additive free and 50 μM SPS curves shown earlier in Figure 10.6. Unfortunately, these measurements do not appear to reflect the actual relationship between surface stress and anodic stripping of copper.

While the overall qualitative shape of the stress profiles is very similar between the sulfate and perchlorate solutions (as seen in Figure 10.7), further investigation is necessary in order to establish a more quantitative understanding of the surface stress behavior in this new electrolytic system. In general, however, the perchlorate based experiments have provided one significant result. That is, that the overall stress evolution during anodic current pulses follows the same

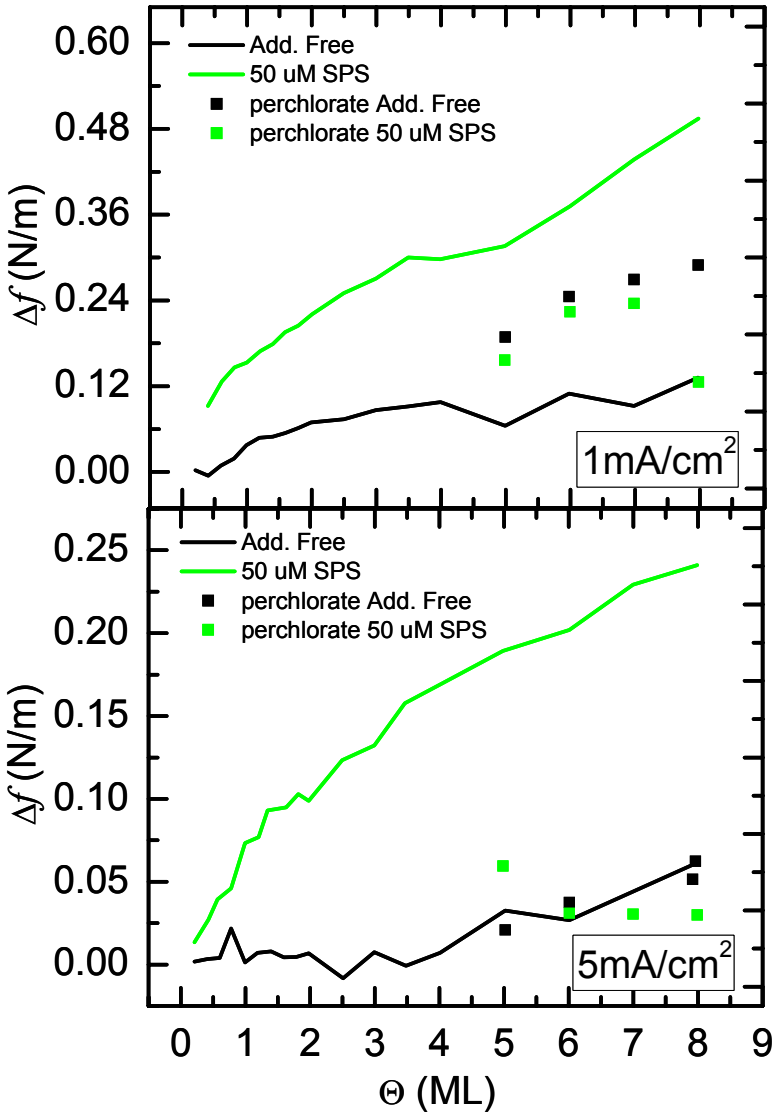

Figure 10.8 - Anomalous results from perchlorate based additive free and full additive (50 μM SPS) solutions (data points) overlaid on the previous results of the sulfate based solutions (lines) as presented in Figure 10.6. Here the stripping event stress behavior does not follow the anticipated trends. These results do not appear to be representative of the actual behavior and additional future investigations are required.

general trend as observed in the sulfate based electrolytes and that the supporting anion plays a minor albeit non-negligible role in the redox processes.

10.4 Summary Outline

- Constant current oxidative stripping pulses on Cu{111} thin film electrodes produce tensile surface stresses up to ~0.5 N/m during the stripping event in all solution combinations investigated herein. A relaxation stress transient that is uniformly compressive is also observed following the current pulse.
- At both 1 and 5 mA/cm^2 current densities, the relationship between event stress and stripped thickness is qualitatively similar. As in the deposition case, the magnitude of the induced stresses is larger for the 1 mA/cm^2 case. At both current densities, the stress appears to scale linearly for all of the solutions at thicknesses greater than one or two monolayers.
- Similar to the deposition case, the stripping event stresses increase strongly as a function thickness and are again larger for events carried out in accelerator containing solutions.
- In contrast to the additive free results, a large "relaxation" stress is observed for stripping events carried out in all solutions that contain the suppressing species, PEG and Cl^-. The presence of this additive combination produces an excess compressive stress that is newly generated in the seconds that follow the oxidizing current pulse. The result is a compressive residual stress ($f_{final} - f_{initial}$) despite the tensile nature of the stripping event stress. The phenomenon is likely associated

with the formation or re-formation of the well known PEG/Cl^- deposition blocking layer.

- The magnitude of the large post-stripping relaxation in the additive containing solutions is independent of the applied current density and only weakly dependent on the magnitude of the initial compressive event stress. Thus, the two main observations are associated with different additive species and are unrelated in origin.
- Qualitatively similar surface stress profiles are produced during oxidative stripping experiments in both sulfate and perchlorate based solution combinations. However, for the case of the perchlorate based solutions, the magnitudes of the event and relaxation stresses appeared to be somewhat anomalous in nature and require further investigation.

CHAPTER 11

EFFECT OF A CUPROUS ION CONCENTRATION

11.1 Introduction

Like other d-block elements, copper has multiple possible oxidation states due to the nature of its electronic structure. For example, stable or quasi-stable forms of copper exist in the +1, +2, +3 and +4 oxidation states and the stability of each can be highly dependent on the environment surrounding the ionic species [212]. Of these multiple ionic species, the cupric (Cu^{2+}) and cuprous (Cu^{+}) ions are the only relevant species under the conditions of this work. The corresponding reduction equations and potentials were given in eqs 3.3 & 3.4. The relative stability of these ions can be represented graphically by a Frost-Ebsworth diagram, as shown in Figure 11.1. The Frost-Ebsworth diagram for copper indicates that the metallic form is thermodynamically favored with respect to its ionic species. Furthermore, the standard reduction potentials indicate that both ions are reduced to metallic copper at potentials within the stability limits of water. This is indicated schematically in Figure 11.2a along with an additional equation that describes the reduction of cupric ions to cuprous ions via a single electron transfer step,

$$Cu^{2+}{}_{(aq)} + e^{-} \leftrightarrow Cu^{+}{}_{(aq)}, \qquad E^{0} = 0.159 \text{ V v.SHE.} \tag{11.1}$$

Considering this relation, a representation of the relevant redox chemistry of copper in aqueous solution is represented by a Latimer diagram in Figure 11.2b.

Still, the relative potentials of each of these reduction steps indicate the existence of a potential range at which cuprous ions (Cu^{+}) may be subject to simultaneous oxidation and reduction. This reaction can be represented by appropriately combining eqs 3.3 & 11.1 to give

$$2Cu^{+}(aq) \leftrightarrow Cu^{2+}(aq) + Cu^{0}(s), \qquad E^{0} = 0.361\,V\ v.SHE. \qquad (11.2)$$

which is known as the copper *disproportionation* reaction. The disproportionation of copper is also represented by the "convex" nature of the curve in Figure 11.1 [212]. That is, the cuprous species lies above a line connecting copper metal and the cupric species, indicating its relative instability with respect to disproportionation. Using the potential value shown in eq 11.2, an equilibrium constant of $K_{eq,Cu} = [Cu^{2+}]/[Cu^{+}]^2 \approx 1.81*10^6$ is calculated and indicates that cuprous ions will disproportionate equally into copper metal and cupric ions except at extremely low concentrations. In fact, for the deposition and stripping experiments presented in this dissertation, the equilibrium (upper limit) cuprous ion concentration of a 0.25 M $CuSO_4$ solution is ca. 400 μM. Furthermore, any dissolved oxygen in the solution would react readily with the free cuprous ions and would lead to further removal from the equilibrium concentration.

Previously published investigations have speculated that cuprous ion complexes play a significant role in the superfilling process. More recently, there has been some disagreement regarding whether the important cuprous species is

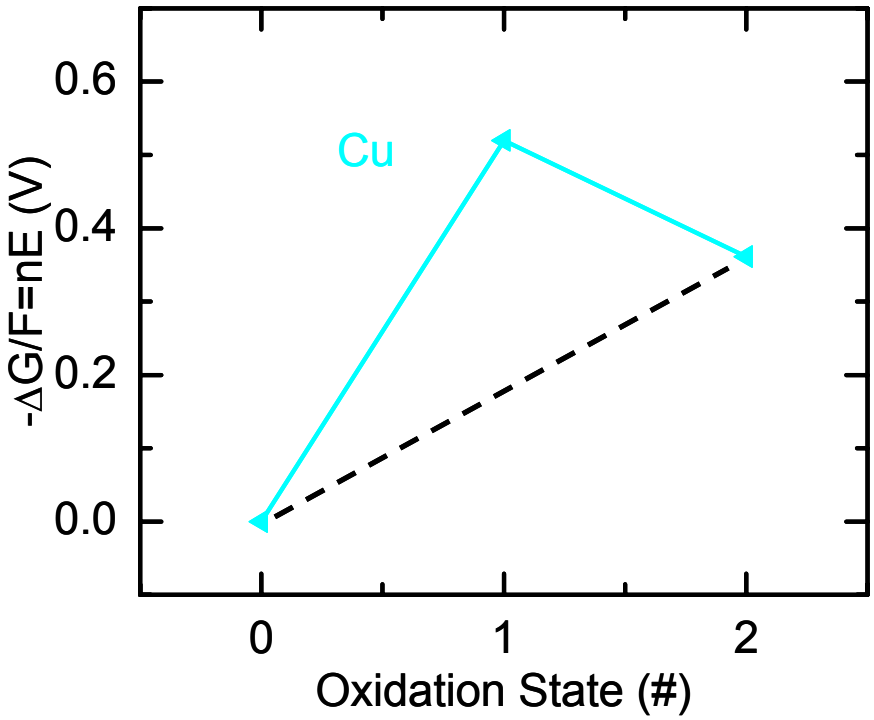

Figure 11.1 - Frost-Ebsworth diagram for metallic copper, Cu^0, and its common ionic species Cu^+ and Cu^{2+} at pH 0. The ordinate axis is proportional to the free energy of each ionic species in units of volts. Figure adapted from Reference[212].

an adsorbed cuprous complex or a near-surface solution phase species[19, 64]. In fact, recent attempts to model the Cu electrodeposition process assuming the presence of either a soluble or adsorbed form of cuprous species have yielded virtually identical results, suggesting that the complexity of this process is still not well understood or defined[44]. Experimental investigations of the role of the cuprous ion are difficult due to a d^{10} electronic configuration and the consequent lack of optical absorption in addition to its tendency to oxidize in the presence of

dissolved oxygen. With respect to the copper damascene process, the copper chemistry is further complicated by the addition of complexing agents, such as Cl^- and MPS, which are known to produce stable cuprous complexes[19]. In 2005, Vereecken et al published a significant paper in the area of damascene plating and the effects of the various additive species on the stability of free cuprous ions or cuprous complexes in the plating solution[19]. In the article, the authors utilized rotating ring-disk electrode investigations to establish a clear relationship between the local concentration of cuprous species and the overpotential/current density of electrodeposition. Specifically, they reported a definite correlation between the "acceleration" of the deposition reaction and the presence of an appreciable concentration of cuprous species generated at the copper electrode surface at open circuit and during electrodeposition at modest current densities (i.e. $\leq$10 mA/cm^2). Due to this linkage between cuprous species and the required overpotential, they found that the plating additives either enhanced or inhibited the plating rate/current density by promoting or retarding the formation of soluble Cu^+ species [19]. Specifically, chloride and accelerators (e.g. SPS) alone were found to promote the production and stability of cuprous intermediates while suppressing additive species (e.g. PEG + Cl^-, etc.) virtually eliminated the presence of cuprous species in the solution.

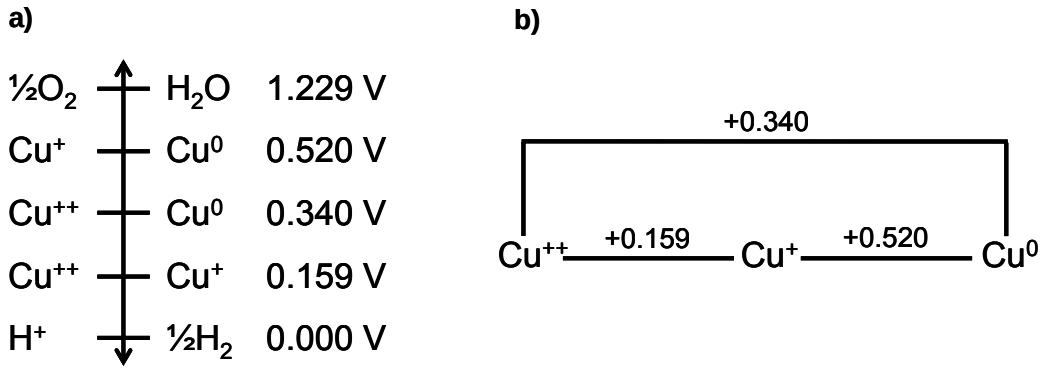

Figure 11.2 - Schematic potential (a) and Latimer (b) diagrams that summarize the relevant redox chemistry of copper in aqueous solution. In both schematics, reduction occurs from left to right. In addition to the two reduction reactions between copper ions and metallic copper, a third reduction reaction is observed between the divalent and monovalent oxidation states. Latimer diagram adapted from Reference[212].

The results presented in this chapter were collected in the same manner as those shown in Chapters 9 & 10. In this case, however, the investigations were centered on the effect of an appreciable concentration of cuprous ions in the plating solution. Specifically, a *cupric* sulfate solution otherwise deficient of cuprous ions (Cu^{+}) was deaerated and agitated via nitrogen sparging in the presence of pure copper metal (Cu^{0}). This *equilibrated* solution was then used as an electroplating bath in the same manner as the previous experiments. The results were then compared to the stress responses of plating/stripping event in

both *aged* and *fresh* (i.e. deaerated, but not equilibrated) solutions of identical composition.

11.2 Experimental details

All of the preparation and setup of the apparatus for these experiments was as described in Chapters 7-10. Similarly, the current densities and pulse durations given in Table 9.3 were again utilized in these experiments. The purpose of this set of experiments was to measure the real time surface stress response of a Cu{111} thin film electrode in three solutions that were identical in composition but prepared differently. This was done for two solution compositions, the suppressing solution (PEG/Cl^-) and a full additive package (i.e. the 50 μM SPS) solution (see Table 9.1).

For each solution composition the old, fresh, and equilibrated solutions were made identically using cupric sulfate ($CuSO_4$) as the copper ion source. First, the equilibrated and aged solutions were produced and loaded into separate deaeration cells. They were then deaerated simultaneously for >140 hours, the equilibrated solutions in the presence of copper metal and the aged solutions in the absence of copper metal. The purpose of the copper metal was to provide a surface on which the copper comproportionation reaction could occur in order to generate an increase in the concentration of cuprous ions (Cu^+) from a negligible amount to the equilibrium value. This occurs as the disproportionation reaction (eq 11.2) occurs in the reverse direction as a small but finite amount of copper atom (Cu^0) and cupric ion (Cu^{2+}) pairs comproportionate (via local electron exchange) and then enter the solution as cuprous ions. Because the aged solution

was deaerated in the absence of copper metal, the production of cuprous ions was not possible. The fresh solution was also included in order to preclude electrolyte aging effects on the surface stress response. The fresh solution was made with the same composition as the aged and equilibrated solutions, but was produced and deaerated in the absence of copper metal (for ~4 hours) on the day in which all three experiments were carried out.

11.3 Results and Discussion

As described above, the purpose of these experiments was to explore the effect of the cuprous ion (Cu^{+}) on film stress generation in order to gain some insight into its relevance to the superfilling mechanism. Because of the surface sensitive nature of surface stress monitoring, the strategy of these experiments was to compare the differences between the equilibrated electrolyte and the aged and fresh solutions. As described below, the equilibration step used in these experiments had different effects for each of the plating solutions investigated: a distinct reduction in the magnitude of stress was observed in the suppressing solution whereas no change was observed for the 50 μM SPS containing solution.

First, Figure 11.3 presents the results from two separate experiments that were carried out using equilibrated and fresh suppressing (PEG/Cl^{-}) solutions. Interestingly, both the deposition and stripping stress profiles are qualitatively similar to each other as well as to the results presented in Chapters 9 & 10. In terms of magnitude, though, a significant difference is observed during both event and relaxation portions of the profiles that correspond to the equilibrated solution. During the deposition event the equilibrated solution produces a ~-0.39 N/m

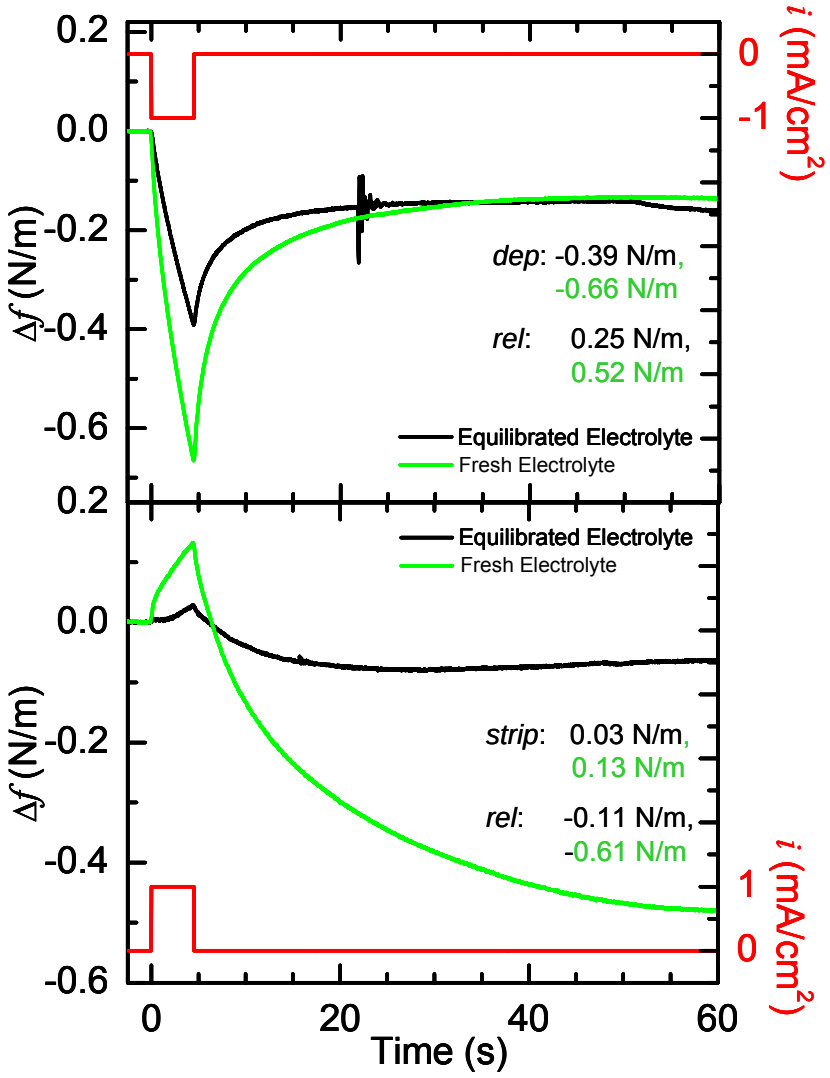

Figure 11.3 - Comparison of surface stress results during ~8 ML galvanostatic pulses of both deposition (top) and stripping (bottom) events. In each case the two solutions were prepared as equilibrated (black) and fresh (green) suppressing (PEG/Cl^-) solutions. In both cases, the equilibrated solution produces smaller stress changes in both the event and relaxation regions. Pulsed current density = 1 mA/cm^2.

surface stress while the fresh electrolyte reaches a compressive stress of ~-0.66 N/m (note the agreement of this number with the PEG/Cl^-curve of Figure 9.6 at 8 ML). This represents a ~40% reduction in stress magnitude due to the presence of an appreciable cuprous ion (Cu^+) concentration compared to the deaerated, fresh solution. In a similar fashion the tensile relaxation is also diminished in magnitude by the presence of the cuprous ion. The film in the equilibrated solution relaxes by ~0.25 N/m whereas the fresh solution produces a relaxation of ~0.52 N/m. In the case of the relaxation following the deposition event the values are less surprising in that the driving force (magnitude of the preceding compressive event stress) for relaxation is decreased in the equilibrated solution and therefore the relaxation decreases. In both cases, the tensile transient represents a 65-75% relaxation of the initial event stress. In the case of the oxidative stripping of ~8 ML of copper, Figure 11.3 again shows a difference in the overall surface stress evolution between the equilibrated and fresh solutions.

During the stripping events the cuprous ion concentration produces an even more significant reduction in stress as the equilibrated solution and the fresh solution show ~0.3 and ~0.13 N/m tensile increases, respectively (again, note the correspondence of fresh solution with the PEG/Cl^-curve of Figure 10.6). During the compressive relaxations, the fresh solution produced a typical value of ~-0.60 N/m and the equilibrated solution ~-0.11 N/m. In contrast to the deposition results, however, the ratio of relaxation to event stress differs between the equilibrated and fresh solutions during stripping (ratio of 3.67 versus 4.69). That is, the compressive relaxation in the equilibrated solution was much smaller

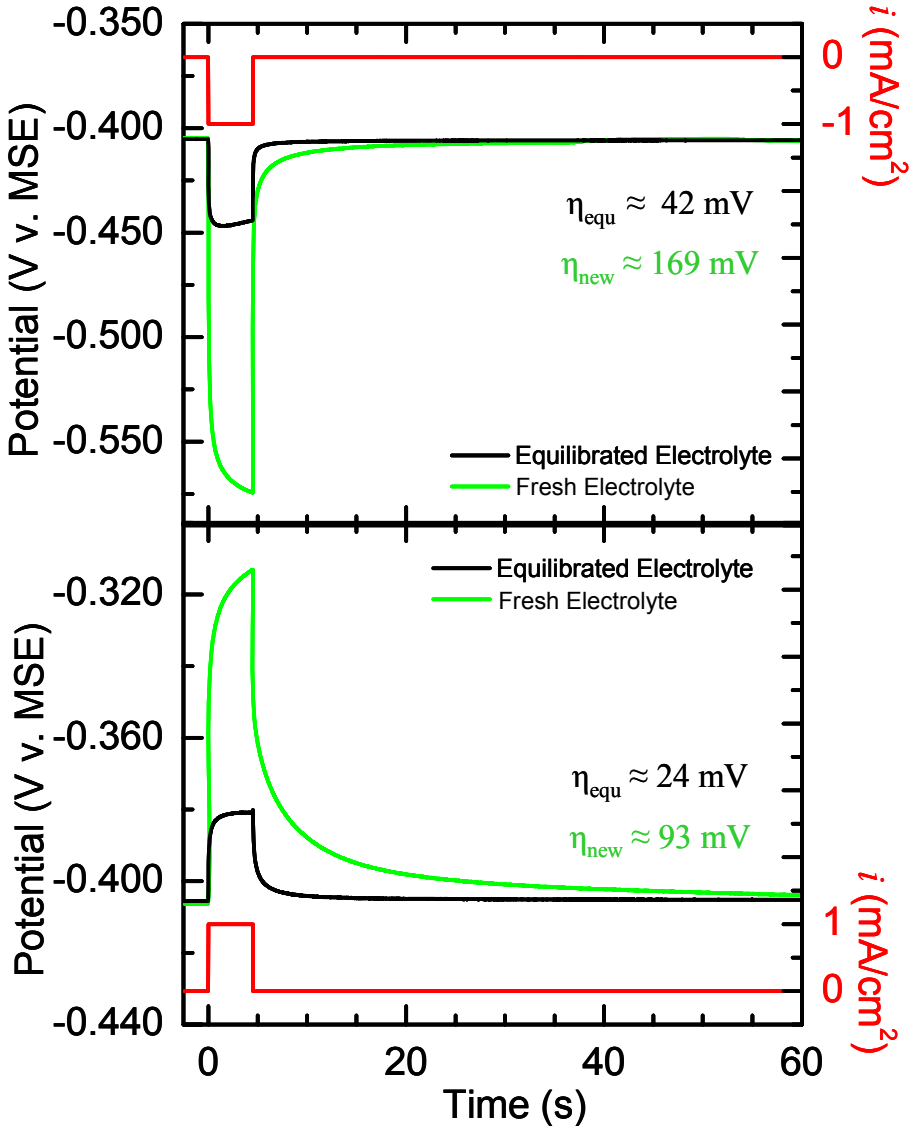

Figure 11.4 – Potential profiles recorded during galvanostatic current pulses corresponding to ~8 ML in suppressing (PEG/Cl^-) solutions. Both electrodeposition (top) and stripping (bottom) events indicate that the equilibrated (black) solution required a lower overpotential to support the 1 mA/cm^2 current density.

(relative to the preceding stripping event stress) than normally observed in the deaerated, fresh solution. This result is not surprising though since the compressive relaxations are relatively decoupled from the tensile stripping event stress, as discussed in Chapter 10. In fact, the smaller relative relaxation that is observed in the equilibrated solution suggests that the cuprous ion plays a role along with the PEG and Cl^- species that are associated with the generation of excess compressive stress following the stripping event.

The potential profiles that were collected simultaneously with surface stress during the deposition and stripping of ~8 ML of copper in the equilibrated and fresh suppressing solutions are shown in Figure 11.4. Here, a clear distinction arises between the potentials required to sustain the 1 mA/cm^2 current pulse. The difference in overpotential was ~130 mV (~169-42 mV) for electrodeposition and ~69 mV (~93-24 mV) for stripping. This result is consistent with the relationship between the concentration of cuprous species and overpotential as reported by Vereecken et al[19] and appears to confirm the presence of Cu^+ species in the solution. Thus, by providing an appreciable concentration of cuprous ions by external means, the deposition process was, in effect, "accelerated" with respect to the deposition reaction in the deaerated, fresh suppressing solution. The simultaneous measurement of potential and surface stress during deposition and stripping of copper provides insight into the relationship between cuprous species and copper thin film stress evolution. Specifically, an appreciable concentration of cuprous species at the interface has been shown to produce (1) an "acceleration" effect in the absence of accelerating

additives and (2) a reduction of both event and relaxation stresses in the suppressing solution chemistry.

In order create the equilibrated solution used in these experiments, it was necessary to perform the deaeration step for an extended period of time relative to the protocol of ~4-18 hours that was typically used. Specifically, using a back-of-the-envelope estimation based on the published values of exchange current density of copper in copper sulfate electrolytes, it was determined that a six-day duration would be more than sufficient time to completely generate an equilibrium cuprous ion concentration within the solution. In an effort to rule out any type of electrolyte aging effect, an identical set of experiments were carried out in an aged solution that was created and deaerated in parallel with the equilibrated solution. The only difference between the aged and equilibrated solutions was the presence of copper metal during the six-day deaeration period.

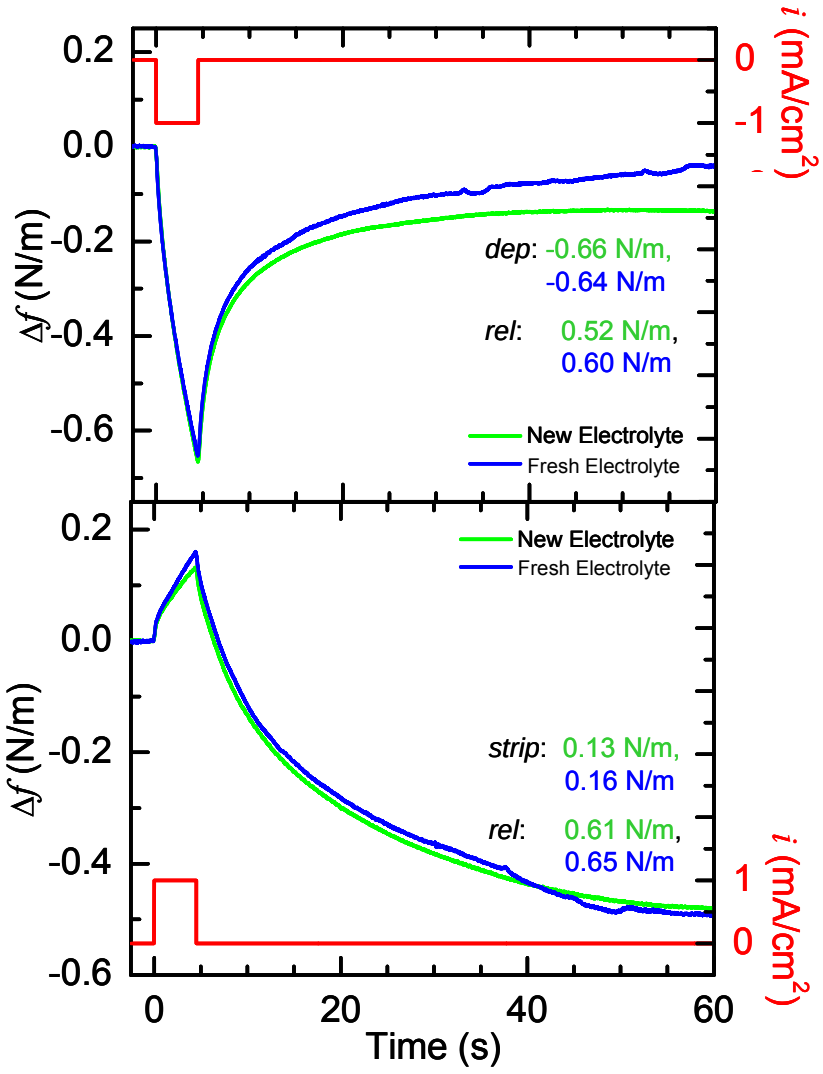

Figure 11.5 - Comparison of surface stress results during ~8 ML galvanostatic pulses of both deposition (top) and stripping (bottom) events. Here the two curves correspond to fresh (green) and aged (blue) suppressing (PEG/Cl^-) solutions. This demonstrates that extended deaeration does not affect the resultant stress profile. Pulsed current density = 1 mA/cm^2.

The purpose of this experiment was to compare the results from the aged solution with those obtained in a fresh, deaerated suppressing solution (~4 hours of deaeration time). Figure 11.5 shows the surface stress results during the deposition and stripping of ~8 ML of copper to and from a Cu{111} thin film electrode in both aged and fresh solutions. It is immediately evident that aside from the small difference in deposition relaxation stress, the stress responses are nearly identical during both electrodeposition and oxidative stripping. This result confirms that the surface stress response is unaffected by the age and deaeration time of the electrolyte and that the reduction in stress magnitude observed in Figure 11.3 is indeed a result of an appreciable cuprous ion concentration.

As stated above, an identical set of experiments was also performed in the full additive, 50 μM SPS containing solution. To be precise, both equilibrium and aged solutions were prepared from a 50 μM SPS full additive solution by the same deaeration and equilibration protocol. In this case however, the cuprous ion concentration had little or no effect of the stress profiles. Figure 11.6 shows the stress results for the same ~8 ML deposition and stripping pulses that were carried out in the equilibrated and aged 50 μM SPS containing electrolytes. In the case of the deposition event the stress profiles are virtually identical both qualitatively and quantitatively. Similarly, the event stress associated with the stripping events are also nearly indistinguishable while the respective relaxation stresses show a slight variation (the difference between the two is <12%). In general, these results indicate that in contrast to the suppressing solution case, the surface stress

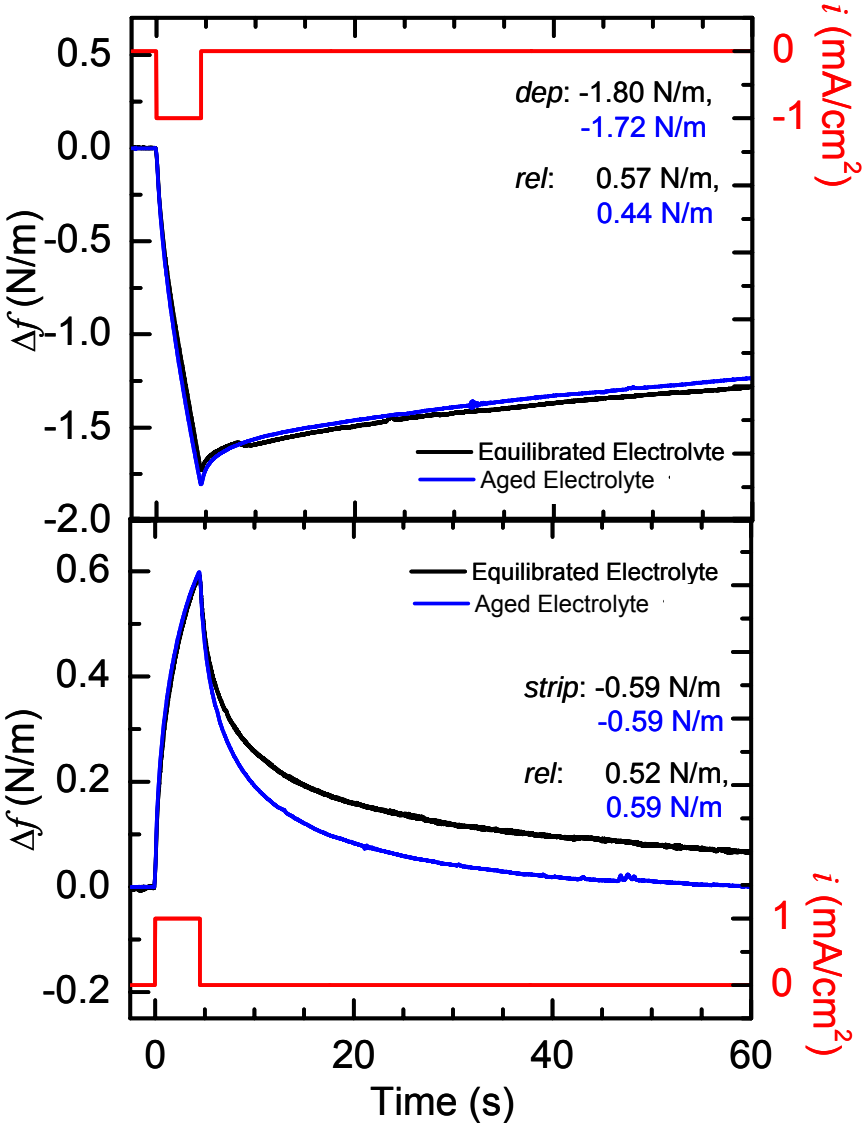

Figure 11.6 - Comparison of surface stress results during ~8 ML galvanostatic pulses of both deposition (top) and stripping (bottom) events. Here the two curves correspond to equilibrated (black) and aged (blue) full additive (50 μM SPS) solutions. In this solution chemistry the equilibration step does not affect the resultant stress profile. Pulsed current density = 1 mA/cm^2.

response in the full additive solution remains relatively unaffected by the presence of a non-zero cuprous concentration.

The interpretation of these stress results follow from the fundamental electrochemical work published by Vereecken et al[19]. Using the rotating ring-disk electrode results, the authors determined that the acceleration effect required for damascene superfilling was correlated to the presence of a local concentration of cuprous species. Additionally, they determined that this phenomenon occurred in the full additive solutions but was virtually nonexistent in suppressing chemistries due to the promotion and inhibition of cuprous ion formation, respectively. The combined potential and surface stress results presented in this present work indicate that by providing an appreciable concentration of cuprous species by external means, the overall magnitude of the stress profile was reduced in the suppressing solution but unaffected in the full additive solution. In the case of the full additive solution, these results indicate that the requisite concentration of cuprous species can be generated at open circuit or at low current densities such that the deposition and stripping reactions remain relatively unaffected by the external cuprous species of the equilibrium solution. However, in the case of the suppressing solution where the production of cuprous species is inhibited by the additive species, the presence of the externally provided cuprous concentration produces an acceleration effect as well as a reduction in overall stress magnitude.

The implications of these results as they pertain to industrial electroplating are related to the possible effects of plating bath chemistry. Specifically, these results have shown that both additive chemistry and preparation can affect the

plating process as well as the as-deposited film properties. The reliability of copper as an IC interconnect material can be affected by intrinsic stresses associated with the deposition process. The results presented herein clearly demonstrate that the chemistry of the plating bath can affect both the superfilling capability of the process (via deposition "acceleration") as well as the amount of intrinsic stress built into the film. Moreover, it is likely that Cu interconnect residual stress resulting from industrial damascene processes could be reduced by implementing similar solution deaeration and equilibration process steps.

11.4 Summary Outline

- Both the deposition and stripping stress profiles are qualitatively similar to each other as well as to the results presented in Chapters 9 & 10, respectively. However, a distinct reduction in the magnitude of both the event and relaxation stresses was observed during experiments carried out in $Cu^{++}/Cu^{+}/Cu^{0}$ equilibrated suppressing solutions. In contrast, no significant effect was observed for the equilibrated 50 μM SPS containing solution.
- The potential profiles that were collected simultaneously with surface stress during the deposition and stripping in the equilibrated and fresh suppressing solutions reveal a clear distinction between the potentials required to sustain the 1 mA/cm^2 current pulse. By providing an appreciable concentration of cuprous ions by external means, the deposition process was, in effect, "accelerated" with respect to the deposition reaction in the deaerated, fresh suppressing solution. This

result is consistent with the relationship between the concentration of cuprous species and overpotential as reported by Vereecken et al and confirms the presence of Cu^{+} species in the solution.

- The surface stress response is unaffected by the age and deaeration time of the electrolyte. Thus the reduction in stress magnitude observed in equilibrated solutions is a result of the appreciable cuprous ion concentration not an electrolyte aging effect.
- According to previous studies, full additive solutions are capable of superfilling and suppressing chemistries are not because of their respective tendencies to promote and inhibit cuprous ion formation. Thus, by providing an appreciable concentration of cuprous species by external means, the overall magnitude of the stress profile was reduced in the suppressing solution where Cu^{+} is generally absent but unaffected in the full additive solution where the concentration of Cu^{+} is already sufficient.

CHAPTER 12

SURFACE STRESS CHANGES AT OPEN CIRCUIT POTENTIAL

12.1 Introduction

As discussed briefly in Chapter 3, the immersion of a metal (e.g. copper) electrode in an electrolytic solution results in the creation of a dynamic interface across which both mass and charge is constantly exchanged. This is true even when the electrode remains at the open circuit potential and the net electrochemical current is zero. Under these conditions, a finite amount of balanced faradaic charge passes between the electrode and the electrolyte. This exchange current density has units of current per area and is defined as[40]

$$i_0 = Fk^0[O]^{(1-\alpha)}[R]^{\alpha} \tag{12.1}$$

where F, k^0, and α are the Faraday constant, the standard reaction rate constant, and the transfer coefficient, respectively, and $[O]$ & $[R]$ are the concentrations of the oxidized and reduced species, respectively. For the case of a copper electrode in a deaerated solution containing copper ions, the exchange current corresponds primarily to the reduction of copper ions and the oxidation of copper atoms. Because this parameter is not measurable by electrochemical means, the actual physical mechanism that corresponds to this constant redox process is not well defined. Furthermore, in the case of an aliovalent system such as copper where more than one oxidation state is possible, the process is likely more complex.

In addition to the electrochemical experiments described in the previous chapters, a very specialized set of experiments was designed to measure stress in the absence of any external electrochemical manipulation. That is, instead of using current or applied potential manipulations as the experimental variable, the solution composition and concentration were the controlled parameters. In one sense this type of experiment draws somewhat on the gas adsorption experiments that have been performed under UHV conditions by other members of the Friesen Research Group[131, 213, 214]. In contrast to those studies, however, the introduction of surfactant species and/or the manipulation of an ionic species' thermodynamic activity in electrochemical systems can have a large effect on the kinetics of the electrode-electrolyte interface and the associated surface stress state.

12.2 Experimental details

The same basic cleaning and preparation steps that were described in Chapter 7 were also used for the solution exchange experiments presented here. The minor differences in the setup of the apparatus were (1) the simultaneous preparation of a second electrolytic solution that was used in the solution exchange event and (2) a few modifications within the electrochemical surface stress cell itself (see Figure 12.1). The purpose of this set of experiments was to measure the surface stress response of a Cu{111} thin film electrode to a change in the electrochemical environment. Even though no electrochemical parameters were controlled during these experiments, the open circuit potential was monitored during the entire process. The potential profile primarily served as a supplementary source of information and also provided a general indication of the

extent of solution exchange during that process. The experimental protocol consisted in two simple steps. First, the initial solution was loaded into the electrochemical surface stress cell and the system was allowed to come to a pseudo-steady-state surface stress value (i.e. low level signal drift [<~0.003 (N/m)/s]). Second, the initial solution was replaced by the final solution via a smooth, continuous solution exchange. Figure 12.1 shows the experimental apparatus used in the solution exchange experiments and illustrates the means by which the solution exchange was accomplished. Based on the experimental requirements of this work, several modifications were made to the electrochemical surface stress cell (compare Figures 12.1 & 7.2). In order to separate the initial and final solutions, a machined PTFE barrier was placed inside the cell. The barrier was designed such that the back-side was sloped and the top-most portion was sharp enough to facilitate a smooth and well defined overflow of liquid during the exchange process. Additionally, Figure 12.1a shows a small sponge (of complementary shape) that was placed on the sloped face of the barrier to smoothly transport the overflowing solution to the overflow compartment of the cell. Again, the overarching goal behind these modifications was to continuously transition the working electrode surface from one electrolytic solution to another without creating excess noise (from e.g. vibration) in the surface stress signal and without breaking electrochemical contact between the working and reference electrodes.

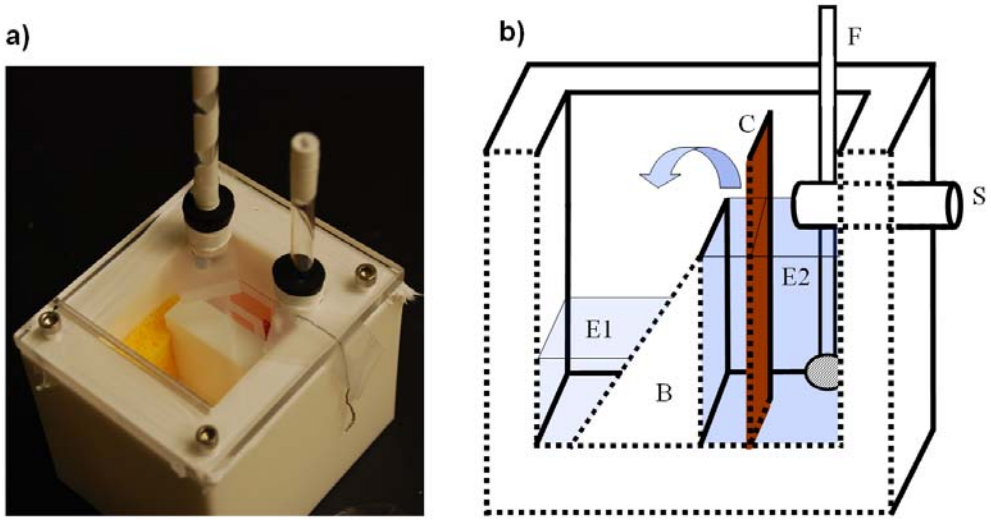

Figure 12.1 - Image (a) and illustration (b) of the modified cell setup used for the solution exchange experiments at the open circuit potential. As before, the cell consisted of a cantilever sample (C) with the working electrode being submersed in electrolyte and the stress monitor sensor (S) fixed adjacent to the sample. Additionally, a barrier (B) was placed in the cell to create two compartments within the cell and separate the initial solution (E1) from the final solution (E2) after flowing over the barrier. The final solution was introduced to the compartment containing the working electrode via a pipette/frit device (F).

Throughout this series of solution exchange experiments, several types of solutions were utilized. The first type of solution was a sulfate based combination of sulfuric acid, copper sulfate and sodium sulfate at the various concentrations

shown in Table 12.1. These sulfate based solutions were specifically designed in order to observe the surface stress due to an increase of copper ion concentration, at constant sulfate concentration. In this first type of exchange experiment, each exchange consisted in the replacement of a low Cu^{++} concentration with a higher concentration where the higher concentration was an order of magnitude larger(e.g. $[Cu^{2+}]=10^{-2}$ M $\rightarrow$ $[Cu^{2+}]=10^{-1}$ M). As an additional experimental

Table 12.1 – Solution components and their corresponding concentrations for the six solutions used in the first type of solution exchange experiments performed at open circuit.

Solution Identifier	$[H_2SO_4]$ (mol/L)	$[Cu_2SO_4]$ (mol/L)	$[Na_2SO_4]$ (mol/L)
10^{-6} M [Cu]	0.1	0.000001	~1
10^{-5} M [Cu]	0.1	0.00001	~1
10^{-4} M [Cu]	0.1	0.0001	~1
10^{-3} M [Cu]	0.1	0.001	~1
10^{-2} M [Cu]	0.1	0.01	0.99
10^{-1} M [Cu]	0.1	0.1	0.9

parameter, a new Cu(111) single crystal sample embodiment was also used in the first solution type. These supplementary experiments were used to probe the role of grain boundaries in the stress changes associated with the solutions exchanges. The second solution type that was used in this series of solution exchanges was a

perchlorate based combination. In this case the anion identity was changed in order to confirm and generalize the stress results observed in the sulfate based solutions just as the perchlorate solutions were used in the deposition and stripping experiments above (see Chapters 9 & 10). For this solution type, only one exchange combination was carried out using the solutions shown in Table 12.2. The perchlorate based solutions were also used to replace a low concentration (0.01 M) of copper ions with a concentration that was ten times larger (0.1 M). Also, it is important to note that during the first and second types of solution exchanges, the anion (sulfate or perchlorate) concentration was held constant across the solution exchange in order to avoid any extraneous effects. The third and final type of solution used in the solution exchange experiments differed from the previous two in that the controlled variable was not the copper ion concentration but rather the presence of copper plating additive species. More specifically, an additive free solution (as defined in Chapters 9 & 10) was replaced by a suppressing solution that contained both PEG and NaCl in the concentrations defined by Table 12.3. Specifically, two versions of this type of solution exchange experiment were carried out, one at concentrations equal to those of the deposition and stripping experiments described above and another at the lower concentrations used in first type of solution exchanges (see Tables 12.1 & 12.3).

Table 12.2 – Solution components and their corresponding concentrations for the two solutions used in the second type of solution exchange experiments at open circuit.

Solution Identifier	$[H_2ClO_4]$ (mol/L)	$[Cu(ClO_4)_2*6H_2O]$ (mol/L)	$[NaClO_4]$ (mol/L)
10^{-2} M [Cu] perchlorate	0.1	0.01	0.98
10^{-1} M [Cu] perchlorate	0.1	0.1	0.8

One of the major challenges associated with this new experimental protocol was the need to either minimize or account for mixing between the two solutions during the exchange process. For the first and second types of solution exchanges involving a change in copper ion concentration, the mixing was minimized by the use of the "pipette/frit device" that was designed minimize turbulence in the solution(s) during the exchange event. The success of this device was predicated on the differences in density between the copper ion containing solutions of varying concentrations. Because the solutions that contained higher concentrations of Cu^{2+} have slightly larger densities, the more concentrated solution settled at the bottom of the cell during the exchange. The role of the pipette/frit device was then to minimize the amount of mixing that occurred due to the convection that was induced by the loading of the final solution. The strategy that was then used to achieve an efficient transition to a

Table 12.3 – Solution components and their corresponding concentrations for the four solutions used in the third type of solution exchange experiments at open circuit.

Solution Identifier	$[H_2SO_4]$ (mol/L)	$[CuSO_4]$ (mol/L)	[PEG] (mol/L)	[NaCl] (mol/L)
Additive Free #1	0.1	0.1	0	0
Suppressing #1	0.1	0.1	$157*10^{-6}$	$1.79*10^{-3}$
Additive Free #2	1	0.25	0	0
Suppressing #2	1	0.25	$157*10^{-6}$	$1.79*10^{-3}$

higher concentration of copper ions was to avoid mixing of the initial and final solutions. Conversely, the strategy that was used in the third type of solution exchange involving plating additives was to anticipate mixing and adjust the additive concentrations accordingly. The motivation behind this strategy was based on lack of a density difference between the additive free and suppressing solutions. In this case, the additive concentrations were scaled such that if the initial and final solutions were perfectly mixed, the concentrations would be equal to those used in the electrodeposition and oxidative stripping experiments in Chapters 9 & 10 (see Table 9.1). Based on the geometry of the electrochemical cell and the volumes of the respective solutions, a scaling factor of 1.79 was calculated. Thus the final composition of the solution above the working electrode in the third type of solution exchange experiments contained at least as much PEG and Cl^- species as the deposition suppressing solutions shown in Table 9.1.

12.3 Results and Discussion

12.3.1a - Sulfate Solution Results

The first type of solution exchange experiments that was carried out was concerned with an increase of copper ion concentration immediately around the working electrode surface. The concept behind this type experiment is somewhat novel, given that the solution exchange provided an increase in activity and chemical potential of Cu^{++} as well as an increase in surface adatom concentration, without the use of an applied potential or net current. This is significant because any change in surface stress during these types of experiments comes in the absence of a net addition or removal of material from the electrode surface. Moreover, the stress changes that are observed during these experiments confirm the existence of a dynamic electrode-electrolyte interfacial region and demonstrate that electrode surfaces can be subjected to large stresses upon immersion into electrolyte, even at open circuit potentials.

Figure 12.2 shows a typical surface stress and potential profile that are collected during the solution exchange experiments. In this specific case, a relatively large compressive stress change (~-8.5 N/m) evolves in response to a transition from 10^{-2} M to 10^{-1} M in cupric ion concentration. Additionally, the change in potential is ~30 mV, which is in agreement with the value predicted by the Nernst equation

$$E = E^0 + \frac{RT}{nF}\ln\left(\frac{[O]}{[R]}\right), \tag{12.2}$$

where the oxidized (O) species is Cu^{2+} and the reduced species (R) is Cu^0 and E, E^0, R, T, n, and F are the electrode potential, the equilibrium potential of the redox couple, the gas constant, temperature, the number of electrons transferred and the Faraday constant, respectively[40, 41].

Surface stress changes associated with the increase in $[Cu^{++}]$ over the range of 10^{-5} M to 10^{-1} M (by one order of magnitude each time) were measured and are shown in Figure 12.3. Initially, at low concentrations, no detectable change in surface stress was measured and the first three points are equal to zero. However, starting with the transition to $[Cu^{++}]=10^{-3}$ M, the stress is found to increase rapidly as a function of final copper ion concentration during these solution exchange experiments. Overall, Figure 12.3 shows that the total stress change of a thin film electrode is ~12 N/m in the range from 0 to 10^{-1} M copper ions.

In concert with the surface stress measurements taken during the solution exchange experiments, electrochemical experiments were performed in each of the six solutions shown in Table 12.1. First, a series of cyclic voltammetric experiments were used to estimate the exchange current density for a Cu{111} thin film electrode in each of copper sulfate concentrations. The resulting current-voltage behavior was analyzed using the Tafel slope extrapolation method as outlined in by Bard and Faulkner[40]. The results from these experiments are plotted in Figure 12.4 as a function of $\log([Cu^{++}])$. Additionally, the data also

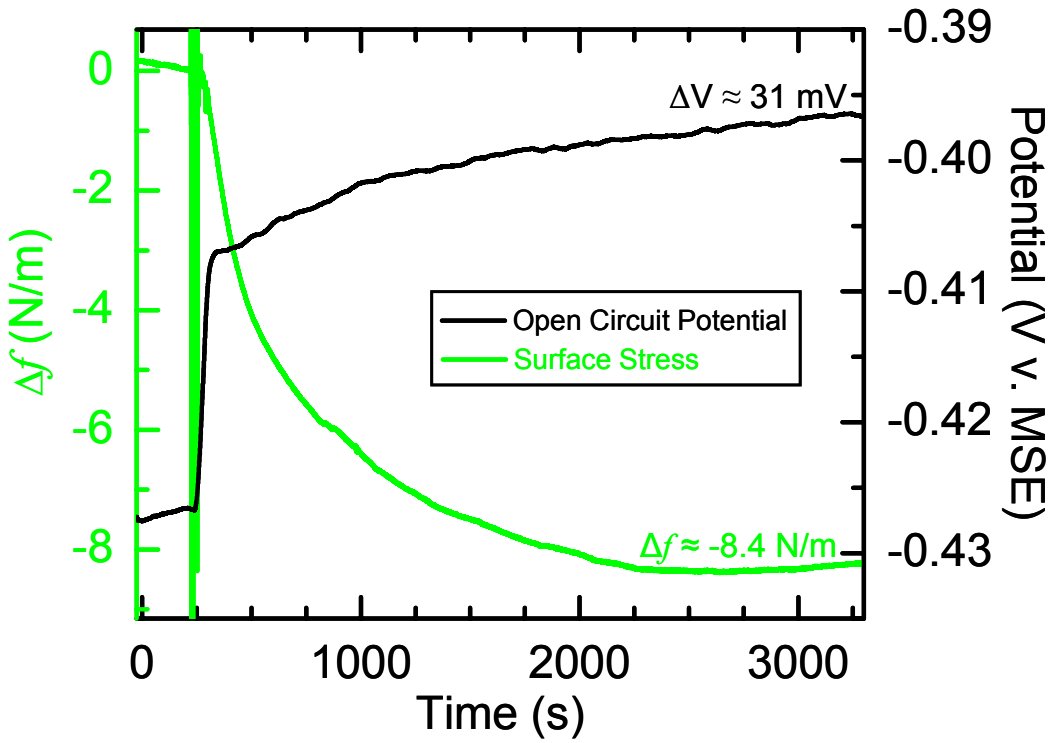

Figure 12.2 - Surface stress (green) and open circuit potential (black) responses of a Cu{111} thin film electrode to a solution exchange process. The starting solution was 0.01 M $CuSO_4$ + 0.1 M H_2SO_4 + 0.99 M Na_2SO_4 followed by replacement by 0.01 M $CuSO_4$ + 0.1 M H_2SO_4 + 0.99 M Na_2SO_4. The large spike in the stress signal at ~250 s corresponds to the physical exchange of solution in electrode compartment of the electrochemical surface stress cell.

correspond to a *turnover frequency* (TOF) shown on the right side ordinate axis. In this context, the TOF was defined from the exchange current density measurements and the Faraday's law type relation as the total amount of Cu (in equivalent monolayers) that is equally deposited and stripped in a unit time period (per second).

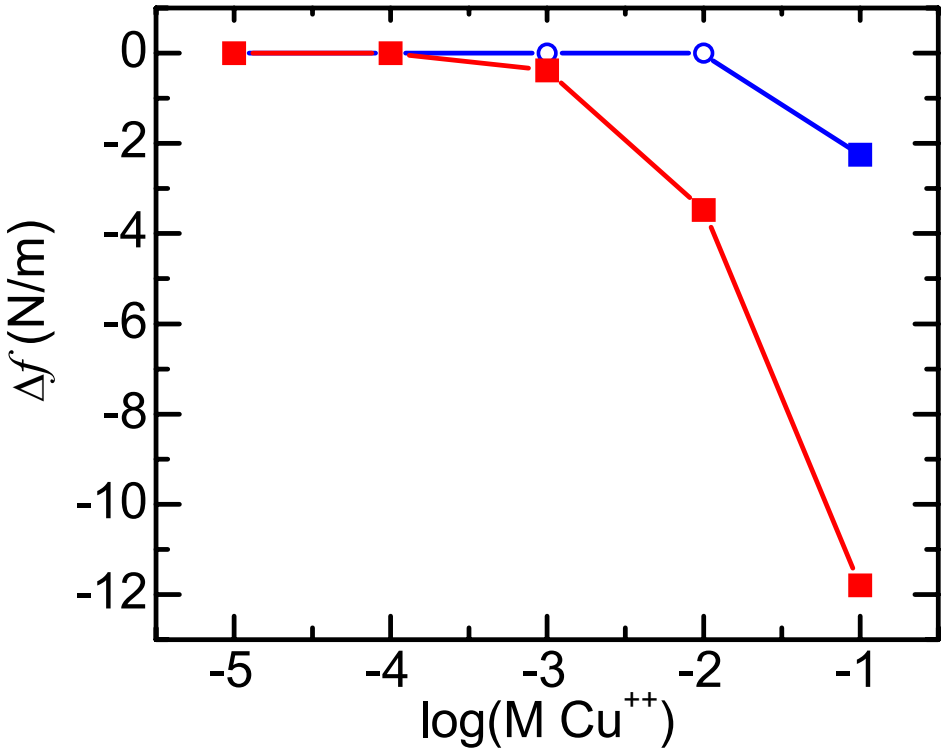

Figure 12.3 – Graphical representation of the surface stress changes observed on Cu{111} thin film (red) and Cu(111) single crystal (blue) electrodes in response to a series of solution exchange processes. Each point corresponds to the change in stress relative to the previous point and is plotted as a function of the logarithm of the final Cu++ concentration. The initial solutions were of the form $10^{(x-1)}$ M $CuSO_4$ + 0.1 M H_2SO_4 + $(1-10^{(x-1)})$ M Na_2SO_4 and the final solutions 10^x M $CuSO_4$ + 0.1 M H_2SO_4 + $(1-10^x)$ M Na_2SO_4, where x is the unit on the abscissa.

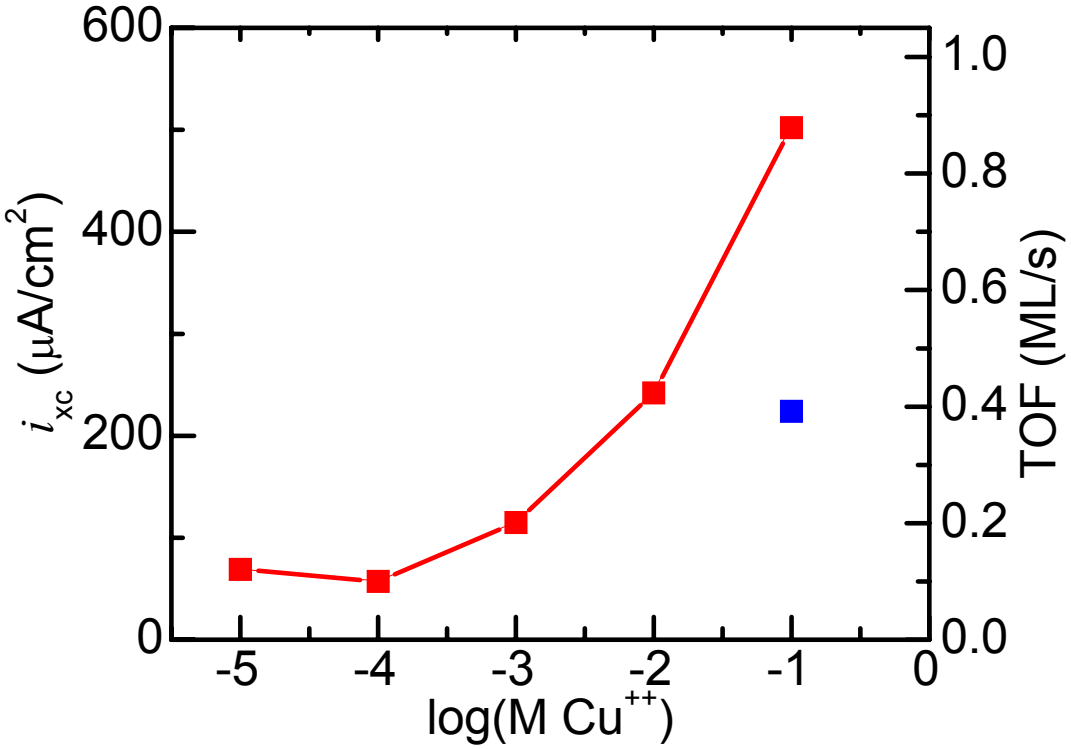

Figure 12.4 – Exchange current density (i_0) values of Cu{111} thin film (red) Cu(111) single crystal electrodes in solutions of 10^x M $CuSO_4$ + 0.1 M H_2SO_4 + (1-10^x) M Na_2SO_4, where x is unit on the abscissa. In each case the exchange current values were determined via the Tafel slope extrapolation of a cyclic voltammetric curves. The right side ordinate axis corresponds to an equivalent turnover frequency in units of monolayers per second

Upon comparison of the data represented in Figures 12.3 & 12.4, a striking similarity in the functionality of the curves becomes apparent. That is, both the exchange current density and the solution exchange stress change curves appear to exhibit exponential-type dependences on the logarithm of the copper ion concentration in the solution. To further explore and quantify the possible relationship between these two measurements, Figure 12.5 was constructed as a parametric plot of the change in surface stress, Δf, and exchange current density, $i_{0,}$ with Cu^{++} concentration as the linking parameter. Immediately, the resulting curve suggests a linear relationship between i_0 and Δf. A linear fit of the data in Figure 12.5 yields a relationship of $\Delta f = -0.027 * i_0 + 2.19$ with an R^2 value of 0.98. While the results of these measurements do appear to be related, it should be noted that only a small number of data points (only three non-zero stress change value) were used to establish relationship, therefore the high R^2 value may be serendipitously large.

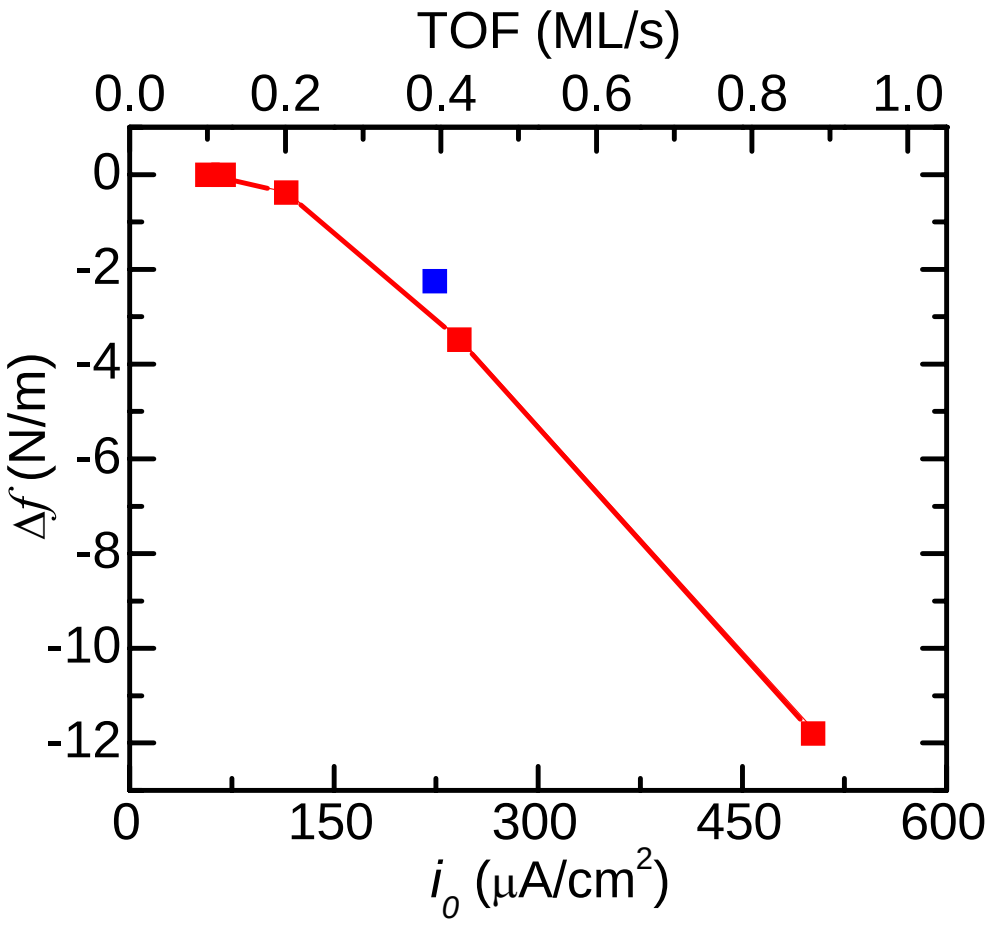

Figure 12.5 – Plot of surface stress response to solution exchange and the resulting exchange current density (and equivalently, turnover frequency on the top axis) of the final solution. Here the Cu{111} thin film (red) and Cu(111) single crystal (blue) results from Figures 12.3 and 12.4 are plotted parametrically with the logarithm of the Cu^{++} concentration as the parameter. A linear fit of the resulting curve is $\Delta f = -0.027 * i_0 + 2.19$ with an R^2 value of 0.98.

12.3.1b - Equilibrated Sulfate Solutions

In addition to the series of solution exchange results presented in Figure 12.3, a supplementary experiment was performed in order to investigate the effect of copper chemistry on the solution exchange induced surface stress. The objective of this single experiment was to use an equilibrated solution of 0.1 M $CuSO_4$ + 0.1 M H_2SO_4 + 0.9 M Na_2SO_4 as a final solution during a transition from a corresponding 0.01 M $CuSO_4$ solution. For this experiment, the equilibrated solution was prepared by following the same protocol that was used for the experiments described in Chapter 11. Following the extended deaeration/equilibration step, the solution exchange process was carried out in the same fashion as the other sulfate based exchange experiments. In this case, the solution exchange produced a compressive change in stress of approximately 6 N/m. The similarity between this value and the ~-8.5 N/m change reported in Figure 12.3 for the equivalent un-equilibrated transition (from 0.01 M to 0.1 M) is significant. In fact, this result allows for the exclusion of extraneous stress generation via cuprous complex interactions with the electrode surface.

12.3.1c - Cu(111) Single Crystal Samples in Sulfate Solutions

An identical set of sulfate based solution exchange experiments was carried out using a new sample embodiment that substituted a Cu(111) single crystal surface as the working electrode. The sample was constructed using a small (~1 cm × ~0.65 cm × ~0.02 cm), electropolished slice from a Cu(111) single crystal and a UHV deposited thin film sample. By cutting the thin film sample and attaching the pieces to the single crystal slice, the new sample

embodiment was used exactly as the thin film samples were previously used. In addition to the change in sample embodiment, a small number of changes to the calibration equation (eq 7.6) were made (see Appendix C).

Figures 12.3, 12.4, and 12.5 show the exchange current density and surface stress values that were similarly collected using the new single crystal sample. In this case, only the 0.01 M to 0.1 M CuSO4 transition yielded a measurable change in stress (~-2 N/m) and is represented by the single blue square. The blue circles indicate that the experiments were carried out for the less concentrated solution exchanges but yielded no discernible change in surface stress. Because of the sample construction, the sensitivity of the stress monitor-sample system was reduced by a factor of two to three, relative to the thin film experiments. It is possible then that the surface stress changes associated with the less concentrated solutions were not actually zero but that the data collection was limited by the resolution of the experimental apparatus. However, the collected single crystal sample results do present a behavior that is strikingly similar to the thin film results. Figure 12.5 indicates that the induced single crystal surface stress evolves in the compressive direction and suggests that it scales with the exchange current density as well. These results demonstrate, at least qualitatively, that a similar stress response is induced on both polycrystalline thin film electrodes as well as single crystal electrodes and that grain boundaries are not required to produce stress in the electrode.

12.3.2 Perchlorate Solution Results

The second type of solution that was used in the exchange experiments were the perchlorate based electrolytes defined in Table 12.2. Again, the research objective behind this set of experiments was supplementary in nature and therefore consisted of only a single pair of solutions. As in the case of the deposition and stripping experiments, the motivation behind the use of the perchlorate based solutions was to investigate the effect of the supporting anion. The perchlorate based exchanges were carried out in the same fashion as the sulfate exchanges. In this case the stress changes results were slightly more scattered, ranging from about -4 to -7 N/m for the transition from 0.01 M to 0.1 M $Cu(ClO_4)_2*6H_2O$. Figure 12.6 shows the actual stress curves that were collected during two runs of the perchlorate solution exchange experiment. While the exact value of the stress change remains somewhat uncertain (due to the scatter in the data), the results are less than a factor of two different than the changes observed in the sulfate solutions. As in the case of the equilibrated solution exchange, the magnitude of these results suggests that the effect of the anion is at most secondary in nature relative to the effect of the copper ion concentration.

12.3.3 The Effect of Additives & a Stress Generation Model

The third type of solution that was utilized in the solution exchange experiments contained the deposition suppressing additives that were used in

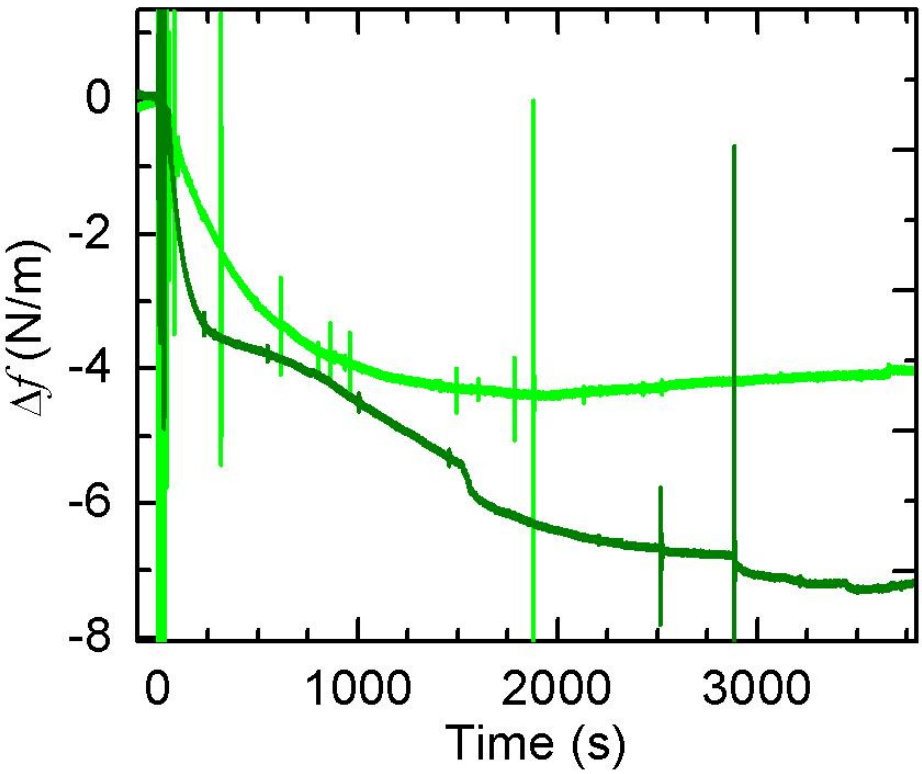

Figure 12.6 – Two curves showing the surface stress response of a Cu{111} thin film electrode to a perchlorate solution exchange process. The starting solution was 0.01 M Cu(ClO4)2*6H2O + 0.1 M HClO4 + 0.98 M NaClO4 that was replaced by 0.1 M Cu(ClO4)2*6H2O + 0.1 M HClO4 + 0.8 M NaClO4. Here the compressive stress changes begin after the solution exchange at ~0 seconds are approximately equal to -4 (light green) and -7 (dark green) N/m.

Chapters 9-11. In this case the solution exchanges occurred at constant copper and sulfate ion concentrations, while PEG and Cl^- species were introduced into the system. As described above, it has been well documented in the literature that

a deposition suppressing adlayer consisting of PEG and Cl^- adsorbs on the copper surface during damascene processing. In addition to suppressing the deposition process, the blocking layer is also known to suppress the exchange current density. This set of experiments was initially performed in anticipation of measuring the adsorption induced surface stress of this PEG/Cl^- blocking layer. However, as shown in Figure 12.7, the stress change associated with the introduction of the additive containing solutions was (1) uniformly tensile in nature and (2) somewhat larger than expected.

First, the sign of the stress change was somewhat surprising in that all of the previous experiments were invariably compressive in sign, albeit the experimental variables were significantly different (concentration increases vs. introduction of additives). Second, the magnitudes were in general larger than expected from purely adsorption type effects, yet were similar to the previous solution exchange experiments (see Figure 12.3). It should be noted, however, that because these results are relatively preliminary in nature there was some scatter in the actual measured values. In the case of the additive free #1 to suppressing #1 exchange, the values ranged from ~+1.8 to +2.6 N/m. For the larger concentrations, the values ranged between ~+2.2 to +8.1 N/m.

In summary, the entire set of solution exchange stress results can be interpreted within the context of exchange current densities and equilibrium surface adatom concentrations. First, consider a modified version of the adatom-grain boundary model as formulated by Chason et al[162]. As described above in

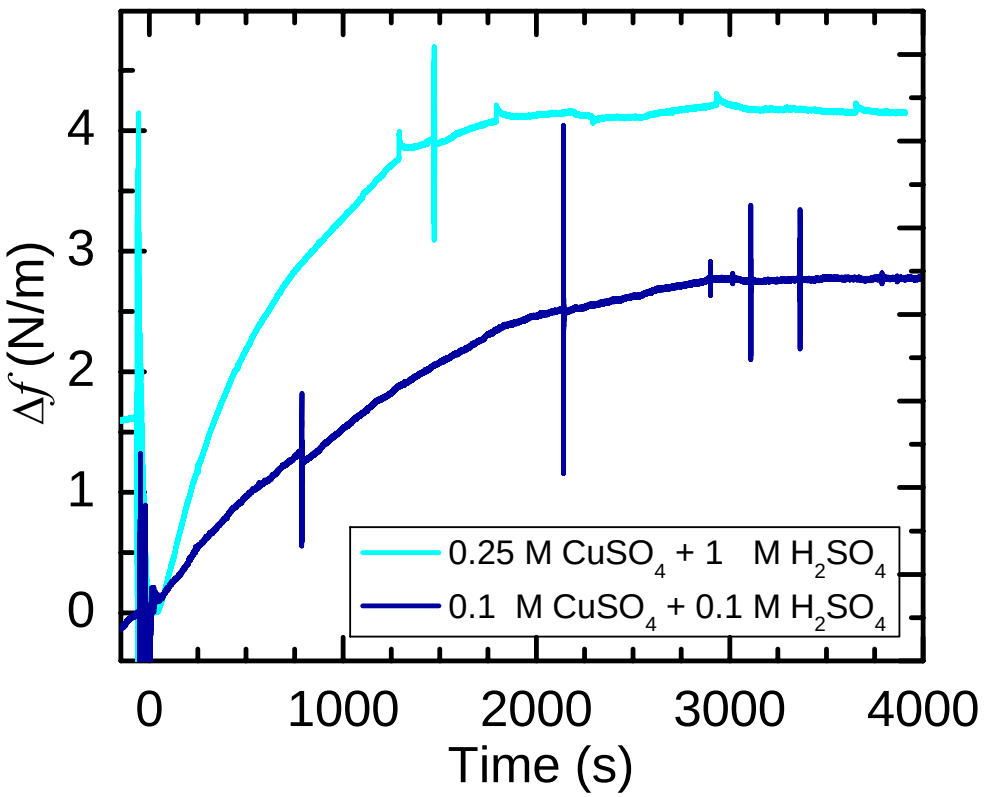

Figure 12.7 – Two curves showing the surface stress response of a Cu{111} thin film electrode to a solution exchange process. The starting solution was an additive free solution of $CuSO_4$ and H_2SO_4 that was replaced by a suppressing solution of equal concentrations plus 157 μM PEG and 1.79 mM NaCl. Here the stress change is tensile and begins after the solution exchange at ~0 seconds.

Section 5.2.4, it is assumed that a difference in chemical potential of adatoms on the film surface (μ_s) and the chemical potential of those in the grain boundaries (μ_{GB}) is the driving force behind a migration of atoms into the grain boundaries

(GBs) and the concomitant increase in compressive film stress. The difference in chemical potential is then[162]

$$\Delta\mu = \mu_s - \mu_{GB} = \Delta\mu_0 + \Delta\mu_s + \sigma\Omega, \tag{12.3}$$

where $\Delta\mu_0$ is the difference between the surface and GB chemical potentials in the absence of growth or a change in adatom concentration, $\Delta\mu_s$ is the difference in surface chemical potential in response to deposition or a change in activity, σ is the normal stress acting across a vertical grain boundary, and Ω is the atomic volume of e.g. copper. The magnitude of $\Delta\mu_0$ is expected to be small ($\Delta\mu_0 \approx 0$) and $\Delta\mu$ is approximately equal to 0 both before and at long times after the solution exchange event. Thus, the stress associated with a change in Cu^{++} activity of an electrolyte can be estimated (through surface concentration values) by rearranging eq 12.2,

$$\sigma = -\frac{\delta\mu_s}{\Omega} = -\frac{RT}{\Omega}\ln\left(\overline{C}_{surf}^{final} \Big/ \overline{C}_{surf}^{initial}\right). \tag{12.4}$$

Next, the equilibrium surface adatom concentrations (see Table 12.4) can be estimated from chronopotentiometric measurements using the method developed by Gerischer[215]. Using the values that were obtained by this method (see Table 12.4), the estimated stress change associated with a $[Cu^{++}]$=0.01 M→$[Cu^{++}]$=0.1 M solution exchange is then ~-33 N/m, which is approximately a factor of four and fifteen larger than the measured values for the polycrystalline thin film (~8.5

N/m) and single crystal (~-2 N/m) electrodes, respectively. There a number of possible explanations for the discrepancy between the estimated and the measured values. First, the value of the copper atomic volume is likely different for adatoms in the grain boundary (or other defect site in the case of a single crystal surface). Second, when the 33 N/m estimate is divided by the thickness of the thin film samples, ~250 nm, the corresponding bulk stress of the Cu film approaches 130 MPa, which is of the same order or larger than the yield strength of bulk copper[216]. A similar calculation for the single crystal electrode gives a bulk stress of ~0.3 MPa. However, even without correction, this simple model seems to agree well with the observed behavior of the solution exchange experiments. Interestingly, the Chason adatom model assumes that a grain boundary migration process is the mechanism by which stress is imparted into the electrode, yet the present results show that a similar stress is also induced in the absence of grain boundaries. This result suggests that compressive stress due to the increase in adatom chemical potential can also occur at other surface sites such as twin boundaries, dislocation cores, or terrace sites.

The surface stress results from the sulfate and perchlorate based solutions demonstrate that the electrode exchange current, equilibrium adatom concentration and compressive surface stress all increase as a function of copper ion concentration. As shown in Figure 12.5, stress and exchange current density appear to be linearly related. This empirical relationship provides a framework in which to interpret the stress changes observed during the introduction of PEG and

Table 12.4 – Equilibrium surface adatom coverages of a Cu{111} thin film electrode as estimated by Gerischer's current pulse method[215]. Solutions contained the indicated Cu^{++} concentration in addition to 0.1 M H_2SO_4 + 1 M Na_2SO_4. Data used with permission from Dr. Lei Tang and Dr. Cody Friesen.

log([Cu^{++}])	$\overline{C}_{surf}^{[Cu^{++}]}$(ML)
-4	0.0003678
-3	0.0004249
-2	0.0014642
-1	0.0021420
0	0.0067817

Cl^- additive species during solution exchanges. First, the exchange current densities of the suppressing #1 and additive free #1 solutions were determined by the same method as the described above (~156 & ~502 μA/cm^2, respectively). Next, using these values and the equation for the linear fit as given in Figure 12.5, an estimate of surface stress change due to the suppression of the exchange current density can be made. In the case of the 0.1 M $CuSO_4$ additive free to suppressing solution exchange, the corresponding stress change was estimated at ~+9.3 N/m and compares favorably to the measured value of ~+2 N/m. This result further supports the proposed relationship between the exchange current density and surface stress state of the Cu{111} film. That is, the somewhat unexpected magnitude and sign of the stress during the third type of solution exchange experiment can be explained as a reduction of the exchange current density by the adsorbed PEG/Cl^- adlayer.

12.4 Summary Outline

- Significant changes in measured surface stress were observed during solution exchange experiments where various experimental parameters were investigated across the solution exchange. Responses were observed in the absence of a net addition or removal of material from the electrode and corresponded to changes in $[Cu^{++}]$ or to the presence of solution additives.
- Surface stress changes associated with the increase in $[Cu^{++}]$ over the range of 10^{-5} M to 10^{-1} M as well as exchange current densities (i_0) at each concentration were measured and shown to be linearly related. The increasingly larger values of i_0 induce increasingly more compressive stress in the Cu electrodes. Similarly, the suppression of the i_0 by adsorbed molecular species (PEG/Cl-) at a given copper ion concentration induces a tensile change in stress.
- Both (1) the identity of the supporting anion (ClO_4^- vs. SO_4^{2-}) and (2) an appreciable concentration of cuprous ions had relatively small effects on the magnitude of the change in stress relative to the overall copper ion concentration.
- Using a modified version of Chason's grain boundary adatom surface stress model, a stress value of ~-33 N/m was estimated for the stress change associated with a 0.01 M to 0.1 M $[Cu^{++}]$ solution exchange experiment. Because this estimate is large enough to account for the stresses measures in the present work, it was proposed that migration of

adatoms into electrode grain boundaries and other defect sites could be responsible for the measured changes in stress for both polycrystalline thin film (~8.5 N/m) and single crystal (~-2 N/m) electrodes.

CHAPTER 13

CONCLUSIONS & FUTURE WORK

This dissertation presents the experimental background and research on the surface stress evolution of Cu{111} thin films in response to various electrochemical and chemical stimuli. Primarily, these results are presented as simultaneous electrochemical and surface stress measurements as a function of time or applied potential. The unifying theme throughout all of this work is that the intimate control of a surface by electrochemical means when paired with the unique sensitivity to the surface condition that is provided by surface stress monitoring can provide new insight into interfacial/surface phenomena. Specifically, this is shown through the surface stress results that provide not only bulk related parameters such as the sign and magnitude thin film residual stresses, but also yield valuable information such as real time stress evolution as it relates to the actual physical phenomena of electrodeposition processes. Although thin film stress evolution during electrodeposition is just one example of the type of work that has been carried out in support of this dissertation, it represents an important and interesting constraint for industrial applications such as metallization of integrated circuit interconnects.

In order to carry out the experiments outlined herein, a novel architecture that combined both the chemical inertness needed for electrochemical work with the technology of capacitive surface stress monitoring had to be designed. This was done through a trial and error process combined with extensive collaboration between several members of the group as well as the Ira A. Fulton Engineering

machine shop. The result is embodied in the multiple electrochemical surface stress cells (see Appendix A) that were used to collect all of the results presented in this dissertation.

The electrocapillarity of a Cu{111} thin film electrode in sulfuric acid electrolyte was explored in Chapter 8. It was found that a relatively simple, yet important relationship between applied potential and induced surface stress response was linear within a potential region that was not affected by oxidation of Cu electrode or hydrogen evolution. Following the characterization of the electrocapillarity (ecap) response in this system, observations of this phenomenon during electrodeposition of Cu were discussed. The most important conclusion drawn from this set of experiments was that the magnitude of the ecap response provided a negligible contribution to the overall surface stress evolution relative to the larger stresses observed during deposition/stripping and open circuit solution exchange experiments.

Significant surface stress evolution was observed during electrodeposition and oxidative stripping events and subsequent relaxations in a variety of solution combinations. In Chapters 9 & 10, six different solutions, ranging from additive free electrolytes to full (three) additive combinations, were used to approximate the range of prevailing conditions believed to exist during Cu damascene deposition. It was found that while the magnitude of the event stresses associated with the actual current pulse (positive or negative) increased with pulse length (i.e. deposit thickness), larger current densities produced reduced magnitudes of stress. Additionally, overall residual stress as well as the individual event and relaxation

stress phenomena was found to increase significantly with the use of plating additives. The complexity of the time dependent relaxation stresses following the current pulses also yielded insight into the dynamic relationship between the metal surface and the multiple ionic and molecular solution species. Furthermore, the surface stress evolution was found to be more or less independent of the identity of the supporting anion as surface stress experiments in perchlorate based solutions yielded results that were generally similar to those collected in the more common sulfate based solutions.

In Chapter 11, the influence of an appreciable cuprous ion (Cu^{+}) concentration in the plating bath was examined. It was found that by deaerating an otherwise identical solution of PEG/Cl^{-}, the magnitudes of both the event and relaxation surface stresses were reduced in response to the deposition and stripping current pulses. These results suggest that an equilibrium or near equilibrium concentration of cuprous ions has a significant effect on the deposition mechanism in suppressing solutions. This is a noteworthy result due to the fact that previous experimental and modeling efforts have been unable to identify the exact role of the cuprous ion. Conversely, for the case of SPS containing solutions, a similar effect on the resulting stress profiles is not observed. These results agree with previous observations on the local production and stability of cuprous species in suppressing and full additive solutions. Whereas cuprous species are produced at low current densities in accelerator containing solutions, they are not observed in the suppressing solutions. Thus, the external source of cuprous species in this work had a significant effect on the

events performed in the suppressing solutions but not on those performed in the accelerator containing electrolytes.

A variety of results collected during open circuit solution exchange experiments were discussed in Chapter 12. It was demonstrated that thin film electrodes are subject to stress inducing phenomena, even in the absence of net deposition or stripping. A modified version of the Chason adatom-grain boundary model was used as a possible explanation for the large stress changes (~8.5 N/m) observed in response to an increase of Cu^{++} concentration. Additionally, an empirical correlation between compressive surface stress and electrode exchange current density was established and subsequently used to predict the magnitude and sign of the stress change during the solution exchange experiments containing deposition suppressing additives.

The investigations presented in this dissertation demonstrate the importance and value that surface stress measurements can provide when combined with electrochemical techniques for the study of surfaces/interfaces. For example, solution exchange induced surface stress taken at the open circuit potential and the insight that it provides has not, to the author's knowledge, been previously studied. Considering the complexity of the copper/electrolyte systems studied in this work, combined with the numerous types of useful electrochemical techniques available, there are multiple research paths that could be pursued in the future of this work.

Fundamentally, a number of scientific aspects of the electrodeposition and oxidative stripping processes are still not well understood. One future research

direction could include a more in depth characterization of cuprous ion concentration and the role that it plays in the deposition/stripping process. To this end, several experiments that follow from the results above could be performed. Specifically, rotating ring-disk-electrode studies could be used to correlate actual Cu^{+} concentration of equilibrated or partially equilibrated solutions with corresponding surface stress results. Furthermore, chloride ions are known to stabilize the cuprous ion through the formation of complex species of the form $[CuCl_x]^{(1-x)}$. A careful exploration of the dependence of deposition/stripping event induced surface stresses as a function of chloride ion concentration could also yield interesting information on the role of Cu^{+}.

In a more practical approach, another future direction would include a more extensive exploration of the current-potential space used for the damascene plating process. As described above in the Chapter 3, a range of conditions must coexist on the non-planar electrodes (i.e. silicon wafer features) in order to create the nonuniform deposition rates necessary to achieve feature superfilling. In this dissertation, current densities of 1 & 5 mA/cm^2 were employed to study the deposition/stripping processes. However, because current densities inside the trenches are thought to be of order 50-100 mA/cm^2, investigations utilizing larger current densities would likely provide a better approximation of film stress generation in IC interconnects. Unfortunately, the magnitude of the current density in this type of experiment will be limited by quiescent nature of the solution as required for surface stress monitoring. Regardless, the above results demonstrate the robustness of this technique and it seems likely that much larger

current densities could easily be explored, especially for the short time scale events (≤4.5 seconds) presented in this work.

REFERENCES

1. U. Landau, in *Chemical Mechanical Planarization IV*, ed. R. L. Opila, The Electrochemical Society, Inc., 2001, pp. 231- 252.

2. T. Gupta, *Copper interconnect technology*, Springer, Dordrecht ; New York, 2009.

3. R. Rosenberg, D. C. Edelstein, C. K. Hu and K. P. Rodbell, *Annual Review of Materials Science*, 2000, **30**, 229-262.

4. G. Moore, *Electronics*, 1965, **38**, 1-4.

5. P. C. Andricacos, C. Uzoh, J. O. Dukovic, J. Horkans and H. Deligianni, *IBM Journal of Research and Development*, 1998, **42**, 567-574.

6. P. Andricacos, *Interface*, 1998, **7**, 2.

7. P. Andricacos, *Interface*, 1999, **8**, 32-37.

8. J. Reid, in *Handbook of Semiconductor Manufacturing Technology*, eds. R. Doering and Y. Nishi, CRC Press, 2007, pp. 16-11 - 16-47.

9. B. Rowe and D. Temple, *The Journal of Technology Transfer*, 2009, 1-13.

10. T. P. Moffat, D. Wheeler, M. D. Edelstein and D. Josell, *IBM Journal of Research and Development*, 2005, **49**, 19-36.

11. T. Moffat, D. Wheeler and D. Josell, *Interface*, 2004, **13**, 46-52.

12. J. P. Healy, D. Pletcher and M. Goodenough, *Journal of Electroanalytical Chemistry*, 1992, **338**, 167-177.

13. J. P. Healy, D. Pletcher and M. Goodenough, *Journal of Electroanalytical Chemistry*, 1992, **338**, 155-165.

14. J. P. Healy, D. Pletcher and M. Goodenough, *Journal of Electroanalytical Chemistry*, 1992, **338**, 179-187.

15. J. J. Kelly and A. C. West, *Journal of the Electrochemical Society*, 1998, **145**, 3472-3476.

16. J. J. Kelly and A. C. West, *Journal of the Electrochemical Society*, 1998, **145**, 3477-3481.

17. M. Yokoi, S. Konishi and T. Hayashi, *Denki Kagaku*, 1983, **51**, 310-316.

18. M. Yokoi, S. Konishi and T. Hayashi, *Denki Kagaku*, 1984, **52**, 218-223.

19. P. M. Vereecken, R. A. Binstead, H. Deligianni and P. C. Andricacos, *IBM Journal of Research and Development*, 2005, **49**, 3-18.

20. J. G. Long, P. C. Searson and P. M. Vereecken, *Journal of the Electrochemical Society*, 2006, **153**, C258-C264.

21. D. Josell, T. P. Moffat and D. Wheeler, *Journal of the Electrochemical Society*, 2007, **154**, D208-D214.

22. T. P. Moffat, D. Wheeler and D. Josell, *Journal of the Electrochemical Society*, 2004, **151**, C262-C271.

23. M. E. H. Garrido and M. D. Pritzker, *Journal of the Electrochemical Society*, 2009, **156**, D175-D183.

24. M. E. Huerta Garrido and M. D. Pritzker, *Journal of the Electrochemical Society*, 2009, **156**, D36-D44.

25. K. R. Hebert, *Journal of the Electrochemical Society*, 2005, **152**, C283-C287.

26. E. K. Yung, L. T. Romankiw and R. C. Alkire, *Journal of the Electrochemical Society*, 1989, **136**, 206-215.

27. I. Teerlinck, Ghent University, Ghent, Belgium, 2002.

28. J. Reid, S. Mayer, E. Broadbent, E. Klawuhn and A. Kaihan, *Solid State Technology*, 2000, **43**, 86-98.

29. A. C. West, *Journal of the Electrochemical Society*, 2000, **147**, 227-232.

30. M. Takenaka, T. Tachibe, S. Kozuka, M. Hayashi and H. Matsunaga, *Japanese Journal of Applied Physics Part 2-Letters*, 1996, **35**, L1628-L1630.

31. M. Quirk and J. Serda, *Semiconductor Manufacturing Technology*, Prentice Hall, 2001.

32. C. S. Yoo, *Semiconductor Manufacturing Technology*, World Scientific Publishing Company, Inc., 2008.

33. D. S. Stoychev, I. Vitanova, T. Vitanov and S. Rashkov, *Surface Technology*, 1980, **10**, 209-217.

34. C. H. Proctor, in *Metal industry*, Metal Industry Pub. Co., 1913, p. 84.

35. K. Buchanan, in *GaAs MANTECH Conference*, GaAS MANTECH, Inc., St. Louis, 2002, pp. 7-9.

36. K. Wetzig and C. Schneider, *Metal Based Thin Films for Electronics*, Wiley-VCH, 2006.

37. M. J. Hampdensmith and T. T. Kodas, *Mrs Bulletin*, 1993, **18**, 39-45.

38. A. Pratt, Advanced Energy, http://www.google.com/url?sa=t&source=web&cd=1&ved=0CBkQFjAA&url=http%3A%2F%2Fwww.advanced-energy.com%2Fupload%2FFile%2FWhite_Papers%2FSL-ELECTROPLATING-270-01.pdf&rct=j&q=advanced%20energy%20overview%20of%20the%20use

%20of%20Copper%20interconnects&ei=cLX2TcS6CoeWsgPg1q3TBw&usg=AFQjCNE751whR6eaLu-0ix7abz98xdwzUA&cad=rja, 2004, p. 20.

39. M. Paunovic, M. Schlesinger and Electrochemical Society., *Fundamentals of electrochemical deposition*, Wiley, New York, 1998.

40. A. J. Bard and L. R. Faulkner, *Electrochemical methods : fundamentals and applications*, John Wiley, New York ; Chichester England, 2001.

41. C. H. Hamann, A. Hamnett and W. Vielstich, *Electrochemistry*, Wiley-VCH, Weinheim ; New York, 1998.

42. R. Tenno and A. Pohjoranta, *International Journal of Control*, 2009, **82**, 883-893.

43. J. Vazquez-Arenas, G. Vazquez, A. M. Melendez and I. Gonzalez, *Journal of the Electrochemical Society*, 2007, **154**, D473-D481.

44. J. Vazquez-Arenas, *Electrochimica Acta*, 2010, **55**, 3550-3559.

45. D. P. Barkey, F. Oberholtzer and Q. Wu, *Journal of the Electrochemical Society*, 1998, **145**, 590-595.

46. U. Bertocci and D. R. Turner, in *Encyclopedia of Electrochemistry of the Elements **II***, ed. A. Bard, Dekker, New York, 1974, p. 383.

47. D. P. Barkey, D. Watt, Z. Liu and S. Raber, *Journal of the Electrochemical Society*, 1994, **141**, 1206-1212.

48. D. Barkey, F. Oberholtzer and Q. Wu, *Physical Review Letters*, 1995, **75**, 2980-2983.

49. V. Fleury and D. Barkey, *Physica A*, 1996, **233**, 730-741.

50. V. Fleury and D. Barkey, *Europhysics Letters*, 1996, **36**, 253-258.

51. F. Oberholtzer, D. Barkey and Q. Wu, *Physical Review E*, 1998, **57**, 6955-6961.

52. F. A. Lowenheim, *Modern electroplating*, Wiley, New York,, 1974.

53. O. Kardos and D. G. Foulke, in *Advances in Electrochemistry and Electrochemical Engineering*, ed. C. W. Tobais, Interscience, New York, NY, 1962, pp. 145-233.

54. D. G. Foulke and O. Kardos, *Technical Proceedings of the Annual Convention of the American Electroplaters Society*, 1956, **43**, 172-180.

55. J. S. Newman and K. E. Thomas-Alyea, *Electrochemical systems*, J. Wiley, Hoboken, N.J., 2004.

56. C. Wagner, *Journal of the Electrochemical Society*, 1951, **98**, 116-128.

57. R. Akolkar and U. Landau, *Journal of the Electrochemical Society*, 2004, **151**, C702-C711.

58. S. Ahmed, T. T. Ahmed, M. O'Grady, S. Nakahara and D. N. Buckley, *Journal of Applied Physics*, 2008, **103**.

59. Y. Cao, P. Taephaisitphongse, R. Chalupa and A. C. West, *Journal of the Electrochemical Society*, 2001, **148**, C466-C472.

60. D. Josell, D. Wheeler and T. P. Moffat, *Electrochemical and Solid State Letters*, 2002, **5**, C49-C52.

61. M. Kang and A. A. Gewirth, *Journal of the Electrochemical Society*, 2003, **150**, C426-C434.

62. T. P. Moffat, D. Wheeler, W. H. Huber and D. Josell, *Electrochemical and Solid State Letters*, 2001, **4**, C26-C29.

63. T. P. Moffat, J. E. Bonevich, W. H. Huber, A. Stanishevsky, D. R. Kelly, G. R. Stafford and D. Josell, *Journal of the Electrochemical Society*, 2000, **147**, 4524-4535.

64. M. L. Walker, L. J. Richter and T. P. Moffat, *Journal of the Electrochemical Society*, 2005, **152**, C403-C407.

65. O. M. Magnussen, *Chemical Reviews*, 2002, **102**, 679-725.

66. P. Broekmann, M. Wilms, M. Kruft, C. Stuhlmann and K. Wandelt, *Journal of Electroanalytical Chemistry*, 1999, **467**, 307-324.

67. D. Pham, H. Keller, S. Breuer, S. Huemann, N. T. N. Hai, C. Zoerlein, K. Wandelt and P. Broekmann, *Chimia*, 2009, **63**, 115-121.

68. S. E. Bae and A. A. Gewirth, *Langmuir*, 2006, **22**, 10315-10321.

69. T. P. Moffat and L. Y. O. Yang, *Journal of the Electrochemical Society*, 2010, **157**, D228-D241.

70. T. P. Moffat and D. Josell, *Israel Journal of Chemistry*, 2010, **50**, 312-320.

71. Wikipedia, 3-Mercapto-1-propanesulfonic acid, ***http://en.wikipedia.org/wiki/3-Mercapto-1-propanesulfonic_acid***.

72. T. P. Moffat, D. Wheeler, S. K. Kim and D. Josell, *Journal of the Electrochemical Society*, 2006, **153**, C127-C132.

73. J. J. Kelly, C. Y. Tian and A. C. West, *Journal of the Electrochemical Society*, 1999, **146**, 2540-2545.

74. M. Georgiadou, D. Veyret, R. L. Sani and R. C. Alkire, *Journal of the Electrochemical Society*, 2001, **148**, C54-C58.

75. M. Hayase, M. Taketani, K. Aizawa, T. Hatsuzawa and K. Hayabusa, *Electrochemical and Solid State Letters*, 2002, **5**, C98-C101.

76. T. P. Moffat, D. Wheeler, S. K. Kim and D. Josell, *Electrochimica Acta*, 2007, **53**, 145-154.

77. S. K. Kim, D. Josell and T. P. Moffat, *Journal of the Electrochemical Society*, 2006, **153**, C616-C622.

78. G. B. McFadden, S. R. Coriell, T. P. Moffat, D. Josell, D. Wheeler, W. Schwarzacher and J. Mallett, *Journal of the Electrochemical Society*, 2003, **150**, C591-C599.

79. T. P. Moffat, D. Wheeler, C. Witt and D. Josell, *Electrochemical and Solid State Letters*, 2002, **5**, C110-C112.

80. D. Josell, D. Wheeler, W. H. Huber, J. E. Bonevich and T. P. Moffat, *Journal of the Electrochemical Society*, 2001, **148**, C767-C773.

81. S. A. Watson and J. Edwards, *Transactions of the Institute of Metal Finishing*, 1957, **34**, 167-198.

82. K. G. Jordan and C. W. Tobias, *Journal of the Electrochemical Society*, 1991, **138**, 1251-1259.

83. C. Madore and D. Landolt, *Journal of the Electrochemical Society*, 1996, **143**, 3936-3943.

84. C. Madore, M. Matlosz and D. Landolt, *Journal of the Electrochemical Society*, 1996, **143**, 3927-3936.

85. C. C. Cheng and A. C. West, *Journal of the Electrochemical Society*, 1997, **144**, 3050-3056.

86. S. S. Kruglikov, N. T. Kudriavtsev, G. F. Vorobiova and A. Y. Antonov, *Electrochimica Acta*, 1965, **10**, 253-261.

87. J. J. Kelly and A. C. West, *Electrochemical and Solid State Letters*, 1999, **2**, 561-563.

88. J. O. Dukovic and C. W. Tobias, *Journal of the Electrochemical Society*, 1990, **137**, 3748-3755.

89. B. C. Baker, M. Freeman, B. Melnick, D. Wheeler, D. Josell and T. P. Moffat, *Journal of the Electrochemical Society*, 2003, **150**, C61-C66.

90. B. C. Baker, C. Witt, D. Wheeler, D. Josell and T. P. Moffat, *Electrochemical and Solid State Letters*, 2003, **6**, C67-C69.

91. D. Josell, S. Kim, D. Wheeler, T. P. Moffat and S. G. Pyo, *Journal of the Electrochemical Society*, 2003, **150**, C368-C373.

92. S. G. Pyo, S. Kim, D. Wheeler, T. P. Moffat and D. Josell, *Journal of Applied Physics*, 2003, **93**, 1257-1261.

93. D. Wheeler, T. P. Moffat, G. B. McFadden, S. Coriell and D. Josell, *Journal of the Electrochemical Society*, 2004, **151**, C538-C544.

94. D. Wheeler, D. Josell and T. P. Moffat, *Journal of the Electrochemical Society*, 2003, **150**, C302-C310.

95. S. Stølen and T. Grande, *Chemical thermodynamics of materials : macroscopic and microscopic aspects*, John Wiley, Chichester, West Sussex, England ; Hoboken, NJ, 2004.

96. G. W. Castellan, *Physical chemistry*, Addison-Wesley, Reading, Mass., 1983.

97. D. C. Grahame, *Chemical Reviews*, 1947, **41**, 441-501.

98. T. Heaton and C. Friesen, *Journal of Physical Chemistry C*, 2007, **111**, 14433-14439.

99. H. Helmholtz, *Annalen der Physik*, 1879, **243**, 337-382.

100. H. Helmholtz, *Annalen der Physik*, 1853, **165**, 211-233.

101. D. L. Chapman, *Philosophical Magazine*, 1913.

102. G. Gouy, *J. Phys Radium*, 1910.

103. G. Gouy, *Compt. Rend.*, 1910.

104. D. M. Kolb, *Progress in Surface Science*, 1996, **51**, 109-173.

105. O. Stern, *Zeitschrift Fur Elektrochemie Und Angewandte Physikalische Chemie*, 1924, **30**, 508-516.

106. S. Trasatti and R. Parsons, *Pure and Applied Chemistry*, 1986, **58**, 437-454.

107. J. O. Bockris, M. A. V. Devanathan and K. Muller, *Proceedings of the Royal Society of London Series a-Mathematical and Physical Sciences*, 1963, **274**, 55-+.

108. C. Friesen, N. Dimitrov, R. C. Cammarata and K. Sieradzki, *Langmuir*, 2001, **17**, 807-815.

109. J. W. Gibbs, *The Scientific Papers of Josiah Williard Gibbs*, Longmans-Green, London, 1906.

110. R. Shuttleworth, *Proceedings of the Physical Society of London Section A*, 1950, **63**, 444-457.

111. P. R. Couchman and C. R. Davidson, *Journal of Electroanalytical Chemistry*, 1977, **85**, 407-409.

112. N. Vasiljevic, T. Trimble, N. Dimitrov and K. Sieradzki, *Langmuir*, 2004, **20**, 6639-6643.

113. L. B. Freund and S. Suresh, *Thin film materials : stress, defect formation, and surface evolution*, Cambridge University Press, Cambridge, UK ; New York, 2003.

114. G. G. Stoney, *Proceedings of the Royal Society of London Series a-Containing Papers of a Mathematical and Physical Character*, 1909, **82**, 172-175.

115. C. A. Friesen, Massachusetts Institute of Technology, 2004, p. 2 v. (272 leaves).

116. E. Engstrom, T. Heaton and C. Friesen, Arizona State University, Tempe.

117. L. Mickelson, in *Ira A Fulton School of Engineering*, Arizona State University, Tempe, 2011.

118. T. Trimble, L. Tang, N. Vasiljevic, N. Dimitrov, M. van Schilfgaarde, C. Friesen, C. V. Thompson, S. C. Seel, J. A. Floro and K. Sieradzki, *Physical Review Letters*, 2005, **95**.

119. C. Friesen, S. C. Seel and C. V. Thompson, *Journal of Applied Physics*, 2004, **95**, 1011-1020.

120. C. Friesen and C. V. Thompson, *Physical Review Letters*, 2002, **89**.

121. M. F. Doerner and W. D. Nix, *Crc Critical Reviews in Solid State and Materials Sciences*, 1988, **14**, 225-268.

122. K. Dahmen, S. Lehwald and H. Ibach, *Surface Science*, 2000, **446**, 161-173.

123. M. Finot and S. Suresh, *Journal of the Mechanics and Physics of Solids*, 1996, **44**, 683-721.

124. E. Bauer, *Zeitschrift fur Kristallographie*, 1958, **110**, 372-394.

125. J. Venables, *Introduction to surface and thin film processes*, Cambridge University Press, Cambridge ; New York, 2000.

126. C. V. Thompson, *Annual Review of Materials Science*, 2000, **30**, 159-190.

127. C. Friesen and C. V. Thompson, *Physical Review Letters*, 2004, **93**.

128. S. C. Seel, C. V. Thompson, S. J. Hearne and J. A. Floro, *Journal of Applied Physics*, 2000, **88**, 7079-7088.

129. J. A. Floro, S. J. Hearne, J. A. Hunter, P. Kotula, E. Chason, S. C. Seel and C. V. Thompson, *Journal of Applied Physics*, 2001, **89**, 4886-4897.

130. R. Abermann and R. Koch, *Thin Solid Films*, 1985, **129**, 71-78.

131. J. K. Kennedy and C. Friesen, *Journal of Applied Physics*, 2007, **101**, 4.

132. L. B. Freund and E. Chason, *Journal of Applied Physics*, 2001, **89**, 4866-4873.

133. E. Chason, B. W. Sheldon, L. B. Freund, J. A. Floro and S. J. Hearne, *Physical Review Letters*, 2002, **88**.

134. P. R. Guduru, E. Chason and L. B. Freund, *Journal of the Mechanics and Physics of Solids*, 2003, **51**, 2127-2148.

135. R. C. Cammarata and K. Sieradzki, *Applied Physics Letters*, 1989, **55**, 1197-1198.

136. R. C. Cammarata, *Surface Science*, 1992, **279**, 341-348.

137. R. C. Cammarata, *Surface Science*, 1992, **273**, L399-L402.

138. R. C. Cammarata, *Progress in Surface Science*, 1994, **46**, 1-38.

139. R. C. Cammarata and K. Sieradzki, *Annual Review of Materials Science*, 1994, **24**, 215-234.

140. R. C. Cammarata, J. C. Bilello, A. L. Greer, K. Sieradzki and S. M. Yalisove, *Mrs Bulletin*, 1999, **24**, 34-38.

141. R. C. Cammarata, T. M. Trimble and D. J. Srolovitz, *Journal of Materials Research*, 2000, **15**, 2468-2474.

142. R. C. Cammarata and K. Sieradzki, *Journal of Applied Mechanics-Transactions of the Asme*, 2002, **69**, 415-418.

143. J. A. Floro, E. Chason, R. C. Cammarata and D. J. Srolovitz, *Mrs Bulletin*, 2002, **27**, 19-25.

144. E. Chason and B. W. Sheldon, *Surface Engineering*, 2003, **19**, 387-391.

145. J. S. Tello, A. F. Bower, E. Chason and B. W. Sheldon, *Physical Review Letters*, 2007, **98**, 4.

146. A. Bhandari, B. W. Sheldon and S. J. Hearne, *Journal of Applied Physics*, 2007, **101**.

147. R. Koch, D. Winau and K. H. Rieder, *Physica Scripta*, 1993, **T49B**, 539-543.

148. R. Koch, *Journal of Physics-Condensed Matter*, 1994, **6**, 9519-9550.

149. R. Koch, *Applied Physics a-Materials Science & Processing*, 1999, **69**, 529-536.

150. R. Koch, D. Z. Hu and A. K. Das, *Physical Review Letters*, 2005, **94**, 4.

151. R. W. Hoffman, *Surface and Interface Analysis*, 1981, **3**, 62-66.

152. J. A. Thornton and D. W. Hoffman, *Thin Solid Films*, 1989, **171**, 5-31.

153. W. Haiss, R. J. Nichols and J. K. Sass, *Surface Science*, 1997, **388**, 141-149.

154. G. R. Stafford, C. Beauchamp and O. Kongstein, *ECS Transactions*, 2007, **2**, 185-196.

155. O. E. Kongstein, U. Bertocci and G. R. Stafford, *Journal of the Electrochemical Society*, 2005, **152**, C116-C123.

156. R. Koch, H. Leonhard, G. Thurner and R. Abermann, *Review of Scientific Instruments*, 1990, **61**, 3859-3862.

157. J. A. Floro, E. Chason, S. R. Lee, R. D. Twesten, R. Q. Hwang and L. B. Freund, *Journal of Electronic Materials*, 1997, **26**, 969-979.

158. R. W. Hoffman, *Thin Solid Films*, 1976, **34**, 185-190.

159. W. D. Nix and B. M. Clemens, *Journal of Materials Research*, 1999, **14**, 3467-3473.

160. C. W. Pao, S. M. Foiles, E. B. Webb, D. J. Srolovitz and J. A. Floro, *Physical Review Letters*, 2007, **99**, 4.

161. A. L. Shull and F. Spaepen, *Journal of Applied Physics*, 1996, **80**, 6243-6256.

162. E. Chason, B. W. Sheldon, L. B. Freund, J. A. Floro and S. J. Hearne, *Physical Review Letters*, 2002, **88**, 4.

163. F. Spaepen, *Acta Materialia*, 2000, **48**, 31-42.

164. R. Koch, *Surface & Coatings Technology*, 2010, **204**, 1973-1982.

165. J. W. Shin and E. Chason, *Physical Review Letters*, 2009, **103**, 4.

166. J. Leib, R. Monig and C. V. Thompson, *Physical Review Letters*, 2009, **102**, 4.

167. A. L. Del Vecchio and F. Spaepen, *Journal of Applied Physics*, 2007, **101**, 9.

168. D. Chocyk, A. Proszynski, G. Gladyszewski, T. Pienkos and L. Gladyszewski, *Optica Applicata*, 2005, **35**, 419-424.

169. K. H. Lau and W. Kohn, *Surface Science*, 1977, **65**, 607-618.

170. L. H. He, *Journal of the Mechanics and Physics of Solids*, 2008, **56**, 2957-2971.

171. Chaudhar.P, *Journal of Vacuum Science & Technology*, 1972, **9**, 520-&.

172. D. Xu, V. Sriram, V. Ozolins, J. M. Yang, K. N. Tu, G. R. Stafford and C. Beauchamp, *Journal of Applied Physics*, 2009, **105**.

173. L. Lu, Y. F. Shen, X. H. Chen, L. H. Qian and K. Lu, *Science*, 2004, **304**, 422-426.

174. D. Xu, W. L. Kwan, K. Chen, X. Zhang, V. Ozolins and K. N. Tu, *Applied Physics Letters*, 2007, **91**, 3.

175. M. Stangl, V. Dittel, J. Acker, V. Hoffmann, W. Gruner, S. Strehle and K. Wetzig, *Applied Surface Science*, 2005, **252**, 158-161.

176. M. Stangl, M. Liptak, J. Acker, V. Hoffmann, S. Baunack and K. Wetzig, *Thin Solid Films*, 2009, **517**, 2687-2690.

177. M. Popereka, *Internal Stresses in Electrolytically Deposited Metals*, Indian National Scientific Documentation Centre, New Delhi, Washington D.C., 1970.

178. L. Mickelson, T. Heaton and C. Friesen, *Journal of Physical Chemistry C*, 2008, **112**, 1060-1063.

179. J.-M. Paik and Y.-C. Joo, in *STRESS-INDUCED PHENOMENA IN METALLIZATION: Seventh International Workshop on Stress-Induced Phenomena in Metallization*, 2004, pp. 27-38.

180. R. Huang, W. Robl, T. Detzel and H. Ceric, in *2010 IEEE International Reliability Physics Symposium (IRPS)*, Anaheim, Ca, 2010, pp. 911-917.

181. R. Huang, W. Robl, H. Ceric, T. Detzel and G. Dehm, *IEEE Transactions on Device and Materials Reliability*, 2010, **10**, 47-54.

182. J. Neuner, I. Zienert, A. Peeva, A. Preusse, P. Kucher and J. W. Bartha, *Microelectronic Engineering*, 2010, **87**, 254-257.

183. M. Stangl, M. Liptak, A. Fletcher, J. Acker, J. Thomas, H. Wendrock, S. Oswald and K. Wetzig, *Microelectronic Engineering*, 2008, **85**, 534-541.

184. K. Shimizu, N. Kasahara, H. Habazaki, P. Skeldon and G. E. Thompson, *Surface and Interface Analysis*, 2003, **35**, 611-617.

185. G. Wanga, D. Gana, S. Groothuisb and P. Hoa, in *Electronic Components and Technology Conference*, IEEE, 2006, pp. 344-349.

186. J. Dunders, *Journal of Applied Mechanics* 1969, **36** 650-652.

187. C. J. Wilson, A. B. Horsfall, A. G. O'Neill, N. G. Wright, S. J. Bull, J. G. Terry, J. T. M. Stevenson and A. J. Walton, *IEEE Transactions on Device and Materials Reliability*, 2007, **7**, 356-362.

188. K. N. Tu, *Journal of Applied Physics*, 2003, **94**, 5451-5473.

189. I. A. Blech, *Journal of Applied Physics*, 1976, **47**, 1203-1208.

190. I. A. Blech and C. Herring, *Applied Physics Letters*, 1976, **29**, 131-133.

191. J. Cho and C. V. Thompson, *Applied Physics Letters*, 1989, **54**, 2577-2579.

192. J. J. Clement and C. V. Thompson, *Journal of Applied Physics*, 1995, **78**, 900-904.

193. C. S. Hau-Riege and C. V. Thompson, *Applied Physics Letters*, 2001, **78**, 3451-3453.

194. M. A. Korhonen, P. Borgesen, K. N. Tu and C. Y. Li, *Journal of Applied Physics*, 1993, **73**, 3790-3799.

195. C. V. Thompson and J. R. Lloyd, *Mrs Bulletin*, 1993, **18**, 19-25.

196. G. B. Alers, J. Sukamto, P. Woytowitz, X. Lu, S. Kailasam and J. Reid, in *International Reliability Physics Symposium*, 2005, pp. 36-40.

197. L. L. Mickelson and C. Friesen, *Journal of the American Chemical Society*, 2009, **131**, 14879-14884.

198. H. Ibach, *Electrochimica Acta*, 1999, **45**, 575-581.

199. H. Ibach, *Journal of Vacuum Science & Technology a-Vacuum Surfaces and Films*, 1994, **12**, 2240-2243.

200. W. Haiss, *Reports on Progress in Physics*, 2001, **64**, 591-648.

201. W. Haiss and J. K. Sass, *Langmuir*, 1996, **12**, 4311-4313.

202. T. A. Brunt, T. Rayment, S. J. Oshea and M. E. Welland, *Langmuir*, 1996, **12**, 5942-5946.

203. J. W. Shin, U. Bertocci and G. R. Stafford, *Journal of Physical Chemistry C*, 2010, **114**, 7926-7932.

204. G. G. Lang, N. S. Sas and S. Vesztergom, *Chemical and Biochemical Engineering Quarterly*, 2009, **23**, 1-9.

205. J. M. Gere and S. Timoshenko, *Mechanics of materials*, PWS Pub Co., Boston, 1997.

206. H. Ibach, C. E. Bach, M. Giesen and A. Grossmann, *Surface Science*, 1997, **375**, 107-119.

207. T. K. Bhandakkar, E. Chason and H. J. Gao, *Philosophical Magazine*, 2010, **90**, 3037-3048.

208. M. L. Walker, L. J. Richter and T. P. Moffat, *Journal of the Electrochemical Society*, 2006, **153**, C557-C561.

209. S. J. Hearne and J. A. Floro, *Journal of Applied Physics*, 2005, **97**, 6.

210. K. R. Hebert, *Journal of the Electrochemical Society*, 2001, **148**, C726-C732.

211. M. Stangl, J. Acker, V. Dittel, W. Gruner, V. Hoffmann and K. Wetzig, *Microelectronic Engineering*, 2005, **82**, 189-195.

212. C. E. Housecroft and A. G. Sharpe, *Inorganic chemistry*, Harlow England ; New York Prentice Hall,, 2001.

213. J. K. Kennedy, T. Trimble and C. Friesen, Arizona State University, 2008.

214. C. M. Koeritz, in *School of Materials*, Arizona State University, Tempe, Arizona, 2007, p. 101.

215. K. J. Vetter, *Electrochemical kinetics : theoretical and experimental aspects*, Academic Press, New York, 1967.

216. W. D. Callister, *Materials science and engineering : an introduction*, Wiley, New York, 2000.

APPENDIX A

SKETCHES & COMPUTER AIDED DESIGNS OF THE ELECTROCHEMICAL SURFACE STRESS MEASUREMENT CELL

The following section is presented in two parts. The first part consists of four pages of hand drawn sketches that were submitted to the Ira A. Fulton School of Engineering Mechanical Machine Shop. The second part of this appendix contains the five CAD drawings that were then produced by the machine shop and used to fabricate the one of the most recent versions (#5) of the electrochemical surface stress monitor. These two sections represent the process of design, refinement, and fabrication that was one of the essential pieces of my education as a graduate student. The initial cell design was a collaboration of ideas and discussions between Jordan Kennedy, Dr. Friesen and I. The actual fabrication of all six of the individual cells was carried out by the excellent machinists in the Engineering Machine Shop, including Fred Sierra, Dave Gillespie, Marty Johnson and Forest (Ben) Schwatken. It was the multiple versions of this novel electrochemical surface stress cell design that have enabled myself and other group members to carry out studies ranging from Pt and Au electrocapillarity to Cu damascene studies to Zn electrodeposition from ionic liquids and Li-ion battery cathode studies. These projects have resulted in multiple academic publications and will comprise a part or all of at least 3 separate PhD dissertations (those belonging to Larry Mickelson, Erika Engstrom, and Thomas Heaton).

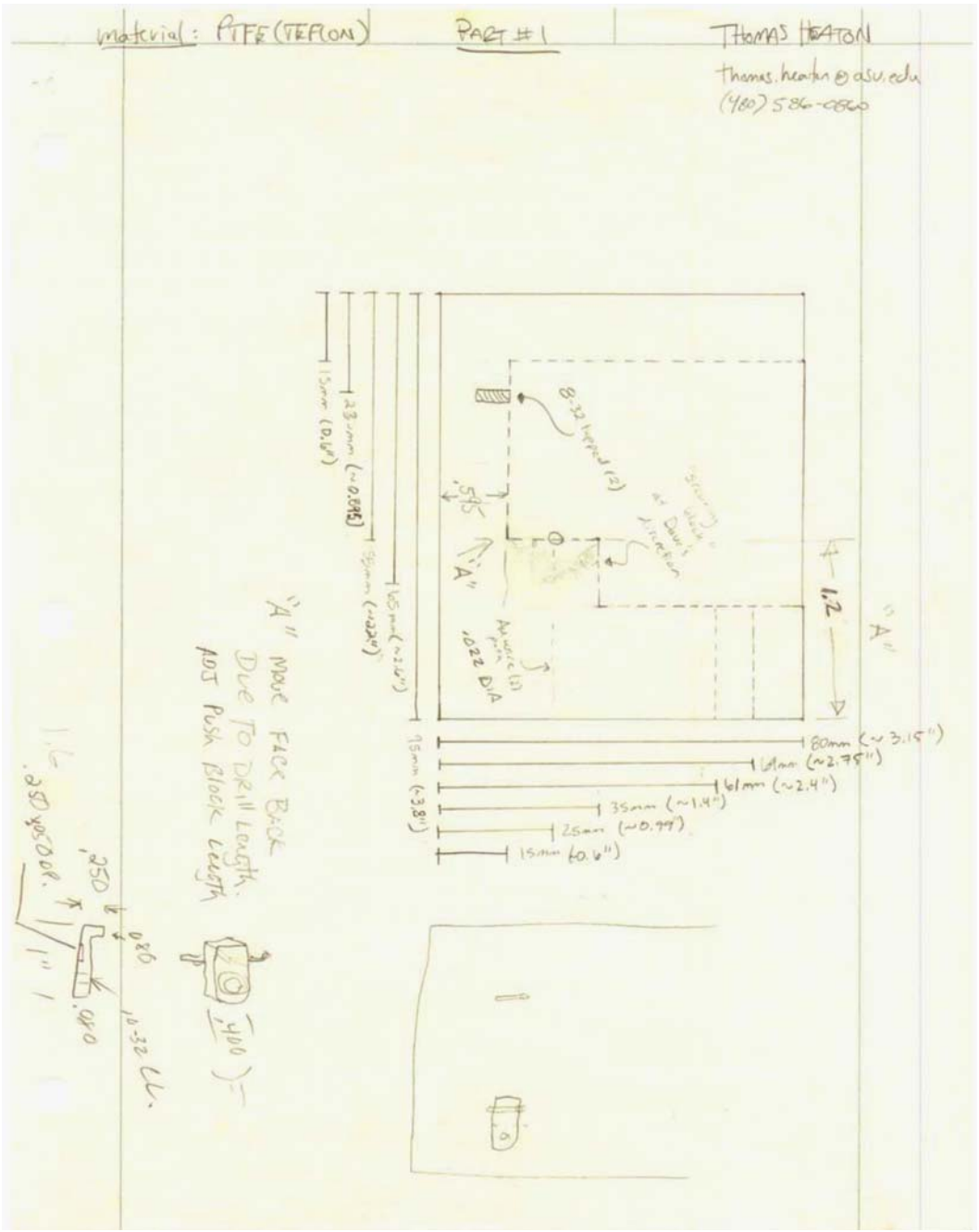
Material: PTFE (TEFLON)
PART #1
THOMAS HEATON
thomas.heaton@asu.edu
(480) 586-0860
8-32 tapped (2)
.595
"A"
.1022 DIA
1.2
"A"
80mm (~3.15")
69mm (~2.75")
61mm (~2.4")
35mm (~1.4")
25mm (~0.99")
15mm (0.6")
95mm (~3.8")
"A" MUST FACE BACK
DUE TO DRILL LENGTH.
ADJ PUSH BLOCK LENGTH
.250
.080
.490
10-32 CL.

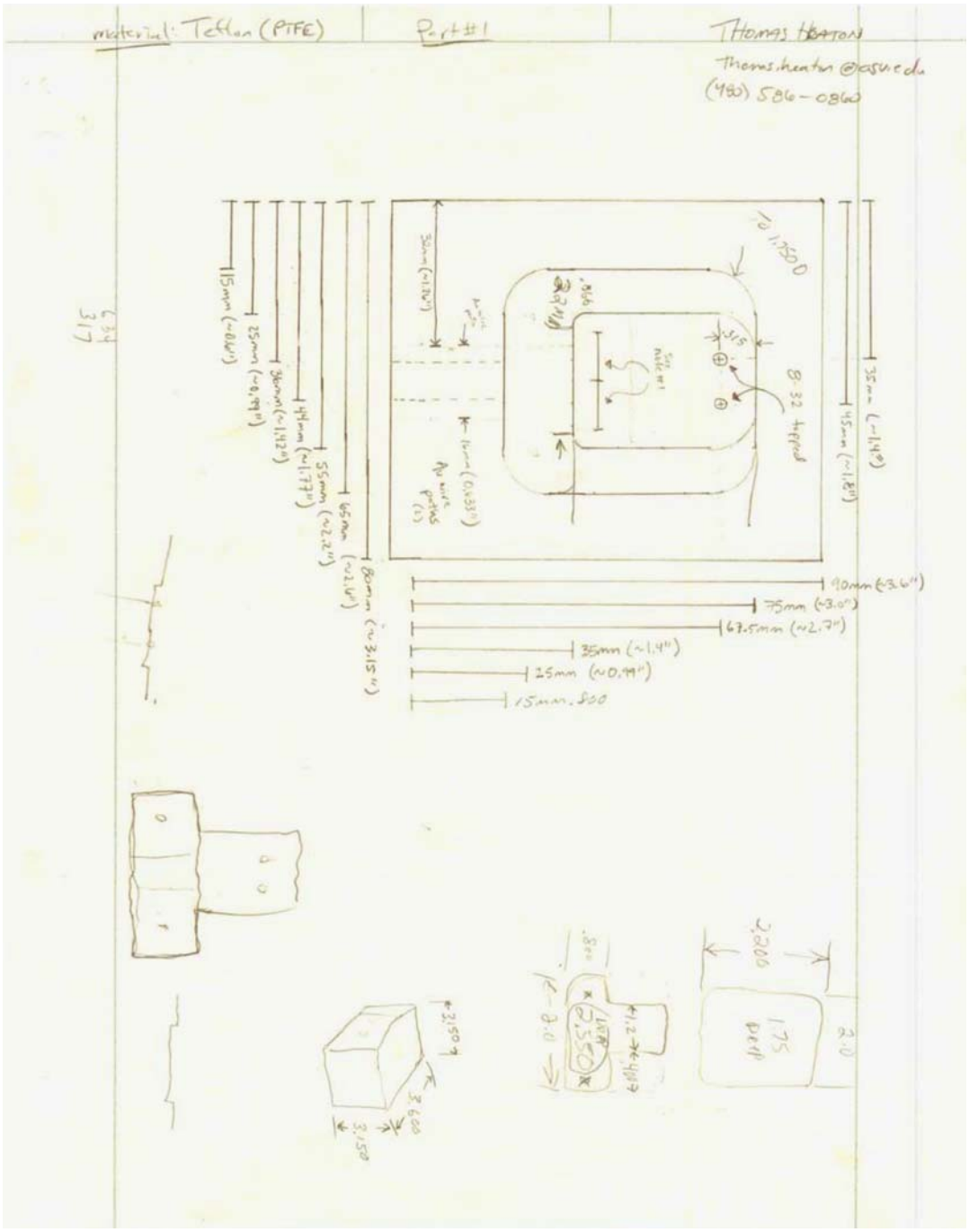
material: Teflon (PTFE)
Part #1
Thomas Heaton
Thomas.heaton@asu.edu
(480) 586-0860
8-32 thread
90mm (~3.6")
75mm (~3.0")
67.5mm (~2.7")
35mm (~1.4")
25mm (~0.99")
15mm (~0.6")
95mm (~3.75")
85mm (~3.35")
55mm (~2.2")
45mm (~1.8")
35mm (~1.4")
25mm (~0.99")
15mm (~0.6")

Material: PTFE (TEFLON) | Part #1

THOMAS HEATON
thomas.heaton@asu.edu
(480) 586-0860

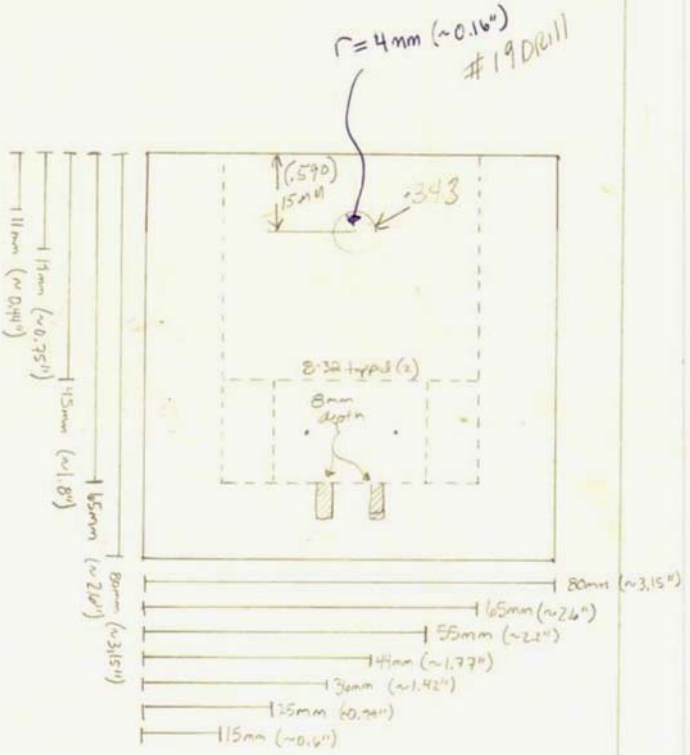

material : PTFE (TEFLON)

part #2

THOMAS HEATON
Thomas.heaton@asu.edu

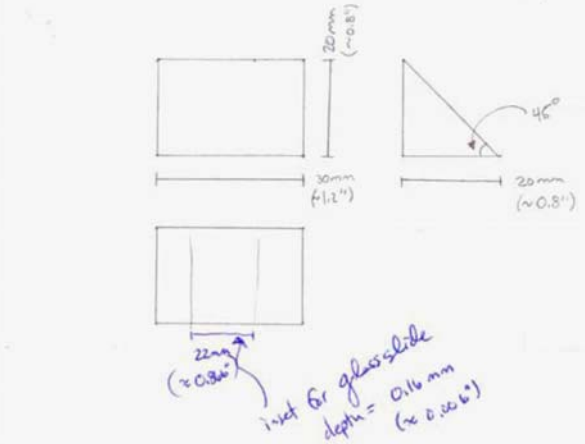

material: PTFE (TEFLON)

part #3

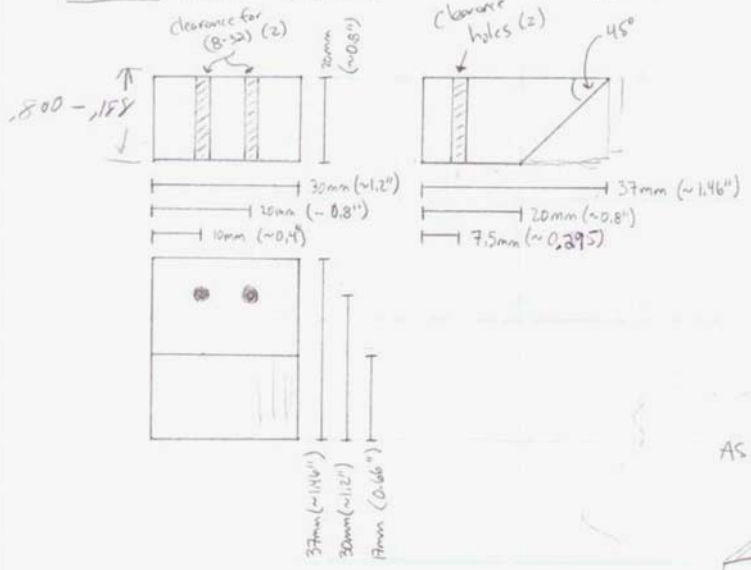

note! These two pieces meet at the 45° angle face (of each one). Then the two fit into the larger apparatus. The clearance holes must line up horizontally with the tapped holes in the larger apparatus. (part #1)

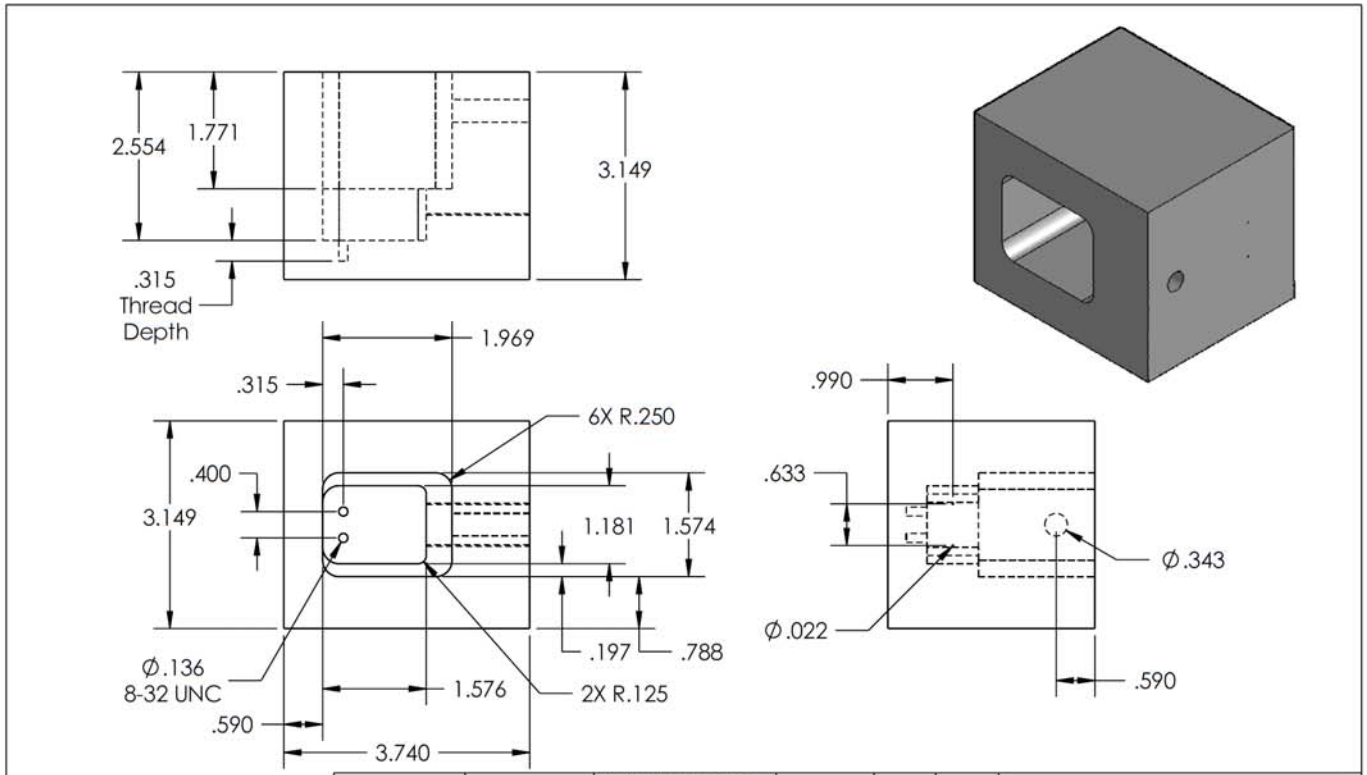

		UNLESS OTHERWISE SPECIFIED:		NAME	DATE
		DIMENSIONS ARE IN INCHES TOLERANCES: FRACTIONAL ± ANGULAR: MACH ± BEND ± TWO PLACE DECIMAL ± THREE PLACE DECIMAL ±	DRAWN		
			CHECKED		
			ENG APPR.		
			MFG APPR.		
		INTERPRET GEOMETRIC TOLERANCING PER:	Q.A.		
		MATERIAL	COMMENTS:		
NEXT ASSY	USED ON	FINISH			
APPLICATION		DO NOT SCALE DRAWING			

PROPRIETARY AND CONFIDENTIAL

THE INFORMATION CONTAINED IN THIS DRAWING IS THE SOLE PROPERTY OF **ASU**. ANY REPRODUCTION IN PART OR AS A WHOLE WITHOUT THE WRITTEN PERMISSION OF **ASU** IS PROHIBITED.

ASU Ira A. Fulton Schools of Engineering
ARIZONA STATE UNIVERSITY

TITLE:

Part1

SIZE	DWG. NO.	REV
A		
SCALE: 1:2	WEIGHT:	SHEET 1 OF 1

5 4 3 2 1

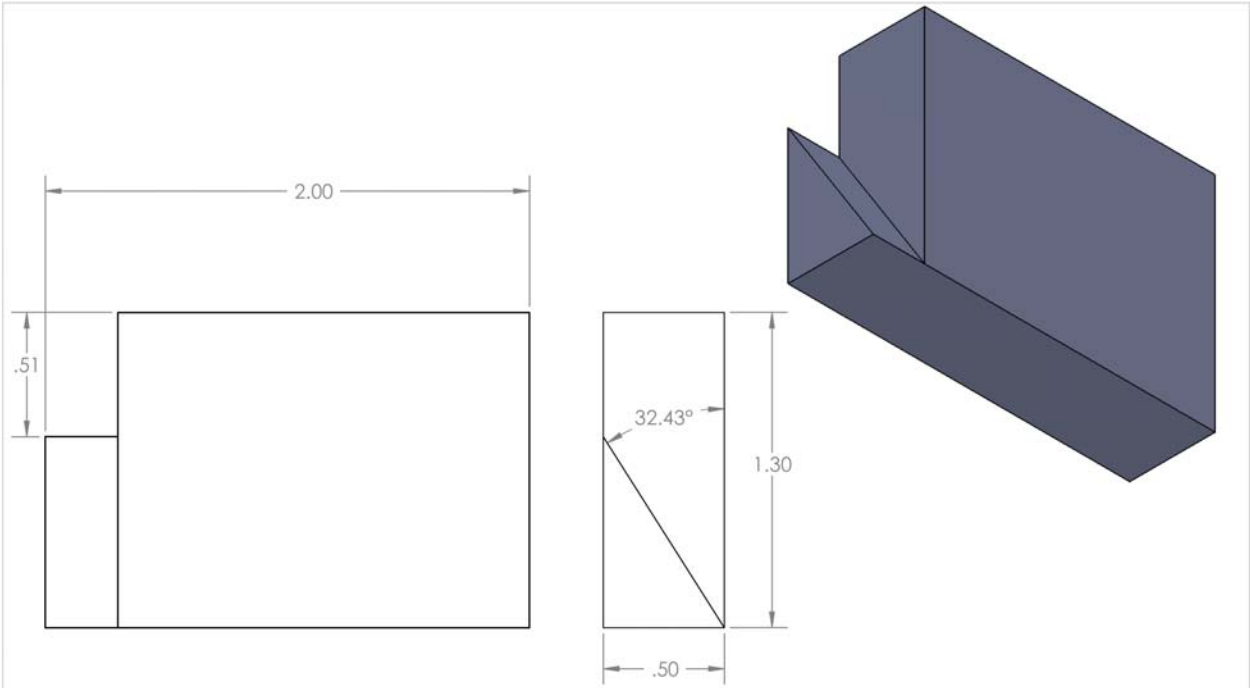

		UNLESS OTHERWISE SPECIFIED:		NAME	DATE
		DIMENSIONS ARE IN INCHES TOLERANCES: FRACTIONAL ± ANGULAR: MACH ± BEND ± TWO PLACE DECIMAL ± THREE PLACE DECIMAL ±	DRAWN	M JOHNSON	3-1-2010
			CHECKED		
			ENG APPR.		
			MFG APPR.		
		INTERPRET GEOMETRIC TOLERANCING PER:	Q.A.		
		MATERIAL	COMMENTS:		
NEXT ASSY	USED ON	FINISH			
APPLICATION		DO NOT SCALE DRAWING			

ASU Ira A. Fulton Schools of Engineering
ARIZONA STATE UNIVERSITY

TITLE:

Maytag_Part_4

SIZE	DWG. NO.	REV
A		
SCALE: 2:1	WEIGHT:	SHEET 1 OF 1

5 4 3 2 1

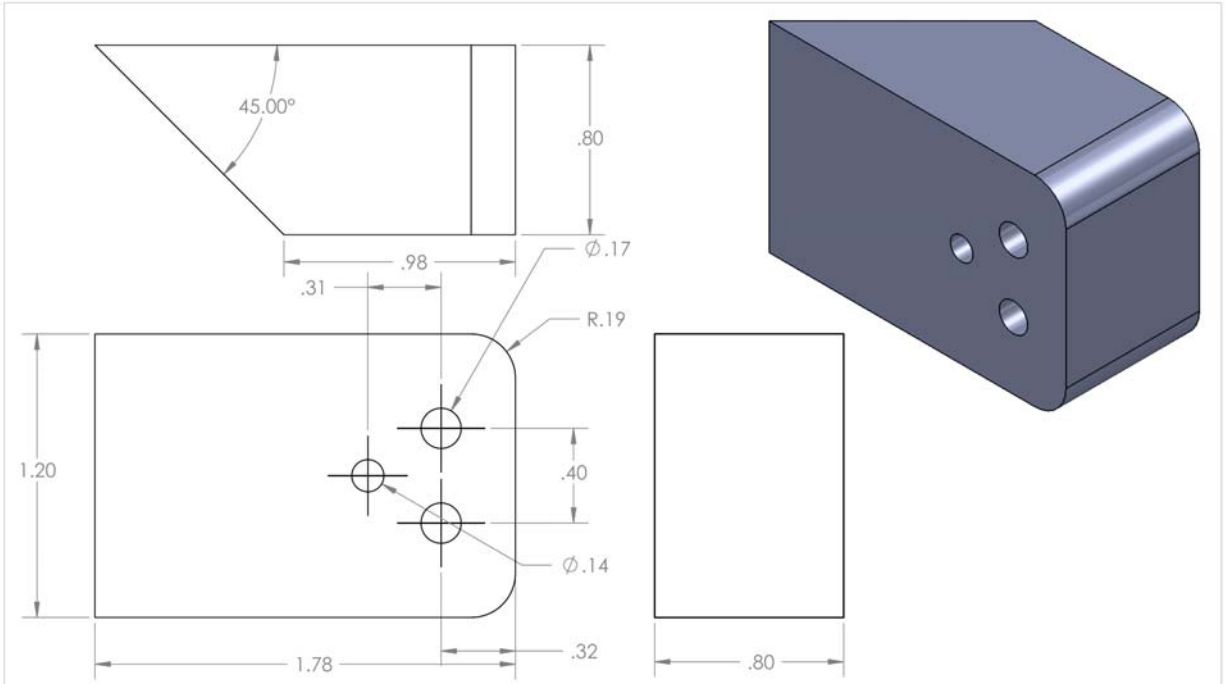

		UNLESS OTHERWISE SPECIFIED:		NAME	DATE
		DIMENSIONS ARE IN INCHES TOLERANCES: FRACTIONAL ± ANGULAR: MACH ± BEND ± TWO PLACE DECIMAL ± THREE PLACE DECIMAL ±	DRAWN	M JOHNSON	3-1-2010
			CHECKED		
			ENG APPR.		
			MFG APPR.		
		INTERPRET GEOMETRIC TOLERANCING PER:	Q.A.		
		MATERIAL	COMMENTS:		
NEXT ASSY	USED ON	FINISH			
APPLICATION		DO NOT SCALE DRAWING			

ASU Ira A. Fulton Schools of Engineering
ARIZONA STATE UNIVERSITY

TITLE:

Maytag_Part_3

SIZE	DWG. NO.	REV
A		

SCALE: 2:1	WEIGHT:	SHEET 1 OF 1

5 4 3 2 1

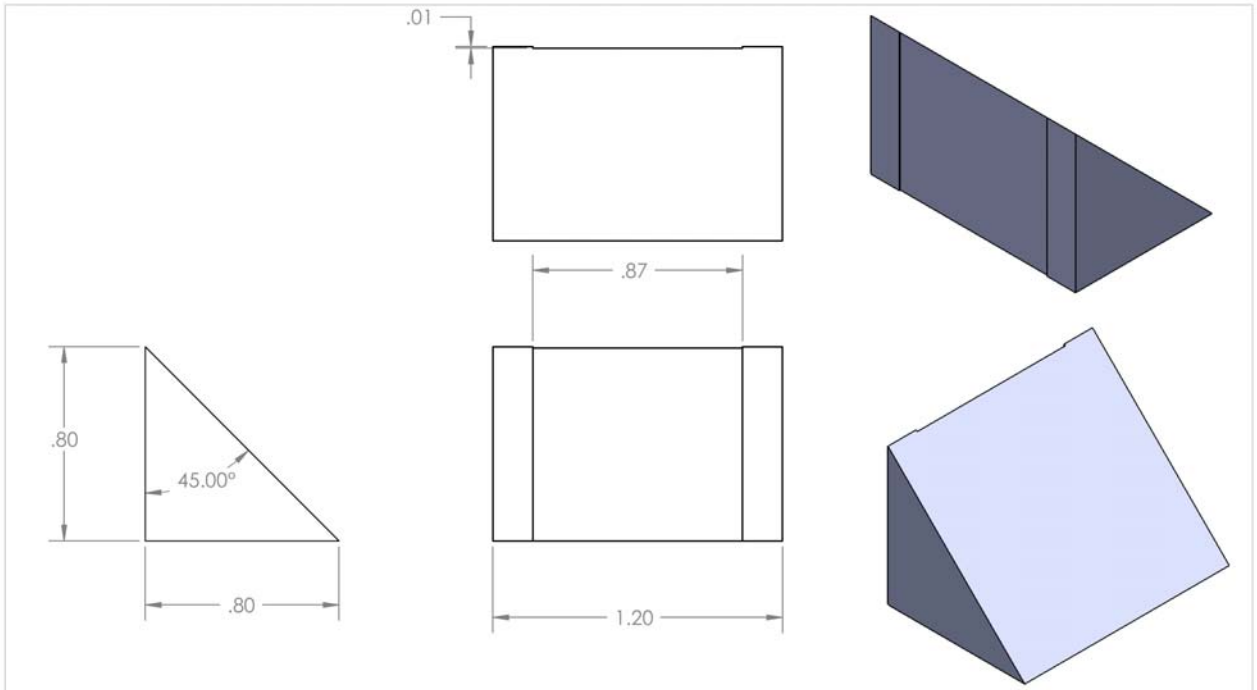

		UNLESS OTHERWISE SPECIFIED:		NAME	DATE
		DIMENSIONS ARE IN INCHES TOLERANCES: FRACTIONAL ± ANGULAR: MACH ± BEND ± TWO PLACE DECIMAL ± THREE PLACE DECIMAL ±	DRAWN	M JOHNSON	3-1-2010
			CHECKED		
			ENG APPR.		
			MFG APPR.		
		INTERPRET GEOMETRIC TOLERANCING PER:	Q.A.		
		MATERIAL	COMMENTS:		
NEXT ASSY	USED ON	FINISH			
APPLICATION		DO NOT SCALE DRAWING			

ASU Ira A. Fulton Schools of Engineering
ARIZONA STATE UNIVERSITY

TITLE:

Maytag_Part_2

SIZE	DWG. NO.	REV
A		
SCALE: 2:1	WEIGHT:	SHEET 1 OF 1

5 4 3 2 1

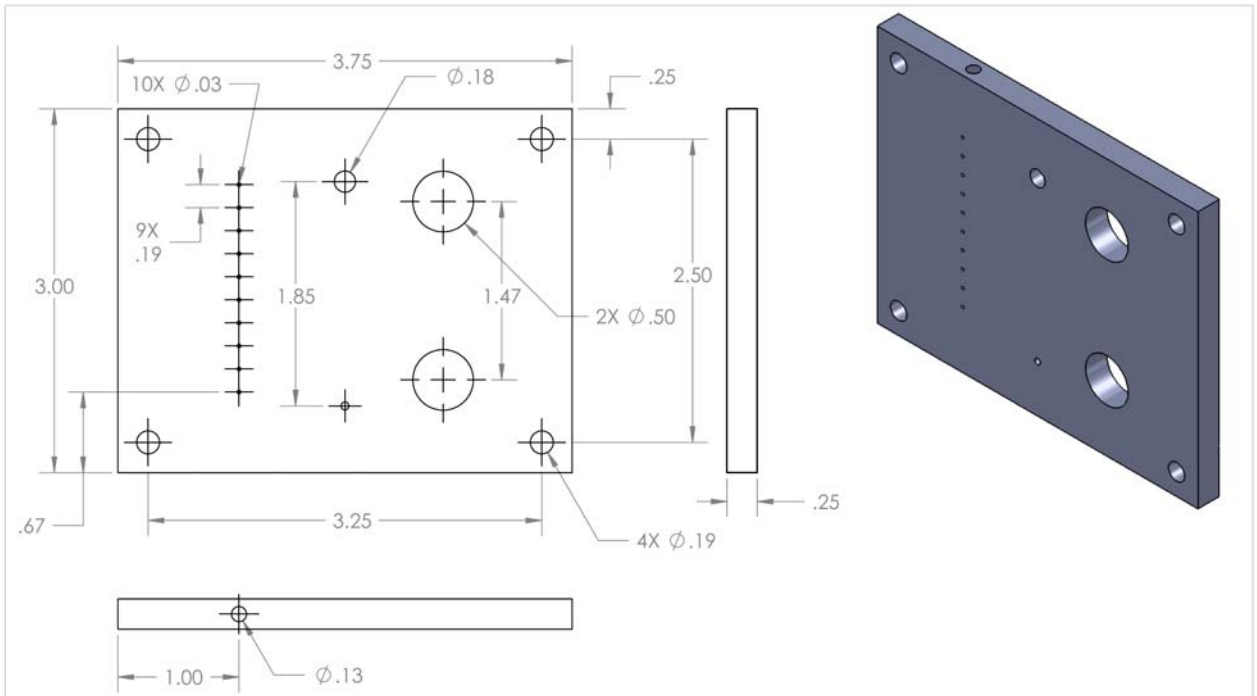

		UNLESS OTHERWISE SPECIFIED:		NAME	DATE
		DIMENSIONS ARE IN INCHES TOLERANCES: FRACTIONAL ± ANGULAR: MACH ± BEND ± TWO PLACE DECIMAL ± THREE PLACE DECIMAL ±	DRAWN	M JOHNSON	3-1-2010
			CHECKED		
			ENG APPR.		
			MFG APPR.		
		INTERPRET GEOMETRIC TOLERANCING PER:	Q.A.		
		MATERIAL	COMMENTS:		
NEXT ASSY	USED ON	FINISH			
APPLICATION		DO NOT SCALE DRAWING			

ASU Ira A. Fulton Schools of Engineering
ARIZONA STATE UNIVERSITY

TITLE:

Maytag_Part_6

SIZE	DWG. NO.	REV
A		

SCALE: 1:1 | WEIGHT: | SHEET 1 OF 1

5 4 3 2 1

APPENDIX B

DATA MINING SCRIPT – MATLAB M-FILE

The following images are copies of the Matlab m-file script that was used extensively during the in the analysis steps of the deposition and stripping experiments presented in Chapters 9 and 10. Specifically it was used on the large four-column data files that were recorded by the oscilloscope. The data files each contained a time column along with the electrochemical potential and current from the potentiostat, as well as the surface stress signal as output by the capacitive stress monitor. Each of the data files spanned a range of about 1000-1500 seconds and around ten deposition and stripping events. The purpose of this script was to pick out the points that corresponded to the beginning and ending points of each stress event and subsequent relaxation in both time and stress. The result of this script was a new data file that contained a time column and a surface stress column with all of the beginning and ending points collected in a simple format.

I recognize the reality that this simple Matlab script played only a small role in the multi-step data analysis process used for one set of experiments. Furthermore, I must also acknowledge the numerous data analysis programs and scripts that were written (and re-written) by Larry Mickelson throughout our time in graduate school. It was his data averaging programs that allowed many of us in the lab to reduce our large raw data files (collected at a rate of 1 kHz) to manageable sizes. In fact, it was with his guidance and patience that I was actually able to create the m-file script presented in this appendix. So while it may not be particularly impressive, this appendix is included in my dissertation

because it represents one of the skills that I acquired and an accomplishment that I reached along the path to a PhD.

```
function Points = copperstress(Data, X, filename, save)
% - This is my first crack at automating the data mining of my
% Cu stress data

% - "Data" is a six column (t, i, v, f, t_smooth, f_smooth),
% 250,000 or 100,000 row data file
% - "X" is is the slope cutoff value between 1 and maybe 100??)
% which yields the right number of points as seen in the
% origin plots
% - "filename" is the name of the output file
% - "save" is the number of events that should be found in file

format short g

N           = length(Data);
FLAG        = 0;
j           = 1;

for i = 2 : N

    DeltaI = Data(i,2) - Data(i-1,2);
    Deltat = Data(i,1) - Data(i-1,1);
    Derive = DeltaI / Deltat;        %time derivative of current

    if Data(i,1) - FLAG > 3*Deltat

        if abs(Derive) > X

        Points(j,1) = i;            % ouput the index for good measure
        Points(j,2) = Data(i-1, 1); % time output
        Points(j,3) = Data(i-1, 2); % current output
        Points(j,4) = Data(i-1, 3); % dep/strip delta stress output

        FLAG        = Data(i-1, 1);

            if j > 1 & i - Points(j-1,1) > 1000

                for k = 1 : 100

                    Relax(k) = Data(i-1249+k,3); % 100 ss values for relaxation output↙
for previous event

                end

                Points(j-1,5) = mean(Relax);    % stress relaxation output for previous↙
event

            elseif j == 2 * save

                for l = 1 : 100
```

```
                    LastRelax(l) = Data(N-101+1,3); % 100 ss values for relaxation output for LAST event

                end

                Points(2*save,5) = mean(LastRelax);   % stress relaxation output for LAST event

            elseif j > 1

                Points(j-1,5) = 0;

            end

        j = j + 1;

        end
    end
end


Numberofevents = length(Points)/2

%save = input('Does this number match the number of peaks in plot? [Yes = 1, No = 0 (default is no]: ');
%if save == 1
 if save == Numberofevents

    [s, errmsg] = sprintf('new%s.txt', filename)
    dlmwrite(s,Points, 'delimiter', '\t', 'precision', '%.5f')
 else

     disp('ERROR: The number of events is not correct. Run program again!')

end
```

APPENDIX C

CU(111) SINGLE CRYSTAL CONSTRUCTION & CALIBRATION

In order to carry out the single crystal experiments that are presented in Chapter 12, a new sample architecture had to be designed to replace the thin film working electrode with a single crystal electrode surface. The main purpose of this new architecture was to simply replace the thin film with the single crystal as the working electrode while maintaining a sample geometry that could be used in the electrochemical surface stress cell as were the thin film samples. In this appendix, both the construction and calibration protocol are briefly reviewed. First, the sample was constructed from (1) a UHV Cu{111} thin film sample, (2) an electropolished Cu(111) single crystal slice, and (3) a chemically inert enamel, (4) silver paint, and (5) an ultra-thin (diameter ≈ 75 μm) nickel wire. This was done by cutting the thin film sample at two locations in order to replace the Cu thin film working electrode with the single crystal slice. This is demonstrated in Figure C.1.

The thin film pieces and the single crystal slice were temporarily fixed in position with transparent adhesive tape and glass microscope slides (see Figure C.1). After fixing the positions of the pieces relative to each other, the silver paint was applied at two locations to provide electrical contact to the working electrode (Cu(111) single crystal surface) and the capacitive sense electrode (see sketches below). After the silver paint was sufficiently dry, the chemically inert enamel was applied as both (1) a structural adhesive to maintain the integrity of the unified pieces as a single sample and (2) an electrically insulating barrier between the electrolyte and the silver paint, edges, and back-side of the Cu single slice (see Figure C.1 and sketches below). Once the enamel was completely dry, the single

crystal sample was inserted in the surface stress cell and utilized in a manner identical to that of the thin film electrode experiments described above.

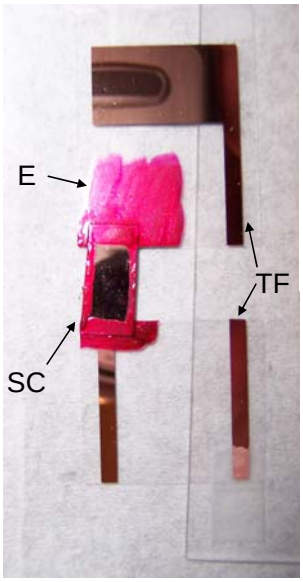

Figure C.1 – Image of the single crystal sample during construction. Sample was made using pieces of a thin film sample (TF), a Cu(111) single crystal slice (SC), and a chemically inert enamel (E).

Due to the nature of the single crystal electrode, an individual calibration of the sample was not possible. Thus, a modified version of the calibration protocol, as presented in Chapter 7, became necessary. This was done by using the manufacturer's output calibration value (100 μm/10 V) of the surface stress monitor for the ΔV_{tot} term shown in eq 7.5. Further modification to eq 7.5 was required due to the fact that the bending of the sample no longer corresponded to

stresses in a thin film-thick substrate system. Rather the bending of the single crystal sample could be treated as a more straightforward beam bending problem. After making these modifications to eq 7.5, the calibration of the single crystal electrode was then a function of the final dimensions of the constructed sample only. The resulting equation given by:

$$\Delta\sigma_f h_f = \left(\frac{W}{w}\right)\left(\frac{M_{Cu(111)}h_B^2}{6}\right)\left(\frac{1}{l\left(x - l/2\right)}\right)\left(\frac{\Delta V}{\Delta V_{tot}}\right), \qquad \text{(C.1)}$$

where $M_{Cu(111)}$ and h_B are the biaxial modulus and thickness of the Cu(111) single crystal slice, respectively, and the other terms refer to the dimensions of the constructed single crystal sample and are defined schematically in the sketches below. An example calculation is included in this appendix to give a sense of the difference in sensitivity between the single crystal sample and the thin film samples. Specifically, the value was calculated as ~36.1 N/m which is of order 3 times larger than the average thin film sample multiplier.

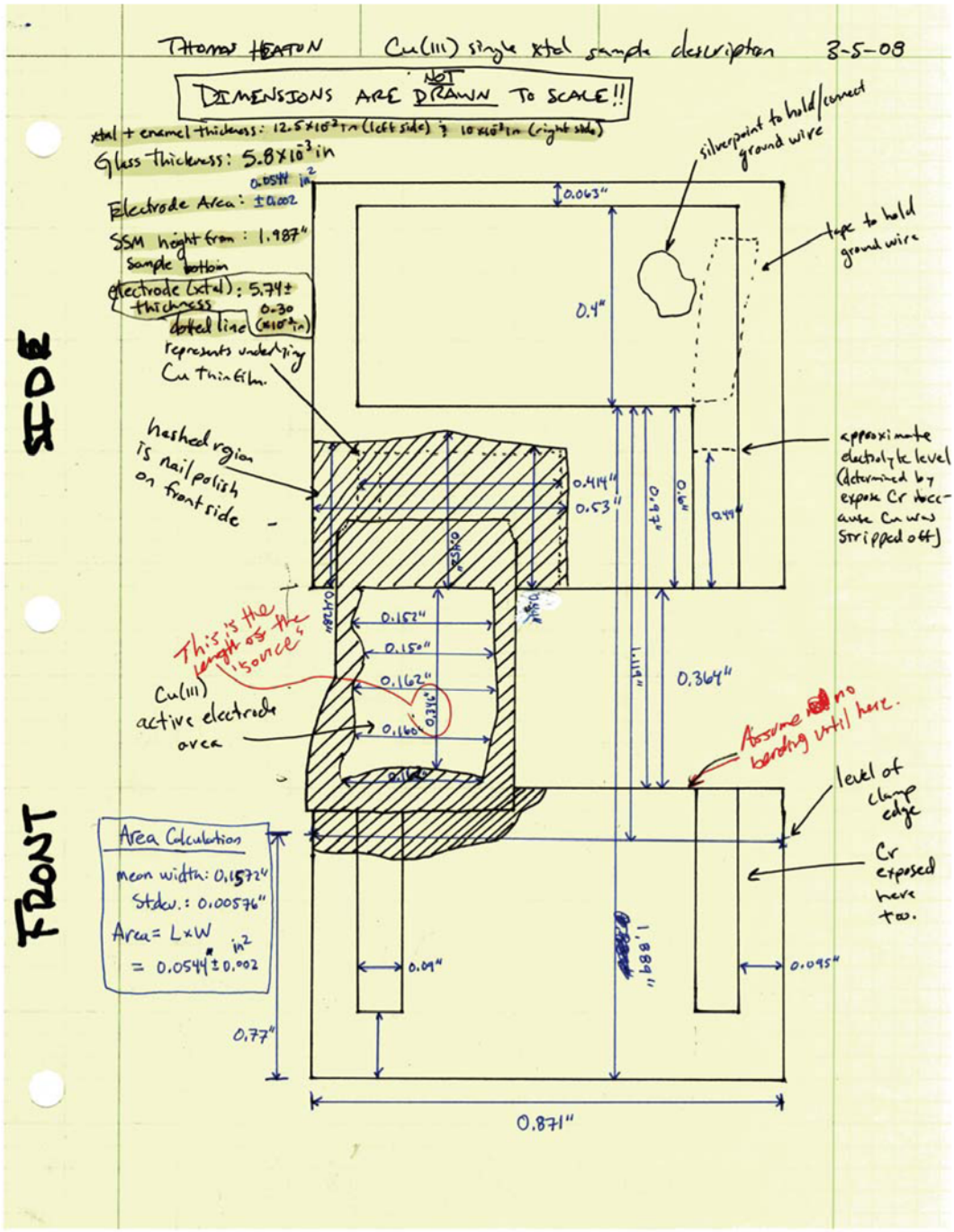
Thomas Heaton Cu(111) single xtal sample description 8-5-08
DIMENSIONS ARE NOT DRAWN TO SCALE!!
xtal + enamel thickness: 12.5×10⁻³in (left side) & 10×10⁻³in (right side)
Glass thickness: 5.8×10⁻³in
Electrode Area: 0.0544 in² ±0.002
SSM height from sample bottom: 1.987"
electrode (xtal) thickness: 5.74 ± 0.30 (×10⁻³in)
dotted line represents underlying Cu thin film.
hashed region is nail polish on front side
silverpaint to hold/connect ground wire
tape to hold ground wire
approximate electrolyte level (determined by exposed Cr because Cu was stripped off)
0.063"
0.4"
0.414"
0.53"
0.97"
0.6"
0.44"
0.152"
0.150"
0.162"
0.160"
0.160"
0.216"
0.364"
1.151"
This is the length of the source
Cu(111) active electrode area
Assume no bending until here.
level of clamp edge
Cr exposed here too.
Area Calculation
mean width: 0.1572"
Stdev.: 0.00576"
Area = L×W
= 0.0544 ± 0.002 in²
0.09"
0.095"
1.884"
0.77"
0.871"
SIDE
FRONT

THOMAS HEATON | Cu(111) single xtal | sample description | 3-5-08

DIMENSIONS ARE NOT DRAWN TO SCALE !!

Cr adhesion layer is on opposite side of sample.

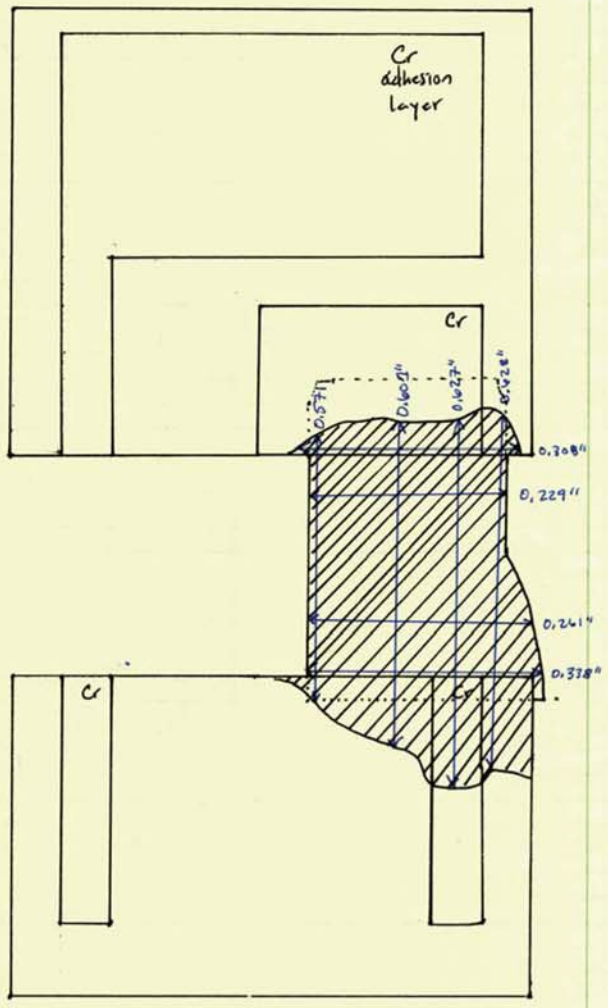

SIDE

BACK

```
>> whos
  Name            Size                    Bytes  Class

  M_111           1x1                         8  double array
  Multiplier      1x1                         8  double array
  W               1x1                         8  double array
  ans             1x1                         8  double array
  c               6x6                       288  double array
  h_s             1x1                         8  double array
  l               1x1                         8  double array
  s               6x6                       288  double array
  w               1x1                         8  double array
  x               1x1                         8  double array

Grand total is 80 elements using 640 bytes

>> s

s =

    1.49e-011    -6.3e-012    -6.3e-012            0            0            0
    -6.3e-012    1.49e-011    -6.3e-012            0            0            0
    -6.3e-012    -6.3e-012    1.49e-011            0            0            0
            0            0            0    1.33e-011            0            0
            0            0            0            0    1.33e-011            0
            0            0            0            0            0    1.33e-011

>> %Copper compliance matrix from Nye;
>> %calculate stiffness matrix;
>> c^(-1)

ans =

    1.49e-011    -6.3e-012    -6.3e-012            0            0            0
    -6.3e-012    1.49e-011    -6.3e-012            0            0            0
    -6.3e-012    -6.3e-012    1.49e-011            0            0            0
            0            0            0    1.33e-011            0            0
            0            0            0            0    1.33e-011            0
            0            0            0            0            0    1.33e-011

>> %in Pa;
>> %Biaxial modulus as given in Freund and Suresh;
>> M_111=6*(c(1,1)+2*c(1,2))*c(4,4)/(c(1,1)+2*c(1,2)+4*c(4,4))

M_111 =

  2.6667e+011

>> %in Pa;
>> %physical constants;
>> W,w,h_s,l,x
```

```
W =

      0.68326


w =

      0.53086


h_s =

       0.0127


l =

       1.0033


x =

        3.048

>> % all given in cm;
>> Multiplier = (W/w)*(100e-6/10)*M_111*(h_s/100)^(2)/6/((l/100)^2/2+(l/100)*((x/100)- ↙
(l/100)))

Multiplier =

       36.115

>> %in N/m/V;
>> % This is spot on since the previous value that Friesen calculated last year for single ↙
xtal;
>> % sample was 19.998 N/m/V for the electronics box that was calibrated to 50 um/10 V and ↙
this;
>> % new multiplier value is for electronics calculated to 100 um/10 V!!!  The factor of ↙
two is;
>> % is almost exact here!;
>>
>> % Thomas Heaton;
>> % 5/21/09;
>>
```

APPENDIX D

ORIGINAL DATA CURVES FOR SOLUTION EXCHANGE INDUCED STRESS CHANGES AND COPPER EXCHANGE CURRENT DENSITY

The following set of figures is included as the original sources of the data that is presented in Figures 12.3, 12.4, and 12.5. In each case below, the figure contains (1) a plot of the surface stress change induced by a solution exchange process and (2) a Tafel analysis of the cyclic voltammetry of a Cu{111} thin film electrode. Each figure corresponds to a single copper ion concentration as indicated in the figure caption.

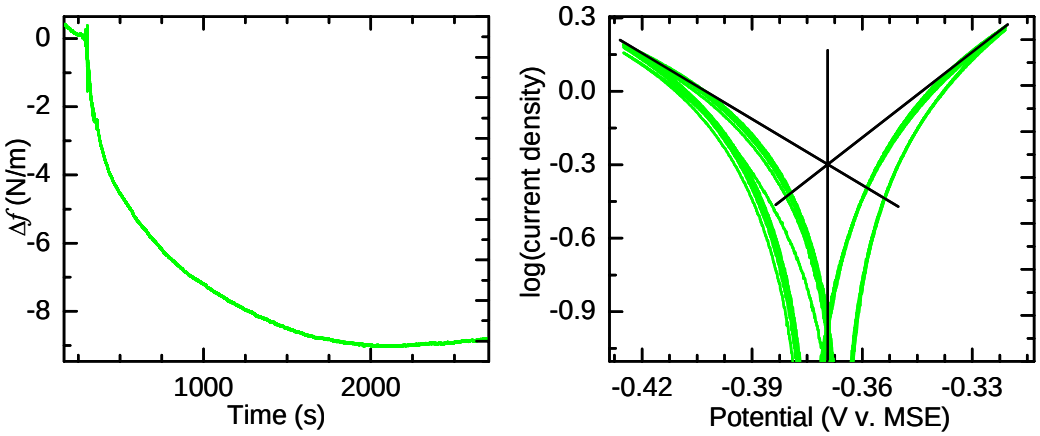

Figure D.1 – Surface stress change (left) during the solution exchange experiment, 0.01 M → 0.1 M $CuSO_4$. Here the stress change is ~-8.7 N/m. Additionally, the Tafel plot (right) that was generated from the cyclic voltammetric response of a Cu{111} thin film in 0.1 M $CuSO_4$ + 0.1 M H_2SO_4 is also shown. Using the slope extrapolation method the OCP and exchange current density were estimated to be -369 mV and log(-0.299) = 502 μA/cm^2, respectively.

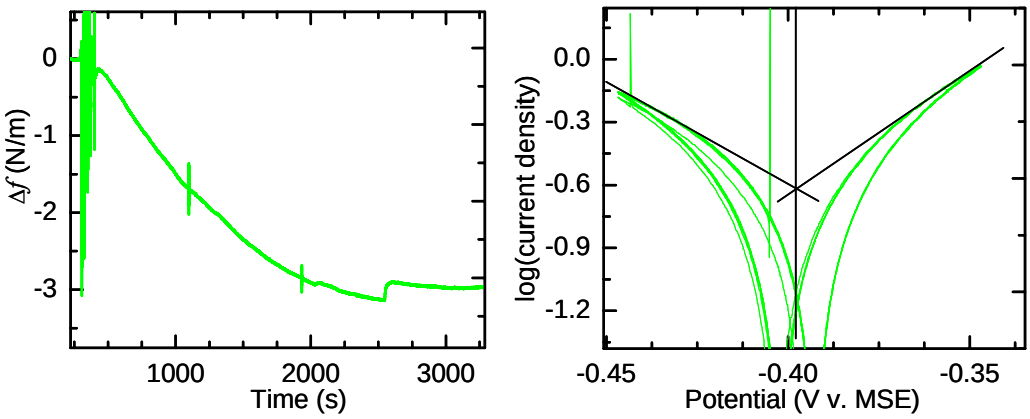

Figure D.2 – Surface stress change (left) during the solution exchange experiment, 0.001 M → 0.01 M $CuSO_4$. Here the stress change is ~-3.1 N/m. Additionally, the Tafel plot (right) that was generated from the cyclic voltammetric response of a Cu{111} thin film in 0.01 M $CuSO_4$ + 0.1 M H_2SO_4 is also shown. Using the slope extrapolation method the OCP and exchange current density were estimated to be -398 mV and log(-0.617) = 242 μA/cm^2, respectively.

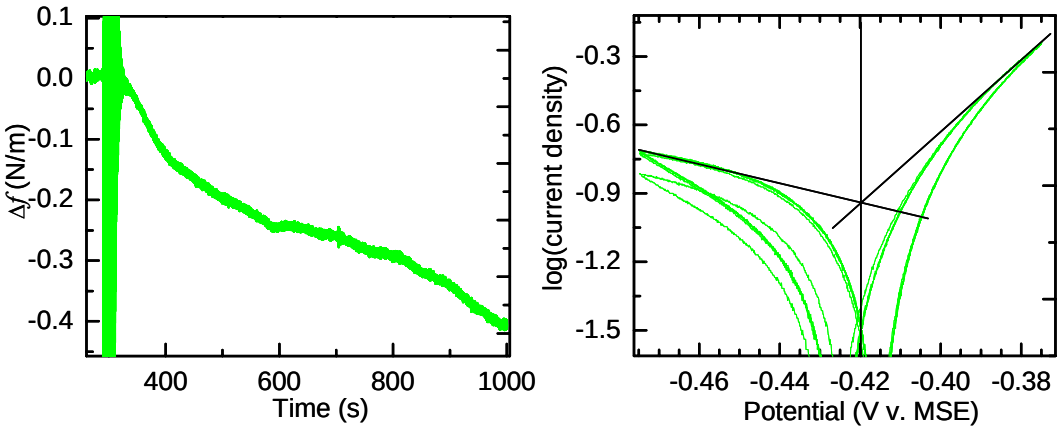

Figure D.3 – Surface stress change (left) during the solution exchange experiment, 10^{-4} M → 10^{-3} M $CuSO_4$. Here the stress change is ~-0.38 N/m. Additionally, the Tafel plot (right) that was generated from the cyclic voltammetric response of a Cu{111} thin film in 10^{-3} M $CuSO_4$ + 0.1 M H_2SO_4 is also shown. Using the slope extrapolation method the OCP and exchange current density were estimated to be -420 mV and log(-0.94) ≈ 115 μA/cm^2, respectively.

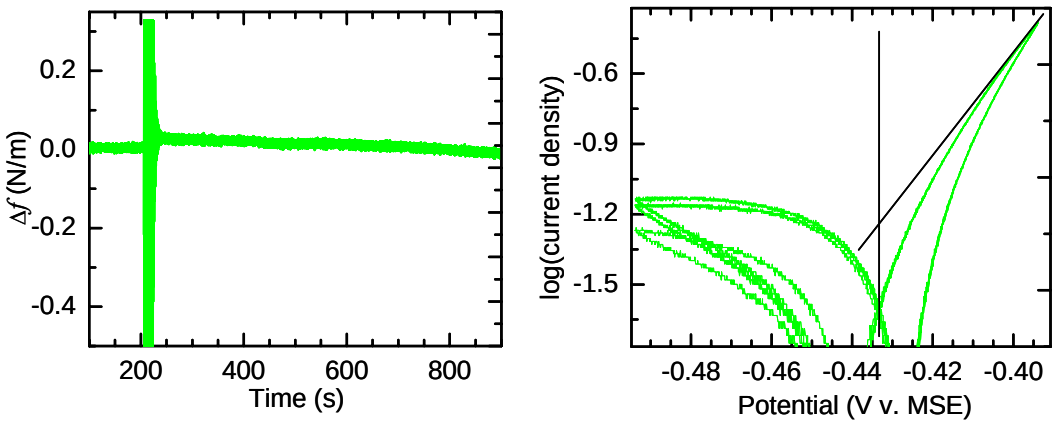

Figure D.4 – Surface stress change (left) during the solution exchange experiment, 10^{-5} M → 10^{-4} M $CuSO_4$. Here the stress change is ~0 N/m. Additionally, the Tafel plot (right) that was generated from the cyclic voltammetric response of a Cu{111} thin film in 10^{-4} M $CuSO_4$ + 0.1 M H_2SO_4 is also shown. Using the slope extrapolation method the OCP and exchange current density were estimated to be -433 mV and log(-1.25) ≈ 57 μA/cm^2, respectively.

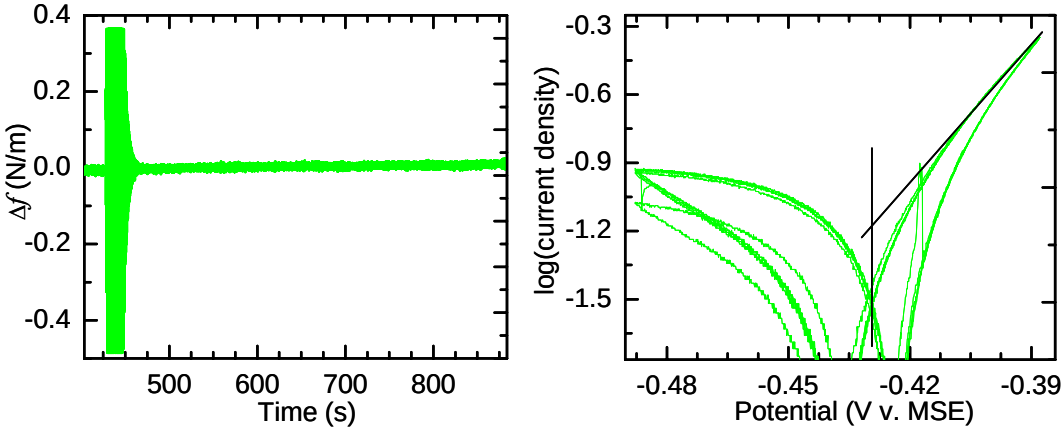

Figure D.5 – Surface stress change (left) during the solution exchange experiment, 10^{-6} M → 10^{-5} m $CuSO_4$. Here the stress change is ~0 N/m. Additionally, the Tafel plot (right) that was generated from the cyclic voltammetric response of a Cu{111} thin film in 10^{-5} M $CuSO_4$ + 0.1 M H_2SO_4 is also shown. Using the slope extrapolation method the OCP and exchange current density were estimated to be -429 mV and log(-1.16) ≈ 69 μA/cm^2, respectively.

APPENDIX E

COPYRIGHT PERMISSIONS

This appendix contains documentation of the copyright permissions that I obtained either through personal e-mail contact or through the online process established by the Copyright Clearance Center (http://www.copyright.com). The permissions are included below in their original format as it was given by email or from http://www.copyright.com. The documentation corresponding to each separate permission is presented on a new page.

from	John J Ritsko <ritsko@us.ibm.com>
to	Thomas Heaton <tsheato@asu.edu>
date	Thu, Mar 24, 2011 at 10:57 AM
subject	Re: Copyright Permission: IBM Journal of Research & Development

We grant permission as requested in your note below.

John J. Ritsko
Editor-in-Chief, IBM Technical Journals
IBM T.J. Watson Research Center, 7-135
P.O. Box 218 Yorktown Heights, NY 10598-0218

From: Thomas Heaton <tsheato@asu.edu>
To: John J Ritsko/Watson/IBM@IBMUS
Cc: Thomas Heaton <tsheato@asu.edu>
Date: 03/23/2011 07:44 PM
Subject: Copyright Permission: IBM Journal of Research & Development

---

3/23/2011

John Ritsko, Editor-in-Chief
IBM TJ Watson Research Center,
Yorktown Heights, NY 10598-0218

Dear Mr Ritsko:

I am completing a doctoral dissertation at Arizona State University entitled "An in situ Surface Stress Study of Electrochemical Phenomena: Electrodeposition & Molecular Adsorption." I would like your permission to reprint in my dissertation an excerpt from the following:

T. P. Moffat, D. Wheeler, M. D. Edelstein & D. Josell, "Superconformal film growth: Mechanism and quantification," *IBM Journal of research & Development*,

49, 19 (2005).

The excerpt to be reproduced is:
Figure 12 of the article by Moffat *et al.*

The requested permission extends to any future revisions and editions of my dissertation, including non-exclusive world rights in all languages, and to the prospective publication of my dissertation by ProQuest through its UMI® Dissertation Publishing business. ProQuest may produce and sell copies of my dissertation on demand. These rights will in no way restrict republication of the material in any other form by you or by others authorized by you. An affirmative response to this e-mail letter will also confirm that you own or your company owns the copyright to the above-described material.

If these arrangements meet with your approval, please respond accordingly via e-mail to thomas.heaton@asu.edu

I would appreciate a response at your earliest convenience.

Thank you very much.

PERMISSION GRANTED FOR THE
USE REQUESTED ABOVE:

_____
[Type name of addressee below signature line]

Date: _____

Sincerely,

Thomas Heaton
Friesen Research Group
Ira A. Fulton School of Engineering
Arizona State University
Tempe, AZ 85287-8706
Lab: 480-965-1061
cell: 480-586-0860
thomas.heaton@asu.edu
http://www.linkedin.com/in/thomasheaton

ELSEVIER LICENSE
TERMS AND CONDITIONS

Mar 24, 2011

This is a License Agreement between Thomas Heaton ("You") and Elsevier ("Elsevier") provided by Copyright Clearance Center ("CCC"). The license consists of your order details, the terms and conditions provided by Elsevier, and the payment terms and conditions.

All payments must be made in full to CCC. For payment instructions, please see information listed at the bottom of this form.

Supplier	Elsevier Limited The Boulevard,Langford Lane Kidlington,Oxford,OX5 1GB,UK
Registered Company Number	1982084
Customer name	Thomas Heaton
License number	2635580018584
License date	Mar 24, 2011
Licensed content publisher	Elsevier
Licensed content publication	Thin Solid Films
Licensed content title	Influence of incorporated non-metallic impurities on electromigration in copper damascene interconnect lines
Licensed content author	M. Stangl, M. Lipták, J. Acker, V. Hoffmann, S. Baunack, K. Wetzig
Licensed content date	27 February 2009
Licensed content volume number	517
Licensed content issue number	8
Number of pages	4
Start Page	2687
End Page	2690
Type of Use	reuse in a thesis/dissertation

Portion	figures/tables/illustrations
Number of figures/tables/illustrations	1
Format	both print and electronic
Are you the author of this Elsevier article?	No
Will you be translating?	No
Order reference number	
Title of your thesis/dissertation	An in situ Surface Stress Study of Electrochemical Phenomena: Electrodeposition & Molecular Adsorption
Expected completion date	Jul 2011
Estimated size (number of pages)	200
Elsevier VAT number	GB 494 6272 12
Permissions price	0.00 USD
VAT/Local Sales Tax	0.0 USD / 0.0 GBP
Total	0.00 USD
Terms and Conditions	

INTRODUCTION

1. The publisher for this copyrighted material is Elsevier. By clicking "accept" in connection with completing this licensing transaction, you agree that the following terms and conditions apply to this transaction (along with the Billing and Payment terms and conditions established by Copyright Clearance Center, Inc. ("CCC"), at the time that you opened your Rightslink account and that are available at any time at http://myaccount.copyright.com).

GENERAL TERMS

2. Elsevier hereby grants you permission to reproduce the aforementioned material subject to the terms and conditions indicated.

3. Acknowledgement: If any part of the material to be used (for example, figures) has appeared in our publication with credit or acknowledgement to another source, permission must also be sought from that source. If such permission is not obtained then that material may not be included in your publication/copies. Suitable acknowledgement to the source must be made, either as a footnote or in a reference list at the end of your

publication, as follows:

"Reprinted from Publication title, Vol /edition number, Author(s), Title of article / title of chapter, Pages No., Copyright (Year), with permission from Elsevier [OR APPLICABLE SOCIETY COPYRIGHT OWNER]." Also Lancet special credit - "Reprinted from The Lancet, Vol. number, Author(s), Title of article, Pages No., Copyright (Year), with permission from Elsevier."

4. Reproduction of this material is confined to the purpose and/or media for which permission is hereby given.

5. Altering/Modifying Material: Not Permitted. However figures and illustrations may be altered/adapted minimally to serve your work. Any other abbreviations, additions, deletions and/or any other alterations shall be made only with prior written authorization of Elsevier Ltd. (Please contact Elsevier at permissions@elsevier.com)

6. If the permission fee for the requested use of our material is waived in this instance, please be advised that your future requests for Elsevier materials may attract a fee.

7. Reservation of Rights: Publisher reserves all rights not specifically granted in the combination of (i) the license details provided by you and accepted in the course of this licensing transaction, (ii) these terms and conditions and (iii) CCC's Billing and Payment terms and conditions.

8. License Contingent Upon Payment: While you may exercise the rights licensed immediately upon issuance of the license at the end of the licensing process for the transaction, provided that you have disclosed complete and accurate details of your proposed use, no license is finally effective unless and until full payment is received from you (either by publisher or by CCC) as provided in CCC's Billing and Payment terms and conditions. If full payment is not received on a timely basis, then any license preliminarily granted shall be deemed automatically revoked and shall be void as if never granted. Further, in the event that you breach any of these terms and conditions or any of CCC's Billing and Payment terms and conditions, the license is automatically revoked and shall be void as if never granted. Use of materials as described in a revoked license, as well as any use of the materials beyond the scope of an unrevoked license, may constitute copyright infringement and publisher reserves the right to take any and all action to protect its copyright in the materials.

9. Warranties: Publisher makes no representations or warranties with

respect to the licensed material.

10. Indemnity: You hereby indemnify and agree to hold harmless publisher and CCC, and their respective officers, directors, employees and agents, from and against any and all claims arising out of your use of the licensed material other than as specifically authorized pursuant to this license.

11. No Transfer of License: This license is personal to you and may not be sublicensed, assigned, or transferred by you to any other person without publisher's written permission.

12. No Amendment Except in Writing: This license may not be amended except in a writing signed by both parties (or, in the case of publisher, by CCC on publisher's behalf).

13. Objection to Contrary Terms: Publisher hereby objects to any terms contained in any purchase order, acknowledgment, check endorsement or other writing prepared by you, which terms are inconsistent with these terms and conditions or CCC's Billing and Payment terms and conditions. These terms and conditions, together with CCC's Billing and Payment terms and conditions (which are incorporated herein), comprise the entire agreement between you and publisher (and CCC) concerning this licensing transaction. In the event of any conflict between your obligations established by these terms and conditions and those established by CCC's Billing and Payment terms and conditions, these terms and conditions shall control.

14. Revocation: Elsevier or Copyright Clearance Center may deny the permissions described in this License at their sole discretion, for any reason or no reason, with a full refund payable to you. Notice of such denial will be made using the contact information provided by you. Failure to receive such notice will not alter or invalidate the denial. In no event will Elsevier or Copyright Clearance Center be responsible or liable for any costs, expenses or damage incurred by you as a result of a denial of your permission request, other than a refund of the amount(s) paid by you to Elsevier and/or Copyright Clearance Center for denied permissions.

LIMITED LICENSE

The following terms and conditions apply only to specific license types:

15. **Translation**: This permission is granted for non-exclusive world **English** rights only unless your license was granted for translation

rights. If you licensed translation rights you may only translate this content into the languages you requested. A professional translator must perform all translations and reproduce the content word for word preserving the integrity of the article. If this license is to re-use 1 or 2 figures then permission is granted for non-exclusive world rights in all languages.

16. **Website**: The following terms and conditions apply to electronic reserve and author websites:
Electronic reserve: If licensed material is to be posted to website, the web site is to be password-protected and made available only to bona fide students registered on a relevant course if:
This license was made in connection with a course,
This permission is granted for 1 year only. You may obtain a license for future website posting,
All content posted to the web site must maintain the copyright information line on the bottom of each image,
A hyper-text must be included to the Homepage of the journal from which you are licensing
athttp://www.sciencedirect.com/science/journal/xxxxx or the Elsevier homepage for books athttp://www.elsevier.com , and
Central Storage: This license does not include permission for a scanned version of the material to be stored in a central repository such as that provided by Heron/XanEdu.

17. **Author website** for journals with the following additional clauses:

All content posted to the web site must maintain the copyright information line on the bottom of each image, and
he permission granted is limited to the personal version of your paper. You are not allowed to download and post the published electronic version of your article (whether PDF or HTML, proof or final version), nor may you scan the printed edition to create an electronic version,
A hyper-text must be included to the Homepage of the journal from which you are licensing
athttp://www.sciencedirect.com/science/journal/xxxxx , As part of our normal production process, you will receive an e-mail notice when your article appears on Elsevier's online service ScienceDirect (www.sciencedirect.com). That e-mail will include the article's Digital Object Identifier (DOI). This number provides the electronic link to the published article and should be included in the posting of your personal version. We ask that you wait until you receive this e-mail and have the DOI to do any posting.
Central Storage: This license does not include permission for a scanned version of the material to be stored in a central repository such as that

provided by Heron/XanEdu.

18. **Author website** for books with the following additional clauses:
Authors are permitted to place a brief summary of their work online only.
A hyper-text must be included to the Elsevier homepage at
http://www.elsevier.com

All content posted to the web site must maintain the copyright information line on the bottom of each image
You are not allowed to download and post the published electronic version of your chapter, nor may you scan the printed edition to create an electronic version.
Central Storage: This license does not include permission for a scanned version of the material to be stored in a central repository such as that provided by Heron/XanEdu.

19. **Website** (regular and for author): A hyper-text must be included to the Homepage of the journal from which you are licensing at http://www.sciencedirect.com/science/journal/xxxxx. or for books to the Elsevier homepage at http://www.elsevier.com

20. **Thesis/Dissertation**: If your license is for use in a thesis/dissertation your thesis may be submitted to your institution in either print or electronic form. Should your thesis be published commercially, please reapply for permission. These requirements include permission for the Library and Archives of Canada to supply single copies, on demand, of the complete thesis and include permission for UMI to supply single copies, on demand, of the complete thesis. Should your thesis be published commercially, please reapply for permission.

21. **Other Conditions**:

v1.6

Gratis licenses (referencing $0 in the Total field) are free. Please retain this printable license for your reference. No payment is required.

If you would like to pay for this license now, please remit this license along with your payment made payable to "COPYRIGHT CLEARANCE CENTER" otherwise you will be invoiced within 48

hours of the license date. Payment should be in the form of a check or money order referencing your account number and this invoice number RLNK10956480.
Once you receive your invoice for this order, you may pay your invoice by credit card. Please follow instructions provided at that time.

Make Payment To:
Copyright Clearance Center
Dept 001
P.O. Box 843006
Boston, MA 02284-3006

For suggestions or comments regarding this order, contact Rightslink Customer Support:customercare@copyright.com or +1-877-622-5543 (toll free in the US) or +1-978-646-2777.

ELSEVIER LICENSE
TERMS AND CONDITIONS

Mar 25, 2011

This is a License Agreement between Thomas Heaton ("You") and Elsevier ("Elsevier") provided by Copyright Clearance Center ("CCC"). The license consists of your order details, the terms and conditions provided by Elsevier, and the payment terms and conditions.

All payments must be made in full to CCC. For payment instructions, please see information listed at the bottom of this form.

Supplier	Elsevier Limited The Boulevard,Langford Lane Kidlington,Oxford,OX5 1GB,UK
Registered Company Number	1982084
Customer name	Thomas Heaton
License number	2636060142517
License date	Mar 25, 2011
Licensed content publisher	Elsevier
Licensed content publication	Microelectronic Engineering
Licensed content title	Influence of initial microstructure and impurities on Cu room-temperature recrystallization (self-annealing)
Licensed content author	M. Stangl, M. Lipták, A. Fletcher, J. Acker, J. Thomas, H. Wendrock, S. Oswald, K. Wetzig
Licensed content date	March 2008
Licensed content volume number	85
Licensed content issue number	3
Number of pages	8
Start Page	534
End Page	541

Type of Use	reuse in a thesis/dissertation
Intended publisher of new work	other
Portion	figures/tables/illustrations
Number of figures/tables/illustrations	1
Format	both print and electronic
Are you the author of this Elsevier article?	No
Will you be translating?	No
Order reference number	
Title of your thesis/dissertation	An in situ Surface Stress Study of Electrochemical Phenomena: Electrodeposition & Molecular Adsorption
Expected completion date	Jul 2011
Estimated size (number of pages)	200
Elsevier VAT number	GB 494 6272 12
Permissions price	0.00 USD
VAT/Local Sales Tax	0.0 USD / 0.0 GBP
Total	0.00 USD
Terms and Conditions	

AMERICAN CHEMICAL SOCIETY LICENSE TERMS AND CONDITIONS

May 16, 2011

This is a License Agreement between Thomas Heaton ("You") and American Chemical Society ("American Chemical Society") provided by Copyright Clearance Center ("CCC"). The license consists of your order details, the terms and conditions provided by American Chemical Society, and the payment terms and conditions.

All payments must be made in full to CCC. For payment instructions, please see information listed at the bottom of this form.

License Number

2671030741122

License Date

May 16, 2011

Licensed content publisher

American Chemical Society

Licensed content publication

Chemical Reviews

Licensed content title

The Electrical Double Layer and the Theory of Electrocapillarity.

Licensed content author

David C. Grahame

Licensed content date

Dec 1, 1947

Volume number

41

Issue number

3

Type of Use

Thesis/Dissertation

Requestor type

Not specified

Format

Print and Electronic

Portion

Table/Figure/Micrograph

Number of Table/Figure/Micrographs

1

Author of this ACS article

No

Order reference number

Title of the thesis / dissertation

An in situ Surface Stress Study of Electrochemical Phenomena: Electrodeposition & Molecular Adsorption

Expected completion date

Jul 2011

Estimated size(pages)

200

Billing Type

Invoice

Customer reference info

Total

0.00 USD

Terms and Conditions

Thesis/Dissertation

ACS / RIGHTSLINK TERMS & CONDITIONS
THESIS/DISSERTATION

ELSEVIER LICENSE
TERMS AND CONDITIONS

May 17, 2011

This is a License Agreement between Thomas Heaton ("You") and Elsevier ("Elsevier") provided by Copyright Clearance Center ("CCC"). The license consists of your order details, the terms and conditions provided by Elsevier, and the payment terms and conditions.

All payments must be made in full to CCC. For payment instructions, please see information listed at the bottom of this form.

Supplier

Elsevier Limited
The Boulevard,Langford Lane
Kidlington,Oxford,OX5 1GB,UK

Registered Company Number

1982084

Customer name

Thomas Heaton

License number

2671511101566

License date

May 17, 2011

Licensed content publisher

Elsevier

Licensed content publication

Progress in Surface Science

Licensed content title

Reconstruction phenomena at metal-electrolyte interfaces

Licensed content author

D. M. Kolb

Licensed content date

February 1996

Licensed content volume number

51

Licensed content issue number

2

Number of pages

65

Start Page

109

End Page

173

Type of Use

reuse in a thesis/dissertation

Portion

figures/tables/illustrations

Number of figures/tables/illustrations

1

Format

both print and electronic

Are you the author of this Elsevier article?

No

Will you be translating?

No

Order reference number

Title of your thesis/dissertation

An in situ Surface Stress Study of Electrochemical Phenomena: Electrodeposition & Molecular Adsorption

Expected completion date

Jul 2011

Estimated size (number of pages)

200

Elsevier VAT number

GB 494 6272 12

Permissions price

0.0 USD

from **Lei Tang** tonitang@gmail.com hide details 1:33 PM
to Thomas Heaton <thomas.heaton@asu.edu>

date Thu, Aug 4, 2011 at 1:33 PM
subject Re: Permission to use images/data
signed-by gmail.com
Important mainly because of the people in the conversation.

Hi, Thomas:

That is OK. Go ahead. And good luck for your graduation.

Toni
- Hide quoted text -

On Thu, Aug 4, 2011 at 1:02 PM, Thomas Heaton <thomas.heaton@asu.edu> wrote:
> 855 E. 8th St.
> Mesa, AZ 85203
>
> August 4, 2011
>
> Dr. Toni Tang:
> I would like to use several STM images and data that you collected in fall
> of 2007. I have attached it here for your reference. I would like to
> include your work in my dissertation as it relates to my Cu electrode
> surface stress project. It will be very helpful in my efforts to put
> together a nice explanation of the behavior that I have measured during
> these experiments.
>
> Thank you very much,
> Thomas Heaton
> Friesen Research Group
> Ira A. Fulton School of Engineering
> Arizona State University
> Tempe, AZ 85287-8706
> Lab: 480-965-1061
> cell: 480-586-0860
> thomas.heaton@asu.edu
> http://www.linkedin.com/in/thomasheaton
>

--
Lei Tang

APPENDIX F

PT{111} AND AU{111} ELECTROCAPILLARITY: INTERPHASE STRUCTURE, THE PZC, AND OXYGEN REDUCTION

The following article titled "Pt{111} and Au{111} Electrocapillarity: Interphase Structure, the pzc, and Oxygen Reduction" appeared in the October issue of the *Journal of Physical Chemistry C*. It constitutes my introductory project and efforts in the areas of surface stress and electrochemistry. Although the results that are presented in this article are not explicitly covered in the body of this dissertation, the discovery and experience that I gained from this first project established the basis for all of my subsequent work. In fact, the original electrochemical surface stress cell, "the Maytag", was designed and fabricated in order to carry out these experiments while I was finishing my undergraduate degree. Note that I am the first co-author on this article and that I secured permission from the other co-author, Professor Cody Friesen, to include this work in my dissertation and that the American Chemical Society extends permission to authors to include full copies of journal articles in their dissertation or thesis.

Pt{111} and Au{111} Electrocapillarity: Interphase Structure, the pzc, and Oxygen Reduction

Th. Heaton and C. Friesen*

School of Materials, Arizona State University, Tempe, Arizona 85287

Received: February 8, 2007; In Final Form: June 22, 2007

Large changes in stress (of order GPa) are observed with relatively modest variations in applied potential (on the order of 500 mV), even in nonspecifically adsorbing electrolyte solutions. Here we present the electrocapillarity behavior (in situ surface stress evolution) of Pt{111} and Au{111} electrodes. We relate the magnitude and anodic/cathodic hysteresis of the stress−potential behavior to the potential dependent water orientation at the electrode/electrolyte interface. We show that our results are strongly correlated to previously published infrared spectroscopy data on the potential dependence of interphase structure. Finally, measurements of Pt in oxygen saturated electrolytes are presented, allowing for a direct comparison between features in the surface stress behavior and the "turn-on" potential for oxygen reduction. We found that oxygen reduction occurs only once the potential was cathodic enough to begin depleting the interface of oxygen-down oriented water.

Introduction

In recent years, surface stress measurements have become a common technique for monitoring a variety of processes in fluid and vacuum environments. Just a few examples include the measurement of stress evolution during thin film growth,[1−5] DNA binding and hybridization processes,[6−9] MEMS devices,[10] and biological process monitoring.[11]

A large amount of work has been performed in aqueous environments where changes in surface stress have been monitored as a function of adsorption processes,[12−16] thin film growth,[13,17,18] and corrosion.[19] In addition, surface stress−potential behavior has been used for the actuation of nanoporous metal structures with strains comparable to those of piezoelectric devices, but at much lower voltages.[20] Studying and understanding the causes of surface stress changes in electrochemical systems presents a significant challenge because there are always a variety of processes occurring.

In this work, we examine surface stress changes as a function of applied electrochemical potential under conditions where only double-layer effects should be observed. Figure 1 shows two representative electrocapillarity curves for Au{111} and Pt{111} in $HClO_4$ and NaF deareated aqueous electrolytes, respectively. These electrolyte−electrode pairs were chosen as prototypical nonspecifically adsorbing systems with large double-layer regimes. Note that in both plots the total change in surface stress is approximately 0.4 N/m, which if divided by a reasonable surface thickness (∼3 Å) gives a bulk stress on the order of 1 GPa. Because of the magnitude of the stress changes, it is currently difficult to interpret these measurements in electrochemical environments. This fact combined with the large interest in using surface stress as a tool for the study of electrochemical systems suggests the need to develop a full understanding of the fundamental aspects of surface stress at the solid electrode/electrolyte interface.

An important feature of the electrocapillarity curves in Figure 1 is the surface stress behavior at the potential of zero charge (pzc). The *surface stress* is not maximized and the slope is significant at the pzc. This behavior is different from that of the *surface free energy*, which is maximized at the pzc, as defined by the Lippmann equation.[26]

* Corresponding author. E-mail: cfriesen@asu.edu.

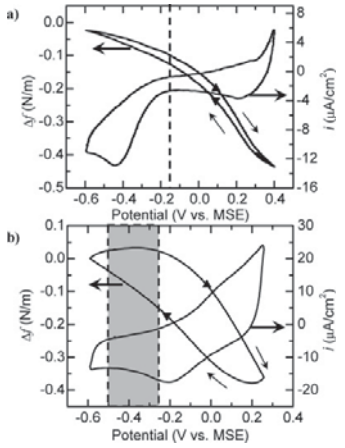

Figure 1. Cyclic voltammetry and electrocapillarity behavior for (a) Au{111} in 0.5 M $HClO_4$ and (b) Pt{111} in deaerated 0.1 M NaF systems. Scan rate for both systems was 20 mV/s. The up-arrow markers are $(\partial^2 f/\partial V^2)^{max}_{anodic}$, and the down-arrow markers are $(\partial^2 f/\partial V^2)^{max}_{cathodic}$. The dashed line and shaded region indicate the value and range of previously reported values for the pzc (at pH 6 or corrected for pH shift).[21−25]

The cyclic surface stress behavior for Au and Pt differ significantly, with Pt displaying a large hysteresis and Au showing almost no difference between anodic and cathodic scans. We show that the observed hysteresis is not time-dependent and that it is connected to the strength of the water−metal interaction. We connect the extensive work done on the potential dependent orientation of water molecules at the electrode−electrolyte interface[21,27−33] to the observed surface

10.1021/jp071109x CCC: $37.00
Published on Web 09/13/2007

stress changes and demonstrate that flattening of the surface stress−potential behavior at the anodic end of the plots in Figure 1 are due to the saturation of water dipole orientation.

We discuss all of our results in the context of oxygen electroreduction on Pt{111}. We present data in oxygen saturated electrolytes that suggest that dipole saturation at the electrode−electrolyte interface prevents dissolved oxygen from accessing the electrode. And we propose that oxygen reduction does not occur until a sufficiently cathodic potential is reached to decrease the population of oxygen-down oriented water at the interface. Finally, all of the results are tied together with work function shift data available in both vacuum and electrochemical environments.

Background

Water−Metal Interface. The structure of water adsorbed from the gas phase onto metal surfaces has been studied extensively.[34,35] As described in detail by Doering and Madey,[36] a $(\sqrt{3} \times \sqrt{3})$R30° bilayer structure is formed when water is adsorbed on a number of close packed metal surfaces. The structure strongly resembles the (0001) face of I_h ice, with hexagonal rings of molecules made up of alternating oxygen-down oriented molecules and molecules with one oxygen−hydrogen pair lying in the plane of the surface with the other hydrogen pointing normal to the surface.[37]

The $(\sqrt{3} \times \sqrt{3})$R30° structure has been reported in the case of both Au(111) and Pt(111).[34,37] In the case of Pt(111), the structure has been observed by a range of techniques including STM[37,38] and LEED.[39−42] Strong evidence of an ordered structure on Au(111) does not exist. Gewirth's group performed STM studies on H_2O/Au(111) and observed an amorphous adlayer.[43] Additionally, they point out that temperature programmed desorption (TPD) work on Au[43,44] results in a single desorption peak in concert with other amorphous water−metal systems and unlike the two-peak observations in well-known ordered systems such as Pt(111). However, more recently, Pirug et al. observed the $(\sqrt{3} \times \sqrt{3})$R30° structure on Au(111).[45] The lack of agreement between groups may serve as a relative measure of the strength of ordering in the case of Au(111) as compared to that of Pt(111).

Work Function Downshift and The Potential of Zero Charge. Adsorption of water on metallic surfaces tends to decrease the work function of the metal. In the case of Pt, a downshift of approximately −1.0 eV is observed; and for Au the change is on the order of −0.6 eV.[34,46,47] Owing to the degree of orientation in the adsorbed layer, a decrease in work function corresponds to water dipoles being preferentially oriented with the oxygen end closer to the surface. The magnitude of the given shifts demonstrates that adsorbed water is much more strongly oriented on Pt surfaces than on that of Au, in agreement with structural observations. The in-vacuum work function shift data correlates well with Trasatti's work on the connection between the degree of dipole alignment at the interface and the position of the pzc.[48] Trasatti arrives at the expression $V_{pzc} = 1/q\ \Phi - 4.61 - 0.4\alpha$, where q is the charge of an electron, Φ is the vacuum work function (in eV), and α describes the degree of orientation at the electrode−electrolyte interface. He assigns a value of $\alpha = 1$ for transition metals and $\alpha = 0$ for Au and Cu, based on empirical results. The observed difference in work function downshift between Pt and Au in vacuum of 0.4 eV corresponds well with the Trasatti picture and further supports the existence of a strong (weak) preference for orientation of water dipoles on Pt (Au).

Interphase Structure and Applied Potential. Several groups have performed spectroscopic studies on the water−electrode interface under potentiostatic control.[21,27−30] The results of these works are in agreement with the classical picture of surface charge dependent interfacial water orientation.[31−33] At potentials positive (negative) of the pzc, water molecules are oriented oxygen down (up), and at the pzc water molecules have an average net dipole near zero.[21] The results of refs 21 and 28 are reproduced for comparison with our data in Figures 2 and 3 in the Results section.

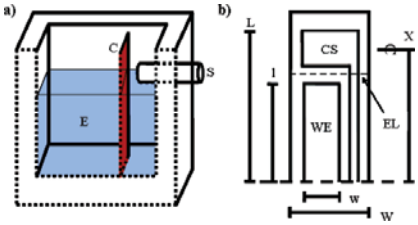

Figure 2. Schematic illustrations of the experimental cell (cross section) (a) and the patterned electrode sample (b). The cell included the cantilevered sample (C), the liquid electrolyte (E), and the capacitive sensor (S) fixed in a single construction. The sample geometry is also shown with the important dimensions (*L*, *l*, *X*, *W*, and *w*) defined. The level of the electrolyte (EL) during the experiment is also shown above the working electrode (WE) and below the capacitive sense (CS) electrode.

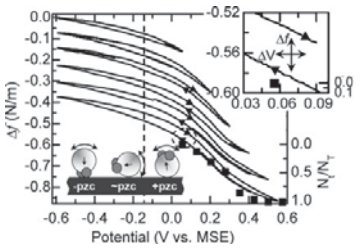

Figure 3. Surface stress change vs potential for Au{111} in 0.5 M $HClO_4$. The lower scan limit was −590 mV vs MSE. The upper scan limits are 60, 210, 310, 410, 510, and 560 mV. Scan rate, 20 mV/s. The inset contains the *coercivity* (ΔV) and the *retentivity* (Δf) of the electrode. The up-arrow markers are $(\partial^2 f/\partial V^2)^{max}_{anodic}$, and the down-arrow markers are $(\partial^2 f/\partial V^2)^{max}_{cathodic}$. Squares represent the Ataka et al.[21] water orientation data. The dashed line indicates a previously reported value of the pzc.[21]

Thermodynamic Formalism

Surface Stress. The thermodynamic surface stress is intrinsic to the formation of a solid surface because it describes the excess free energy associated with surface deformation and is given by the Shuttleworth equation[49]

$$f_{ij} = \gamma\delta_{ij} + \frac{\partial\gamma}{\partial\epsilon_{ij}} \tag{1}$$

where f_{ij}, γ, δ_{ij}, and ϵ_{ij} are the surface stress, surface energy, Kronecker delta, and surface strain, respectively. For a surface of ≥threefold symmetry, the Shuttleworth equation simplifies to a scalar (e.g., $f = \gamma + \partial\gamma/\partial\epsilon$).

Clean metal surfaces in vacuum have surface stress values in the range of 1−6 N/m. Thermodynamics places no restrictions on the sign of the surface stress, but typically for close-packed surfaces f is positive or "tensile" and larger in magnitude

than γ. The magnitude of the surface stress is sensitive to any modification to the surface. For example, adsorption processes not only modify this quantity but can also change the sign of surface stress.[12]

Electrocapillarity Behavior in Adsorbing/Nonadsorbing Electrolytes. Vasiljevic et al.[14] were the first to contrast the interfacial free energy and surface stress changes for 1×1 bulk-terminated Au(111) electrodes in both weakly and strongly adsorbing electrolytes. The two electrolytes were the extreme cases: one contained sulfate anions, which are known to strongly adsorb, and the other contained fluoride anions, the prototypical nonadsorbing or (very) weakly adsorbing anion.

It is generally not possible to directly monitor changes in interfacial free energy in an experiment. However, by examining the chronocuolometry of the Au(111) single crystal electrode the authors deduced the change in γ as a function of potential by integrating $d\gamma = -q\ dV$. They found the pzc to occur at about -130 mV vs MSE in Na_2SO_4 and -120 mV in NaF, corresponding to the maximum in the γ versus potential plot.

Variation of Surface Stress with Interphase Structure. We will demonstrate in the Results and Discussion sections that the large surface stress changes anodic of the pzc are most likely due to the dipolar alignment of the water molecules (oriented oxygen-down). The Gibbs adsorption equation for a solid at constant temperature is given by

$$d\gamma = 2(f - \gamma)d\epsilon - q\ dV - \Gamma_i\, d\mu_i \qquad (2)$$

where γ is the surface energy, f is the surface stress, ϵ *is* the equibiaxial elastic strain ($\epsilon = \epsilon_{xx} = \epsilon_{yy}$), μ_i and Γ_i are the chemical potential and specific surface excess of species i, dV is the change in applied voltage, and q is the charge.[50] For solid surfaces, the surface stress term is required to appropriately treat the ability of solids to support shear stress. Adding a polarization work term to eq 2 and taking the Legendre Transform $d(\gamma - \Gamma_i\mu_i)$ gives

$$d(\gamma - \Gamma_i\mu_i) = 2(f - \gamma)\, d\epsilon + \left(\rho \frac{1}{l_{DL}} - q_{dis}\right)dV + \mu_i\, d\Gamma_i \qquad (3)$$

where ρ is the surface excess polarization, and l_{DL} is the thickness of the double layer. The addition of the polarization term implies the partitioning of the double-layer capacity into polarization and free charge displacement, q_{dis}, terms. At fixed Γ_i there is the Maxwell Relation

$$\left(\frac{\partial f}{\partial V}\right)_\epsilon = \left(\frac{\partial \gamma}{\partial V}\right)_\epsilon + \frac{1}{2l_{DL}}\left(\frac{\partial \rho}{\partial \epsilon}\right)_V - \frac{1}{2}\left(\frac{\partial q_{dis}}{\partial \epsilon}\right)_V = \left(\frac{\partial \gamma}{\partial V}\right)_\epsilon - \frac{1}{2l_{DL}}\left(\frac{\partial \rho}{\partial V}\right)_\epsilon \left(\frac{\partial V}{\partial \epsilon}\right)_\rho + \frac{1}{2}\left(\frac{\partial q_{dis}}{\partial V}\right)_\epsilon \left(\frac{\partial V}{\partial \epsilon}\right)_{q_{dis}} \qquad (4)$$

At the pzc, γ is maximized; and at fixed Γ_i, $(\partial V/\partial \epsilon)_{\rho;q}$ is reasonably taken as constant and may be approximated by a number of approaches.[14,51,52] At the pzc, under these conditions

$$\left(\frac{\partial f}{\partial V}\right)_\epsilon = \frac{1}{2}\left(-\frac{1}{l_{DL}}\frac{\partial \rho}{\partial V} + C_{dis}^{pzc}\right)_\epsilon \left(\frac{\partial V}{\partial \epsilon}\right) \qquad (5)$$

Experimentally, it has been observed that $(\partial\rho/\partial V)^{+pzc} > (\partial\rho/\partial V)^{-pzc}$ because water is more readily polarized oxygen-down anodic of the pzc than it is polarized hydrogen-down cathodic of the pzc.[21] It follows then that $(\partial f/\partial V)^{+pzc} > (\partial f/\partial V)^{-pzc}$ so that a transition in slope should occur at the pzc. Therefore, under these conditions a maximum in $\partial^2 f/\partial V^2$ should be experimentally observed at the pzc. It is important to note that this is in the absence of specific adsorption. When specifically adsorbing anions are present, one would expect that the maximum in $\partial^2 f/\partial V^2$ would occur positive of the pzc. We will refer to maxima in $\partial^2 f/\partial V^2$ as $(\partial^2 f/\partial V^2)^{max}$. In Figure 1, markers have been placed at the points of $(\partial^2 f/\partial V^2)^{max}$ on both the anodic and cathodic branches of the stress−potential plots.

In the absence of adsorption, the maximum value of $\partial f/\partial V$ at the pzc is about -0.6 C/m^2. Examining the work of Friesen et al.[13] and Vasiljevic et al.[14] and extracting $\partial f/\partial V$ in the cases of Au(111) electrodes in NaF, $NaClO_4$, Na_2SO_4 electrolytes provides values of -0.94, -0.85, and -1.8 C/m^2, respectively. These values are larger than expected from pure double-layer effects, and this was interpreted by Vasiljevic et al. as owing to adsorption processes.

Experimental Section

The in situ surface stress monitoring is carried out by a cantilever curvature based device. The device is unique in that to measure cantilever tip deflection it utilizes a capacitive technique that allows for subnanometer deflection sensitivity and >1 kHz time base resolution.[1,53] The PTFE cell, shown schematically in Figure 2a, is machined to hold both the capacitance sensor (S) and vertically oriented cantilevered electrode (C); this monolithic design significantly reduces drift and sample placement error. The capacitance sensor must operate in air, so the electrochemically active area and sensing pad are separate elements and are created by depositing through a hard mask, as shown in Figure 2b. The samples are moved immediately from the UHV system to the carefully prepared electrochemical environment. For each sample, a calibration is performed with a straightforward gravitational technique. Because the sample holder, cell, and detector are in a single unit, calibration is performed by orienting the plane of the cantilever beam so that Earth's gravity is collinear with its bending direction; doing this for both the device facing up and for the device facing down, we get a response associated with the weight of the cantilever. Performing the calibration in this way yields the governing relation for the change in surface stress per change in device output voltage

$$\frac{\Delta f^* h_f}{\Delta V} = \left(\frac{W}{w}\right)\left(\frac{\rho_s^* a_g}{6(1-\upsilon)}\right)\left(\frac{X^2(6L^2 - 4LX + X^2)}{\frac{l^2}{2} + l(X - l)}\right)\left(\frac{1}{\Delta V_{tot}}\right) \qquad (6)$$

where ΔV_{tot} is the stress voltage, ρ_s is the density of the substrate, a_g is the gravitational constant, υ is Poisson's ratio, and W, w, X, L, and l are dimensional parameters defined by the sample geometry as shown in Figure 2b. Calibrating the measurement in this way removes the elastic moduli of the cantilever and a squared term in cantilever thickness, two significant sources of error in wafer curvature stress measurements.

The cantilever/electrode assembly consisted of an 80 μm thick cleaned cover glass substrate and patterned metallic film. Samples were prepared in a 5×10^{-10} Torr base pressure ultrahigh vacuum system (UHV) fitted with two UHV compatible DC magnetron sources (Angstrom Sciences). The electrodes were prepared by first depositing 10 nm of Cr as an adhesion layer followed by a Pt or Au deposition to 100 nm at approximately 1 Å/s. Under the stated growth conditions, the films have a strong {111}-texture. In all cases, the working electrode surface area is 2 cm^2.

The cyclic voltammetry was performed with a BASi Epsilon Potentiostat (model no. E2-020000). The corresponding data (potential, current, and stress) was collected via a Nicolet Sigma

60 oscilloscope (model no. 986A0147). The working, reference, and counter electrodes were placed in the cell prior to the loading of the electrolyte in the cell. The systems considered in these experiments were Au in 0.5 M $HClO_4$, Pt in 0.1 M NaF, and Pt in 0.1 M $HClO_4$. In all cases, the electrolyte was deareated with nitrogen or saturated with oxygen in a separate deareation cell and then transferred to the PTFE cell with a corresponding gas overpressure.

All of the glassware, the PTFE electrochemical cell, and the Pt wire counter electrode utilized in the experiment and preparation of the samples and electrolyte were cleaned in heated, concentrated HNO_3 and H_2SO_4 baths followed by rinsing in 18 MΩ water. In addition, the platinum counter electrode was flame annealed in a hydrogen flame and rinsed again in the 18 MΩ water immediately before being placed in the PTFE cell. For all experiments, a MSE (+640 mV vs SHE) reference electrode (Princeton Applied Research − Model no. G0093) was used.

Results

Figure 3 shows a progression of surface stress curves for Au in 0.5 M $HClO_4$. The curves are shifted for clarity, and each subsequent curve corresponds to an increase in the anodic most potential. A representative cyclic voltammetry curve is shown in Figure 1a. Because the hysteresis in this case is so small, the loops were plotted separately, also elucidating the nearly identical character of the curves. As the upper bound of the applied potential increases above the pzc, the stress begins to turn sharply compressive. The potential at which $(\partial^2 f/\partial V^2)^{max}$ occurs has been marked, in curves with a tractable maximum, (up-arrows, anodic; down-arrows, cathodic). The average $(\partial^2 f/\partial V^2)^{max}$ for the cathodic sweep is ∼68 mV, and that for the anodic sweep is ∼94 mV. The average value is ∼81 mV, and we take this as the potential at which there is no net dipole orientation. For Au, both anodic and cathodic scans are similar and the hysteresis is small. As shown in the inset, the average difference between the anodic and cathodic $(\partial^2 f/\partial V^2)^{max}$ is ΔV = ∼25 mV and Δf = ∼0.04N/m. Also included in Figure 3 is spectroscopic data from Ataka et al. (squares), which describes the degree of orientation of water dipoles at the Au−electrolyte interface (identical electrolyte) as a function of potential.[21] The ordinates for this data range between 1 (perfectly oriented) and 0 (no preferential orientation). Note the striking similarity in curve shape between the orientation data and our stress data. Specifically, there is only an ∼80 mV difference in potential at the inflection points of the two sets of data (determined by polynomial fits of both data sets). Also, our $(\partial^2 f/\partial V^2)^{max}$ potential corresponds to the potential at which the Ataka et al. data goes to zero net orientation. The previously reported value of the pzc is shown as a vertical dashed line[21] and is approximately 200 mV negative of both our $(\partial^2 f/\partial V^2)^{max}$ potential and the potential where Ataka et al. also observes no net orientation.

The Pt system behaves quite differently from the Au system, with a large hysteresis observed. A representative cyclic voltammogram from the Pt{111} in 0.1 M NaF system is shown in Figure 1b.

As in Figure 3, Figure 4 represents a progression of increasing anodic potential. The qualitative characteristics of these curves are strikingly different from those of the Au system. The electrocapillarity loop is significantly wider in the case of Pt. The average $(\partial^2 f/\partial V^2)^{max}$ potential in the cathodic direction was −220 mV as compared to the anodic scan, which had an average of −25 mV, a ΔV of 195 mV, and a Δf of 0.15 N/m.

Figure 4 also includes data from Habib et al.[28] (squares) plotted with the same ordinate range as that in Figure 3. Again, the similarity of the spectroscopic orientation data and our electrocapillarity measurements is striking, especially noting the saturation range at the anodic end of the curves.

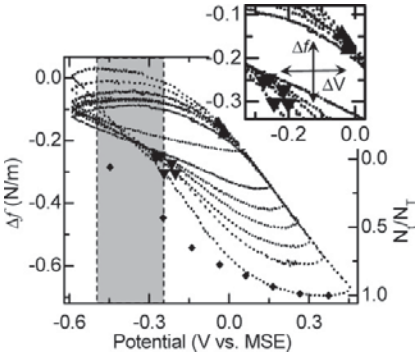

Figure 4. Surface stress change vs potential for Pt{111} in 0.1 M NaF. The lower scan limit was −590 mV vs MSE. The upper scan limits are −40, 60, 160, 210, 260, 310, 360, and 460 mV. Scan rate, 20 mV/s. Diamonds represent the Habib and Bockris[28] water orientation data. The shaded region indicates previously reported values of the pzc.[22−25]

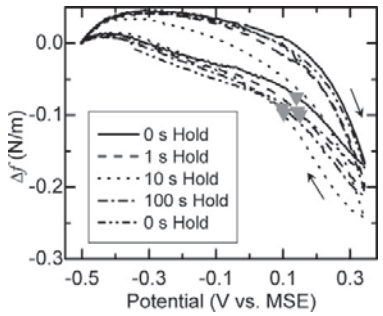

Figure 5. Plot of surface stress behavior for several potential hold times for Pt{111} in 0.5 M $HClO_4$ system. The lower scan limit was −500 mV vs MSE. Potentiostatic holds imposed at upper potential limit (350 mV) for 0, 1, 10, 100, and 1 s (progressively through cycles during a single voltammetric measurement). Scan rate, 20 mV/s.

Figure 5 represents a set of surface stress measurements, each curve having a hold at the anodic limit of the scan for 0, 1, 10, 100, and 0 s, respectively. This data demonstrates that the hysteretic observations are not temporal in nature because the curves are all qualitatively the same. The hold periods may account for the subtle changes in the shape of the stress−potential loop; however, the range of stress values is very similar and the variance is within experimental error. The total change in surface stress over this potential range varies from 0.28 N/m (100 s hold) to 0.21 N/m (1 s hold). Most importantly, there is no change in the surface stress behavior in the cathodic scan due to any hold time imposed. This is demonstrated by the small cluster of the $(\partial^2 f/\partial V^2)^{max}_{cathodic}$ markers.

The correlation between the electrocapillarity and water orientation data in Figures 3 and 4 led the authors to consider electrocapillarity in oxygen saturated solutions. Figure 6 presents the results for Pt{111} immersed in 0.1 M $HClO_4$. The cyclic voltammetry and surface stress are displayed; the surface stress is relatively noisy due to an oxygen flow kept over the cell

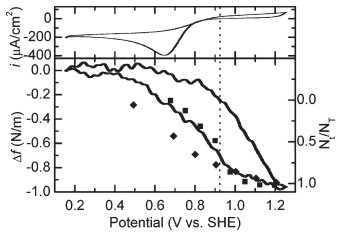

Figure 6. Plot of cyclic voltammetry and surface stress behavior for Pt{111} in an oxygen saturated 0.1 M $HClO_4$ system. The lower scan limit was −500 mV vs MSE. Scan rate, 20 mV/s. Square markers are water orientation data from Ataka et al. (Au in 0.5 M $HClO_4$),[21] and diamonds represent water orientation data reproduced from Habib and Bockris with a +300 mV shift to account for pH difference (Pt in 0.1 M NaF).[28] The dotted line is the oxygen reduction turn-on potential.

during the experiment. Reproduced again on this plot is the Ataka et al.[21] and Habib and Bockris[28] data. The Habib et al. data is presented with a shift of +300 mV to account for the pH difference in the present and cited work. Note again that the qualitative shape of the cathodic scan is strikingly similar to the water orientation data. Perhaps most interesting is the correlation between the "turn-on" potential of ~910 mV versus SHE for oxygen reduction and the potential at which the oxygen-down saturated interphase begins to diminish.

Discussion

In this work, we have examined the electrocapillarity behavior of Au{111} and Pt{111} in aqueous, nonspecifically adsorbing electrolytes. As discussed in the Introduction and Background sections, it is expected from the appropriate Gibbs adsorption equation that the thermodynamic surface stress does *not* go through a maximum at the pzc, unlike the surface free energy. However, the observed magnitude of $\partial f/\partial V$ at the pzc is significantly larger than that expected from double-layer effects (at about -0.6 C/m^2), even in electrolytes where anion specific adsorption is not expected. In the absence of specific adsorption, we suggested that a measure of the pzc is given by the $(\partial^2 f/\partial V^2)^{max}$ potential and have shown that in all cases our values were positive of previously reported values. The observed differences between our measure of the pzc and those reported on our plots are most likely due to a combination of differences in electrode preparation, pH, the large variance in reported values of the pzc as a function of measurement technique, and effects related to specific adsorption.

Trasatti empirically established that the work function of a metal is correlated to its pzc.[48] On the basis of the discussion in the Background section comparing Trasatti's pzc expression and work function downshift data for Au and Pt, it appears that the capacity for interfacial water orientation to modify the work function is on the order of 0.4α eV, with $\alpha = 0$ and $\alpha = 1$ for Au and Pt, respectively. In-vacuum work performed by ref 54 also supports the idea that dipoles dominate the work function downshift for the H_2O/Pt{111} system, with essentially the entire downshift occurring within the first 2 ML of adsorption. If polar effects are the dominant source of the work function shift, then this result correlates well with Trasatti's interpretation. Figures 3 and 4 show a strong correlation between the surface stress−potential behavior and the reproduced spectroscopy data for both the Au and Pt systems. Between the most anodic potential (fully oriented) and the pzc (no preferential orientation), the observed surface stress change is approximately −0.3 N/m (Au) and −0.4 N/m (Pt).

The work function shift associated with going from nonoriented to fully saturated orientation is $\Delta\Phi \approx -0.4$ eV, and our measured change in surface stress going from the pzc to a potential at which fully oriented dipoles are expected is $\Delta f \approx -0.4$ N/m. The observed change in surface stress associated with a change in work function may then be taken as $\Delta f/\Delta\Phi \approx 6 \times 10^{18}$ m^{-2}. Lang and Kohn[55] calculated the work function of jellium over a range of charge densities, Needs and Godfrey[56] did the same for surface stress. Combining these two data sets provides the variation of f with respect to Φ in the charge density range of Pt ($r_s \approx 2.8a_0$) and Au ($r_s \approx 3.0a_0$), giving a value of $\Delta f/\Delta\Phi \approx 3 \times 10^{18}$ m^{-2}. This number could plausibly represent the ability for work function shifts to alter surface stress from purely free-electron considerations. The agreement between the above two values of $\Delta f/\Delta\Phi$ may be fortuitous. However, considering the very different paths used to obtain them, it is possible that potential induced reorientation of water at the electrode interface could alone account for the measured surface stress change positive of the pzc.

The $(\sqrt{3} \times \sqrt{3})$R30° structure of the water−metal interface is well defined and experimentally verified in the case of Pt(111), whereas in the case of Au(111) strong evidence of a well-ordered interface is lacking. Also, TPD results discussed in the Background section, in which water was observed to most likely be amorphous on Au(111) and ordered on Pt(111), confirm this difference. These results combined with the overlap of Pt 5d states and unoccupied water states and the lack of any such interaction with the much deeper Au d-electrons, provide experimental and conceptual evidence for a significantly stronger interaction of water with Pt than water with Au.

A strong preference for ordering also suggests a strong dipole−dipole interaction of water molecules at the interface. Comparing the electrocapillarity curves for Pt and Au, the most significant qualitative difference is the magnitude of hysteresis in the cyclic stress curves. If we make an analogy to ferroelectric materials, then a measure of the *coercivity* is given by ΔV, as shown in Figures 3 and 4. In the same way, a measure of *retentivity* of polarization is given by Δf, as marked in Figures 3 and 4 (because retentivity is measured at the point of zero net polarization, the assumption made here is that the hysteresis in $(\partial^2 f/\partial V^2)^{max}$ is symmetric about zero so that the midpoint of ΔV provides this measure). It is classically understood that the pzc (in the absence of specific adsorption) and the potential at which there is zero net solvent orientation occur at the same potential. The Δf (retentivity) at the potential of zero orientation provides a measure of polarization remanence and a measure of the strength of the water−metal interaction. As expected from the above arguments, the Δf and ΔV values are small in the case of Au{111} ($\Delta f \sim 0.04$ N/m, $\Delta V \sim 26$ mV) and considerable for Pt{111} ($\Delta f \sim 0.15$ N/m, $\Delta V \sim 195$ mV).

To make the case that the observed hysteresis is not temporal in nature, we performed the experiments in Figure 5. To determine whether the hysteresis was time dependent, the potential was held at the anodic limit of the scan range. We found only a small variation in hysteresis going from no anodic hold to a 100 s hold.

The sum of this work is that the potential dependent water dipole orientation appears to have a large effect on the electrocapillarity behavior of solid electrodes. The magnitude of the surface stress positive of the pzc and the previously reported work function changes demonstrate that oxygen-down oriented water interacts strongly with metal surfaces. The

question that arose during this work was the following: can an interface saturated with potential induced oxygen-down water dipoles block oxygen reduction? And, is the origin of the overpotential for oxygen reduction related to this blocking? In Figure 6, it was shown that in oxygen saturated electrolytes, oxygen reduction on Pt{111} does not occur until the surface stress begins to decrease in magnitude (become less compressive) and the dipole saturation decreases. The observed turn-on potential of ~910 mV is approximately 300 mV negative of the reversible potential for oxygen reduction. If an oxygen-down saturated interface is playing a significant role, then the 0.4 eV potential drop across the oriented interphase is large enough to account for the required overpotential. Additionally, the saturation of an electrified interface with oriented water molecules tends to "pack" the first layer of water into a high density phase.[57] This packing could physically block molecular oxygen from reaching the electrode surface.

Oxygen electroreduction on Pt has been studied by many groups over a long period of time.[58−66] Much of that work has focused on the need to understand the origins of the large overpotential for this reaction. The typical outcome of these works is the suggestion of a reaction pathway and/or a rate limiting step in the reaction. However, the authors have not found any prior work suggesting that the saturation and subsequent packing of the interface with oriented water molecules could create both a deleterious potential drop and physically block oxygen from reaching the interface.

Concluding Remarks

In summary, we have shown that electrocapillarity induced surface stress changes in nonspecifically adsorbing electrolytes are large over modest potential changes. We have shown that electrocapillarity in the Au and Pt systems are significantly different and have described a method for quantifying and comparing the resulting hysteretic loops. By comparing these surface stress results to published spectroscopic data, we have proposed a means of observing water dipole orientation at the polarized water/electrode interface. This potential dependent structure of the interphase appears to have a dominant role in the electrocapillarity of solid electrodes positive of the pzc. Additionally, we have observed in oxygen saturated environments that the onset of oxygen reduction occurs only when the degree of oxygen-down saturated water at the interface is decreased. We have proposed that anodic of this point the saturated interface may retard oxygen reduction by both blocking molecular oxygen from the electrode and by the dipole induced potential drop.

Our future work in this area will focus on the verification of our proposed mechanism for the retardation of oxygen reduction by an oxygen-down saturated water/electrode interface. Ongoing work will involve electrocapillarity of Pt electrodes as a function of, for example, pH, in order to further explore this subject.

Acknowledgment. We gratefully acknowledge the Department of Energy, Basic Energy Sciences for support through contract no. DE-FC02-05ER46257

References and Notes

(1) Friesen, C.; Thompson, C. V. *Phys. Rev. Lett.* **2004**, *93*, 056104.
(2) Friesen, C.; Thompson, C. V. *Phys. Rev. Lett.* **2002**, *89*, 12.
(3) Friesen, C.; Seel, S. C.; Thompson, C. V. *J. Appl. Phys.* **2004**, *95*, 1011.
(4) Koch, R. *J. Phys. Condens. Matter* **1994**, *6*, 9519.
(5) Floro, J. A.; Hearne, S. J.; Hunter, J. A.; Kotula, P.; Seel, S. C.; Thompson, C. V. *J. Appl. Phys.* **2001**, *89*, 4886.
(6) Fritz, J.; Baller, M. K.; Lang, H. P.; Rothuizen, H.; Vettiger, P.; Meyer, E.; Guntherodt, H. J.; Gerber, Ch; Ginzewski, J. K. *Science* **2000**, *288*, 316.
(7) Hood, L.; Heath, J. R.; Phelps, M. E.; Lin, B. *Science* **2004**, *306*, 640.
(8) Majumdar, A. *Disease Markers* **2002**, *18*, 167.
(9) Cho, Y. K.; Kim, S.; Lim, G.; Granick, S. *Langmuir* **2001**, *17*, 7732.
(10) Seel, S. C.; Thompson, C. V. *Rev. Sci. Instrum.* **2005**, *76*, 075103.
(11) Ziegler, C. *Anal. Bioanal. Chem.* **2004**, *379*, 946.
(12) Haiss, W. *Rep. Prog. Phys.* **2001**, *64*, 591.
(13) Friesen, C.; Dimitrov, N.; Cammarata, R. C.; Sieradzki, K. *Langmuir* **2001**, *17*, 807.
(14) Vasiljevic, N.; Trimble, T.; Dimitrov, N.; Sieradzki, K. *Langmuir* **2004**, *20*, 6639.
(15) Weissmuller, J.; Kramer, D. *Langmuir* **2005**, *21*, 4592.
(16) Viswanath, R. N.; Kramer, D.; Weissmuller, J. *Langmuir* **2005**, *21*, 4604.
(17) Sotirova, G.; Sarnev, S.; Armyanov, S. *Electrochim. Acta* **1989**, *34*, 1237.
(18) Serre, C.; Yaakoubi, N.; Martinez, S.; Perez-Rodriguez, A.; Morante, J. R.; Esteve, J.; Montserrat, J. *Sens. Actuators, A* **2005**, *123*−*124*, 633.
(19) Nelson, J. C.; Oriani, R. A. *Corros. Sci.* **1993**, *34*, 307.
(20) Weissmuller, J.; Viswanath, R. N.; Kramer, D.; Zimmer, P.; Wurschum, R.; Gleiter, H. *Science* **2003**, *300*, 312.
(21) Ataka, K.; Yotsuyanagi, T.; Osawa, M. *J. Phys. Chem.* **1996**, *100*, 10664.
(22) Bockris, J. O'M.; Argade, S. D.; Gileadi, E. *Electrochim. Acta* **1969**, *14*, 1259.
(23) Iwasita, T.; Xia, X. *J. Electroanal. Chem.* **1996**, *411*, 95.
(24) Climent, V.; Attard, G. A.; Feliu, J. M. *J. Electroanal. Chem.* **2002**, *532*, 67.
(25) Attard, G. A.; Ahmadi, A. *J. Electroanal. Chem.* **1995**, *389*, 175.
(26) Grahame, D. C. *Chem. Rev.* **1947**, *41*, 441.
(27) Bockris, J. O'M.; Jeng, K.-T. *Adv. Colloid Interface Sci.* **1990**, *33*, 1.
(28) Habib, M. A.; Bockris, J. O'M. *Langmuir* **1986**, *2*, 388.
(29) Toney, M. F.; Howard, J. N. et al. *Surf. Sci.* **1995**, *335*, 326.
(30) Schultz, Z. D.; Shaw, S. K.; Gewirth, A. A. *J. Am. Chem. Soc.* **2005**, *127*, 15916.
(31) Bockris, J. O'M.; Khan, S. U. M. *Surface Electrochemistry: A Molecular Level Approach*; Plenum Press: New York, 1993; Chapter 2.
(32) *Structure of Electrified Interfaces*; Lipkowski, J., Ross, P. H., Eds.; VCH: New York, 1993.
(33) Damaskin, B. B.; Frumkin, A. N. *Electrochim. Acta* **1974**, *19*, 173.
(34) Thiel, P. A.; Madey, T. E. *Surf. Sci. Rep.* **1987**, *7*, 211.
(35) Henderson, M. A. *Surf. Sci. Rep.* **2002**, *46*, 1.
(36) Doering, D. L.; Madey, T. E. *Surf. Sci.* **1982**, *123*, 305.
(37) Clay, C.; Hodgson, A. *Curr. Opinion Solid State Mater. Sci.* **2005**, *9*, 11.
(38) Morgenstern, M.; Muller, J.; Michely, T.; Comsa, G. *Z. Phys. Chem. Int. J. Res. Phys. Chem. Chem. Phys.* **1997**, *198*, 43.
(39) Firment, L. E.; Somorjai, G. A. *J. Chem. Phys.* **1975**, *63*, 1037.
(40) Firment, L. E.; Somorjai, G. A. *Surf. Sci.* **1976**, *55*, 413.
(41) Tucker, C. W., Jr. *J. Appl. Phys.* **1964**, *35*, 1897.
(42) Fisher, G. B.; Gland, J. L. *Surf. Sci.* **1980**, *94*, 446.
(43) Ikemiya, N.; Gewirth, A. A. *J. Am. Chem. Soc.* **1997**, *119*, 9919.
(44) Kay, B. D.; Lykle, K. P.; Creighton, J. R.; Ward, S. J. *J. Chem. Phys.* **1989**, *91*, 5120.
(45) Pirug, G.; Bonzel, H. P. *Surf. Sci.* **1998**, *405*, 87.
(46) Fisher, G. B. General Motors Research Publication No. 1982, GMR-4007/PCP-171.
(47) Heras, J. M.; Viscido, L. *Appl. Surf. Sci.***1980**, *4*, 238.
(48) Trasatti, S. *J. Electroanal. Chem.***1971**, *33*, 351.
(49) Shuttleworth, R. *Proc. R. Soc. London, Ser. A* **1950**, *63*, 444.
(50) Couchman, P. R.; Davidson, C. R. *J. Electroanal. Chem.* **1977**, *85*, 407.
(51) Ibach, H. *Physics of Surfaces and Interfaces*; Springer Press: New York, 2006.
(52) Umeno, Y.; Elsasser, C.; Meyer, B.; Gumbsch, P.; Nothacker, M.; Weissmüller, J.; Evers, F. *Europhys. Lett.* **2007**, *78*, 13001.
(53) Friesen, C.; Seel, S. C.; Thompson, C. V. *J. Appl. Phys.* **2004**, *93*, 1011.
(54) Harnett, J.; Haq, S.; Hodgson, A. *Surf. Sci.***2003**, *528*, 15.
(55) Lang, N. D.; Kohn, W. *Phys. Rev. B.* **1971**, *3*, 1215.
(56) Needs, R. J.; Godfrey, M. J. *Phys. Rev. B.* **1990**, *42*, 10933.
(57) Toney, M. F.; Howard, J. N. et al. *Nature* **1994**, *368*, 444.
(58) *Comprehensive Treatise of Electrochemistry*, Vol. 7; Conway, B. E., Bockris, J. O'M., Yeager, E., White, S. U. M., Eds.; Plenum Press: New York, 1983; p 301−398.
(59) Murthi, V. S.; Urian, R. C.; Mukerjee, S. *J. Phys. Chem.* **2004**, *108*, 11011.

(60) Norskov, J. K.; Rossmeisel, J.; Logadottir, A.; Lindqvist, L.; Kitchin, J. R.; Bligaard, T.; Jonsson, H. *J. Phys. Chem. B* **2004**, *108*, 17886.
(61) Marković, N. M.; Ross, P. N., Jr. *Surf. Sci. Rep.* **2002**, *45*, 117.
(62) Marković, N. M.; Gasteiger, H. A.; Ross, P. N., Jr. *J. Phys. Chem.* **1995**, *99*, 11.
(63) Marković, N. M.; Adžić, R. R.; Cahan, B. D.; Yeager, E. B. *J. Electroanal. Chem.* **1994**, *377*, 249.
(64) Marković, N. M.; Gasteiger, H. A.; Grgur, B. N.; Ross, P. N. *J. Electroanal. Chem.* **1999**, *467*, 157.
(65) Marković, N. M.; Gasteiger, H. A.; Ross, P. N. *J. Electrochem. Soc.* **1997**, *144*, 5.
(66) El Kadiri, F.; Faure, R.; Durand, R. *J. Electroanal. Chem.* **1991**, *301*, 177.